DOCTORAL THESIS

RHEOLOGY OF PASSIVE AND ACTIVE SUSPENSIONS WITH ANISOTROPIC STRUCTURES IN SHEAR FLOWS: MICRO AND MACRO SCALES

Igor Dal Osto Pereira

Brasília, November of 2024.

UNIVERSITY OF BRASÍLIA

FACULTY OF TECHNOLOGY
DEPARTMENT OF MECHANICAL ENGINEERING

UNIVERSITY OF BRASÍLIA
Faculty of Technology
Department of Mechanical Engineering

DOCTORAL THESIS

REOLOGIA DE SUSPENSÕES PASSIVAS E ATIVAS COM ESTRUTURAS ANISOTRÓPICAS EM ESCOAMENTOS CISALHANTES: ESCALAS MICRO E MACRO

Igor Dal Osto Pereira

Thesis submitted to the Department of Mechanical Engineering in partial fulfillment of the requirements for obtaining the title of doctor on mechanical sciences.

Examining Committee

Prof. Francisco Ricardo da Cunha, PhD
Advisor (ENM-UnB)

Prof. Alysson Martins Almeida Silva, PhD
Internal Member (ENM-UnB)

Prof. Edson José Soares, PhD
External Member to the Institution (UFES)

Prof. Paulo César de Morais, PhD
External Member to the Institution
(Physics Department - UCB)

Brasília, November of 2024.

Dedico este trabalho aos meus avós, pais e irmão.

"I seem to have been only like a boy playing on the seashore, and diverting myself in now and then finding a smoother pebble or a prettier shell than ordinary, whilst the great ocean of truth lay all undiscovered before me".

(Isaac Newton)

"Measure what is measurable, and make measurable what is not so".

(Galileo Galilei)

Acknowledgements

Agradeço ao meu orientador, Prof. Francisco Ricardo da Cunha, por sua paciência, generosidade e confiança ao longo deste período de trabalho conjunto. Sou grato por todos os ensinamentos compartilhados, pelas críticas construtivas que tanto contribuíram para o meu crescimento acadêmico e pessoal, e por ser um orientador sempre presente, que inspira em seus alunos o amor pela ciência e pela busca incessante pelo conhecimento.

Aos meus pais, Carlos e Marilei, manifesto minha mais profunda gratidão pelo esforço incansável que sempre fizeram para me proporcionar uma formação moral sólida e a melhor educação possível, a mim e ao meu irmão. Agradeço por nunca desistirem diante das dificuldades da vida e pelo carinho e dedicação incondicionais com que sempre me acolheram. Ao meu pai, agradeço por ser o alicerce da nossa família, representando força, equilíbrio e sabedoria, mesmo nos momentos mais desafiadores. À minha mãe, agradeço pelo amor inabalável e pelos cuidados generosos que tornam qualquer dificuldade mais leve. Ao meu irmão, Fábio, sou grato pelos conselhos valiosos e por sua constante presença nos bons e maus momentos.

Aos amigos do Grupo de Mecânica dos Fluidos de Escoamentos Complexos (VORTEX), minha sincera gratidão, em especial aos colegas Filipe, Gesse, Yuri Zeniti, Marcos Fabrício e Érick Marcelino. Obrigado por tornarem as longas jornadas de trabalho mais leves, suportáveis e, muitas vezes divertidas. Ao Filipe, agradeço por sua amizade genuína e sua constante disposição para ajudar, tanto em questões acadêmicas quanto pessoais. Sou grato também pelas ricas trocas de conhecimento, muitas delas fruto de sua paixão contagiante pelas ciências naturais. Ao Gesse, agradeço pelo companheirismo exemplar e pelos ensinamentos compartilhados ao longo dessa jornada. Você é um modelo de dedicação e excelência como pesquisador. Ao Yuri Zeniti, agradeço pela amizade, pelo companheirismo e pelas discussões sempre produtivas sobre experimentos e análises de resultados, que enriqueceram significativamente este trabalho. Aos amigos Marcos Fabrício, Victor Shumyatsky, Érick Marcelino e Leonardo Inácio minha gratidão pelo apoio, pela troca de ideias e pelas muitas risadas que compartilhamos, tornando essa jornada do doutorado ainda mais especial.

Por fim, agradeço à CAPES pelo apoio financeiro, fundamental para a realização deste doutorado.

Resumo

Neste trabalho, investigam-se fluidos complexos inovadores, de grande relevância para futuras aplicações em engenharia. Esses fluidos são classificados em dois grupos: ativos e passivos. No que diz respeito aos fluidos ativos, abordam-se duas suspensões magnetoreológicas (MRS): uma contendo partículas de magnetita dispersas em óleo mineral, e outra formada pela dispersão de ferro carbonílico no mesmo fluido base. Vale destacar que as estruturas induzidas nesses fluidos pela aplicação de um campo magnético possuem escala micrométrica. São considerados fluidos ativos devido à capacidade de suas propriedades reológicas serem moduladas ativamente por campos magnéticos externos. Verifica-se ainda um aumento expressivo nas propriedades reológicas em comparação com os ferrofluidos, cujos solutos possuem escala nanométrica. Quanto aos fluidos passivos, estudam-se a reologia de suspensões de nanotubos de carbono de parede múltipla e de oleogéis — suspensões de fibras de celulose em uma matriz de amido de batata e óleo de soja. Além do interesse acadêmico, esses fluidos apresentam grande potencial para aplicações práticas, como na redução de arrasto em fluidos com fibras rígidas, no caso dos nanotubos, e em setores como a indústria alimentícia e cosmética, no caso dos oleogéis.

O trabalho adota uma abordagem teórico-empírica, empregando três metodologias experimentais principais. A primeira metodologia envolve ensaios de cisalhamento contínuo, realizados tanto na presença quanto na ausência de campo magnético. Esses testes permitem examinar a viscosidade aparente e a tensão de cisalhamento dos fluidos em função da taxa de cisalhamento e da fração volumétrica de partículas, além da dependência dessas propriedades em relação à intensidade do campo magnético, no caso das MRs. Essa análise possibilita a verificação da aderência ao comportamento predito por modelos de fluido newtoniano generalizado. A segunda metodologia aborda ensaios de escoamento transiente, baseados na aplicação de impulsos de deformação, tanto com quanto sem campo magnético. A partir desses experimentos, são obtidas as funções de relaxação de tensão para os diferentes fluidos, as quais, no caso das MRs, dependem também da intensidade do campo magnético. Com base nessas funções, calculam-se os tempos de relaxação dos fluidos. Observa-se, nas suspensões magnetoreológicas, que a tensão de cisalhamento não se reduz a zero na presença de um campo magnético, mas converge para um valor residual, o qual é avaliado em função da intensidade do campo. A terceira metodologia refere-se aos testes de cisalhamento oscilatório, realizados no regime de viscoelasticidade linear, também sob diferentes intensidades de campo magnético. Nesses ensaios, são determinados os módulos viscoelásticos dos fluidos em função da frequência de oscilação, sendo que, para as MRs, a intensidade do campo magnético também é considerada. Além disso, o módulo de cisalhamento elástico no limite de baixa frequência é calculado e analisado em termos da fração volumétrica de partículas e da intensidade do campo magnético.

Palavras-chaves: Suspensão magnetoreológica, Nanotubos de carbono de parede múltipla, oleogéis efeito magnetoviscoso, efeito pseudoplástico, módulos viscoelásticos, função relaxação de tensão, tensão residual, anisotropia.

Abstract

This work investigates innovative complex fluids that are highly relevant for future engineering applications. These fluids are classified into two groups: active and passive. Regarding active fluids, two magnetorheological suspensions (MRS) are studied: one containing magnetite particles dispersed in mineral oil and the other formed by dispersing carbonyl iron in the same base fluid. It is important to highlight that the structures induced in these fluids by the application of a magnetic field are on a micrometric scale. These fluids are considered active because their rheological properties can be actively modulated by external magnetic fields. Additionally, a significant increase in the rheological properties of MRS is observed compared to ferrofluids, whose solutes are on a nanometric scale. As for passive fluids, the study focuses on the rheology of multi-walled carbon nanotube suspensions and oleogels — which consist of cellulose fibers dispersed in a matrix of potato starch and soybean oil. Beyond academic interest, these fluids have great potential for practical applications, such as drag reduction in fluids with rigid fibers (as in the case of carbon nanotubes) and in the food and cosmetic industries (as in the case of oleogels).

This work follows a theoretical-empirical approach and employs three main experimental methodologies. The first methodology involves steady shear tests, conducted both in the presence and absence of a magnetic field. These tests allow for the evaluation of the apparent viscosity and shear stress of the fluids as a function of shear rate and particle volume fraction. In the case of MRS, the dependence of these properties on the magnetic field intensity is also assessed. This analysis verifies whether the rheological behavior of these fluids adheres to generalized Newtonian fluid models. The second methodology focuses on transient flow tests, applying deformation pulses both with and without a magnetic field. From these experiments, the stress relaxation functions of the different fluids are obtained, which, in the case of MRS, also depend on the magnetic field intensity. Based on these functions, the relaxation times of the fluids are calculated. It is observed that, in magnetorheological suspensions, the shear stress does not decay to zero in the presence of a magnetic field but instead converges to a residual stress, which is evaluated as a function of the field intensity.The third methodology involves oscillatory shear tests, conducted under conditions of linear viscoelasticity and varying magnetic field intensities. In these tests, the viscoelastic moduli of the fluids are determined as a function of the oscillation frequency, with the magnetic field intensity also considered in the case of MRS. Additionally, the elastic shear modulus is calculated in the low-frequency limit and analyzed in terms of particle volume fraction and magnetic field intensity.

Key-words:Magnetorheological suspension, Multi-walled carbon nanotubes, Oleogels, Magnetoviscous effect, Pseudoplastic effect, Viscoelastic moduli, Stress relaxation function, Residual stress, Anisotropy.

List of Figures

List of Tables

List of abbreviations and acronyms

SAOS	Small amplitude oscillatory shear
GNF	Generalized Newtonian fluid

Symbols

Latine symbols

A_j	Amplitude of tension Generalized Maxwell's model
D	Stokes-Einstein's diffusion coefficient
$\boldsymbol{D}$	Strain rate tensor
$\boldsymbol{D}_S$	Hydrodynamic dipole of particle
$E()$	Experimental error
$E_i()$	Instrumental error
$E_r()$	Random error
$\boldsymbol{f}$	force over a particle
L	Macroscopic characteristic scale
$\mathcal{F}$	Functional
$\boldsymbol{J}$	Density of electric current
k_B	Boltzmann's constant
$\boldsymbol{L}$	Antisymmetric part of the hydrodynamic dipole
$\boldsymbol{m}$	Magnetic moment of dipole
$\boldsymbol{M}$	Magnetization
$G''(\omega)$	Loss modulus
$G'(\omega)$	Storage modulus
$\boldsymbol{H}$	Magnetic field
$\mathcal{P}$	Material particle
p	Mechanic pressure
p_0	Thermodynamic pressure
$\boldsymbol{S}$	Symmetric part of the hydrodynamic dipole
$\boldsymbol{t}$	Torque over a particle
$\boldsymbol{Q(t)}$	Orthogonal tensor
$\boldsymbol{F(t)}$	Gradient of deformation tensor
$\boldsymbol{x}$	Position vector
$\mathcal{V}$	Measured variable
V	Volume of a continuous body
v_p	Particle volume

W	Work

Greek symbols

a	particle diameter
α	Nondimensional magnetic field
γ	Angular deformation
δ	Virtual variation
$\delta(\boldsymbol{x}-\boldsymbol{x}_i)$	Dirac's delta function
$\Delta\eta$	Viscosity increment
λ	Dipolar interaction parameter
h	Gap between the disks of the rheometer
ω	Angular frequency
ϕ	Volume fraction
ϕ_h	Hydrodynamic volume fraction
$\Phi(s)$	Stress relaxation function
Φ_R	Residual stress relaxation parameter
ρ	Density
ρ_s	Density of free charges
$\eta''(\omega)$	Complex viscosity
$\eta'(\omega)$	Viscosity modulus
η_ϕ	Einstein's viscosity
η_ϕ	rotational viscosity
$\dot{\gamma}$	Shear rare
Ω	Angular velocity
τ_f	Characteristic time of the flow
τ	Time of relaxation
τ_B	Brownian time of relaxation
τ_m	Time of relaxation for the weaker magnetic field condition
τ_N	Néel's time of relaxation
τ_j	time of relaxation assossiated with the j-th Maxwell's element
τ_p	Main relaxation time
$\boldsymbol{I}$	Identity tensor
$\boldsymbol{\Sigma}$	Stress tensor
$\boldsymbol{\sigma}$	Deviatoric part of the stress tensor
σ_R	Residual stress
ξ	initial position
μ	Vacuum magnetic permeability
η_0	Viscosity in the absence of magnetic field
$\boldsymbol{u}$	Velocity vector

δV	Volume of a continuum particle
$\delta v'$	Volume of the smallest continuum particle

Summary

1 INTRODUCTION

1.1 Motivation

A suspension is chemically a kind of mixture formed by two or more phases. At least one of these phases is a liquid or a semi-solid and the other phases are solid particles. In this work, two types of suspensions are treated: magneto-rheological suspensions (MRS) and suspensions of double-walled carbon nanotubes (DWCN).

Since the seminal work of Rabinow (RABINOW, 1948) in the 1940s, magnetorheology has become a multidisciplinary field that has incited strong research interest in the last 20 years. According to Vicente, Klingenberg and Hidalgo-Alvarez (2011), the rheology of magnetorheological fluids is very attractive since they are intelligent materials which show a reversible and very fast (in a fraction of milliseconds) transition from liquid to a nearly solid-state under the presence of external magnetic fields (magnetoviscous effect). Their strength (yield stress) can change from 0 to 100 kPa by the action of an external magnetic field. This advantage of these fluids over conventional mechanical interfaces makes them very suitable for applications in mechanical systems that deal with vibration control or torque transmission. Important examples are dampers (DYKE et al., 1996; JR et al., 1997), brakes and clutches (WANG; MENG, 2001), seismic vibration dampers, control valves and artificial joints (KLINGENBERG, 2001). De Vicente *et al.* (VICENTE; KLINGENBERG; HIDALGO-ALVAREZ, 2011) present other applications of this type of fluids, which are in the fields of energy transfer, biomedics , precision polishing, sound propagation, isothermal magnetic advection and chemical sensing among others.

Suspensions of carbon nanotubes are polyphasic systems generated by the dispersion of a given type of nanotubes (rod-shaped) in a matrix, which can vary from liquids of small viscosity to polymer solutions of high viscosity (HOBBIE, 2010). There are two types of nanotubes that are used in the production of the suspensions: single walled carbon nanotubes (SWCN) and the multi-walled ones (MWCN) (FAN; ADVANI, 2007). This difference of solute is observed to impact the resulting rheological properties of the suspensions due to the fact that the SWCN tend to be stronger than the MWCN. This type of suspension is part of the field of nanomaterials and nanotechnology, presenting the following most important applications: solar energy (KARAMI et al., 2014), biomechanics / biomedicine (ARUTYUNYAN; BAKLASHEV; OBRAZTSOVA, 2010), electronics

(MANZETTI; GABRIEL, 2019) and optics (WANG; CHEN; BLAU, 2009).

This work is motivated by interests on the complex rheology of magnetorheological suspensions and suspensions of carbon nanotubes, when subjected to different types of shearing flows. Specifically, in the case of the MRSs there is a preponderant interest on their rheological behavior under the application of an external magnetic field. It is important to remark that these topics are actual and researches in their field are constantly generating new and ever evolving applications. In this work, it will be studied the rheological behavior of two MRSs, which differ on the solid particles used on its formulation: one is made of magnetite and the other of carbonyl iron. The rheological behavior of a suspension of double walled carbon nanotubes will be also extensively examined.

As an exemple of the greatest possibilities of applications of magnetic fluids is given by Contreras-Mateus et al. (2024). This review examines the potential integration of ferrofluid technologies into key oil industry processes: recovery and transportation, which are essential components of the oil supply chain. It discuss critical theoretical aspects, focusing on the stability of ferrofluids—a pivotal yet underexplored topic, particularly in the context of nanoparticle applications in oil recovery and transportation. The review also delves into magnetic properties, constitutive equations of ferrohydrodynamics, and magnetoviscous effects that explain the diverse rheological behaviors of ferrofluids under uniform and oscillating magnetic fields. Additionally, experimental studies are highlighted, simulating real-world scenarios to analyze the physicochemical interactions between ferrofluids and crude oils under external magnetic fields and reservoir-like thermodynamic conditions.

It is important to emphasize that this work is also deeply motivated by other studies dealing with rheology of complex fluids. These works comprehend theoretical, numerical and experimental studies. Pereira and Cunha (2020) shows important methodologies useful on dealing with experimental determination of material functions of complex fluids, arising from both permanent and transient shearing flows. Cunha, Sinzato and Pereira (2022) present experimental evidence that ferrofluids may be represented as a colloidal suspension of ellipsoidal particles. This paper presents experimental evidence obtained from capillary and rheometry in the presence of an external magnetic field, which are compared to a numerical simulation. It is important to remark that an innovative stress tensor of the magnetic fluid, based on principles of microhydrodynamics and electromagnetism, is proposed and used, showing a good agreement with the experimental data. Sinzato and Cunha (2020) investigate the flow of a non-symmetric ferrofluid undergoing a uniform magnetic field in axial symmetry through both theoretical and experimental approaches. The magneto viscous effect is investigated for a fully developed laminar flow. A regular perturbation method is used to obtain new asymptotic solutions on the limits of very low and very high flow intensities. Additionally, numerical integration of the governing equations system provides a solution for the entire range of flow intensities. The magnetization profiles and more global quantities like wall viscosity and the relative viscosity are determined. The numerical and asymptotic solutions present an excellent agreement in the application range of the asymptotic solution. Finally, the magneto viscous effect in capillary flow is also determined through an experimental investigation, showing a very good agreement with the asymptotic solution corresponding to the limit of a low flow intensity. Sinzato and Cunha (2021) provide a clear view of a phenomena that impacts the rheology of particulate systems. In the case of the referred work, magnetic suspensions flowing in circular capillars are the focus of analysis. The phenomena is the shear-induced dispersion, which arises either due to particle roughness or non-sphericity (i.e., shape anisotropy). The study is carried out numerically, considering first rough spheres, with the results showing that the dispersive flux by shear rate gradient produces a particle migration toward the center of the tube. When prolate spheroidal particles are considered, the anisotropy of the particles are found to intensify or reduce the viscous dissipation depending upon the physical parameters. For weak applied fields and weak shear rates, the relative viscosity presented a rising dependence with the aspect ratio. In contrast, at strong flows and/or large applied fields, the net result was a relative viscosity reduction in comparison with a suspension of spheres.

Rosa and Cunha (2019) discuss the role of the dipolar particle interactions on the rheological behavior of a ferrofluid. They present the results of magnetization and rheology in terms of a rotational viscosity obtained by applying Brownian dynamics simulations for a periodic magnetic suspension, where the many body long-range dipole-dipole interactions are numerically calculated. The dependence of these macroscopic properties on the dipolar interactions is explored in ferrofluids undergoing both weak and strong shear flows in the presence of a uniform magnetic field. We show that for weak shear flows the dipole-dipole interactions produces a magnetization increasing. In contrast, for strong shear flows, the dipolar interactions always have an effect of decreasing magnetization. The numerical simulations show chain-structure formation oriented in the direction of the magnetic field (i.e., perpendicular to the direction of the shear) for weak flows, which explains the remarkable increasing of the suspension rotational viscosity as a function of the applied magnetic field and of the dipolar interactions parameters. Cunha and Rosa (2021) investigate the viscoelastic behavior of a magnetic colloidal fluid undergoing an oscillatory simple shear flow and also under the influence of an external magnetic field. The main goal of the referred work is to examine the influence of the dipolar interactions and formation of anisotropic structures on the macroscopic rheological response of these complex fluids. This study is performed by direct numerical simulation of neutrally buoyant, Brownian magnetic spheres in the limit of vanishingly small Reynolds numbers using Brownian dynamics The results show that the viscoelastic transition in the fluid is anticipated in the presence of dipolar interactions. the authors offer evidence that the relaxation time has a quadratic power law scaling dependence on the dipolar interaction parameter and that the dipolar interactions are the main physical mechanics, which creates elastic response of the ferrofluid investigated here as a direct consequence of the gain of memory at the microscopic level due to the action of the magnetic torque on the particles and the formation of oriented aggregative structures like anisotropic chains. Malvar and Cunha (2021) present an study in which a nonlinear phenomenological model for neutrally buoyant force-free active suspension of nematodes is proposed and tested. This paper is very important due to the fact that it presents innovative techniques on developing constitutive equations for the stress tensor of the active suspension and also very useful methodologies to deal with non-linear oscillatory shear.

1.2 Bibliografic review

1.2.1 Magneto-rheological suspensions

Kumar et al. (2019) explain that magnetorheological (MR) fluids are composed of three primary components: magnetic particles, a carrier fluid, and additives. The magnetic particles typically consist of carbonyl iron with 99% purity, owing to its high saturation magnetization ($\mu_0 M_S = 2.1$ T) (VICENTE; KLINGENBERG; HIDALGO-ALVAREZ, 2011; ASHTIANI; HASHEMABADI; GHAFFARI, 2015). These particles, usually spherical in shape, are produced through the chemical vapor decomposition of iron pentacarbonyl. Their concentration in MR fluids generally falls between 20% and 40% by volume, with particle sizes typically ranging from 3 to 5 μm and averaging around 4.25 μm (KUMAR et al., 2019). The carrier fluid can be mineral oil, silicone oil, polyesters, polyethers, synthetic hydrocarbons, or water. The choice of base fluid depends on the intended application of the MR fluid—for example, water is commonly used for polishing due to its properties, while silicone oil is preferred for vibration control due to its high viscosity and other beneficial characteristics (ASHTIANI; HASHEMABADI; GHAFFARI, 2015). It is crucial that the carrier fluid does not chemically react with the iron particles. Additives are essential to prevent sedimentation and particle aggregation, as well as to enhance lubricating properties. These include thixotropic agents, surfactants, and polymers.

Vicente, Klingenberg and Hidalgo-Alvarez (2011) attribute the magnetoviscous effect observed in MR fluids under an external magnetic field to the field-induced magnetization of the suspended particles. When a magnetic field is applied, the particles become magnetized and align along the field lines to minimize their magnetic interaction energy, forming anisotropic structures (GENÇ; PHULÉ, 2002). MR fluids exhibit a high static yield stress, defined as the minimum shear stress required to induce flow in the suspension. Genç and Phulé (GENÇ; PHULÉ, 2002) state that this static yield stress increases with the intensity of the applied magnetic field. Additionally, MR fluids demonstrate shear rate-dependent viscosity and enhanced viscoelastic behavior under the influence of a magnetic field. In the absence of such a field, MR fluids resemble liquid paints in terms of consistency, with apparent viscosities ranging between 0.1 and 1 Pa.s^{-1} at low shear rates.

Various other types of MR fluids have also been described in the literature. Cunha, Rosa and Dias (2016) discuss highly diluted MR fluids containing micrometric clusters formed by nanometric magnetite particles, which assemble under the influence of an external magnetic field. The rheological behavior of these suspensions is strongly influenced by the field-induced microstructure (degree of anisotropy) and the particle volume fraction. Another significant class of MR fluids is inverse ferrofluids, which consist of micron-sized non-magnetizable particles dispersed in a ferrofluid (VICENTE; KLINGENBERG; HIDALGO-ALVAREZ, 2011). The mechanical properties of these fluids can be tailored by adjusting the strength of the magnetic field or the saturation magnetization of the ferrofluid. Inverse ferrofluids are particularly attractive for applications due to the wide variety of available non-magnetizable particles, which offer a broad range of sizes and shapes.

1.2.2 MR fluids preparations and compositions

The preparation of magnetorheological fluids includes two main components: solid phase and liquid phase. Since these fluids are micron-scale particulate suspensions, their components present a density mismatch, turning the problem of settling a very important issue (VICENTE; KLINGENBERG; HIDALGO-ALVAREZ, 2011). Besides that, other significant phenomena to be addressed is the tendency of aggregation of the particles, which is primarily due to the action of the magnetic dipolar interactions between them.

De Vicente (VICENTE; KLINGENBERG; HIDALGO-ALVAREZ, 2011) argues that a very direct way to avoid the settling of particles and enhance the overall kinetic stability of the suspension is by reducing the magnetic particles' size. Nonetheless, it is important to note that the size reduction is limited to the range near to the nanometer, because of the prevalence of Brownian forces in this condition.

Most MR fluid compositions show poor redispersibility, that is, once the particles settle out, they form a very tightly bound network or “cake", which is extremely difficult to remix (PHULÉ; MIHALCIN; GENC, 1999). This phenomenon is related to small levels of remnant magnetization of the fluid's particles, which boosts the magnetic interactions, which summed with the action of Van-der-Waal's forces create a strong bond between the particles. Therefore, a large amount of mechanical energy is required to breakdown the chain structures and agglomerates (ASHTIANI; HASHEMABADI; GHAFFARI, 2015), which is translated in the necessity of using shear-rates of large magnitude for the fluid flow even in the “off" state. It is important to note that the “cake" remains even after the magnetic field is turned off, resulting in non-homogeneous behavior of the magnetorheological fluid.

According to Kumar *et al.* (KUMAR et al., 2019), to prevent settling and formation of aggregates, several strategies are discussed in the literature. Surfactants have been used to delay the time of settling and to facilitate redispersion (LÓPEZ-LÓPEZ et al., 2008;

LÓPEZ-LÓPEZ; KUZHIR; BOSSIS, 2009). To mitigate the clustering of iron particles, oleic acid, and tetramethylammonium hydroxide have been used as surfactants (SARKAR; HIRANI, 2013). Aiming to slow down the sedimentation process of the magnetic particles in suspension, it is reported the use of thickeners like fluorocarbon grease (IYENGAR; YURGELEVIC; FOISTER, 2010), colloidal clays (organoclays) (FOISTER; IYENGAR; YURGELEVIC, 2003; HATO et al., 2011), and fumed silica (IYENGAR; FOISTER, 2002), being the clays the most effective ones.

Thixotropic agents networks can be prepared by using nano-structured fumed silica, anisotropic carbon fibers, acicular iron oxide nanoparticles, and surfactants such as stearate and oleate (VICENTE; KLINGENBERG; HIDALGO-ALVAREZ, 2011). These agents are used to separate the magnetic particles by forming strand or chain-like structures that encompass and trap the particles. As an alternative to surfactants, coatings have also been considered. The use of polyvinyl butyral as a coating for iron particles showed improved anti-corrosion characteristics and reduction of the density of the particles, preventing, thus, the formation of hard clusters (ZHANG et al., 2009).

Another approach is the production of MR fluids based on a mixture of magnetic nanoparticles (up to 3% volume) and magnetic micron-particles (up to 32% volume). These suspensions have shown excellent stability against sedimentation and aggregation (KUMAR et al., 2019). This occurs since the nanoparticles occupy the voids between the micron-particles and form regular chains on the application of an external magnetic field. The addition of nanoparticles also affects the overall rheological behavior of the suspension. Ashtani *et al.* (ASHTIANI; HASHEMABADI; GHAFFARI, 2015) show that the addition increases the yield stress of the fluid and Portillo and Iglesias (PORTILLO; IGLESIAS, 2017) found that the shear stress was higher in suspension with the addition of nanoparticles in comparison to those formed just by micron-sized particles. The latter authors also discovered that the nanoparticles formed a “halo" around the magnetic iron particles, as shown in figure (1). This helps in preventing agglomeration and aids in re-dispersion. Nanoparticles addition is considered nowadays a better solution to avoid sedimentation problems than surfactant addition.

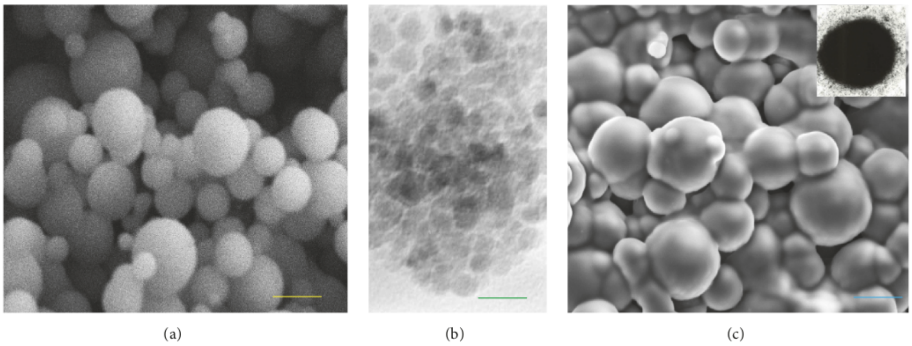

Figure 1 – (a) SEM picture of the iron micro particles; bar length 5 μm. (b) TEM picture of the magnetite nanoparticles; bar length 20 μm. (c) SEM picture of the iron micro particles and magnetite nanoparticles; bar length 5 μm (inset picture: cloud of nanoparticles around one Fe micro particle). Adapted from (PORTILLO; IGLESIAS, 2017).

The durability of an MR fluid is directly related to the oxidation process of its magnetic particles. This process causes the rusting of the iron particles and, as a result, severely affects the performance of the magnetorheological fluids. An effect that results from the oxidation of the particles is the “in-use-thickening", which is the increase of the off-state viscosity of MR fluids over time (VICENTE; KLINGENBERG; HIDALGO-ALVAREZ, 2011; WAHID et al., 2016). This is believed to be caused by the increase of the solid volume (particle’s oxide layer) and perhaps by colloidal forces acting between the small particles generated in the oxidation process. It is also reported that the magnetic field-induced yield stress decreases with the increasing extent of oxidation, which is caused by the fact that when the particle oxidizes, its shell grows, which results in weaker particle magnetizability (SUNKARA et al., 2009).

1.2.3 Rheological behavior of MR fluids

1.2.3.1 Physical mechanisms, micromechanical models and structures formation

Magnetorheological fluids are known for having field-induced magnetization and tunable anisotropic behavior. A widely accepted mechanism to account for these effects is the so-called particle magnetization model (VICENTE; KLINGENBERG; HIDALGO-ALVAREZ, 2011). According to this model, the magnetorheological effect (MR effect) is attributed to the magnetic permeability mismatch between the constituent (continuous and dispersed) phases.

Although the particles in magnetorheological suspensions behave as magnetic multidomains, to study the interactions between particles in suspension, it is usual to neglect multipole and multibody magnetostatic interactions between them. In the linear magnetization regime, an isolated particle of relative permeability μ_p surrounded by a fluid of relative permeability μ_f, which is placed in an external magnetic field $\boldsymbol{H_0}$, acquire a magnetic moment: $\boldsymbol{m} = 4\pi\mu_0\mu_f\beta a^3\boldsymbol{H_0^2}$, where a is the radius of the particle, μ_0 is the permeability of the vacuum and $\beta = (\mu_p - \mu_f)/(\mu_p + 2\mu_f)$ is a coupling parameter. Considering this model, the interaction energy between two dipoles of moment m is given by (BOSSIS et al., 2002):

$$W = \frac{1}{4\pi\mu_0\mu_f}\left(\frac{\boldsymbol{m_\alpha m_\beta}}{r^3} - \frac{3(\boldsymbol{m_\alpha r})(\boldsymbol{m_\beta r})}{r^5}\right), \tag{1.1}$$

where $\boldsymbol{r}$ is the separation vector between the centers of the two particles. This energy is minimum when the two dipoles are aligned with $\boldsymbol{r}$ and maximum when they are perpendicular, leading to a preferential aggregation of chains of particles in the direction of the field. The formation of aggregates of particles will depend on the ratio of this interaction to the thermal energy kT. Taking as reference the energy of two dipoles in the linear regime, the referred rate is given by:

$$\lambda = \frac{1}{4\pi\mu_0\mu_f}\frac{\boldsymbol{m}^2}{r^3}\frac{1}{kT} = \frac{\pi\mu_0\mu_f\beta^2a^3\boldsymbol{H_0}^2}{2kT}. \tag{1.2}$$

This parameter is commonly addressed in the literature as the parameter of dipolar interaction (ROSENSWEIG, 2013). It is important to note that for usual magnetic field intensities the magnetic forces dominate the Brownian forces. In conditions of small values of λ, Brownian motion dominates and field-induced aggregates do not form. In equation (1.2), $0 < \beta < 1$ represents conventional MR fluids and $-0.5 < \beta < 0$ for inverse ferrofluids, in which the base fluid is magnetizable and the particles are non-magnetizable.

Bossis *et al.* (BOSSIS et al., 2002) argue that the quantity λ is the key quantity, which together with the volume fraction of particles $\phi = Nv_p/V$, will determine the equilibrium structure of a suspension of monodisperse particles as a function of the applied magnetic field. Aiming to understand all the quantities which rule the suspension behavior, it is important to start from the equation of motion for one particle and then put it in a non-dimensional form. Considering an approach of Brownian and Stokesian dynamics, for a given particle in suspension, it can be written (BRADY; BOSSIS, 1988; BONNECAZE; BRADY, 1992):

$$m\frac{d\boldsymbol{v}}{dt} = \boldsymbol{F^H} + \boldsymbol{F^{ext}} + \boldsymbol{F^I} + \boldsymbol{F^B}, \tag{1.3}$$

where $\boldsymbol{v}$ is the particle's velocity. $\boldsymbol{F^H}$ is the hydrodynamic force acting upon the test particle, which results from the hydrodynamic friction, being proportional to $-\xi(\boldsymbol{v} - \boldsymbol{v^0})$, where $\xi = 6\pi\mu a$ with μ representing the viscosity of the suspending fluid and $\boldsymbol{v^0}$ the imposed velocity field at the location x of the particle. $\boldsymbol{F^{ext}}$ is the hydrodynamic force due to the symmetric part of the velocity gradient tensor, which in the case of a pure shear, characterized by the shear-rate $\dot{\gamma}$, scales as $6\pi\mu\dot{\gamma}a^2$. The force $\boldsymbol{F^I}$ is the interparticle force coming from the dipole-dipole interaction, being given as minus the gradient of equation (1.1). Considering two particles α and β, the force on α will be (BOSSIS et al., 2002):

$$\boldsymbol{F^I_\alpha} = 12\pi\mu_0\mu_f a^2\beta^2H_0^2\left(\frac{a}{r}\right)^4\left[\left(2\cos^2\theta_{\alpha\beta} - \sin^2\theta_{\alpha\beta}\right)\boldsymbol{e_r} + \right. \tag{1.4}$$

$$\left. + \sin 2\theta_{\alpha\beta}\boldsymbol{e_\theta}\right]. \tag{1.5}$$

The different vectors are displayed on figure (2).

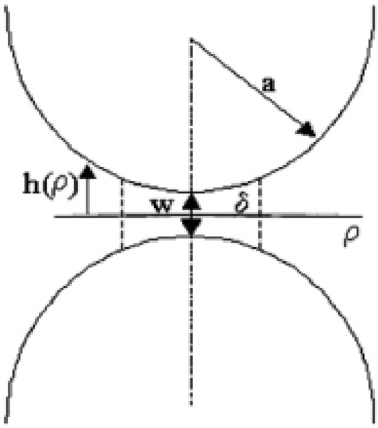

Figure 2 – Two particles in a magnetic field. Adapted from (BOSSIS et al., 2002).

Considering the case of interest, in which two identical spheres are placed side-by-side ($r = 2a$,$\theta_{\alpha\beta} = 90°$), it comes that $F^I_\alpha = f_d = -(3/4)\pi\mu_0\mu_f a^2\beta^2 H_0^2$, which implicates in the choice of $-f_d$ as the scaling factor of the interparticle force. $\boldsymbol{F^B}$ is the Brownian random force which scales with kT/a. Generally, the inertial force can be neglected, since the time τ needed for the particle to reach a constant velocity is much smaller than the other characteristic times, for example for an iron particle of radius 1 μm, τ = 1.7 μs (BOSSIS et al., 2002). Dividing all the terms of equation (1.3) by $6\pi\mu\dot{\gamma}a^2$ and rearranging, one obtains:

$$\frac{\boldsymbol{v} - \boldsymbol{v^0}}{\dot{\gamma}a} = \frac{\left[\boldsymbol{F^I}\right]}{Mn} + \frac{\left[\boldsymbol{F^B}\right]}{Pe} + \left[\boldsymbol{F^{ext}}\right], \tag{1.6}$$

where the terms in brackets indicate that the force has been divided by its own scaling factor.

Mn is the mason number, defined as:

$$Mn = -\frac{6\pi\mu\dot{\gamma}a^2}{f_d} = \frac{8\mu\dot{\gamma}}{\mu_0\mu_f\beta^2H_0^2}. \tag{1.7}$$

This non-dimensional parameter expresses the ratio of shear to magnetic forces. Pe is the Peclét number, expressed by:

$$Pe = \frac{6\pi\mu\dot{\gamma}a^3}{kT}, \tag{1.8}$$

which represents the ratio of shear to Brownian forces. It is important to note that for particles larger than one micron and usual shear-rates, Pe is large, meaning that the Brownian force can be neglected. From the definition of the dimensionless parameters, it can be seen that the dimensionless equation of motion depends on two of those quantities because they are related as follows: $Mn\lambda = 2Pe/3$. According to Bossis *et al.* (BOSSIS et al., 2002), this implicates that for a given suspension, all the trajectories and hence all the properties and, in particular, the viscosity will be the same for the same values of Mn and λ. It is important to note that this conclusion only applies to systems of particles starting in the same initial conditions, that is, the same volume fraction and initial configuration. The last constraint is not critical when the interest is on equilibrium properties, therefore it can be said that for monosized hard spheres with particles having the same magnetic permeability, the viscosity (normalized by the one of the carrier fluid) will depend only on three quantities, which are ϕ, Mn and λ.

When a magnetorheological fluid is under the action of an external magnetic fluid, its particulate phase will aggregate and form a different kind of structures depending on the initial volume fraction ϕ and on the parameter of dipolar interaction λ. This is only true if the equilibrium state is reached, which is achieved by raising the magnetic field intensity. Mohebi *et al.* (MOHEBI; JAMASBI; LIU, 1996) observed, from an experimental point of view, that the rate of increase of the magnetic field and the container size profoundly impact the final particle structuration. Increasing the field too quickly will give a kind of labyrinthine structure, whereas increasing the field too slowly gives well-separated columns. Another important feature is that large volume fractions always tend to form labyrinthine structures.

The Kinetic aggregation process is typically divided into two well-differentiated regimes. the first one is characterized by the formation of linear chains of particles. According to Bossis *et al.* (BOSSIS et al., 2002), the average lengths of the referred chains follow the Smoluchowski equation. The second effect is the formation of columnar structures by laterally aggregation of single-width chain-like structures. De Vicente *et al.* (VICENTE; KLINGENBERG; HIDALGO-ALVAREZ, 2011) affirm that mechanisms explaining this lateral aggregation are the coalescence through torque-driven zippering motion and thermal fluctuations of particle positions.

1.2.3.2 Yield stress

The yield stress (τ_y) of MR fluids developed in the presence of a magnetic field is by far its most important rheological property, being considered a parameter of efficiency since it is the main parameter observed in the design of applications. Colloquially, this material function is known as the strength of the fluid owing to the fact that it is the maximum shear stress that must be applied for the fluid to start flowing. From a micromechanical point of view, the restoring force per unit of surface which resists to the deformation of the structure is given by the derivative of the magnetic energy per unit of volume, given by equation (1.1), relative to the strain γ: $\tau = -dW/d\gamma$. The yield stress represents the maximum of the stress versus strain: $\tau_y = max(\tau)$, since above a critical shear strain γ_c, the microstructure will start to break (BOSSIS et al., 2002).

According to Bossis *et al.*, in order to understand and predict the yielding behavior of MR fluids, it is necessary to deal with two scales. The first one is the particle scale that will give the force between two particles as a function of their physical properties and respective positions. The second one is the scale of the device (container), in which is necessary to know the behavior of the mesostructure of the particles' aggregates and its deformation. Besides that, two situations can be distinguished depending on the permeability of the particles. If the permeability is high ($\sigma = \mu_p/\mu_f \gg 1$), it is the particle scale which is important since the forces strongly depend on the particle gap. If σ is low, dipolar approximations can be used and the separation between the particles does not change significantly the energy, therefore it is the shape of the mesostructure and its inclination relative to the field which generates the yield stress.

The case of interest here is the one of high permeability ($\sigma \gg 1$) since it represents the behavior of strong MR fluids (micron-sized magnetizable particles dispersed on a non-magnetizable carrier fluid). In this case, the standard model for the structure is used, which is based on a cubic network of infinite chains of particles aligned in the direction of the field. When the material is strained, the chains are supposed to deform affinely with the strain, that is, the particles take place only along the velocity lines as shown in figure (3). Therefore, the distance between any pair of neighbors in the chains is the same and increases at the same rate. Considering these hypotheses and accounting for the dipolar interactions between the particles, Bossis (et al.) (BOSSIS et al., 2002) calculate analytically the yield stress for an MR fluid composed of equal spheres as:

$$\tau_y = 2.31\phi\mu_0 M_S^{1/2} H^{3/2}, \tag{1.9}$$

where M_S is the magnetization of saturation of the particles.

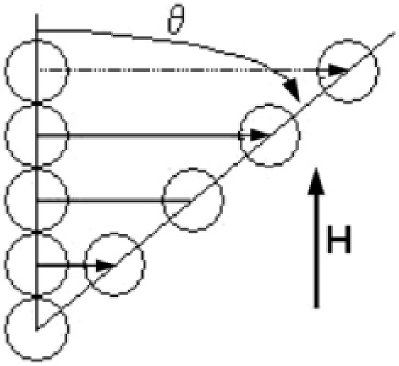

Figure 3 – Modelling the yield stress. Affine deformation of a chain. Adapted from (BOSSIS et al., 2002).

Bossis and his coworkers (BOSSIS et al., 2002) also punctuate that generally, the yield stress has a dependence on the intensity of the magnetic field in a power-law fashion, $\tau_y \sim H^n$. Several groups (CHEN et al., 1998; RANKIN; HORVATH; KLINGENBERG, 1999; PHULÉ; MIHALCIN; GENC, 1999) have found a power law with an exponent close to 3/2 as predicted by equation (1.9). Nonetheless, linear dependence has been observed (JIANG et al., 1997) and also an exponent 1.27 in conditions of weak low magnetic field intensity for a suspension of iron spheres (BOSSIS et al., 2002). For strong magnetic fields, the yield stress was found to be independent of the magnetic field intensity, being proposed by Ginder *et al.* (GINDER; DAVIS; ELIE, 1996), that in this regime the yield stress is well modeled by:

$$\tau_y = 0.086\phi M_S^2. \tag{1.10}$$

From finite element analysis and analytical deductions, the yield stress was found to be proportional to the volume fraction of particles (see equation (1.9)). This fact is observed experimentally at not too high volume fractions ($\phi < 0.2 - 0.3$)(RANKIN; HORVATH; KLINGENBERG, 1999; KORDONSKY et al., 1990; GENÇ; PHULÉ, 2002). For higher volume fractions a more rapid increase than linear is observed, which can be understood by the fact that thick aggregates are more difficult to break than individual chains. It can also be associated with the non-affine motion of the aggregates.

Yield stress can be measured by direct and indirect experimental approaches, which involve steady and/or oscillatory shearing flow tests. From figure (4)(a), which is a plot of the shear stress as a function of the strain, it can be defined three yield stresses (VICENTE; KLINGENBERG; HIDALGO-ALVAREZ, 2011):

- Elastic limit yield stress: this rheological property represents the maximum shear stress that can be applied while still obtaining complete recovery when the stress is removed;
- Static yield stress: this material function is the minimum stress required to cause the fluid to flow; and
- Dynamic yield stress: this property corresponds to the stress needed to continuously break the aggregates which constantly reform in the presence of the magnetostatic forces once the stress exceeds the static yield stress.

Figure (4)(b) presents an example of experimental data concerning the growth of the yield stress after the start-up of a shearing flow as a function of the shear strain at a weak shear rate for inversed ferrofluids. In this context, according to De Vicente *et al.* (VICENTE; KLINGENBERG; HIDALGO-ALVAREZ, 2011), it is important to note that the static yield stress is usually estimated using creep tests, the tangent method, and low-shear-extrapolation of stress-controlled data in double logarithmic representations of stress versus shear rate. Besides that, the dynamic yield stress can be obtained by adjusting a viscoplastic constitutive model, such as Bingham, Herschel-Bulckley, or Casson to experimental data at non-zero shear rates.

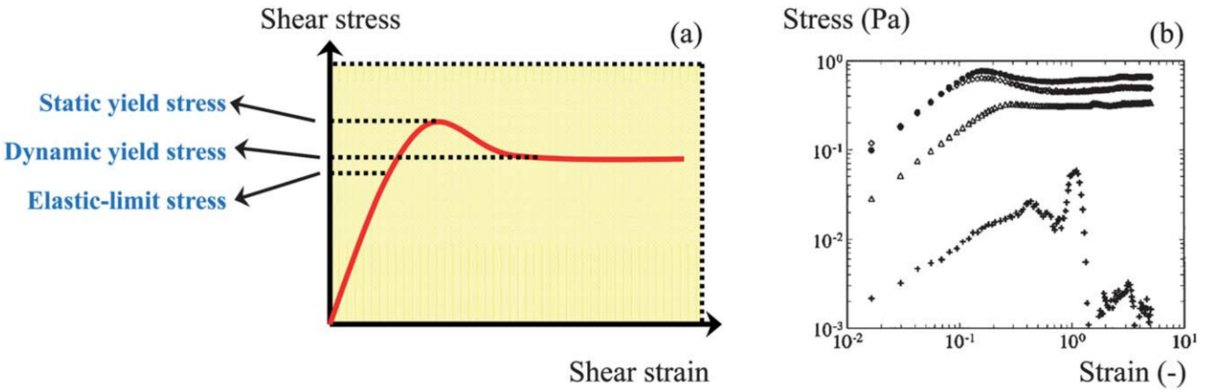

Figure 4 – (a) Typical yield stresses under stress growth (start-up) shearing flow tests. Adapted from (VICENTE; KLINGENBERG; HIDALGO-ALVAREZ, 2011) (b) An example of the shear stress growth after start-up as a function of the shear strain at a shear rate of $\dot{\gamma} = 0.0103s^{-1}$ for inverse ferrofluids. The magnetic field is 76.7 kAm^{-1} and the volume fraction of the nonmagnetic particles is $\phi = 0.18$. Particle radii: 53 nm (+), 84 nm (△), 138 nm (●), 189 nm (◊). Adapted from (VICENTE; KLINGENBERG; HIDALGO-ALVAREZ, 2011; GANS et al., 2000).

1.2.3.3 Flow regime

Magnetorheological fluids, when in the presence of an external magnetic field, show a strong shear-thinning behavior. According to Bossis *et al.* (BOSSIS et al., 2002), in steady shear flow regime, the relation between shear stress and shear-rate is usually well described by the Bingham model: $\tau = \tau_d + \eta_0\dot{\gamma}$. Calling η_s the effective viscosity (defined by $\tau = \eta_s\dot{\gamma}$) and then normalizing by the stress at zero field, one obtains the following expression for the relative viscosity: $\eta_r = \eta_s/\eta_0$. This rheological property decreases as $\tau_d/\eta_0\dot{\gamma}$, that is, proportional to Mn^{-1}, where Mn is the mason number defined by equation (2.28). However, experiments (FELT et al., 1996; GANS et al., 1999) and simulations (BAXTER-DRAYTON; BRADY, 1996) show that the Mason number does not allow to collapse all the results on the same flow curve. The reduced viscosity still follow a law of the kind $\eta_r = Mn^{\nu}$, where ν varies from 0.68 to 1.

Marshall *et al.* (MARSHALL; ZUKOSKI; GOODWIN, 1989) employed dimensional analysis to show that, in the limit of $\lambda \to \infty$, when the Bingham model can explain the steady shear flow behavior and the yield stress scales as $\alpha\mu_0\mu_f\beta^2H^2$, the dimensionless viscosity can be written as:

$$\eta/\eta_\infty = 1 + Mn^*(\phi)Mn^{\Delta}, \tag{1.11}$$

where $\Delta = -1$, η_∞ is the high shear viscosity (independent of the magnetic field intensity) and Mn^* is the critical Mason number. This parameter according to De Vicente *et al.* (VICENTE; KLINGENBERG; HIDALGO-ALVAREZ, 2011), determines the transition from magnetization to hydrodynamic control of the suspension structure. Models based on the micromechanics of chain-like interactions have been developed aiming to comprehend the dependence of Mn^* on the particle volume fraction (VICENTE et al., 2004; VOLKOVA et al., 2000). Such models are based on balancing hydrodynamic and magnetostatic forces and torques on field-induced structures. These models give the following relation: $Mn^* = C\phi\eta_0/\eta_\infty$, in which different values for C depend on the distinct assumptions and simplifications of the mechanical model.

A very efficient way to investigate the structure of magnetorheological fluids is to observe their response to the application of oscillatory flow. This is so because this kind of flow allows the assessment of a wide range of time scales for a given structure. This type of rheological flow also permits the determination of yield stress with less ambiguity in comparison to strategies using simple shear flow (VICENTE; KLINGENBERG; HIDALGO-ALVAREZ, 2011).

A panorama of the oscillatory response of viscoelastic fluids, which is the case of field-dependent fluids (electrorheological and magnetorheological), is given by the Pipkin diagram (PIPKIN, 2012), which is a plot of the strain amplitude versus the excitation frequency. This plot can depict the overall dynamic response of a viscoelastic fluid, that is, it summarizes the qualitative dependence of the flow behavior on operating conditions (PARTHASARATHY; KLINGENBERG, 1999). The curves inside a Pipkin diagram delimit the different possible dynamic behavior of the fluid. Parthasarathy and Klingenberg (PARTHASARATHY; KLINGENBERG, 1999) plotted the Pipkin diagram representing the dynamic flow response of an electrorheological fluid under the action of an external electric field. Although the focus of this work is on MR fluids, the referred work can be used as a reference because the general behavior of the two kinds of fluids under the action of an external field, electrical for ER fluids and magnetic for MR fluids, is usually qualitatively similar, being different only the intensity of the rheological effects. The referred diagram is shown in figure (5).

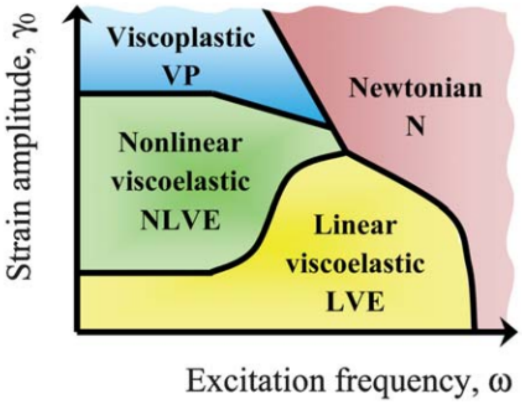

Figure 5 – The Pipkin diagram (stain versus dimensionless frequency) of the dynamic rheological behavior of ER fluids. The curves demarcate regions of different rheological behavior. Adapted from (PARTHASARATHY; KLINGENBERG, 1999).

It can be seen from figure (5) that in a regime of small strain for a great range of dimensionless frequencies, the fluid has a linear viscoelastic response (LVE). As the strain is enhanced until a critical value (γ_1^{crit}), the response of the system changes to a nonlinear viscoelastic regime (NLVE), which is characterized by the appearance of other (higher) harmonics in the shear stress response of the fluid. Rising the strain even further, it reaches another critical value (γ_2^{crit}), from which a viscoplastic (VP) response is observed in the fluid. In the case characterized by severely high strains or dimensionless excitation frequencies, the fluid has a Newtonian behavior, owing to the fact that in this case, the elastic properties of the fluid are negligible (PARTHASARATHY; KLINGENBERG, 1999; VICENTE; KLINGENBERG; HIDALGO-ALVAREZ, 2011).

In the regime of linear viscoelasticity, the storage modulus G' in the presence of a magnetic field has a high value, typically at least one order of magnitude larger than the loss modulus G", which is related to the appearance of field-induced structures in the fluid. Upadhyay *et al.* (UPADHYAY; LAHERISHETH; SHAH, 2013) carried out several experiments in oscillatory shear of an MR fluid consisting of flake shaped iron particles. They observed from tests on amplitude sweep mode that for very small shear amplitude strain, G' is independent of the applied strain, which signifies that the system is under a viscoelastic regime. In this condition, magnetic-field induced structures remain undisturbed. However, as the strain amplitude is enhanced, the chain structures start to break, which leads the system to nonlinear behavior. A special condition is reached for the strain where the storage and the loss modulus intersect, which is $G' = G''$, due to the fact that above this point the system starts to flow. This point rises when the magnetic field intensity enhances.

Macroscopic (using the energy minimization principle) and microscopic (taking into account inter-particle interactions) approaches have been used to the investigation of the yield stress as discussed in section (1.2.3.2). Such models have also been applied to understand and to predict the values of G'. In the case of intermediate magnetic field strengths, it was found that $G' = 3\phi\mu_0 M_S H$ (GINDER; DAVIS; ELIE, 1996). Instead of the quadratic dependence on the magnetic field predicted for the yield stress, the storage modulus presents a linear dependence to it, which is a result of the fact that when the magnetic field rises, the magnetic particles start to saturate near the poles in chain-like aggregates. In the case o very high magnetic field intensities, the magnetization of the particles is fully saturated, resulting in an elastic modulus independent of the magnetic field intensity, being given by $G' = 0.3\phi\mu_0 M_S$ (GINDER; DAVIS; ELIE, 1996).

The response of MR fluids in the presence of an external magnetic field to a frequency sweep with constant shear strain is not clear. Some experiments and simulations show that the viscoelastic moduli may remain constant and then passes through a maximum or even decrease or increase depending on the MR fluid (systems) under analysis. Nonetheless, Chin *et al.*(CHIN; WINTER, 2002), reported by experimental analysis that the evolution of $G'(\omega)$ and $G''(\omega)$ has similarity with the evolving moduli of crosslinking copolymer, even presenting a region where the loss tangent is found to be independent of the frequency, which corresponds to a gelation transition point (Winter - Chambon criteria). At frequencies that characterize the relaxation of internal modes on length scales where the systems have self-similar structure, power-law dependence of G' and G" on the frequency is expected (VICENTE; KLINGENBERG; HIDALGO-ALVAREZ, 2011).

Large amplitude oscillatory shear regime (LAOS) is very important to understand the dynamical response of an MR fluid. The reason can be directly understood by analyzing the Pipkin diagram, displayed on figure (5), where it is shown that the regime of linear viscoelasticity is really small, in terms of applied strain amplitude, in comparison to the non-linear viscoelastic regime. Thus LAOS is the main operational mode of the majority of applications. Deshmukh and McKinley (DESHMUKH; MCKINLEY, 2004) report a microscopic visco-elastoplastic model inspired by soft-glassy rheology models that were successfully used on predicting LAOS behavior of MR fluids.

The material functions of MR fluids obtained in conditions of permanent simple shear and oscillatory shear flows are found to be related by a modified Cox-Merz rule. Flow curves η versus $\dot{\gamma}$ closely overlap $|\eta^*|$ versus $\gamma\omega$ plots. This agreement is found to apply since LAOS and steady shear behavior share a common structural mechanism, which is the aggregation and fragmentation of clusters (VICENTE; KLINGENBERG; HIDALGO-ALVAREZ, 2011).

According to (VICENTE; KLINGENBERG; HIDALGO-ALVAREZ, 2011), a research line that still can be addressed is the investigation of MR fluids composed by magnetic particles whose average size is in the range between the one characteristic of ferrofluids and the one usual of classic MR fluids. Besides that, the investigation of the use of non-spherical magnetic particles is also an open problem.

1.2.4 Aqueous suspensions of double-walled carbon nanotubes

Research into the rheology of suspensions involving double-walled carbon nanotubes (DWCNs) is still emerging, though a variety of studies on multiwalled carbon nanotubes (MWCNs) provide useful insights. The behavior of these suspensions is primarily influenced by the interactions between the nanotubes and the surrounding fluid matrix, which impacts both viscosity and shear thinning effects.

For example, suspensions of untreated carbon nanotubes (CNTs) typically exhibit a pronounced shear-thinning behavior, largely due to the formation of networks or aggregates of CNTs in the fluid. In contrast, chemically treated CNTs tend to show less pronounced shear-thinning, likely because of changes in their structure that reduce aggregation. These treatments result in CNTs that behave more like rigid, short fibers that align in the flow direction, influenced by Brownian motion and hydrodynamic interactions (YEARSLEY et al., 2012; MA; CHINESTA; MACKLEY, 2008).

Modeling of the rheological properties often involves sophisticated approaches, such as the Fokker-Planck-based orientation model. This model considers the alignment of CNTs as fibers in the suspension and accounts for the concentration and aspect ratio of the nanotubes. The viscosity of these suspensions is also significantly dependent on the CNT concentration, with higher concentrations leading to increased viscosity (MA; CHINESTA; MACKLEY, 2009; RAZMARA; NAMARVARI; MENEGHINI, 2019).

Additionally, research suggests that when CNTs aggregate into larger structures in untreated suspensions, this aggregation adds another layer of complexity to the rheological behavior. In these cases, the so-called Aggregation/Orientation (AO) model is applied to better describe the observed flow behavior (YEARSLEY et al., 2012).

These insights are crucial for developing applications in various industries, including the creation of composite materials and fluid systems where the rheology of CNT suspensions plays a critical role in processing and performance.

1.2.5 Oleogels

Oleogels have emerged as a promising alternative to trans and saturated fats, which are well-documented for their adverse effects on human health (PUȘCAȘ et al., 2020). These systems are classified as semisolid materials formed by immobilizing liquid oil within a three-dimensional network, without altering the chemical properties of the oil (MANZOCCO et al., 2017; PATEL et al., 2013). Oleogels are extensively studied not only in the food sector but also across various fields, including pharmaceuticals (drug delivery systems), cosmetics (stability enhancers), environmental engineering, mechanical lubrication, and materials science (PATEL et al., 2015; WANG; CHEN; NAGUIB, 2021).

Typically, the structuring of oleogels relies on oleogelators, which can be categorized into low molecular weight compounds (such as waxes, lecithin, esters, and ceramides) and high molecular weight substances (such as proteins and polysaccharides) (LI et al., 2022). Biopolymers, particularly polysaccharides, are effective even at lower concentrations and are well-established in the food industry as stabilizing and thickening agents in aqueous systems. Due to their polymeric nature, oleogels derived from these materials exhibit viscoelastic properties influenced by factors such as molecular weight, conformation, and concentration. Their GRAS (Generally Recognized as Safe) status and consumer perception as natural food additives also make them suitable for structuring edible oils (DAVIDOVICH-PINHAS, 2019; PATEL, 2018).

Oleogels can be produced using direct methods, which involve high temperatures and mechanical agitation. However, these processes may degrade nutraceutical compounds and promote oil oxidation (KAVYA et al., 2024; LIU et al., 2023). To address these issues, indirect methods like emulsion templates, solvent exchange, and porous solid matrices (e.g., foams and aerogels) have been developed (KAVYA et al., 2024). Patel et al. (2013) introduced a method involving hydroxypropyl methylcellulose (HPMC) foamed and freeze-dried to create porous structures that absorb oil and yield rheologically solid-like oleogels.

Aerogels, known for their high surface area, porosity, and low density, are typically fabricated using supercritical CO2 drying or freeze-drying techniques (LAVOINE; BERGSTRÖM, 2017). These porous materials have shown potential in oleogel production by offering enhanced nutrient protection and antioxidant capacity compared to direct methods (ZHAO et al., 2023). Additionally, bio-based aerogels made from biopolymers like starch are safe, biocompatible, and biodegradable. Starch, a widely used edible polysaccharide, is non-toxic, non-allergenic, and capable of forming gels in aqueous environments. However, its hydrophilicity and low mechanical strength limit its application. These issues can be mitigated by incorporating cellulose nanomaterials (AGO; FERRER; ROJAS, 2016).

Recent studies highlight the benefits of combining cellulose and starch to improve the properties of aerogels. For instance, cellulose nanofibers in starch/clay aerogels have been shown to enhance structural stability, compressive strength, and thermal properties (ZHAO; TIAN; HUANG, 2021). Similarly, starch aerogels supplemented with chitosan exhibit reduced shrinkage and improved oil structuring capabilities (ALAVI; CIFTCI, 2023). Shan et al. (2024) demonstrated that dual-reinforced aerogels using sodium carboxymethylcellulose and soy protein isolate significantly enhanced mechanical properties, elasticity, and oil-holding capacity. Nevertheless, the potential of composite bio-aerogels based on cellulose and starch for edible oleogelation remains underexplored.

Cellulose, an abundant biopolymer derived from plant, animal, or microbial sources (e.g., straw, wood, bagasse), offers remarkable reinforcing capabilities, particularly in its microfibrillated form (MFC). These nanostructures create strong entangled networks with desirable rheological properties, even at low concentrations, making them ideal as stabilizers, thickeners, and gelling agents (LAVOINE et al., 2012; WÜSTENBERG, 2014). Furthermore, dietary fiber derived from cellulose provides health benefits, including the prevention of gastrointestinal disorders (GILL et al., 2021; ONG et al., 2020). However, no studies have yet explored the incorporation of microfibrillated cellulose in starch-based bio-aerogels for food-grade oleogel production.

This study investigates the effect of combining starch and cellulose on the rheological properties and functionality of oleogels. Experimental procedures, both in permanent and transient shear will be applied to samples, allowing the study of several material functions, such as viscosity and moduli viscoelastic depending both on particle volume fraction of cellulose, shear rate and frequecy of excitation.

1.3 Objectives

The primary goal of this study is to characterize the rheological behavior of two distinct magnetorheological suspensions (MRS), differentiated by the type of particles used in their formulation: one containing magnetite powder and the other, carbonyl iron. Additionally, the rheology of aqueous suspensions of double-walled carbon nanotubes (DWCN) and oleogels will be explored.

A key unifying theme across these fluids is anisotropy. For the MRS, anisotropy is induced by the application of an external magnetic field, while for DWCN suspensions and oleogels, anisotropy arises naturally due to their intrinsic structural properties. This study aims to provide insights into the role of anisotropy in governing the rheological behavior of these complex fluid systems.

The analysis will primarily rely on experimental techniques, utilizing a parallel plate rheometer equipped with two distinct assemblies:

1. Standard Assembly: Used for conventional rheological testing;
2. Magnetic Assembly: Designed to enable the application of controlled magnetic fields while subjecting the fluid sample to various shear flow regimes.

The magnetic assembly facilitates precise control over both the shear conditions and the magnetic field intensity within the testing zone, allowing for detailed investigation of the anisotropic behavior of magnetorheological suspensions. This setup is critical for studying how external fields influence the structural and flow properties of these complex fluids.

This report has the following specific objectives concerning the study of magnetorheological suspensions:

1. Conduct a comprehensive review of the constitutive modeling of magnetorheological suspensions and the rheological phenomena arising from their interaction with magnetic fields. This will include an analysis of theoretical models and experimental findings;
2. Characterize, using optical microscopy, the average length of the magnetic field-induced chain-like structures as a function of particle volume fraction and magnetic field intensity;
3. Investigate the rheological behavior of magnetorheological suspensions under steady shear in the presence of a magnetic field. The study will focus on:
   a) Apparent viscosity as a function of magnetic field intensity and shear rate;
   b) Characterization of the magnetoviscous effect and pseudoplastic behavior induced by the external magnetic field.

4. Perform step-strain tests to obtain stress relaxation functions under varying magnetic field intensities. Analyze the likely complex relaxation behavior and determine primary and secondary relaxation times as functions of magnetic field intensity. Assess the fit of the stress relaxation data to Maxwell's generalized viscoelastic model. Evaluate residual stress and its dependence on magnetic field intensity.

The study of aqueous suspensions of double-walled carbon nanotubes has the following specific objectives:

1. Perform a systematic review of the literature concerning the rheology of DWCN suspensions;

2. Characterize, using optical microscopy the average length of the double-walled carbon nanotubes;

3. Through a series of experiments in permanent simple shear, study the dependence of the viscosity of the suspensions on the particle volume fraction and on the applied shear rate. Observe if the fluid exhibits pseudoplastic behavior;

4. Using experimental trials in the regime of step-strain, determine the stress relaxation function and the relaxation times in terms of the particle volume fraction. Determine the residual stress as a function of the particle volume fraction;

5. Applying small amplitude oscillatory shear, determine the viscoelastic properties of the suspensions as functions of the excitation frequency. Determine the shear elastic modulus and the zero-shear viscosity, if possible.

The study of the rheology of oleogels has the following objectives:

1. Perform a thorough review of the literature concerning the rheology of oleogels composed of potato starch and cotton cellulose;

2. Analyze how the viscosity of the oleogels responds to changes in temperature;

3. Investigate the behavior of the oleogels under varying shear rates to determine if the fluid exhibits pseudoplasticity;

4. In small amplitude oscillatory shear, determine the viscoelastic moduli as functions of the excitation frequency. Additionally, if possible, determine the zero-shear viscosity and the shear elastic modulus.

2 CONSTITUTIVE MODELS

In this chapter, classical types of non-Newtonian fluid constitutive formalism are presented. The first class is the generalized Newtonian fluid, also called viscous non-Newtonian fluid. They are models based on the fact that viscosity, for non-Newtonian fluids, are not constant as a function of shear rate. Based on this, very useful models for modeling this relationship are proposed in the literature, which are developed from empirical observations of the behavior of the most diverse fluids, usually performed in simple permanent shear experiments. However, a defining feature of these models is that they do not clearly capture the characteristics arising from the elastic properties of many non-Newtonian fluid classes, such as memory effects.

Then, the linear-viscoelastic models will be treated, aiming the proposition of constitutive equations capable of modeling the behavior of viscoelastic fluids, that is, of materials that present, at the same time, elastic characteristics, associated with the typical behavior of solids and dissipative effcts, typical of fluids. These models will be demonstrated from the approach of small deformations, which, in turn, will allow the linearization of the problem.

In addition, analogies with other physical systems such as mass spring-damper systems will be discussed to obtain the constitutive equations in order to capture the elastic and dissipative moduli. Also, the stress relaxation function will be described, from which it is possible to determine the relaxation time spectrum for the most complex fluids is shown. It will also be presented the general model, proposed by Oldroyd (1956), for the constitutive equations in linear-viscoelasticity regime.

The next topic of interest is the description of constitutive models for suspensions, which briefly can be described as systems composed of a solid phase (particles) dispersed in a base fluid. It is presented, based on microhydrodynamic concepts, the form of the stress tensor for a diluted suspension os rigid spheres, leading to the definition of Einstein's viscosity. We will also discuss a constutive model for a suspension of highly anisotropic particles with rheological magnetic effects (chains of magnetic particles) and with no magnetic interaction (double wall carbon nanotubes).

2.1 The generalized Newtonian fluids

The constitutive equation for generalized Newtonian fluids (GNF), according to Morrison (2001), was developed based on the constitutive equation of incompressible Newtonian fluids, which is given by :

$$\boldsymbol{\sigma} = \mu \dot{\boldsymbol{\gamma}}, \tag{2.1}$$

where,

$$\dot{\boldsymbol{\gamma}} = \sqrt{2\boldsymbol{D} : \boldsymbol{D}}. \tag{2.2}$$

In those equations, $\boldsymbol{\sigma}$ is the stress tensor, $\dot{\boldsymbol{\gamma}}$ is the shear-rate tensor and $\boldsymbol{D}$ is the tensor rate of strain, defined as the symmetric part of the tensor gradient of velocity $\nabla \boldsymbol{u}$. However, equation (2.1) predicts a constant viscosity, independent from the shear-rate $\dot{\gamma}$. This feature must be changed in order to cope with the dynamical description of materials whose viscosity is not constant, what leads to the adequacy of equation (2.1) to the following form:

$$\boldsymbol{\sigma} = \eta(\dot{\gamma}) \dot{\boldsymbol{\gamma}}, \tag{2.3}$$

where, $\eta(\dot{\gamma})$ is a scalar function and $\dot{\gamma} = |\dot{\boldsymbol{\gamma}}|$. The material function $\eta(\dot{\gamma})$ is called apparent viscosity, due to the fact that it varies as a function of the shear-rate. Nonetheless, it is related to the effective viscosity of the fluid μ as follows:

$$\lim_{\dot{\gamma} \to 0} \eta(\dot{\gamma}) = \mu. \tag{2.4}$$

It is important to note that, even though the form of the stress tensor for the generalized Newtonian fluids are given by equation (2.3), for it to truly represent the rheological characteristics of a given material, it is necessary to propose constitutive models for the apparent viscosity function $\eta(\dot{\gamma})$. Bird, Armstrong and Hassager (1987) argues that the majority of models for this material function come from experimental observations, being referred as ad-hoc expressions. The models used in the analysis carried out in this dissertation are describe in the next subsections.

2.1.1 Power-law model

One of the best known viscous non-Newtonian fluid models in the literature is the power-law model, also called the Ostwald-De-Waele model (BIRD; ARMSTRONG; HASSAGER, 1987). This model describes viscosity as a function proportional to some power of the shear-rate ($\dot{\gamma}$), being mathematically expressed by:

$$\eta(\dot{\gamma}) = K \dot{\gamma}^{n-1}, \tag{2.5}$$

which presents two parameters that must be adjusted to experimental data. The first one is the power $(n-1)$ of $\dot{\gamma}$, which represents the slope of the line obtained by representing equation (2.5) on a *log-log* graph. The second parameter is the consistency index, K, whose logarithm indicates the intersection with the ordinates axis in the graph of $\log(\eta)$ vs $\log(\dot{\gamma})$. Besides that, K directly related to the magnitude of the fluid's viscosity.

The power law model can be used to describe a Newtonian fluid, in this case $K = \mu$ and $n = 1$. For $n > 1$, the graph of $\log(\eta)$ vs $\log(\dot{\gamma})$ is a rising line and the material is said Shear-thickening, since it has the property of its apparent viscosity increasing with the intensification of the applied shear-rate. For $n < 1$, the $\log(\eta)$ vs $\log(\dot{\gamma})$ graph is a descending line and the fluid behavior is said to be shear-thinning, showing a decrease in apparent viscosity as a function of increased shear-rate. These behaviors are shown in the figure (6).

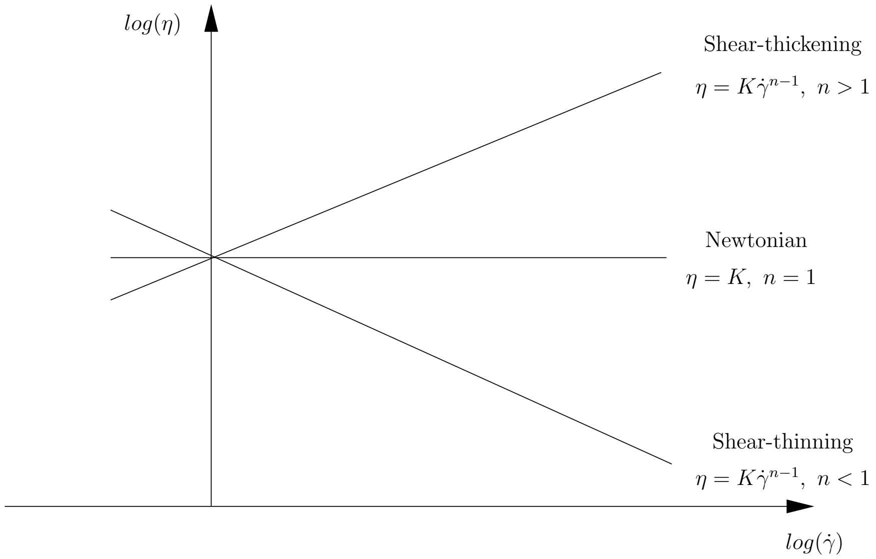

Figure 6 – Schematic representation of the three possible rheological behaviors of a power-law fluid.

According to Morrison (2001), this model is well suited for modeling non-Newtonian fluids subjected to medium to high shear-rate regimes, such as polymer extrusion processes. In addition, this model allows simplified calculations and good modeling in predicting flow measurements as a function of pressure drop in various industrial applications. However, this has some limitations, such as not capturing the Newtonian plateau at small shear-rates η_0. Another disadvantage is that this model is purely experimental and, therefore, its description of a particular material is specific, that is, it is not possible to predict the behavior of a material knowing the parameters of the power-law model of a similar material. It may be added, furthermore, that this model has no temporal constant between its parameters, what makes it unable to capture any material relaxation time, i.e. this model is not able to predict how quickly the fluid will relax after the flow is finished.

2.1.2 Sisko's model

This model was proposed by Sisko (1958) as an excellent alternative for modeling the rheological behavior of shear-thinning fluids, such as greases, emulsions and many other complex fluids when subjected to medium-high shear-rates. The constitutive equation for the relation between the apparent viscosity and the shear-rate suggested by this model is

$$\eta(\dot{\gamma}) = \eta_{\infty} + K_s \dot{\gamma}^{(n-1)}. \tag{2.6}$$

As it can be immediately seen, this model comes from the addition of another parameter to the power-law model. This parameter is the infinite shear viscosity η_{∞}, that represents the constant value to which the viscosity tends when the shear-rate increases. The other parameters K_s and $(n-1)$ have the same interpretation that was for the parameters of the power-law model.

2.2 The general linear viscoelastic fluids

The word viscoelasticity refers to the simultaneous existence of viscous and elastic characteristics in a material. According to Barnes, Hutton and Walters (1989), it is reasonable to assume that all materials are viscoelastic, *i.e.* in all of them, both viscous and elastic properties coexist. This is because the response of a given material sample in a given experiment depends on the relationship between the observer's time scale and the characteristic time scale of the material (the time it takes the material to respond to a given external stimulus.). For example, if an experiment is relatively slow, the sample will be more viscous than elastic, however, if the experiment is relatively fast, the effect will be opposite and therefore the sample will behave more elastic than viscous. However, if the experiment scale has an order of magnitude compatible with the material's natural time scale, a viscoelastic response is observed.

The above description leads to the definition of a very important dimensionless number, the Deborah number (De), defined as the ratio of a material's timescale τ, whose origin is closely related to its microstructure, and a characteristic time scale of the flow τ_f, of macroscopic origin, that is:

$$De = \frac{\tau}{\tau_f}. \tag{2.7}$$

In this context, it is clear that a Hookean solid has $De = \infty$, since its characteristic relaxation time is theoretically infinite, on the other hand, Newtonian fluids have $De = 0$, since its characteristic time is very small compared to common experiment scales. It also appears that viscoelastic materials have $De \approx 1$, as both time scales have the same order of magnitude.

2.2.1 Linear viscoelasticity

According to (CUNHA, 2016), linear viscoelasticity is a description of the viscoelastic response ($De \approx 1$) of non-Newtonian fluids, whose main feature is to be a small deformation regime. It was, according to Barnes, Hutton and Walters (1989), the first study for transient description of non-Newtonian fluids, where the elastic response of the fluid becomes important. In this type of approach, the fluid response, i.e., the stress at any time is directly proportional to the strain or strain rate.

Due to linearity, the differential equations that govern the phenomenon are linear and the coefficients of the temporal derivatives are constant,i.e. they are independent of strain and stress. Nevertheless, according to Barnes, Hutton and Walters (1989), the main consequence of linearity is that the principle of effects superposition can be applied to the system, a fact explored in the proposition made by Oldroyd (1956) of an general equation for the linear viscoelasticity regime, which is:

$$\left(1+\tau_1\frac{\partial}{\partial t}+\tau_2\frac{\partial^2}{\partial t^2}+...+\tau_n\frac{\partial^n}{\partial t^n}\right)\boldsymbol{\sigma}(t)=\left(\beta_0+\beta_1\frac{\partial}{\partial t}+\beta_2\frac{\partial^2}{\partial t^2}+...+\beta_m\frac{\partial^m}{\partial t^m}\right)\boldsymbol{\gamma}(t) \tag{2.8}$$

where τ_n and β_m are material parameters, which can be measured experimentally, $\boldsymbol{\sigma}(t)$ and $\boldsymbol{\gamma(t)}$ are, respectively, the stress tensor and the strain tensor.

Bird, Armstrong and Hassager (1987) state that there are many reasons to determine the viscoelastic-linear response of fluids, firstly, it allows the understanding of the effects of the microstructure of the material on its behavior when flowing. In addition, the experimentally measured parameters and material functions in small deformation flow have been very useful in the quality control of industrial processes. Another important reason is the fact that a good basis in linear viscoelasticity is of paramount importance for understanding nonlinear viscoelastic models.

2.2.2 Maxwell's viscoelastic model

Maxwell was a pioneer on the proposition of a constitutive model to described the characteristics of viscoelastic materials. According to Bird, Armstrong and Hassager (1987), Maxwell developed the theory of elasticity, in the belief that gases could exhibit viscoelastic behavior.

In order to obtain the constitutive equation of Maxwell's model in a two-dimensional approach,Barnes, Hutton and Walters (1989) propose a system composed by a spring whose elastic constant is G, and a damper with damping constant μ, connected in series and subjected to periodic small amplitude excitations, in which the spring continuously shifts γ and the damper observes a damping rate $\dot{\gamma}$. This system is known as the Maxwell element and is represented in the figure (7).

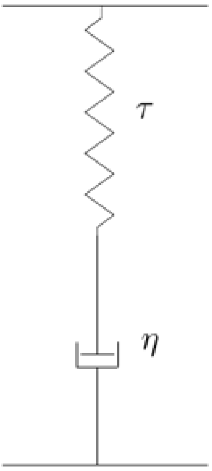

Figure 7 – Schematics of a Maxwell's element.

Considering a Hookean spring, it comes that

$$\sigma_E = G\gamma_E. \tag{2.9}$$

Then, differentiating equation (2.9), one obtains:

$$\dot{\sigma_E} = G\dot{\gamma}_E, \tag{2.10}$$

on the other hand, for the damper:

$$\sigma_V = \eta\dot{\gamma}_V. \tag{2.11}$$

Since the system is composed of elements in a series arrangement, the spring and the damper will suffer the same stress and the total damping rate will be the sum of the damping rate of both components, i.e.:

$$\sigma_E = \sigma_v = \sigma \quad e \quad \dot{\gamma} = \dot{\gamma}_E + \dot{\gamma}_V, \tag{2.12}$$

Therefore, substituting the results obtained from the equations (2.10) and (2.11) in the equation (2.12), we obtain that:

$$\dot{\gamma} = \frac{\dot{\sigma}_E}{G} + \frac{\sigma_V}{\eta} = \frac{\dot{\sigma}}{G} + \frac{\sigma}{\eta}. \tag{2.13}$$

By reorganizing the terms of the equation (2.13), we arrive at the differential one-dimensional formulation of Maxwell's model, given by the following ordinary differential equation:

$$\sigma + \frac{\eta}{G}\frac{\partial\sigma}{\partial t} = \eta\dot{\gamma}. \tag{2.14}$$

In this analogy, the viscous effects and hence the dissipative characteristics, related to the liquid behavior of the viscoelastic material, are represented by the damper and the elastic characteristics, linked to the solid behavior, are represented by the spring.

A general formulation of Maxwell's model, in tensor notation, is obtained by observing that this constitutive model is based on the precepts of linear viscoelasticity, and therefore its constitutive equation must meet Oldroyd's general form, equation (2.8), discussed in the previous section. Keeping nonzero only the terms τ_1 and β_1 in the equation (2.8) and equating β_1 with the viscosity η, one obtains the following differential equation:

$$\boldsymbol{\sigma} + \tau_1 \frac{\partial \boldsymbol{\sigma}}{\partial t} = \eta \frac{\partial \boldsymbol{\gamma}}{\partial t}, \tag{2.15}$$

where

$$\dot{\boldsymbol{\gamma}} = \partial \boldsymbol{\gamma} / \partial t = 2\mathbf{D}. \tag{2.16}$$

In these expressions, $\mathbf{D}$ is the rate of strain tensor and $\tau_1 = \eta / G$ is a material time constant, more specifically named time of relaxation, and G is the elastic modulus. With this alteration, equation (2.15) becomes:

$$\boldsymbol{\sigma} + \tau_1 \frac{\partial \boldsymbol{\sigma}}{\partial t} = 2\eta \boldsymbol{D}. \tag{2.17}$$

The solution of the ordinary differential equation (2.17) is obtained by the method of the integrating factor ($F.I.$). Defining $F.I. = e^{(1/\tau_1 t)}$ and multiplying both sides of equationi (2.17) by this factor, one obtains:

$$e^{(t/\tau_1)} \frac{d\boldsymbol{\sigma}}{dt} + \frac{1}{\tau_1} e^{(t/\tau_1)} = \frac{2\eta}{\tau_1} \boldsymbol{D}(t) e^{(t/\tau_1)}, \tag{2.18}$$

and, thus:

$$\frac{d}{dt}\left(\boldsymbol{\sigma} e^{(t\tau_1)}\right) = \frac{2\eta}{\tau_1} \boldsymbol{D}(t) e^{(t/\tau_1)}. \tag{2.19}$$

Integrating equation (2.19), it is obtained the constitutive equation for the stress tensor for a Maxwell's fluid, which is expressed by:

$$\boldsymbol{\sigma}(t) = \frac{2\eta}{\tau_1} \int_{-\infty}^{t} e^{-(t-t')/\tau_1} \boldsymbol{D}(t') dt'. \tag{2.20}$$

From this equation, it is defined the stress relaxation function as:

$$\Phi(t-t') = \frac{2\eta}{\tau_1} e^{-(t-t')/\tau_1} \tag{2.21}$$

where, $\Phi(t-t')$ is a positive function that depends on the nature of the fluid. Besides that, it decreases monotonically for zero as $t - t' \longrightarrow 0$. Based on this, the stress tensor of a Maxwell's fluid can be rewritten as:

$$\boldsymbol{\sigma}(t) = \int_{-\infty}^{t} \Phi(t-t') \boldsymbol{D}(t') dt'. \tag{2.22}$$

That is, according to Salas (2006), for a viscoelastic incompressible fluid subject to small displacement gradients or arbitrary strain rates, the expression for the total stress tensor $\boldsymbol{\Sigma}$ is given by:

$$\boldsymbol{\Sigma}(t) = -p\boldsymbol{I} + \boldsymbol{\sigma}(t), \tag{2.23}$$

where $-p\boldsymbol{I}$ is the isotropic part of the stress tensor and $\boldsymbol{\sigma}(t)$ is its deviatoric part, that in this case is given by equation (2.22).

The equation (2.22) is interpreted from the perspective of the causality principle, which states that stress depends on the history of loading, i.e., the stress in the present-time (t) depends on the strain-rate or history of deformation in earlier times (t'). In this context, the exponential shown in the equation (2.21), which mathematically represents the stress relaxation function, can be understood as a multiplicative factor of that equation, which assumes higher values ??for times closer to the present time and smaller for later times, thus indicating that stress is more susceptible to the more recent history of deformation. As a result, Maxwell fluids are said to have memory, as their current state depends on past states and, moreover, their memory decreases rapidly for events that occurred at a time away from the present, showing that this model fits the principle of fading memory.

2.2.3 Generalized Maxwell's viscoelastic model

It was previously stated that Maxwell's fluid has memory and that a good measure of this parameter is the relaxation time τ_1. Now consider a complex material composed of N Maxwell's elements, as shown in the figure (8).

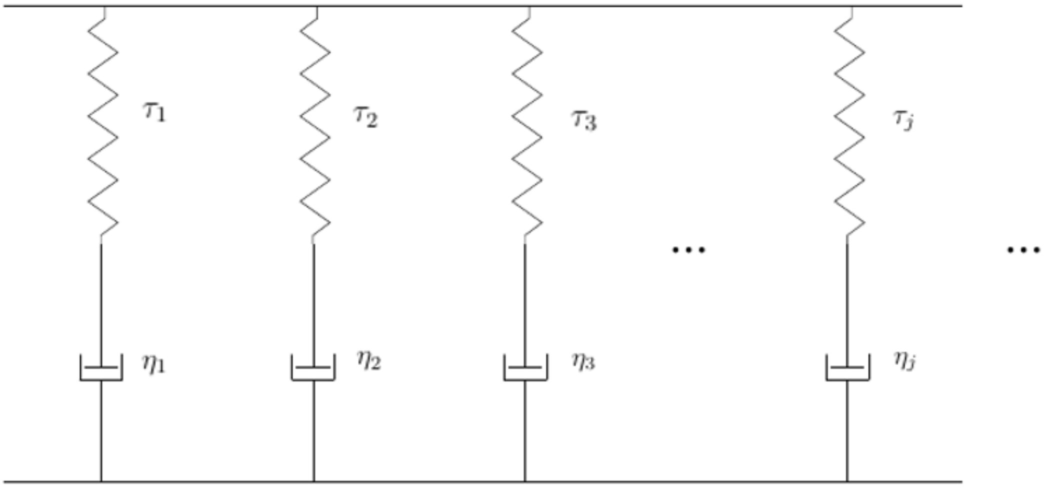

Figure 8 – Schematics of a complex fluid composed by N Maxwell's elements.

The two-dimensional form of Maxwell's model is obtained by integrating equation (2.15) through the integrating factor technique, whose procedure is analogous to that approached for the general solution addressed in the section (2.14). Solving the said ordinary differential equation, one obtains that:

$$\sigma(t) = \frac{\eta}{\tau_1} \int_{-\infty}^{t} e^{(-t-t')/\tau_1} \dot{\gamma}(t') dt'. \tag{2.24}$$

Regarding the principle of superposing effects, which is one of the foundations of linear viscoelasticity theory, it can be stated that the total stress felt by the material formed by N Maxwell's elements is given by the sum of the stress for each element, that is:

$$\sigma(t) = \sum_{j=1}^{N} \frac{\eta_j}{\tau_j} \int_{-\infty}^{t} e^{-(t-t')/\tau_j} \dot{\gamma}(t') dt', \tag{2.25}$$

which, in terms of the stress relaxation function can be rewritten as follows:

$$\sigma(t) = \int_{-\infty}^{t} \sum_{j=1}^{N} \Phi_j(t-t') \dot{\gamma}(t') dt'. \tag{2.26}$$

This equation shows us that in a linear viscoelastic regime the relaxation of a given stress applied to a complex material develops as a combined relaxing effect of the N elements that compose it, i.e. there are N relaxation times which characterize the typical time scale of a complex fluid in this flow regime. One can, therefore, write the stress relaxation function by considering Maxwell's N elements as follows:

$$\Phi(s) = \sum_{j=1}^{N} \Phi_j(s) = \sum_{j=1}^{N} \frac{\eta_j}{\tau_j} e^{-s/\tau_j}, \tag{2.27}$$

where $s = t - t'$.

2.2.4 Determination of the viscoelastic modules

Consider a Maxwell's fluid subjected to a small amplitude oscillatory shear. In this conditions, from equation (2.24), one obtains:

$$\sigma(t) = \frac{\eta_1}{\tau_1} \int_{-\infty}^{t} e^{-(t-t')/\tau_1} \dot{\gamma}(t') dt', \tag{2.28}$$

where, η_1 is the viscosity of the fluid for a condition of null frequency (equilibrium) and τ_1 its characteristic time of relaxation. Given the characteristics of the small amplitude oscillatory shear, it is defined that:

$$\sigma(t) = \dot{\gamma}(t) \eta^*(\omega), \tag{2.29}$$

in which, $\eta^*(\omega)$ is the complex viscosity modulus of the fluid.

Besides that, the angular strain is given by:

$$\gamma(t') = \gamma_0 e^{i\omega t'}. \tag{2.30}$$

Now, the shear-rate is defined by differentiating equation (2.30), which results in:

$$\dot{\gamma}(t') = i\omega\gamma_0 e^{i\omega t'}. \tag{2.31}$$

Replacing this expression into equation (2.28), one obtains:

$$\sigma(t) = \frac{\eta_1}{\tau_1} \int_{-\infty}^{t} e^{-(t-t')/\tau_1} i\omega\gamma_0 e^{i\omega t'} dt'. \tag{2.32}$$

Applying a substitution of variables $s = t - t'$ in equation (2.32), that results in $ds = -dt'$, and inverting the limits of integration, one obtains:

$$\sigma(t) = \frac{\eta_1}{\tau_1} \int_0^\infty e^{-s/\tau_1} i\omega\gamma_0 e^{i\omega(t-s)} ds. \tag{2.33}$$

Removing constant terms from the integral,

$$\sigma(t) = \frac{\eta_1}{\tau_1} i\omega\gamma_0 e^{i\omega t} \int_0^\infty e^{-s/\tau_1} e^{-i\omega s} ds, \tag{2.34}$$

and using equation (2.31), (2.34) can be rewritten in the following form:

$$\sigma(t) = \frac{\eta_1}{\tau_1} \dot{\gamma}(t) \int_0^\infty e^{-s/\tau_1} e^{-i\omega s} ds. \tag{2.35}$$

Now, adding the powers of the exponentials in the integrand of (2.35), factorizing s and rearranging the terms, one obtains:

$$\sigma(t) = \frac{\eta_1}{\tau_1} \dot{\gamma}(t) \int_0^\infty e^{[-s(1+i\omega\tau_1)/\tau_1]} ds. \tag{2.36}$$

Integrating (2.36),

$$\sigma(t) = \frac{\eta_1}{\tau_1} \dot{\gamma}(t) \left[\frac{-\tau_1}{(1 + i\omega\tau_1)} e^{[-s(1+i\omega\tau_1)/\tau_1]} \right] \Bigg|_{s=0}^{s\to\infty}, \tag{2.37}$$

and taking equation (2.37) into account, one obtains:

$$\sigma(t) = \frac{\eta_1}{(1 + i\omega\tau_1)} \dot{\gamma}(t). \tag{2.38}$$

Besides that, using the definition stated on equation (2.29), it comes that:

$$\eta^* = \frac{\eta_1}{(1 + i\omega\tau_1)}. \tag{2.39}$$

Multiplying and dividing equation (2.39) by the conjugate of the denominator:

$$\eta^* = \frac{\eta_1 - i\omega\tau_1\eta_1}{(1 + \omega^2\tau_1^2)}, \tag{2.40}$$

and observing that:

$$\eta^*(\omega) = \eta'(\omega) - i\eta''(\omega), \tag{2.41}$$

it is easily shown that:

$$\eta'(\omega) = \frac{\eta_1}{(1 + \omega^2\tau_1^2)} \tag{2.42}$$

and

$$\eta''(\omega) = \frac{\eta_1\tau_1\omega}{(1 + \omega^2\tau_1^2)}. \tag{2.43}$$

Finally, using the definition $G^* = i\omega\eta^*$, one obtains that:

$$G^*(\omega) = \frac{i\omega\eta_1}{(1 + i\omega\tau_1)}, \tag{2.44}$$

from which, through a process analogous to the one carried out on equation (2.40), it is obtained that:

$$G'(\omega) = \omega\eta''(\omega) = \frac{\eta_1\tau_1\omega^2}{(1+\omega^2\tau_1^2)}, \tag{2.45}$$

and

$$G''(\omega) = \omega\eta'(\omega) = \frac{\eta_1\omega}{(1+\omega^2\tau_1^2)}. \tag{2.46}$$

Now admitting a fluid composed of N elements of Maxwell, as discussed in the section (2.2.3), it is shown by the superposition principle that:

$$\eta'(\omega) = \sum_j^N \frac{\eta_j}{(1+\omega^2\tau_j^2)}, \tag{2.47}$$

$$\eta''(\omega) = \sum_j^N \frac{\eta_j\tau_j\omega}{(1+\omega^2\tau_j^2)}, \tag{2.48}$$

$$G'(\omega) = \sum_j^N \frac{\eta_j\tau_j\omega^2}{(1+\omega^2\tau_j^2)}, \tag{2.49}$$

e

$$G''(\omega) = \sum_j^N \frac{\eta_j\omega}{(1+\omega^2\tau_j^2)}. \tag{2.50}$$

2.2.5 Relationship between the stress relaxation function and viscoelastic modules

Consider again a Maxwell fluid subjected to a small amplitude oscillatory shear. In this case, the system excitation given in terms of the shear-rate is expressed as:

$$\dot{\gamma}(t') = \dot{\gamma_0}cos(\omega t'). \tag{2.51}$$

Replacing the expression (2.51) into the bidimensional constitutive equation for the stress tensor of a Maxwell's fluid, equation (2.24), one obtains:

$$\sigma(t) = \int_{-\infty}^{t} \Phi(t-t')\dot{\gamma_0}cos(\omega t')dt'. \tag{2.52}$$

Defining $s = t - t'$ on equation (2.52), it comes that:

$$\sigma(s) = \int_{-\infty}^{t} \Phi(s)\dot{\gamma_0}cos(\omega(t-s))ds. \tag{2.53}$$

Developing the term $cos(\omega(t-s))$, ic can be easily shown that:

$$\sigma(s) = \int_{-\infty}^{t} \left[\Phi(s)cos(\omega s)ds\right]\dot{\gamma_0}cos(\omega t)ds + \int_{-\infty}^{t} \left[\Phi(s)sen(\omega s)ds\right]\dot{\gamma_0}sen(\omega t)ds. \tag{2.54}$$

Comparing this result with equation (**??**), it is obtained that:

$$\eta'(\omega) = \int_{-\infty}^{t} \Phi(s)cos(\omega s)ds, \tag{2.55}$$

$$\eta''(\omega) = \int_{-\infty}^{t} \Phi(s)sen(\omega s)ds. \tag{2.56}$$

Alternatively, using complex variables, one obtains:

$$\eta^*(\omega) = \eta'(\omega) - i\eta''(\omega) = \int_{-\infty}^{t} \Phi(s) e^{-i\omega s} ds. \tag{2.57}$$

Using the inverse Fourier transform, it is immediate that:

$$\Phi(s) = \frac{2}{\pi} \int_{-\infty}^{t} \eta'(\omega) cos(\omega s) d\omega \tag{2.58}$$

$$\Phi(s) = \frac{2}{\pi} \int_{-\infty}^{t} \eta''(\omega) sen(\omega s) d\omega \tag{2.59}$$

2.2.6 Determination of the relaxation time from the stress relaxation function

The relaxation time (τ) for a simple Maxwell's fluid (composed of one Maxwell element) or the main relaxation time for a complex memory fluid can be calculated from the stress relaxation function. For that, lets calculate the following relation:

$$\lim_{\omega \to 0} \frac{\eta''(\omega)/\omega}{\eta'(\omega)}, \tag{2.60}$$

where $\eta'(\omega)$ and $\eta''(\omega)$ are given by (2.55), thus:

$$\lim_{\omega \to 0} \frac{\eta''(\omega)/\omega}{\eta'(\omega)} = \lim_{\omega \to 0} \left[\frac{\displaystyle\int_{-\infty}^{t} \frac{\Phi(s) \sin(\omega s)}{\omega} ds}{\displaystyle\int_{-\infty}^{t} \Phi(s) \cos(\omega s) ds} \right]. \tag{2.61}$$

Evaluating the limit of the denominator of the fraction located on the left side of equity on equation (2.61), one obtains:

$$\lim_{\omega \to 0} \eta'(\omega) = \lim_{\omega \to 0} \int_{-\infty}^{t} \Phi(s) \cos(\omega s) ds = \int_{-\infty}^{t} \Phi(s) ds = \eta(0) = \eta_0, \tag{2.62}$$

where η_0 is the viscosity of the fluid in the limit of flow absence (equilibrium). The limit of the numerator is calculated as follows:

$$\lim_{\omega \to 0} \frac{\eta''(\omega)}{\omega} = \lim_{\omega \to 0} \int_{-\infty}^{t} \frac{\Phi(s) \sin(\omega s)}{\omega} ds \tag{2.63}$$

to which, applying the rule of L'Hôpital, it is obtained that:

$$\lim_{\omega \to 0} \frac{\eta''(\omega)}{\omega} = \lim_{\omega \to 0} \int_{-\infty}^{t} s\Phi(s) \cos(\omega s) ds = \int_{-\infty}^{t} s\Phi(s) \cos(\omega s) ds. \tag{2.64}$$

Now, substituting the results obtained in (2.63) and (2.64) into (2.61), one obtains that:

$$\lim_{\omega \to 0} \frac{\eta''(\omega)/\omega}{\eta'(\omega)} = \frac{\int_{-\infty}^{t} s\Phi(s) \cos(\omega s) ds}{\int_{-\infty}^{t} \Phi(s) ds} = \frac{\beta}{\mu}, \tag{2.65}$$

By dimensional analysis, knowing that s has unit of time and $\Phi(s)$ unit of tension, it is obtained, as a result, that $[\beta] = Pa.s^2$ and $[\mu] = Pa.s$, then the quotient shown on equation (2.65) has unit of time, being defined as the relaxation time τ of the material. Based on that:

$$\tau = \frac{\int_{-\infty}^{t} s\Phi(s) \cos(\omega s) ds}{\int_{-\infty}^{t} \Phi(s) ds}. \tag{2.66}$$

2.3 Constitutive equation of a statistical homogeneous suspension: the bulk stress tensor

2.3.1 Force and torque free particles

The idea of this section is to discuss how a suspension can be modeled as a continuous equivalent fluid considering by hypotheses that no external forces and torques are acting upon the particles. The particles in suspension are considered neutrally buoyant, that there is no net effect resulting from the action of the gravity over the particles. Besides that, the suspension is considered statistical homogeneous, which means that any material volume of the suspension presents the same probability density function of particles. This signifies that there are no void of particles nor agglomeration in any representative volume of the suspension.

As a primary assumption, we will consider that the base fluid is Newtonian and incompressible, whose stress tensor is given by

$$\boldsymbol{\Sigma}^N = -p\boldsymbol{I} + 2\eta_0\boldsymbol{D}, \; \boldsymbol{x} \in V_f. \tag{2.67}$$

Observe that $\boldsymbol{x}$ is a position in the suspension and V_f is the volume of fluid.

That being said, consider an element of the suspension, its volume can be represented as

$$V = V_f + \sum_{k=1}^{N} V_k, \tag{2.68}$$

where V_f is the volume of fluid and V_k is the volume of each particle. We define the volumetric average of he stress tensor as

$$\overline{\boldsymbol{\Sigma}} = \frac{1}{V}\int_V \boldsymbol{\Sigma}\, dV = \lim_{V' \to V} \frac{1}{V'}\boldsymbol{\Sigma}\, dV. \tag{2.69}$$

that can be evaluated separately over V_f and $V_s = \sum_k^N V_k$, that is:

$$\overline{\boldsymbol{\Sigma}} = \frac{1}{V}\int_{V_f} \boldsymbol{\Sigma}\, dV + \frac{1}{V}\int_{V_s} \boldsymbol{\Sigma}\, dV \tag{2.70}$$

Substituting equation (2.67) into the first integral on (2.70) and regarding that

$$2\eta_0\boldsymbol{D} = \eta_0\left[\nabla\boldsymbol{v} + (\nabla\boldsymbol{v})^T\right], \tag{2.71}$$

one obtains:

$$\overline{\boldsymbol{\Sigma}} = \frac{1}{V}\int_{V_f}\left\{-p\boldsymbol{I} + \eta_0\left[\nabla\boldsymbol{v} + (\nabla\boldsymbol{v})^T\right]\right\} dV + \frac{1}{V}\int_{V_k}\sum_{k=1}^{N}\boldsymbol{\Sigma}\, dV. \tag{2.72}$$

Rearranging the therms, one gets:

$$\overline{\boldsymbol{\Sigma}} = -\frac{1}{V}\int_{V_f} p\boldsymbol{I}\, dV + \eta_0\frac{1}{V}\int_{V_f}\nabla\boldsymbol{v}\, dV + \eta_0\frac{1}{V}\int_{V_f}(\nabla\boldsymbol{v})^T\, dV + \frac{1}{V}\sum_{k=1}^{N}\int_{V_k}\boldsymbol{\Sigma}\, dV. \tag{2.73}$$

Let us consider the calculation of the first integral. The average pressure of the fluid is given by:

$$\frac{1}{V}\int_{V_f} p\boldsymbol{I}\, dV = -\overline{p}_f\boldsymbol{I} \tag{2.74}$$

As a result, the volumetric average of the stress tensor can be rewritten as

$$\overline{\boldsymbol{\Sigma}} = -\overline{p}_f\boldsymbol{I} + \eta_0\frac{1}{V}\int_{V_f}\nabla\boldsymbol{v}\, dV + \eta_0\frac{1}{V}\int_{V_f}(\nabla\boldsymbol{v})^T\, dV + \frac{1}{V}\sum_{k=1}^{N}\int_{V_k}\boldsymbol{\Sigma}\, dV. \tag{2.75}$$

Now, observe that

$$\overline{\nabla\boldsymbol{v}} = \frac{1}{V}\int_{V_f}\nabla\boldsymbol{v}\, dV - \frac{1}{V}\sum_{k=1}^{N}\int_{V_k}\nabla\boldsymbol{v}\, dV. \tag{2.76}$$

Applying the theorem of Gauss, this expression can be rewritten as

$$\overline{\nabla\boldsymbol{v}} = \frac{1}{V}\int_{V_f}\nabla\boldsymbol{v}\, dV - \frac{1}{V}\sum_{k=1}^{N}\int_{S_k}\boldsymbol{v}\hat{\boldsymbol{n}}\, dS. \tag{2.77}$$

Analogously,

$$\overline{(\nabla\boldsymbol{v})^T} = \frac{1}{V}\int_{V_f}(\nabla\boldsymbol{v})^T\, dV - \frac{1}{V}\sum_{k=1}^{N}\int_{S_k}\hat{\boldsymbol{n}}\boldsymbol{v}\, dS. \tag{2.78}$$

As a result, the expression for the volumetric average stress tensor can be modified to

$$\overline{\boldsymbol{\Sigma}} = -\overline{p}\boldsymbol{I} + 2\eta_0\overline{\boldsymbol{D}} + \frac{1}{V}\sum_{k=1}^{N}\int_{V_k}\boldsymbol{\Sigma}\, dV - \eta_0\frac{1}{V}\sum_{k=1}^{N}\int_{S_k}\left(\boldsymbol{v}\hat{\boldsymbol{n}} + \hat{\boldsymbol{n}}\boldsymbol{v}\right)\, dS. \tag{2.79}$$

Let's analyze the last integral in the right side of equation (2.79). To do that, firs let us recall the following identity:

$$\boldsymbol{\Sigma} = \nabla\cdot(\Sigma\boldsymbol{x}) - \boldsymbol{x}\left(\nabla\cdot\boldsymbol{\Sigma}\right). \tag{2.80}$$

Now, applying it, one obtain:

$$\int_{V_k}\boldsymbol{\Sigma}\, dV = \int_{V_k}\nabla\cdot(\boldsymbol{x}\boldsymbol{\Sigma})\, dV - \int_{V_k}\boldsymbol{x}\left(\nabla\cdot\boldsymbol{\Sigma}\right)\, dV. \tag{2.81}$$

Due to the fact that there is no force acting upon the particles, the last integral on (2.81) is identically zero. Analyzing the first integral on the right side of equation (2.81), one obtains by the application of Gauss theorem:

$$\int_{V_k}\nabla\cdot(\boldsymbol{x}\boldsymbol{\Sigma})\, dV = \int_{S_k}\boldsymbol{x}(\hat{\boldsymbol{n}}\cdot\boldsymbol{\Sigma})\, dS = \int_{S_k}\boldsymbol{x}\boldsymbol{t}\, dS. \tag{2.82}$$

In this equation $\boldsymbol{t}$ is the tension vector also called traction. The last integral is the hydrodynamic dipole related to the k-th particle $\boldsymbol{\mathcal{D}}^k$. As a second order tensor, $\boldsymbol{\mathcal{D}}^K$ can be written in therms of its symmetric and anti-symmetric parts:

$$\boldsymbol{\mathcal{D}}^k = \frac{1}{2}\int_{S_k}\left(\boldsymbol{x}\boldsymbol{t} + \boldsymbol{t}\boldsymbol{x}\right)\, dS + \frac{1}{2}\int_{S_k}\left(\boldsymbol{x}\boldsymbol{t} - \boldsymbol{t}\boldsymbol{x}\right)\, dS = \boldsymbol{S}^k + \boldsymbol{L}^k \tag{2.83}$$

The symmetric part is called stresslet $\boldsymbol{S}^k$ and the anti-symmetric of rotlet $\boldsymbol{L}^k$ associated to the k-th particle. $\boldsymbol{D}^k$ is also called particle tension and is associated with the extra stresses acting on the fluid due to the presence of the particles, whereas $\boldsymbol{L}^k$ is the torque tensor.

The volumetric average stress tensor for the continuous equivalent fluid can be then expressed by

$$\overline{\boldsymbol{\Sigma}} = -\overline{p}\boldsymbol{I} + 2\eta_0\overline{\boldsymbol{D}} + \frac{1}{V}\sum_{k=1}^{N}\left(\boldsymbol{S}^k + \boldsymbol{L}^k\right) - \eta_0\frac{1}{V}\sum_{k=1}^{N}\int_{S_k}\left(\boldsymbol{v}\hat{\boldsymbol{n}} + \hat{\boldsymbol{n}}\boldsymbol{v}\right)\, dS. \tag{2.84}$$

For torque-free particles:

$$\boldsymbol{L}^k = \boldsymbol{0}. \tag{2.85}$$

Thus,

$$\boldsymbol{\mathcal{D}}^k = \boldsymbol{S}^s. \tag{2.86}$$

Hence,

$$\overline{\boldsymbol{\Sigma}} = -\overline{p}\boldsymbol{I} + 2\eta_0\overline{\boldsymbol{D}} + \frac{1}{V}\sum_{k=1}^{N}\boldsymbol{S}^k - \eta_0\frac{1}{V}\sum_{k=1}^{N}\int_{S_k}\left(\boldsymbol{v}\hat{\boldsymbol{n}} + \hat{\boldsymbol{n}}\boldsymbol{v}\right)\, dS. \tag{2.87}$$

The total stresslet is defined as:

$$\boldsymbol{S}_T^k = \boldsymbol{S}^k - \eta_0\int_{S_k}\left(\boldsymbol{v}\hat{\boldsymbol{n}} + \hat{\boldsymbol{n}}\boldsymbol{v}\right)\, dS. \tag{2.88}$$

Using equation (2.86), the latter equation can be rewritten as:

$$\boldsymbol{S}_T^k = \int_{S_k}\left[\boldsymbol{x}\left(\hat{\boldsymbol{n}}\cdot\boldsymbol{\Sigma}\right) - \eta_0\left(\boldsymbol{v}\hat{\boldsymbol{n}} + \hat{\boldsymbol{n}}\boldsymbol{v}\right)\right]\, dS. \tag{2.89}$$

There are two cases to analyze when dealing with force and torque-free particles:. In the first one, the particles in suspension ar deformable. In this case, the bulk stress tensor is written as a function of the total stresslet $\boldsymbol{S}_T^k$ as follows:

$$\overline{\boldsymbol{\Sigma}} = -\,\overline{p}\boldsymbol{I} + 2\eta_0\overline{\boldsymbol{D}} + \frac{1}{V}\sum_{k=1}^{N}\boldsymbol{S}_T^k \tag{2.90}$$

$$\overline{\boldsymbol{\Sigma}} = -\,\overline{p}\boldsymbol{I} + 2\eta_0\overline{\boldsymbol{D}} + \frac{n}{N}\sum_{k=1}^{N}\boldsymbol{S}_T^k. \tag{2.91}$$

where n is number of density, defined as $n = N/V$.

The second case is the one in which the particles are rigid. Let us evaluate the deformation term over the particles:

$$\int_{S_k}\left(\boldsymbol{v}\hat{\boldsymbol{n}} + \hat{\boldsymbol{n}}\boldsymbol{v}\right)\, dS = \int_{v_k}\left[\nabla\boldsymbol{v} + \left(\nabla\boldsymbol{v}\right)^T\right]\, dV = \int_{v_k} 2\boldsymbol{D}\, dV. \tag{2.92}$$

As the particles as rigid, $\boldsymbol{D} = \boldsymbol{0}$, thus:

$$\int_{S_k}\left(\boldsymbol{v}\hat{\boldsymbol{n}} + \hat{\boldsymbol{n}}\boldsymbol{v}\right)\, dS = \boldsymbol{0}. \tag{2.93}$$

As a result, the total stresslet becomes:

$$\boldsymbol{S}_T^k = \int_{S_k} \boldsymbol{x}\,(\hat{\boldsymbol{n}} \cdot \boldsymbol{\Sigma}) = \boldsymbol{\mathcal{D}}^k = \boldsymbol{S}^k, \tag{2.94}$$

and, as a result, the bulk stress tensor for a suspension of force and torque free rigid particles can be expressed as:

$$\overline{\boldsymbol{\Sigma}} = -\,\overline{p}\boldsymbol{I} + 2\eta_0\overline{\boldsymbol{D}} + \frac{1}{V}\sum_{k=1}^{N}\boldsymbol{S}^k \tag{2.95}$$

$$\overline{\boldsymbol{\Sigma}} = -\,\overline{p}\boldsymbol{I} + 2\eta_0\overline{\boldsymbol{D}} + \frac{n}{N}\sum_{k=1}^{N}\boldsymbol{S}^k. \tag{2.96}$$

2.3.2 Einstein's equivalent Newtonian fluid

Consider the case of a rigid sphere of radius a subjected to a linear flow

$$\boldsymbol{v}^{\infty}(\boldsymbol{x}) = \boldsymbol{D}^{\infty} \cdot \boldsymbol{x} + \boldsymbol{\omega}^{\infty} \times \boldsymbol{x}. \tag{2.97}$$

From the third faxèn law (KIM; KARRILA, 2013), the stresslet produced by the sphere on the fluid is given by

$$\boldsymbol{S} = \frac{20}{3}\pi\eta_0 a^3 (1 + \frac{a^2}{10}\nabla^2)\boldsymbol{D}^{\infty}(\boldsymbol{x}_0). \tag{2.98}$$

Due to the fact that $\boldsymbol{D}^{\infty}$ is linear in this flow, the stresslet reduces to

$$\boldsymbol{S} = \frac{20}{3}\pi\eta_0 a^3 \boldsymbol{D}^{\infty}(\boldsymbol{x}_0). \tag{2.99}$$

Now, considering a diluted solution ($\phi << 1$) of N rigid spheres of small radius dispersed on a Newtonian fluid, the stresslet produced by the i-th sphere is

$$\boldsymbol{S}_i = \frac{20}{3}\pi\eta_0 a^3 \boldsymbol{D}_i^{\infty}. \tag{2.100}$$

By an ensemble average over the number of particles, one obtains

$$\bar{\boldsymbol{S}} = \frac{1}{N}\sum_{i=1}^{N}\boldsymbol{S}^i = \frac{20}{3}\pi\eta_0 a^3 \frac{1}{N}\sum_{i=1}^{N}\boldsymbol{D}_i^{\infty} = \frac{20}{3}\pi\eta_0 a^3 \bar{\boldsymbol{D}}^{\infty}. \tag{2.101}$$

As a result, the average particle stress tensor can be evaluated as a volumetric average of $\bar{\boldsymbol{S}}$, that is

$$\bar{\boldsymbol{\Sigma}}^p = n\bar{\boldsymbol{S}} = \frac{20}{3}\pi\eta_0 a^3 \bar{\boldsymbol{D}}^{\infty} = 5\eta_0 \left(\frac{4}{3}\pi a^3\right) n\bar{\boldsymbol{D}}^{\infty} = 5\eta_0\phi\bar{\boldsymbol{D}}^{\infty}. \tag{2.102}$$

Therefore, the average stress tensor of the equivalent fluid is given by

$$\begin{aligned}
\bar{\boldsymbol{\Sigma}} &= -\,\bar{p}\boldsymbol{I} + 2\eta_0\bar{\boldsymbol{D}} + \bar{\boldsymbol{\Sigma}}^p \\
\bar{\boldsymbol{\Sigma}} &= -\,\bar{p}\boldsymbol{I} + 2\eta_0\bar{\boldsymbol{D}} + 5\mu\phi\bar{\boldsymbol{D}} \\
\bar{\boldsymbol{\Sigma}} &= -\,\bar{p}\boldsymbol{I} + 2\eta_0^{eff}\bar{\boldsymbol{D}}
\end{aligned} \tag{2.103}$$

Then, the effective viscosity can be calculated as

$$\eta_0^{eff} = \eta_0\left(1 + \frac{5}{2}\phi\right). \tag{2.104}$$

This expression is called Einstein's viscosity.

2.4 Anisotropy

In the study of nanotubes and fibers, in this work, we will recall the slender body theory. The lecture should comprehend that this theory is general and can be applied to study the behavior of highly elongated drops (before the beak up in extensional flow) and the flagellar propulsion of micro-organisms. The basis for slender body theory is to make two asymptotic approximations in two regions: inner and outer (BATCHELOR, 1970a; CUNHA, 2024).

The inner region is at separations from the fiber that are small compared with the fiber length . The outer region is for separations large compared with the radius of the fiber a. There is a matching region $a << \rho << l$ for wich both the inner and outer solutions are valid. The constants in our assymptotic solutions are obtained by applying boundary conditions on the fiber to inner solution, boundary conditions at infinity to the outer solution and a conditionthat the two solutions coincide in the matching region.

We will consider a fiber of length $L = 2\ell$ and radius a(s). s is a coordinate measured parallel to the fiber's axis that varies from $-\ell$ to ℓ as you traverse the fiber. We allow the fiber radius to be a function of s, so that we can treat spheroids as well as cylinders and other shapes. The $\boldsymbol{\rho}$ vector is the two-dimensional plane perpendicular to the fiber and we have a vector $\boldsymbol{r}$ that is position relative to the center of the fiber in three dimensional space. Observe equation (9)

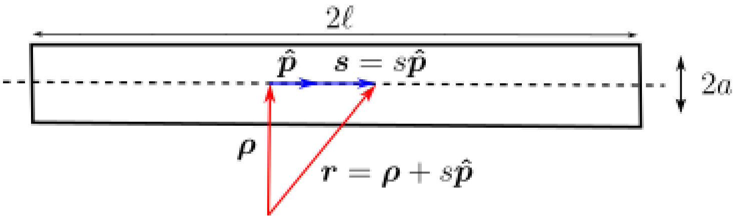

Figure 9 – Schematics of a fiber for slender body theory.

2.4.1 Heat transfer problem - suspension of anisotropic particles

We shall consider that the fiber is highly conducting, so that its temperature remains approximately constant $T = T_0$.

In the inner solution ($|\boldsymbol{\rho} << \ell|$) we are close to the fiber compared to its length so it looks like it is infinitely long to a first approximation (as long as you are not near an end.) Furthermore, although the temperature field may be changing as we go along the fiber, we will assume that the variations in T along the fiber are on length scales comparable to the fiber length L. Thus, we can look at this as a two-dimensional problem. The solution for a circle, that is a source of heat per unit of Q is:

$$T_{in} = T_0 - \frac{Q(s)}{2\pi k} \ln\left(\frac{\rho}{a}\right) \tag{2.105}$$

When we are in the outer solution ($|\boldsymbol{\rho} >> a|$), the fiber looks like it is infinitessimaly thin. Thus, we can adopt an approximation in which we treat the fiber as a line of sources (singularities) as shown in Figure (10).

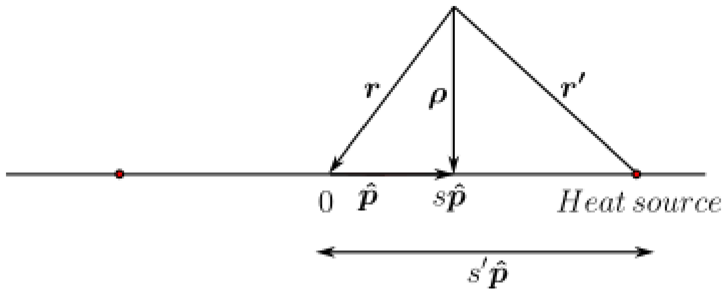

Figure 10 – Schematics of a fiber for slender body theory.

Observe that: $s'\hat{\boldsymbol{p}} + \boldsymbol{r'} = \boldsymbol{r}$, thus $\boldsymbol{r'} = \boldsymbol{r} - s'\hat{\boldsymbol{p}}$. Besides that, $|\boldsymbol{r'}|^2 = (s - s')^2 + \rho^2$. The infinitesimal source of heat is given by $\frac{1}{4\pi k}\frac{Q(s')}{|\boldsymbol{r'}|}ds'$. Thus, the temperature in an outer position is:

$$T_{out} = T^{\infty} + \frac{1}{4\pi k}\int_{-l}^{l}\frac{Q(s')}{\sqrt{(s-s')^2+\rho^2}}ds' \tag{2.106}$$

Note that this integral is singular , substracting the singularity:

$$T_{out} = T^{\infty} + \frac{1}{4\pi k}\int_{-l}^{l} ds' \frac{Q(s')}{\sqrt{(s-s')^2+\rho^2}} + \frac{1}{4\pi k}\int_{-l}^{l} ds' \frac{[Q(s') - Q(s)]}{(s-s')^2+\rho^2}, \tag{2.107}$$

$$T_{out} = T^{\infty} + \frac{Q(s)}{2\pi k}\ln\left[\frac{2(\ell^2 - s^2)^{1/2}}{\rho}\right] + \frac{1}{4\pi k}\int_{-l}^{l} ds' \frac{[Q(s') - Q(s)]}{|\boldsymbol{s} - \boldsymbol{s'}|} \tag{2.108}$$

In the matching position, we have $T_{out} = T_{in}$, thus:

$$T_{out} = T^{\infty} + \frac{Q(s)}{2\pi k}\ln\left[\frac{2(\ell^2 - s^2)^{1/2}}{a(s)}\right] + \frac{1}{4\pi k}\int_{-l}^{l} ds' \frac{[Q(s') - Q(s)]}{|\boldsymbol{s} - \boldsymbol{s'}|}. \tag{2.109}$$

Non dimensionalizing s by ℓ and a with a* (typical):

$$T_{out} = T^{\infty} + \frac{Q(s)}{2\pi k}\left\{\ln(2\gamma) + \ln\left[\frac{(1 - s^2)^{1/2}}{a(s)}\right]\right\} + \frac{1}{4\pi k}\int_{-1}^{1} ds' \frac{[Q(s') - Q(s)]}{|\boldsymbol{s} - \boldsymbol{s'}|}, \tag{2.110}$$

where $\gamma = l/a$. Equation (2.110) is an integral equation for the distribution of heat sources Q(s) as a function of the position throughout he fiber s for a given field T_{∞} applied.

2.4.1.1 Determination of the coefficient of heat transfer

We want to determine the flux of heat necessary to keep a fiber heated at a given temperature T_0. From the solution for the leading order, we have:

$$Q(s) = \frac{2\pi k T_0}{\ln(2\gamma)}, \tag{2.111}$$

which is local. Thus, for computing the global heat:

$$Q = \int_{-l}^{l} Q(s)ds \rightarrow Q = \frac{4\pi k \ell T_0}{\ln(2\gamma)}. \tag{2.112}$$

2.4.1.2 Effective conduction of the composite material

According to (CUNHA, 2024), we shall assume that there are no interactions between the fibers in the suspension. Thus, in the bulk, we have:

$$k\nabla^2\langle T\rangle = n\int d\hat{p}\Omega(\hat{p})\int_{z-l}^{z+l} dz_\perp Q(s=z-z_\perp, z_\perp). \tag{2.113}$$

$z_\perp$is the coordinate for the center of the fiber measured in the direction $\hat{p}$. Replacing the leading order for Q, we have:

$$k\nabla^2\langle T\rangle = \frac{2\pi kn}{\ln(2\gamma)}\int d\hat{p}\Omega(\hat{p})\int_{z-l}^{z+l} dz'\left[\langle T\rangle - \frac{1}{2\ell}\int_{-l}^{l} ds'\langle T\rangle(z'+s')\right], \tag{2.114}$$

where Ω is the fiber orientation distribution. Developing $\langle T\rangle(z'+s')$ in Taylor series, we obtain:

$$\langle T\rangle(z'+s') \approx \langle T\rangle(z') + s'\frac{\partial\langle T\rangle}{\partial z}\bigg|_{z} = z' + \frac{1}{2}s'^2\frac{\partial^2\langle T\rangle}{\partial z^2}\bigg|_{z=z'} \tag{2.115}$$

Substituting and computing the derivatives and algebric manipulations, we obtain (generalizing for 3D):

$$-k\nabla^2\langle T\rangle - \frac{4\pi knl^3}{3\ln(2\gamma)}\int d\hat{p}\Omega(\hat{p})\hat{p}\hat{p} : \nabla\nabla\langle T\rangle = 0 = \tag{2.116}$$

$$-k\nabla^2\langle T\rangle - \frac{4\pi knl^3}{3\ln(2\gamma)}\langle\hat{p}\hat{p}\rangle : \nabla\nabla\langle T\rangle = 0. \tag{2.117}$$

Observing that $-\nabla\cdot\langle\boldsymbol{q}\rangle$ and that $\boldsymbol{q} = -\boldsymbol{K}\cdot\nabla\langle T\rangle$, we have:

$$\boldsymbol{K} = k\left[I + \frac{4\pi nl^3}{3\ln(2\gamma)}\langle\hat{p}\hat{p}\rangle\right]. \tag{2.118}$$

The reader should pay attention that in a suspention of anisotropic fibers, the first order correction of the bulk propriety, in this case the effective conduction, is not dependent on $n\phi$, but on nl^3. Because of it, the conduction coefficient is very impacted, even using a low amount of fibers.

2.4.2 Stokes flow problem - slender body theory

In the problem of applying a Stokes flow around an slender body is similar to the problem analyzed for heat transfer. We will have an inner and outer region. In the inner region (separation much smaller than ℓ), the flow is nearly two-dimensional in a sense that the velocity varies slowly in the direction along the fiber. According to Batchelor (1970a), Cunha (2024), the inner velocity ($\rho << a$) is given by:

$$u_i^{in} = U_i + \epsilon_{ijk}\Omega_j p_k s - \frac{1}{4\pi\mu}F_j(s)(\delta_{ij}+p_ip_j)\ln\left(\frac{\rho}{a}\right) + \frac{1}{4\pi\mu}F_j(s)\left[\frac{\rho_i\rho_j}{\rho^2} - \frac{(\delta_{ij}-p_ip_j)}{2}\right] + \mathcal{O}(1/\rho^2). \tag{2.119}$$

Here, $\boldsymbol{F}$ is the force per unit of area along the fiber.

In the outer region ($\rho >> a$), we cannot detect the finite thickness of the fiber and so, in this problem we will trear the fiber as a line of point forces. Thus, we express the velocity disturbance caused by the fiber in the outer region as an integral over the fiber length of the Green's function (Oseen tensor) dotted into the force per unit length that the fiber exerts on the fluid.

$$u_i^{\text{out}} = U_i^{\infty}(\boldsymbol{r}) + \frac{1}{8\mu\pi}\int_{-l}^{l} ds' \left[\frac{\delta_{ij}}{r'} + \frac{r'_i r'_j}{r'^3}\right] F_j(s'), \tag{2.120}$$

where:

$$r'_i = r_i - s' p_i. \tag{2.121}$$

Now we can match the inner and outter solutions. As before we do this by taking the limit $\rho << \ell$ in the outer solution, neglecting algebraically small terms in γ, avoinding logarithimically singular integrals. The integral equation is given by:

$$U_i + \epsilon_{ijk}\Omega_j p_k s = U_i^{\infty}(sp_i) + \frac{1}{4\pi\mu} F_j(\delta_{ij} + p_i p_j)\left\{ \ln(2\gamma) + \ln\left[\frac{(1-s^2)^{1/2}}{a(s)}\right]\right\} + \tag{2.122}$$

$$+ \frac{1}{8\pi\mu} F_j(\delta_{ij} - 3p'_i p'_j) + \frac{1}{8\pi\mu}(\delta_{ij} + p_i p_j)\int_{-1}^{1} \frac{F_j(s') - F_j(s)}{|s - s'|} ds'. \tag{2.123}$$

Aiming to avoid resolving this integral, it is possible to expand the solution in powers of $1/\ln(2\gamma)$. With this strategy we obtain the leading solution for the force as:

$$\frac{1}{4\pi\mu} F_j(\delta_{ij} + p_i p_j)\ln(2\gamma) = U_i + \epsilon_{ijk}\Omega_j p_k s - U_i^{\infty}. \tag{2.124}$$

Considering a neutrally buoant fiber (force and torque free) subjected to a linear shear flow, the force distribution in the fiber is, according to (BATCHELOR, 1970a):

$$F_i = \frac{-2\pi\mu s}{ln(2\gamma)} p_i p_j D_{jk} p_k \tag{2.125}$$

2.4.2.1 Suspension of non-interacting fibers

We will obtain the average stress from the calculation for a linear velocity field by using the relationship of the contribution of a particle to the stress to the symmetric part of the first moment of the force distribution.

$$\Sigma_{ij} = -n\int d\boldsymbol{p}\Omega(\boldsymbol{p})\int_{-l}^{l} \frac{dA}{2}(r_i f_i + r_j f_j) \tag{2.126}$$

Here $\boldsymbol{f}$ is the force per unit area on the particle surface, $\boldsymbol{r}$ is the position measured relative to the center of the particle and $\boldsymbol{T}^p$ is the contributionof the particle to the local stress in the suspension. The position can be approximated as $\boldsymbol{r} \approx \boldsymbol{p}s$ and integrating over the circumference of the fiber, gives:

$$\Sigma_{ij}^{p} = \frac{2\pi n\mu}{\ln(2\gamma)}\int \boldsymbol{p}\Omega(\boldsymbol{p})\int_{-l}^{l} s^2 ds p_i p_j p_k p_l D_k l. \tag{2.127}$$

Thus:

$$\Sigma_{ij}^{p} = \frac{4\pi\mu n l^3}{3\ln(2\gamma)} \langle p_i p_j p_k p_l \rangle D_k l. \tag{2.128}$$

We have calculated so far the extra stress on the fluid coming from the fiber. Now we are going to separated the total stress into a part isotropic and other deviatoric:

$$\Sigma_{ij} = -p\delta_{ij} + \sigma_{ij}. \tag{2.129}$$

And

$$\sigma_{ij} = 2\mu D_{ij} + 2\mu_{ijkl} D_{kl}, \tag{2.130}$$

As a result:

$$\mu_{ijkl} = \frac{2\pi\mu n l^3}{3\ln(2\gamma)} \left[\langle p_i p_j p_k p_l \rangle - \frac{1}{3}\delta_{ij} \langle p_k p_l \rangle \right]. \tag{2.131}$$

Equation (2.127) reveals that the extensional viscosity, η_e, is influenced by nl^3. Thus, it can be argued that, when treating the system as an equivalent homogeneous fluid, the tubes introduce an additional stress (stresslet) similar to that of an Einstein suspension composed of boundary spheres with radius ℓ.

3 MATERIALS AND METHODS

3.1 Experimental apparatus

3.1.1 Rheometer

The rheological properties of the fluids under analysis in this work are obtained using a high performance Physica Modular Compact Rheometer - MCR 301, illustrated in figure (11). As its name states, this rheometer works based on modules, a feature that makes this device really versatile. Each module is composed by a measuring system and a measuring cell, which combined permit the user to measure several material functions of both, Newtonian and non-Newtonian fluids, in a variety of shear flow conditions (permanent and transient). Depending on the module mounted on the rheometer, not only flow-related effects on the rheological behavior of a given fluid can be measured, but also, one can measure the dependence of the material functions on different external variables, like temperature and magnetic field.

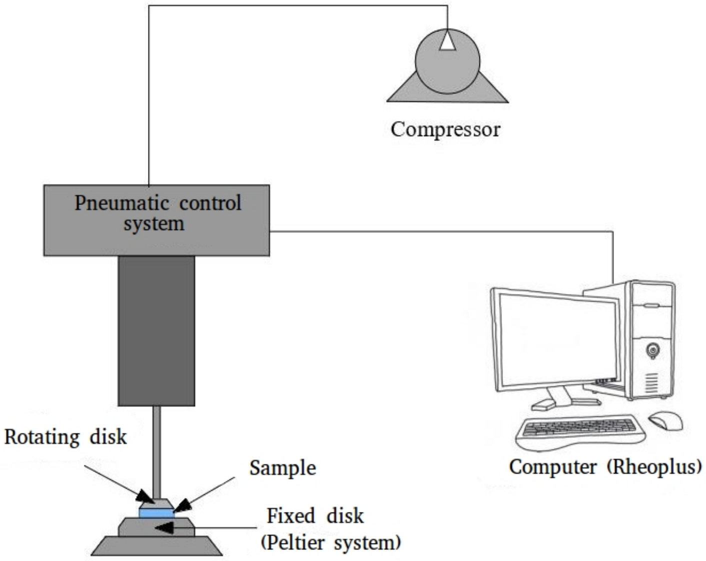

Figure 11 – Schematic view of the rheometer.

The MCR 301 rheometer is very robust. The measuring system is powered by a permanent magnet synchronous drive motor placed on the measuring head, which is able to apply torques from 0.1μN.m to $200\,m$N.m with resolution of $0.001\,\mu$N.m and accuracy of $0.2\,\mu$N.m. The capability of the device to apply a wide range of torques is the key factor that allows the measurement of several rheological properties of a considerable variety of fluids. The motor can also apply oscillations in a range from 0.0001 to 100 Hz. Those characteristics can only be achieved due to the fact that the shaft of the measuring system is sustained by an pressurized air bearing, what strongly reduces the friction between the components of the drive system.

Temperature greatly influences the rheological behavior of almost all substances (BIRD et al., 1987; BARNES; HUTTON; WALTERS, 1989). As a result, it is of high importance, for obtaining significant measurements, the rheometric devices can provide means of effectively control the temperature of samples under analysis. In this context, The Physica MCR 301 rheometer presents different systems of temperature control, also called environmental systems, whose utilization depend on the measuring cell mounted on the flange ring of the device. It is important to note that the temperature control systems are highly accurate, with minimal thermal gradients. In addition, traceable automatic temperature calibration sensors are available to ensure that the system is always operating within specifications.

An environmental system designed to work with all the measuring cells is the liquid temperature control, which operates based on the flow of a liquid with controlled temperature through the measuring cell. The fluid exchange heat with the metal disk, where the material sample is placed. When thermal equilibrium is reached, the temperature of the sample under analysis tends to the temperature of flowing fluid (despite a small uncertainty). The refrigeration/heating fluid must have a well controlled temperature and flow with a high mass flux in order to fulfill the heat exchange needs for keeping the sample at a prescribed temperature. These properties of the flowing fluid are provided by an external thermal bath, which is coupled to the rheometer. This device is capable of working with water or oil as circulating fluid.

Other environmental system available is the Peltier temperature control. In this technical solution, the temperature of the sample is controlled by a Peltier thermoelectric plate, that is attached to the fixed disk of the measuring cell. This system operates based on the Peltier effect, characterized by maintaining a temperature difference in the union of two conductors (or semiconductors) of distinct materials in a closed circuit when it is passed through by an electric current. This device allows fast, precise and active control of the sample temperature in a range from -40 to $200\,^{\circ}$C. It is interesting to note that the Peltier system cannot be used in applications where external magnetic fields are applied to the sample. In this case, temperature control is only done using the thermal bath.

Figure (11) summarizes the systems involved in the acquisition of the data concerning the rheological properties of a fluid sample. Despite the pneumatic control system already discussed in this section, the referred schematic representation shows that the rheometer is connected to a microcomputer, through which it is operated with the help of the software Rheoplus. In this software, all conditions necessary for performing different types of rheological experimental trials are defined, such as the shear rate, the oscillation frequency, the amplitude of strain , the magnetic field intensity, the temperature of the sample or the heating-rate profile, among other parameters. Additionally, the software presents in real-time the collected data arranged in the form of graphs and tables. Several *ad-hoc* rheological models are available and automated in its database, what enables a preliminary post-processing analysis and, as a result, a previous verification of the adequacy of theoretical models to the data obtained from measurements.

The assemblies of the rheometer used in this work are all of the parallel plate type. They are characterized by the fact that its test region, in which the fluid under analysis is placed, is a fictitious cylinder delimited by two discs, one mobile (measuring system) and the other fixed (measuring cell). The height of this cylinder, which is also the gap between the discs is a function of the fluid viscosity and should be optimized for each type of fluid under analysis. It is important to note that the device is equipped with the TruGap technology (Anton Paar GmbH, Germany), which permits the precise adjustment of the gap between the parallel plates to the value prescribed by the operator, independently of the temperature and thermal expansion of the assembly components. With this feature, small gaps ($< 0.5\,\mathrm{mm}$) can be achieved with micrometric precision. The volume of the fluid sample required to obtain a consistent experimental trial can be approximated by the volume of the fictitious cylinder, however it is a good practice to use a slightly larger volume to ensure that the space between the plates is fully filled during data collection.

3.1.1.1 Standard assembly

This mouting s measuring system is denominated PP-50, which is a stainless steel rod that in one of its ends presents a disk with a diameter of 49.963 ± 0.005 mm.

The measuring cell in this assembly is a Peltier-temperature-controlled bottom plate. This assembly is used to measure rheological properties of Newtonian and non-Newtonian fluids in regimes of permanent and transient shear. Those properties can be assessed as functions of time, shear-rate and, especially of temperature, due to the fact that this parameter is precisely controlled in this assembly.

3.1.1.2 Magneto-rheology assembly

This assembly is used to investigate the effects caused by the application of an external homogeneous magnetic field on the rheological behavior of a given magnetizable fluid. Generally, ferrofluids and magneto-rheological suspensions are investigated utilizing this apparatus. In this assembly, the measuring system is denominated PP-20. It has the same geometry of PP-50, differing only in the diameter of the disk, that in this device measures 19.946 ± 0.005mm.

In this assembly, the measuring cell is denominated MRD (magneto-rheological device) and it consists of a liquid-temperature-controlled bottom plate with built-in coils that produce magnetic field. A magnetic yoke covers the plate to ensure a homogeneous field and perpendicular field lines with respect to the plate. The parallel-plate system is made of non-magnetized metal, preventing radial forces acting on the shaft. The yoke can be temperature-controlled up to 70°C with the liquid used in the bottom plate. It is important to note that the Peltier temperature controller cannot be used in this assembly owing to the fact that it works based on an eletric circuit, that would be certainly damaged by the external magnetic field applied by the coils located under the bottom plate. The MRD is fully integrated in the rheometer's software, which controls the magnetic field and records all important parameters. Measurements of the magnetic field are made using an external Hall sensor. All the features summarized here ar displayed on figure (12).

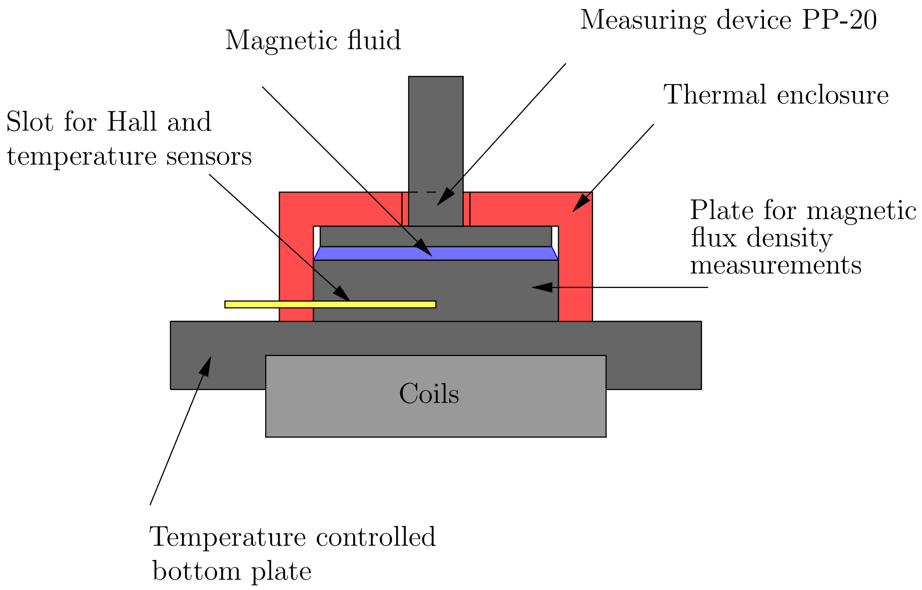

Figure 12 – MRF assembly: schematic of the measuring cell.

The continuous current needed to generate the magnetic field by the coils of the measuring cell is provided by a DC power supply. This device can furnishes continuous currents up to 5A between its terminals. In this maximum condition of operation, the coils produce an magnetic field of up to 1.3 Tesla in the air gap between the parallel disks.

3.2 Rheometer calibration

In order to obtain meaningful measurements, the gap of the rheometer have been calibrated through the measurement of the viscosity of a series of different Newtonian fluids. Figure (13) shows the result of the measurement of the viscosity of water, at a constant temperature of 25°C, when subjected to a fixed shear rate of $100\,\mathrm{s}^{-1}$. The gap used in the referred measurement was 0.08 mm, that resulted on a viscosity of 0.89 ± 0.01

mPa.s. This result is in agreement with the consolidated value presented for the viscosity of water at the referred temperature, what can be easily verified on Tanner (2000). As a result, such value of gap is the ideal for performing rheological measurements on fluids whose viscosities are of the same order of magnitude of the one observed for water.

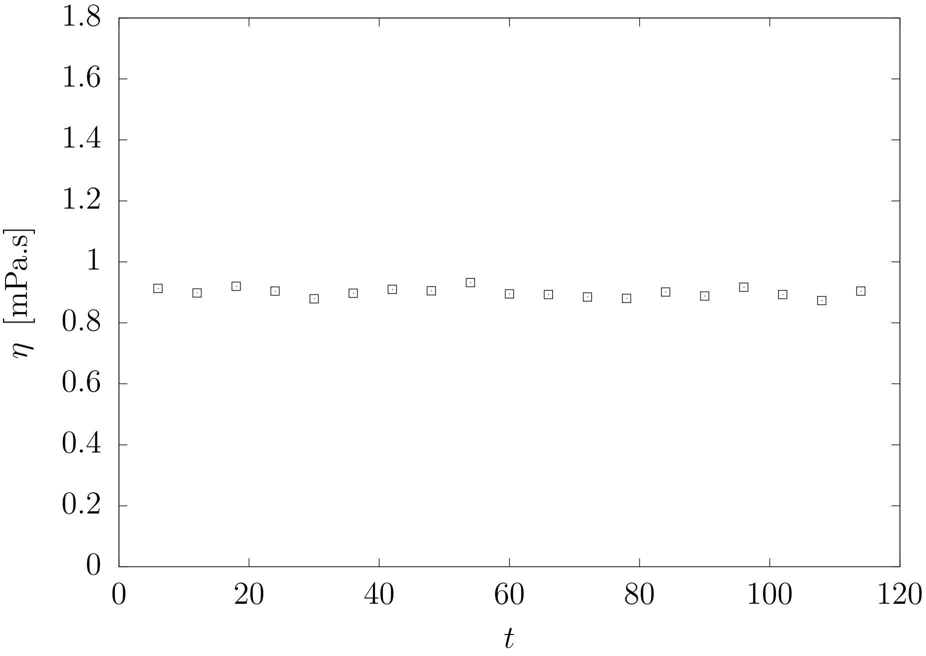

Figure 13 – Viscosity of distilled water as a function of time, measured on the rheometer of parallel plates Physica MCR-301. The shear rate is fixed at 100 s^{-1} and the temperature, at 25°C. The gap between the parallel plates is 0.8 mm.

Using the same methodology, it was possible to establish a reference of optimal gaps to be used in the measurement of the rheological properties of fluids with a wide range of viscosity. The results of this calibration are summarized on table (1).

Table 1 – Optimal gaps for carrying out rheological experiments on fluids, as a function of the order of magnitude of their kinematic viscosity.

Fluid	Viscosity [$\mathrm{mPa} \cdot \mathrm{s}$] (order of magnitude)	Optimal gap [mm]
Water	1	0.08
Ethylene glycol	10	0.1
Mineral oil	100	0.3
Glycerin	1000	0.5
Silicon oil	> 10000	0.8

It is also important to analyze the fact that the geometry of measurement, parallel disks has a gradient of shear rate in the radial direction. In order to estimate the time that a particle would take to move by one radii, we shall use the concept of shear induced diffusion (CUNHA; HINCH, 1996). The diffusivity is given by $D = \dot{\gamma} a^2 \phi$, in which $\dot{\gamma}$ is the shear rate, a is the particle diameter and ϕ, the particle volume fraction. Considering the time to displace the particle δt and the radius of the rheometer as r. The diffusivity D scales with a length L multiplied by a velocity U, thus:

$$D \sim LU \sim r\frac{r}{\delta t_d} \tag{3.1}$$

Then:

$$\delta t_d \sim \frac{r^2}{\dot{\gamma}a^2} \sim \left(\frac{r}{a}\right)^2 \frac{1}{\dot{\gamma}\phi} >> \frac{1}{\dot{\gamma}} \tag{3.2}$$

Considering $\dot{\gamma} = 100s^{-1}$, $r = 20mm$, $a = 5\mu m$ and $\phi = 0.01$, which are good approximations of the scales in the experiments, we have that the time for a particle to migrate of radius of displacement is much bigger that the experimental time $\delta t_e = \frac{1}{\dot{\gamma}}$.

Shear-induced diffusion and potential slip effects due to solids are second-order phenomena and are therefore accounted for in the error bars accompanying each experimental data point. It is also worth noting that each data point represents the average of a series of measurements, as detailed in Appendix (A).

3.3 Fluids under analysis

3.3.1 Magnetorheological suspensions

Two types magnetorheological suspensions are analyzed in this work. The first one is composed of magnetite nanoparticles with 8 nm of average diameter and density 5.3 g/ml dispersed in a Newtonian mineral oil of density 0.87 g/ml and viscosity of 147.69 ± 4.51 mPa.s at 25 °C as the fluid base. The magnetization of saturation of the magnetite particles is 4.46×10^5A/m.

The second one is made of particles of iron with an average size between 5-9 μm and density of 7.86 g/ml. These particles are also dispersed in the same mineral oil matrix used to compose the magnetorheological suspensions of magnetite. The magnetization of saturation of the magnetite particles is 175 emu/g (BOMBARD et al., 2003). This value was converted to S.I. units resulting in 1.37×10^6A/m.

3.3.2 Aqueous suspensions of doubel-walled carbon nanotubes

The aqueous suspensions of double-walled carbon nanotubes are biphasic systems composed by distilled water and DWCN powder. In order to produce suspensions with varied particle volume fractions, it was necessary to determine the density of its components. As a result we obtained at 25°C: for the distilled water - ρ_w= 0.99 ± 0.01g/ml and - for the DWCN powder - ρ_D= 1.91 ± 0.05g/ml. The suspensions produced are the ones detailed at table (2).

Table 2 – Properties of the aqueous suspensions of DWCN

Suspension label	Volume fraction, ϕ	Mass of DWCN, m_D
A	0.004	0.38
B	0.005	0.47
C	0.006	0.57
D	0.007	0.66
E	0.008	0.76

3.4 Rheometry

3.4.1 Measurement of the apparent viscosity on a parallel plate rheometer

The following equation is used to determine the apparent viscosity of a fluid in a torsional rheometer of parallel disks:

$$\eta(\dot{\gamma}_R) = \frac{\mathcal{T}}{2\pi R^3 \dot{\gamma}_R}\left[3 + \frac{d\log(\frac{\mathcal{T}}{2\pi R^3})}{d\log\dot{\gamma}_R}\right]. \tag{3.3}$$

Therefore, to measure the apparent viscosity of any given fluid on a parallel disk rheometer based on the shear-rate evaluated on the border of the disk $\dot{\gamma}_R$, it is necessary to obtain experimental data of the viscosity for multiple values of $\dot{\gamma}_R$, that is, for a wide range of Ω, so that the torque derivative shown in equation (3.3) can be calculated. Based on this, one can finally apply the correction represented by the bracketed term in this equation to each pair of data $(\mathcal{T}, \dot{\gamma}_R)$.

It is important to note that the material particles do not experience the same angular deformation (γ) because it varies with the radius, as shown in equation (**??**). On the other hand, the torque $\mathcal{T}$ is an integral quantity and, as a result, it represents the contribution of all fluid elements subjected to shear, which is also verified for viscosity, since it is obtained from the measurement of the torque. Therefore, this property represents an average viscosity that would be calculated for each element subjected to a different shear rate. This only poses a problem for fluids that are very sensitive to angular deformation, such as liquid crystals and multiphase fluids.

The formula (3.3) permits the obtainment of the viscosity as a function of torque for any fluid in a parallel disc rheometer. Therefore, it is also applicable to Newtonian fluids, for which it is considerably simpler. By developing the exact differentials of the numerator and denominator on the right side of the equation (3.3), we obtain that:

$$d\left[\log\left(\frac{\mathcal{T}}{2\pi R^3}\right)\right] = \frac{2\pi R^3}{\ln(10)} d\left(\frac{\mathcal{T}}{2\pi R^3}\right), \tag{3.4}$$

and

$$d\left[log\left(\dot{\gamma}_R\right)\right] = \frac{1}{\ln(10)\dot{\gamma}_R} d\left(\dot{\gamma}_R\right). \tag{3.5}$$

Dividing equations (3.4) and (3.5), we obtain that:

$$\frac{d\log(\dfrac{\mathcal{T}}{2\pi R^3})}{d\log\dot{\gamma}_R} = \frac{2\pi R^3\dot{\gamma}_R}{\mathcal{T}}\frac{d\left(\dfrac{\mathcal{T}}{2\pi R^3}\right)}{d\left(\dot{\gamma}_R\right)}. \tag{3.6}$$

For a Newtonian fluid, it is easily shown that the applied torque on a parallel disks configuration (Couette flow) is ggiven by:

$$\mathcal{T} = \pi\dot{\gamma}_R\eta\frac{R^3}{2}. \tag{3.7}$$

Replacing this result on equation (3.6), it comes that:

$$\frac{d\log(\dfrac{\mathcal{T}}{2\pi R^3})}{d\log\dot{\gamma}_R} = \frac{4}{\eta}\frac{d\left(\dfrac{\dot{\gamma}_R\eta}{4}\right)}{d\left(\dot{\gamma}_R\right)}. \tag{3.8}$$

Since viscosity η is constant with respect to shear-rate variations for a Newtonian fluid, one obtains:

$$\frac{d\log(\dfrac{\mathcal{T}}{2\pi R^3})}{d\log\dot{\gamma}_R} = \frac{d\left(\dot{\gamma}_R\right)}{d\left(\dot{\gamma}_R\right)} = 1. \tag{3.9}$$

Because of this result, it can be shown that equation (3.3) for a Newtonian fluid reduces to:

$$\eta(\dot{\gamma}_R) = \frac{\mathcal{T}}{2\pi R^3\dot{\gamma}_R}\left[3+1\right] = \frac{2\mathcal{T}}{\pi R^3\dot{\gamma}_R}. \tag{3.10}$$

Therefore, one obtains:

$$\eta(\dot{\gamma}_R) = \frac{2\mathcal{T}h}{\pi\Omega R^4}. \tag{3.11}$$

3.4.2 Measurement of the viscoelastic moduli on a parallel plate rheometer in regime of small amplitude oscillatory shear - SAOS

SAOS experiments were also carried out to examine the dynamic viscoelastic moduli $G'(\omega)$ (elastic component) and $G''(\omega)$ (viscous component) of the ferrofluids in the presence of an external uniform magnetic field H_0 and a strain $\gamma(t) = \gamma_0\sin(\omega t)$. The stress response $\sigma(t) = \sigma_0\sin\left(\omega t + \beta_0\right)$, where ω is the forcing frequency, β_0 is the phase angle, $\gamma_0 \sim R/h$ denotes the strain amplitude and σ_0 is the stress amplitude. Here R is the disk radius and h is the gap height. Under SAOS regime, $G'(\omega) = \sigma_0\cos\left(\beta_0\right)/\gamma_0$ and $G''(\omega) = \sigma_0\sin\left(\beta_0\right)/\gamma_0$. More specifically, for parallel-disk apparatus as the rheometer used here, the viscoelastic material functions can be evaluated experimentally by the following expressions (BIRD; ARMSTRONG; HASSAGER, 1987):

$$G'(\omega) = \frac{2hT_0\cos\left(\beta_0\right)}{\pi R^4\theta_0}, \tag{3.12}$$

and

$$G''(\omega) = \frac{2hT_0\sin\left(\beta_0\right)}{\pi R^4\theta_0}, \tag{3.13}$$

where T_0 is the applied torque and θ_0 the is the angular displacement.

4 RHEOLOGY OF MAGNETORHEOLOGICAL SUSPENSIONS

4.1 A brief overview on ferrofluid's rheology

This study of the rheology of magnetorheological suspensions represents a natural extension of previous research on ferrofluid rheology conducted by the Laboratory of Microhydrodynamics and Rheology (MicroRheo) within the Vortex group at the University of Brasília. Ferrofluids, which consist of ferri/ferromagnetic nanoparticles dispersed in a non-magnetic carrier fluid, have been extensively investigated. In a comprehensive study of the rheological properties of two commercial ferrofluids, Pereira and Cunha (2023) examined both permanent simple shear and transient shear conditions. Their findings revealed that ferrofluids exhibit viscoelastic behavior in the presence of an external magnetic field, with the elastic properties linked to the formation of a microstructure via dipolar interactions. Notably, it was also observed that ferrofluids display residual stress in the presence of a magnetic field, as their shear stress does not relax to zero.

Another important characteristic shared by ferrofluids and magnetorheological suspensions is their shear-thinning behavior under an external magnetic field. The results presented by Pereira and Cunha (2023) align with other literature, thereby validating the equipment and methodologies employed in the MicroRheo laboratory.

In their work, Pereira and Cunha (2023) provide Figure (14), illustrating the increase in the magnetic viscosity increment as a function of the magnetic parameter (α). The plot depicts the viscosity increment due to magnetic effects for the ferrofluid EFH1 (Ferrotec - USA), composed of magnetite hard particles (with a magnetic dipole locked in the particle) at a volume fraction of 7.9%, under conditions of very weak flow ($\mathrm{Pe} = 4.64 \times 10^{-4}$). An insert within the figure compares their experimental measurements with those from Odenbach (2009). Included in this comparison is the theoretical prediction provided by the equation:

$$\eta_r(\alpha,\phi) = \Delta\eta = \eta(\alpha,\phi) - \eta_0 = \frac{3}{2}\eta_0\phi\frac{\alpha L^2(\alpha)}{\alpha - L(\alpha)}, \tag{4.1}$$

where η_r is the rotational viscosity (magnetoviscous effect), ϕ is the volume fraction of magnetic nanoparticles, α is the non-dimensional external magnetic field, η_0 is the viscosity of the carrier fluid, and $L(\alpha) = 1 - \coth(1/\alpha)$ represents the Langevin equation. The circles in the insert represent experimental data from Odenbach and Thurm (2002) for a ferrofluid comprising magnetite particles at a volume fraction of 7.2% and Pe $= 1.85 \times 10^{-2}$, conditions that are consistent with our experiments.

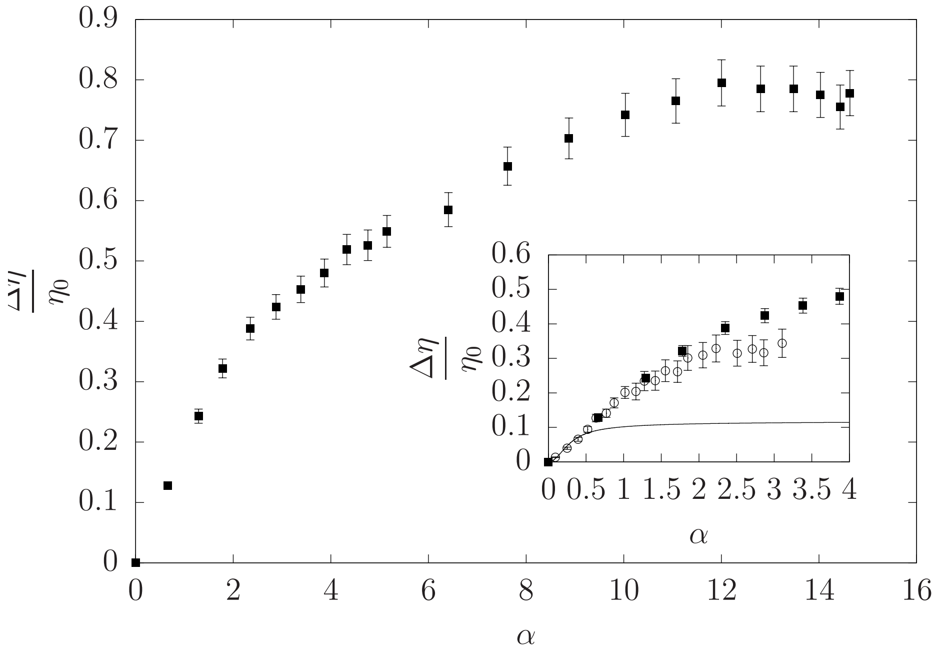

Figure 14 – Non-dimensional magnetic viscosity increment $\Delta\eta/\eta_0$ as a function of the non-dimensional magnetic parameter α subjected to weak flow with Pe $= 4.64 \times 10^{-4}$ (■). The insert compares the behavior of $\Delta\eta/\eta_0$ as a function of α for two magnetic fluids: (■) represents data for the ferrofluid EFH1 composed of magnetite particles with a mean diameter of 10 nm, $\phi = 7.9\%$, and Pe $= 4.64 \times 10^{-4}$; (○) represents data from (ODENBACH, 2009) for a colloidal suspension of magnetite particles with a mean diameter of 10 nm, $\phi = 7.2\%$, subjected to a similar weak flow with Pe $= 1.85 \times 10^{-2}$. The solid line in the plot corresponds to the theoretical prediction given by equation (4.1) with $\phi = 7.9\%$. The theoretical curve fits the data only in the linear regime of the plot (i.e., $O(\alpha)$). The viscosity in the absence of a magnetic field, η_0, is constant at 0.94×10^{-2} Pa.s at $25°C$.

From Figure (14) and its insert, it is evident that the dependence of the viscosity increment on the intensity of the magnetic field is significantly stronger than predicted by the non-interacting model in equation (4.1). While this equation suggests a viscosity increment $\Delta\eta \approx 0.1\eta_0$, experimental results indicate a much stronger nonlinear regime with $\Delta\eta \approx 0.8\eta_0$. The theoretical curve only aligns with experimental data within the linear regime of the plot (i.e., $O(\alpha)$), which corresponds to small values of α (i.e., ≤ 0.5).

As noted by Odenbach (2009), the discrepancies between theoretical predictions and experimental observations arise from the neglect of dipolar interactions between particles in the dilute limit, leading to a linear dependence of the magnetic viscosity increment on α. However, real ferrofluids typically have particle volume fractions ranging from 7% to 10%, indicating they are not dilute. In these non-dilute ferrofluids, interparticle interactions become crucial, resulting in the formation of particle chains and agglomerates. These structures require considerably stronger hydrodynamic torques from the shear flow to rotate against the magnetic torque that aligns them with the applied field. This competition between the magnetic field and the flow leads to a significant increase in fluid viscosity, as clearly demonstrated in Figure (14). Thus, the rheological properties of ferrofluids are profoundly influenced by their internal structures induced by flow and magnetic fields, as emphasized by Odenbach (2009).

All the rheological effects discussed for ferrofluids also apply to magnetorheological suspensions (MRS), but are intensified due to the larger average magnetic particle dimensions, which are micrometric compared to the nanometric dimensions observed in ferrofluids.

4.2 Characterization of magnetic structures

4.2.1 The magnetic field generated by a rectangular neodymium permanent magnet - an experimental analysis

The static characterization of the elements of the microstructure of the magnetorheological suspensions both, in the presence and in the absence of an external magnetic field, was carried out using the microscope described in the section (**??**) associated with an apparatus consisting of a rule and a rectangular neodymium magnet, as shown in figure (15). This apparatus was important in order to obtain and calibrate an expression which gives the intensity of the effective magnetic field H_x as a function of the coordinate x.

As a result, a gaussmeter probe was placed in the origin of the coordinate system, which corresponds to the x position of the geometric center of the microscope slide. First the magnet is placed in the x-position 10.5 cm and the magnetic field intensity is measured, after that, the magnet is approximated in steps corresponding to decrements of 0.5 cm until the position 1cm is reached. The measuments continue from that decreasing the distance of the magnet to the center of the slide by decrements of 0.2cm.

Based on the values obtained for H_x as a function of the distance x, it is proposed a seventh-order polynomial fit for the experimental data:

$$H_x \times 10^{-5} = a_1x^7 + a_2x^6 + a_3x^5 + a_4x^4 + a_5x^3 + a_6x^2 + a_7x + a_8. \tag{4.2}$$

This idea is inspired by the work of Furlani (2001), where it is shown that polynomial expressions for this relationship are more suited than the well know formula derived by McCaig and Clegg (1987) in conditions where the magnet is very near the point of measurement (probe of the gaussmeter). The measured data is displayed in figure (16), where is also shown the curve resulting of the adjustment of the experimental to expression (4.2). The resulting fit parameters are displayed on table (3).

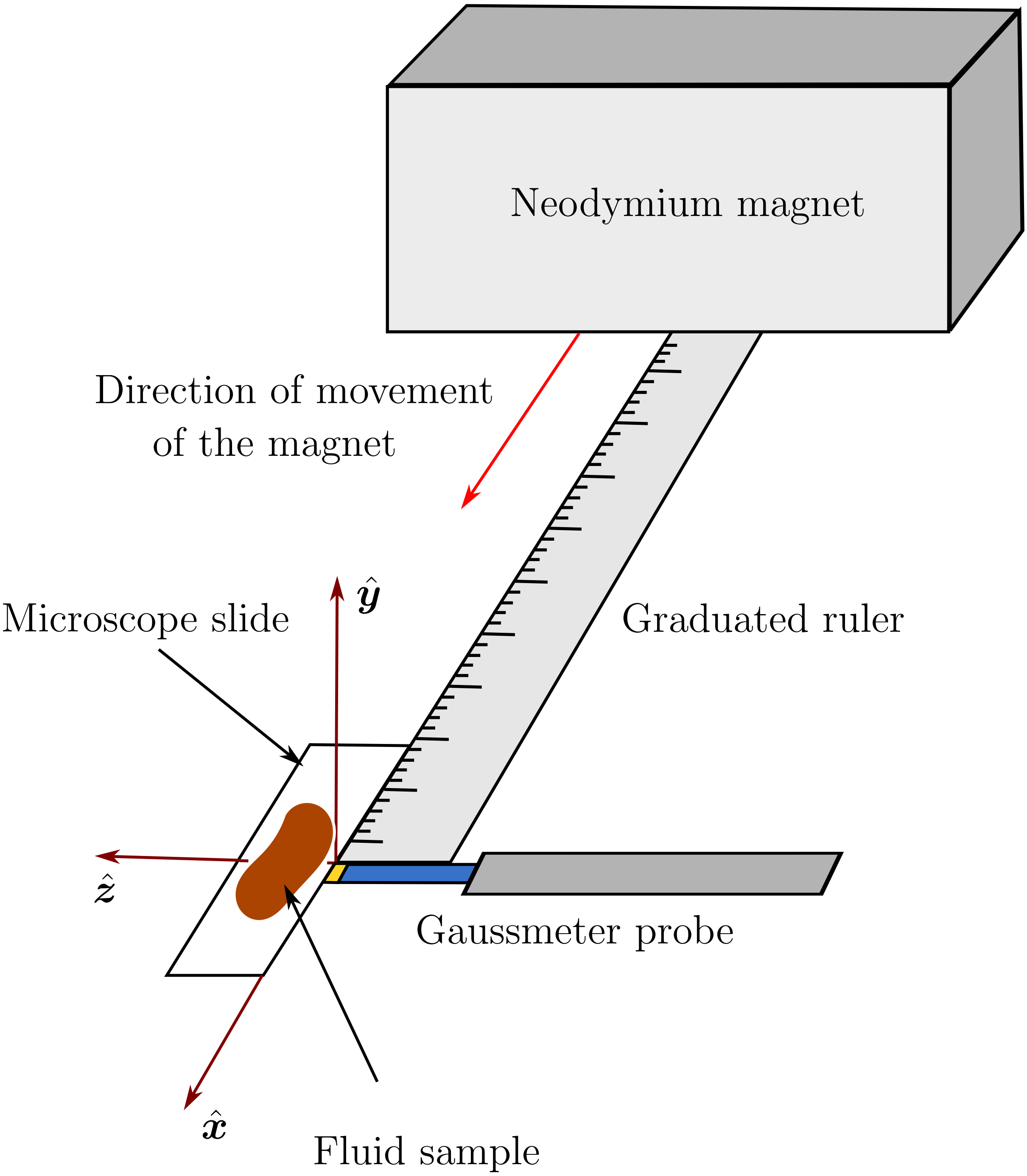

Figure 15 – Schematics of the apparatus used for measuring the effective magnetic field intensity for a given neodymium permanent magnet placed at a given x distance from the fluid sample.

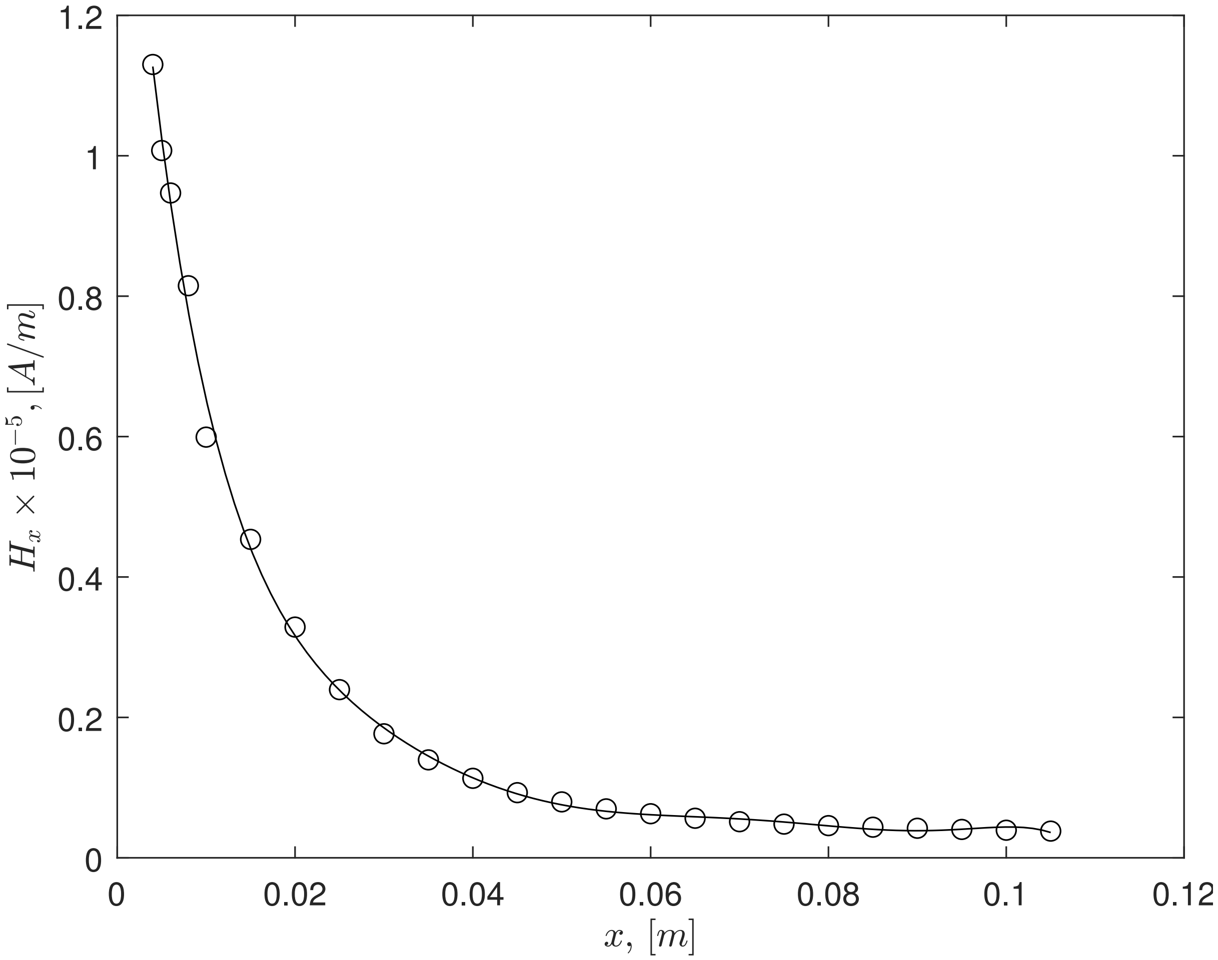

Figure 16 – H_x- component of the effective magnetic field as a function of the x position. The circles depict experimental data and the curve is a fit of the referred data to a seventh-order polynomial model, given by $H_x \times 10^{-5} = a_1x^7 + a_2x^6 + a_3x^5 + a_4x^4 + a_5x^3 + a_6x^2 + a_7x + a_8$. The resulting fit parameters are displayed on table (3).

Table 3 – Fitting parameters: adjustment of the experimental data concerning H_x as a function of x to a seventh-order polynomial, given by $H_x \times 10^{-5} = a_1x^7 + a_2x^6 + a_3x^5 + a_4x^4 + a_5x^3 + a_6x^2 + a_7x + a_8$.

Parameter	Numeric value
a_1	-6.91×10^8
a_2	2.95×10^8
a_3	-5.18×10^7
a_4	4.86×10^6
a_5	-2.65×10^5
a_6	8.62×10^3
a_7	-1.65×10^2
a_8	1.67×10^0

4.2.2 Determination of initial conditions - static measurement of the length of magnetic structures depending on the strength of the applied magnetic field

In the absence of external magnetic field, the suspension of iron has the following size distribution [1]:

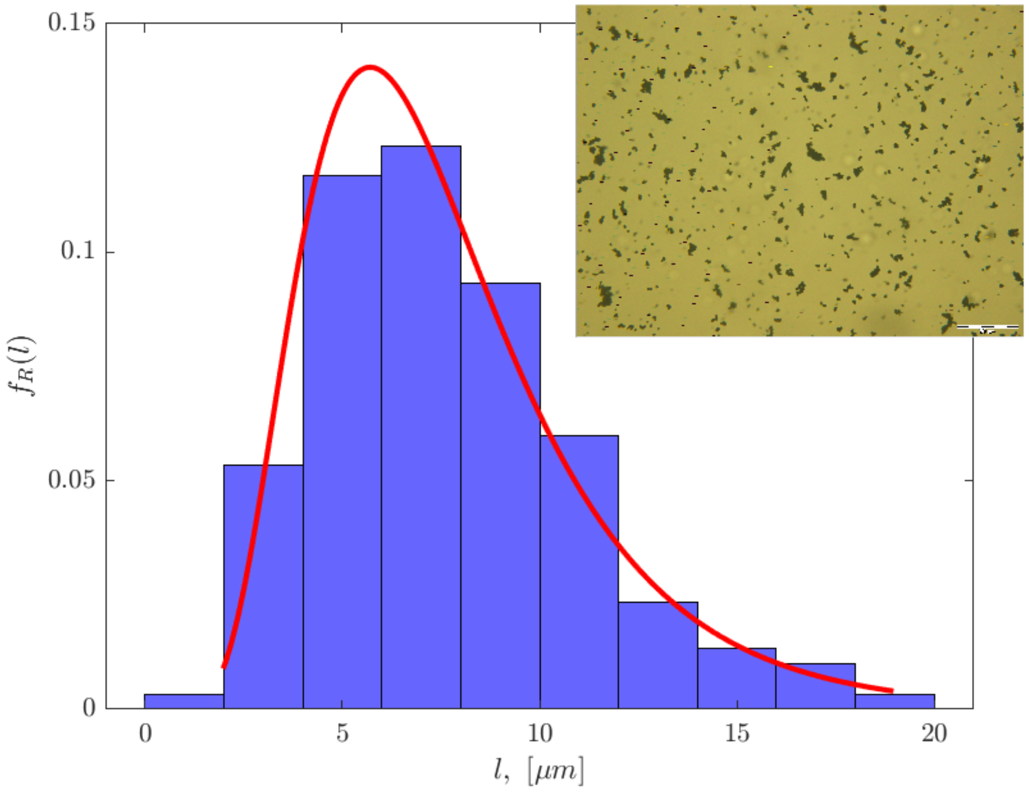

Figure 17 – Size distribution of the iron particles in the absence of external magnetic field. The average particle length $\bar{\ell}$ is 6.98μm with standard deviation of $RMS = 1.2\mu$m. "The inset in the plot shows a typical sample of the particles wit average length of 6.98 μm and $RMS = 1.2\mu m$. The scale bar in the figure of the inset is $50\mu m$.

As a direct consequence of the dipolar interactions between the particles that compose the the magnetorheological suspensions of magnetite and cabonyl-iron, chain-like agglomerates are formed when an external magnetic field is applied to any sample of these materials. This implicates that the initial configuration is composed by very anisotropic structures, which ressonates in the appearance of deeply non-Newtonian behavior as we will opportunely discuss in this thesis.

That being said and regarding the papers of Batchelor (1970a) and Shaqfeh and Fredrickson (1990), one can easily ponctuates that measure the mean lenght of the anisotropic structures as a function of the intensity of the applied magnetic field is impera-

---

[1] The number of columns was found by using Sturges rule (STURGES, 1926)

tive due to the fact that this information impacts directly on the bulck stresslet generated by the microstructure and, as a result on the rheology of these suspensions when seen as a continuous equivalent fluid.

Using the optical microscope and the apparatus shown on figure (15), five individual micographies are captured considering the following distances from the center of the sample (microscope slide): 7, 6.5, 6, 5.5 and 5cm. Besides that, it is easy to determine the magnetic field intensity considering equation (16) and the parameters shown at table (3). The results a resumed at table (4).

x, $[m]$	H_x, $[kA/m]$
0.050	7.56
0.055	6.63
0.060	6.14
0.065	5.84
0.070	5.54

Table 4 – Valores de H_x para diferentes valores de x

Consider the case of the magnetorheological suspension (MRS) of magnetite. Figure (18) presents two micrographs of this MRS, both corresponding to the lowest volume fraction of magnetic particles, $\phi = 0.2\%$. Observe that, although the magnetite particles are nanometric, in the presence of an external magnetic field, it mean length becomes micrometric. Figure (18a) depicts the MRS when the magnet is positioned closest to the sample (5 cm), whereas Figure (18b) shows the same suspension with the magnet in the farthest position (7 cm).

In Figure (18a), due to the proximity of the magnet, the structures formed by the magnetic field are highly aligned with the magnetic field lines, resulting in pronounced anisotropy. In contrast, Figure (18b) reveals that not all particle structures are aligned with the magnetic field. This misalignment occurs because, at this greater distance and small particle volume fraction, the magnetic field is insufficient to induce the same degree of alignment observed in Figure (18a).

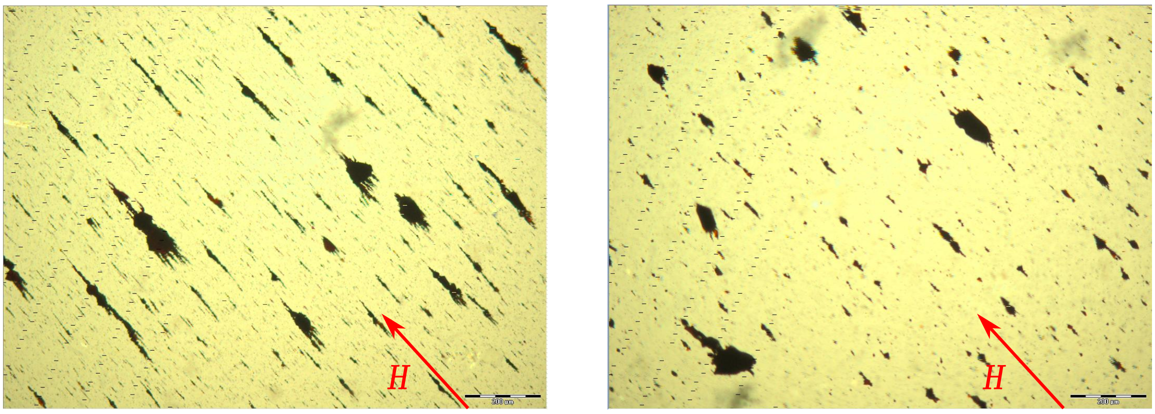

(a) $x = 5$cm, $H_x = 7.56$kA/m

(b) $x = 7$cm, $H_x = 5.54$kA/m

Figure 18 – Micrographies of the SMR of magnetite powder with $\phi = 0.2\%$.

In Figures (19a) and (19b), we observe that, under both intensities of the effective magnetic field, a highly anisotropic and aligned microstructure is formed. This demonstrates that the rheology of these fluids strongly depends on the magnetic particle volume fraction, as well as the direction and intensity of the applied magnetic field.

Figure (20a) shows the size distribution of the chain-like structures in the magnetorheological suspension (MRS) of magnetite with $\phi = 0.2\%$ under a strong magnetic field, while Figure (20b) depicts the same under the weakest magnetic field. It is evident that the stronger the magnetic field, the larger the chain-like structures that form. This phenomenon is attributed to the intensified dipolar interactions between magnetic particles in a stronger magnetic field, facilitating the formation of longer particle chains. The same conclusions can be drawn from the results presented in Figure (21).

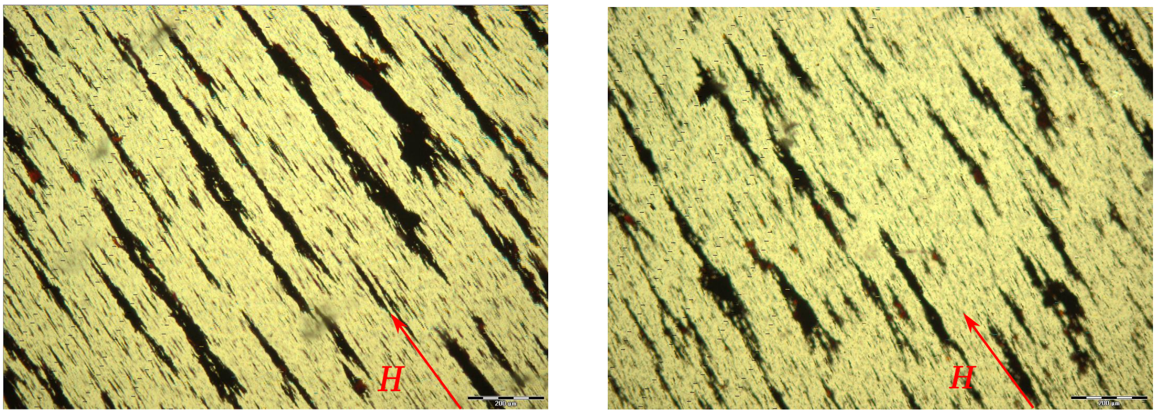

(a) $x = 5\text{cm}$, $H_x = 7.56\text{kA/m}$

(b) $x = 7\text{cm}$, $H_x = 5.54\text{kA/m}$

Figure 19 – Micrographies of the SMR of magnetite powder with $\phi = 1\%$.

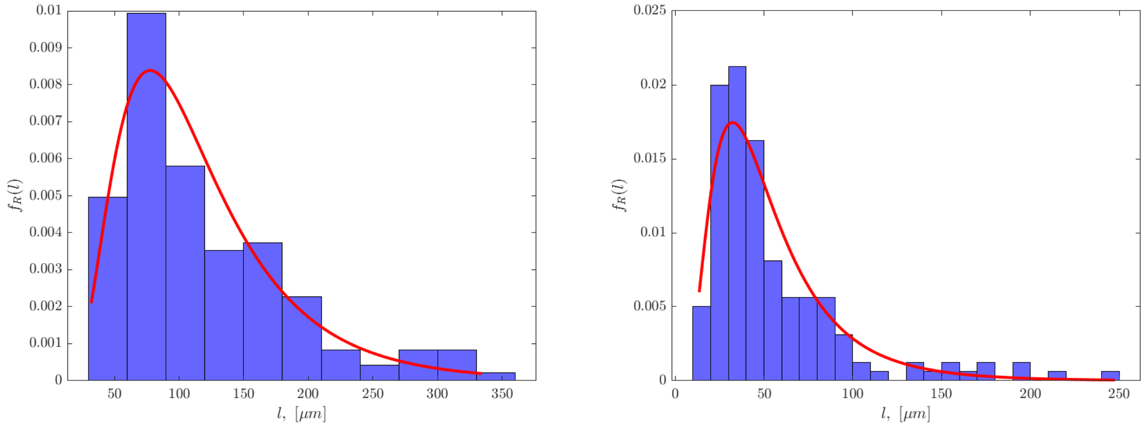

(a) $x = 5\text{cm}$, $H_x = 7.56\text{kA/m}$

(b) $x = 7\text{cm}$, $H_x = 5.54\text{kA/m}$

Figure 20 – Size distribution of the chain-like structures for the SMR of magnetite with $\phi = 0.2\%$.

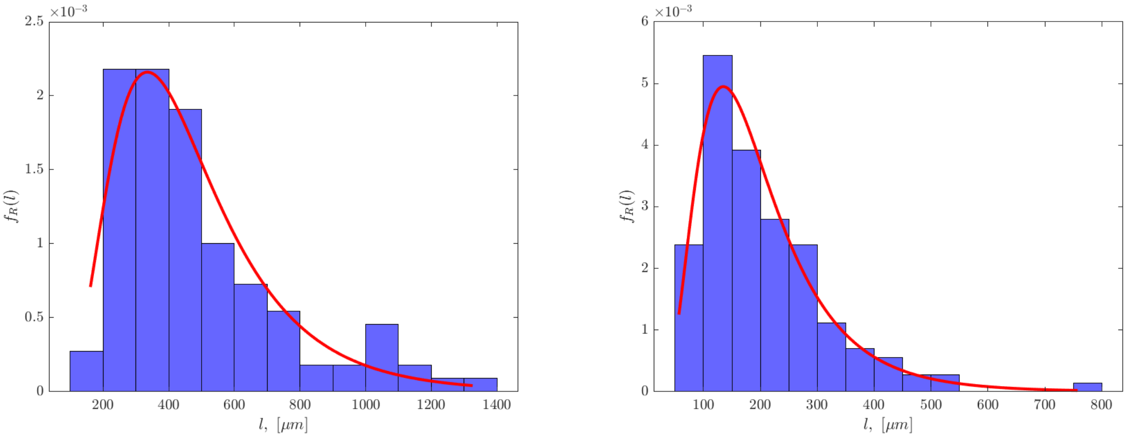

(a) $x = 5\text{cm}$, $H_x = 7.56\text{kA/m}$

(b) $x = 7\text{cm}$, $H_x = 5.54\text{kA/m}$

Figure 21 – Size distribution of the chain-like structures for the SMR of magnetite with $\phi = 1\%$.

Table (5) presents, for each magnetic particle volume fraction used, the mean chain length $\bar{\ell}$, the mean anisotropy parameter $\bar{\ell}/\bar{a}$, and their associated errors, represented as the standard deviation (SD), under five different magnetic field intensities. As observed, for a fixed ϕ, an increase in H results in an increase in both $\bar{\ell}$ and $\bar{\ell}/\bar{a}$. This indicates that as H intensifies, not only does the mean length of the chain-like structures grow, but the structures also become more anisotropic.

Table 5 – Mean chain length $\bar{l}$ and mean anisotropy parameter of the chains $\frac{\bar{l}}{a}$ and their associated errors as functions of the magnetic field strength H and magnetic particle volume fraction ϕ for the magnetorheological suspensions of magnetite powder.

ϕ	H (kA/m)	$\bar{l}$ (µm)	$RMS(l)$ (µm)	$\bar{l}/a$	$RMS(\bar{l}/a)$
0.01	7.55	4.81×10^2	1.63	6.01×10^4	1.59×10^2
	6.63	3.35×10^2	1.51	5.45×10^4	2.24×10^2
	6.14	2.75×10^2	1.63	4.19×10^4	1.68×10^2
	5.84	2.17×10^2	1.78	2.72×10^4	2.56×10^2
	5.54	1.66×10^2	1.68	1.83×10^4	1.27×10^2
0.008	7.55	3.10×10^2	2.03	3.88×10^4	1.27×10^2
	6.63	2.81×10^2	1.73	3.52×10^4	2.67×10^2
	6.14	2.48×10^2	1.59	3.10×10^4	3.74×10^1
	5.84	1.98×10^2	2.00	2.48×10^4	2.36×10^1
	5.54	1.07×10^2	1.75	1.33×10^4	6.08×10^1
0.006	7.55	2.44×10^2	1.92	3.05×10^4	2.16×10^1
	6.63	2.22×10^2	1.54	2.77×10^4	4.37×10^1
	6.14	1.67×10^2	1.99	2.09×10^4	8.93×10^1
	5.84	1.37×10^2	1.99	1.71×10^4	7.93×10^1
	5.54	8.78×10^1	1.99	1.10×10^4	3.59×10^1
0.004	7.55	1.82×10^2	1.75	2.28×10^4	8.21×10^1
	6.63	1.53×10^2	1.86	1.91×10^4	7.26×10^1
	6.14	9.29×10^1	1.43	1.16×10^4	1.06×10^2
	5.84	8.12×10^1	1.75	1.01×10^4	6.47×10^1
	5.54	6.55×10^1	1.81	8.18×10^3	2.99×10^1
0.002	7.55	1.19×10^2	1.21	1.49×10^4	1.23×10^2
	6.63	9.10×10^1	1.70	1.14×10^4	8.97×10^1
	6.14	8.33×10^1	1.79	1.04×10^4	5.19×10^1
	5.84	5.76×10^1	1.79	7.20×10^3	2.82×10^1
	5.54	5.58×10^1	1.65	6.97×10^3	5.16×10^1

The same conclusions drawn for the magnetorheological suspension (MRS) of magnetite can also be applied to the MRS of iron. As shown in Figures (22) and (23), under the influence of an external magnetic field, both the MRS with $\phi = 0.2\%$ and $\phi = 1\%$ exhibit a highly anisotropic, chain-like microstructure. The histograms in Figures (24) and (25) demonstrate that an increase in the intensity of the magnetic field leads to a greater mean length of the chain-like structures. This trend is further corroborated by the data presented in Table (6).

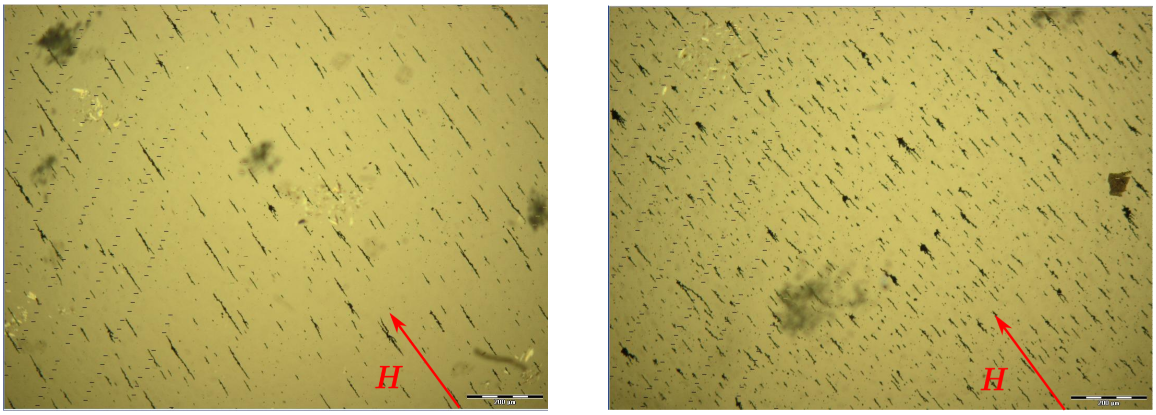

(a) $x = 5\text{cm},\ H_x = 7.56\text{kA/m}$ (b) $x = 7\text{cm},\ H_x = 5.54\text{kA/m}$

Figure 22 – Micrographies of the SMR of iron particles with $\phi = 0.2\%$.

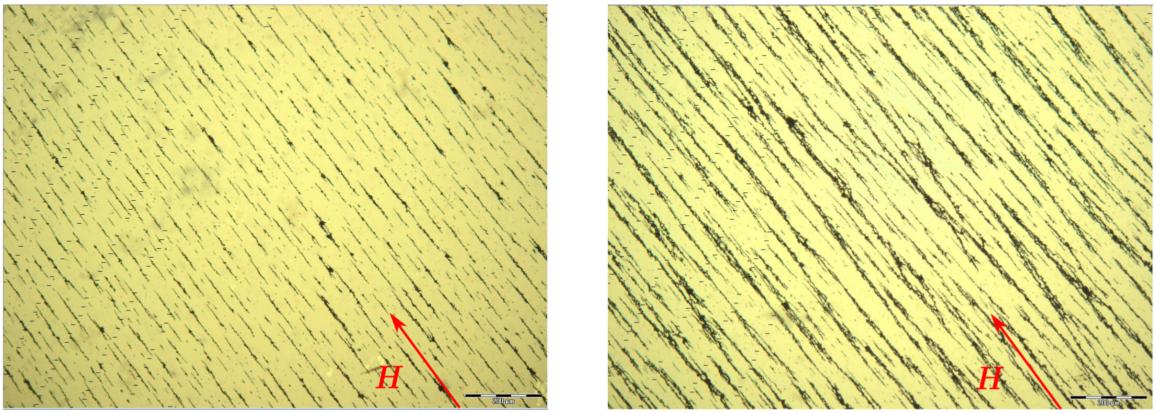

(a) $x = 5\text{cm},\ H_x = 7.56\text{kA/m}$ (b) $x = 7\text{cm},\ H_x = 5.54\text{kA/m}$

Figure 23 – Micrographies of the SMR of iron particles with $\phi = 1\%$.

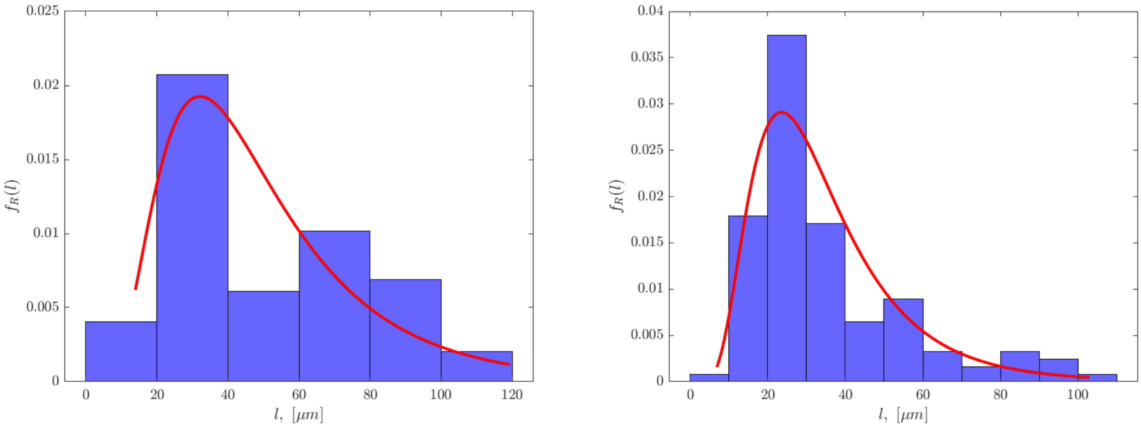

(a) $x = 5\text{cm},\ H_x = 7.56\text{kA/m}$ (b) $x = 7\text{cm},\ H_x = 5.54\text{kA/m}$

Figure 24 – Size distribution of the chain-like structures for the SMR of iron with $\phi = 0.2\%$.

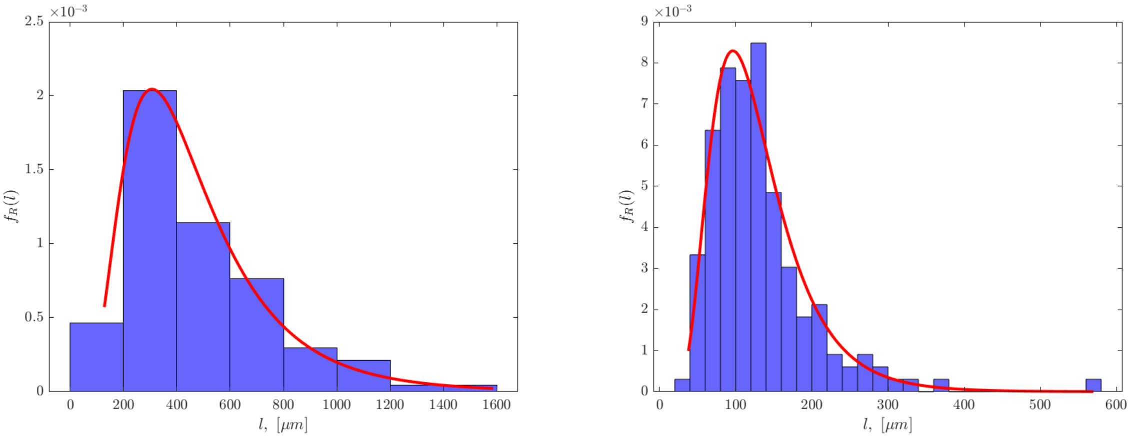

(a) $x = 5$cm, $H_x = 7.56$kA/m (b) $x = 7$cm, $H_x = 5.54$kA/m

Figure 25 – Size distribution of the chain-like structures for the SMR of iron with $\phi = 1\%$.

Table 6 – Mean chain length $\bar{l}$ and mean anisotropy parameter of the chains $\frac{\bar{l}}{a}$ and their associated errors as functions of the magnetic field strength H and magnetic particle volume fraction ϕ for the magnetorheological suspensions of iron particles.

ϕ	H (kA/m)	$\bar{l}$ (µm)	$RMS(l)$ (µm)	$\bar{l}/a$	$RMS(\bar{l}/a)$
0.01	7.55	5.35×10^2	1.61	7.65×10^1	1.04×10^{-1}
	6.63	3.52×10^2	2.05	5.03×10^1	1.66×10^{-1}
	6.14	2.96×10^2	1.78	4.23×10^1	7.30×10^{-2}
	5.84	1.81×10^2	1.92	2.58×10^1	2.15×10^{-2}
	5.54	1.31×10^2	1.57	1.88×10^1	5.73×10^{-2}
0.008	7.55	5.01×10^2	1.73	7.15×10^1	3.72×10^{-1}
	6.63	3.11×10^2	1.76	4.45×10^1	8.02×10^{-2}
	6.14	2.01×10^2	1.86	2.87×10^1	2.22×10^{-1}
	5.84	1.69×10^2	1.73	2.41×10^1	3.24×10^{-2}
	5.54	1.22×10^2	1.80	1.75×10^1	2.80×10^{-2}
0.006	7.55	4.00×10^2	1.54	5.71×10^1	1.80×10^{-1}
	6.63	2.84×10^2	1.99	4.06×10^1	1.61×10^{-1}
	6.14	1.68×10^2	1.99	2.40×10^1	1.64×10^{-1}
	5.84	1.44×10^2	1.82	2.06×10^1	8.27×10^{-2}
	5.54	1.01×10^2	1.68	1.45×10^1	1.29×10^{-1}
0.004	7.55	2.04×10^2	1.84	2.92×10^1	1.61×10^{-1}
	6.63	1.51×10^2	1.91	2.15×10^1	1.62×10^{-1}
	6.14	1.37×10^2	1.86	1.95×10^1	1.19×10^{-1}
	5.84	1.09×10^2	1.59	1.56×10^1	5.16×10^{-2}
	5.54	5.83×10^1	1.72	8.32	4.50×10^{-2}
0.002	7.55	5.04×10^1	1.74	7.20	5.64×10^{-2}
	6.63	4.08×10^1	1.61	5.83	4.84×10^{-4}
	6.14	2.67×10^1	1.55	3.81	5.87×10^{-5}
	5.84	2.48×10^1	1.66	3.54	1.78×10^{-2}
	5.54	2.21×10^1	1.66	3.16	1.77×10^{-2}

To better understand the dependence of the mean length of the chain-like structures $\bar{\ell}$ on the applied magnetic field H, Figures (26) and (27) illustrate this relationship for the magnetorheological suspension (MRS) of magnetite and iron, respectively. In both figures, it is evident that for a fixed ϕ, $\bar{\ell}$ increases linearly with H. This demonstrates that the external magnetic field H induces the formation of structures via dipolar interactions, which intensify as H increases. Another noteworthy observation is that the effect of H is significantly more pronounced at higher particle volume fractions. This is because a larger ϕ provides more particles available to form chains under the influence of the magnetic field.

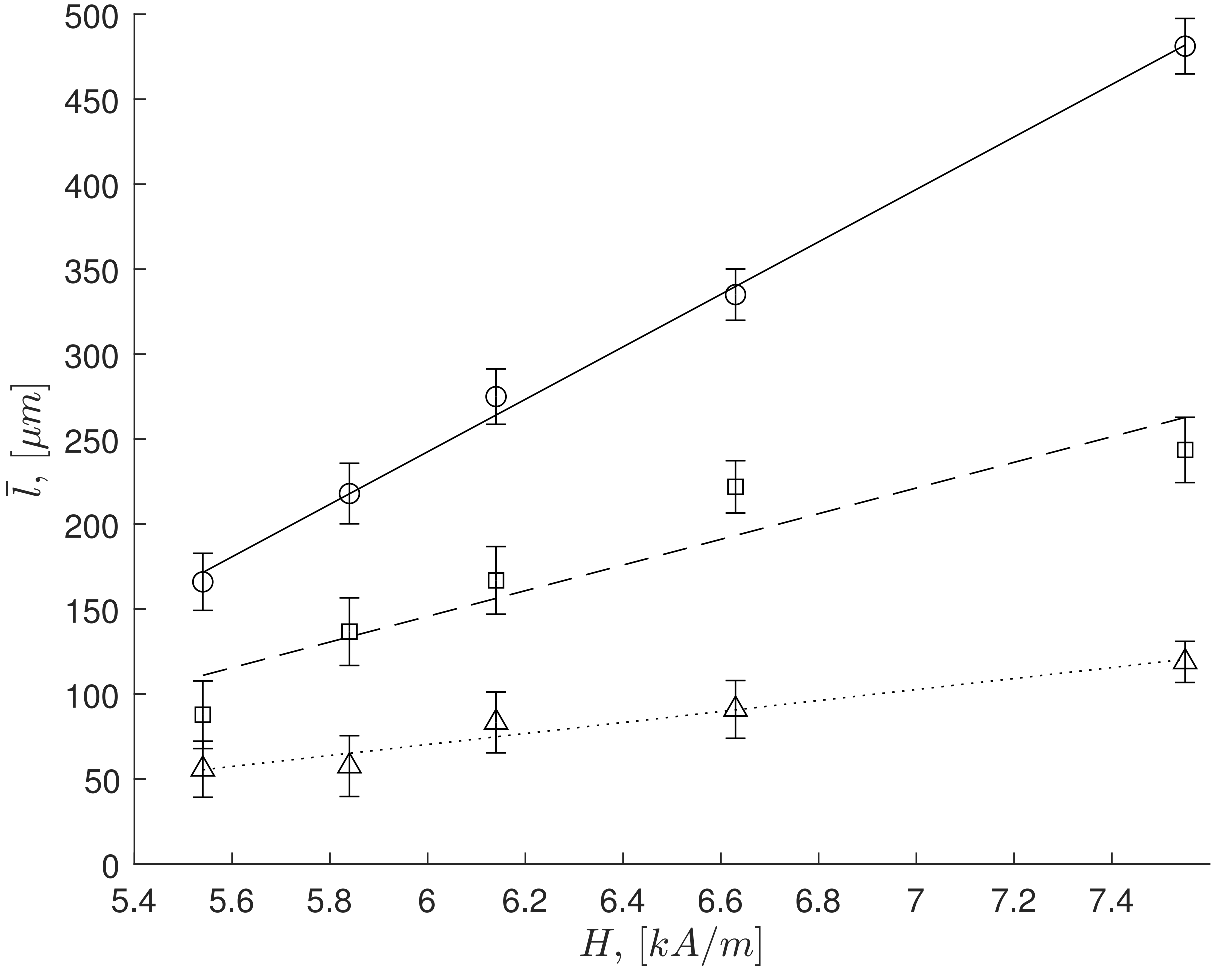

Figure 26 – Mean length of the chain-like structures for the MRS of magnetite. (△) - $\phi = 0.2\%$, (□) - $\phi = 0.6\%$ and (○) - $\phi = 1\%$. The fitting curves are of the form: $\bar{\ell} = a_1 H + a_2$. For the MRS with $\phi = 0.2\%$: $a_1 = 32.34$ and $a_2 = -123.75$. For the MRS with $\phi = 0.6\%$: $a_1 = 75.51$ and $a_2 = -307.36$. For the MRS with $\phi = 1\%$: $a_1 = 154.37$ and $a_2 = -683.73$.

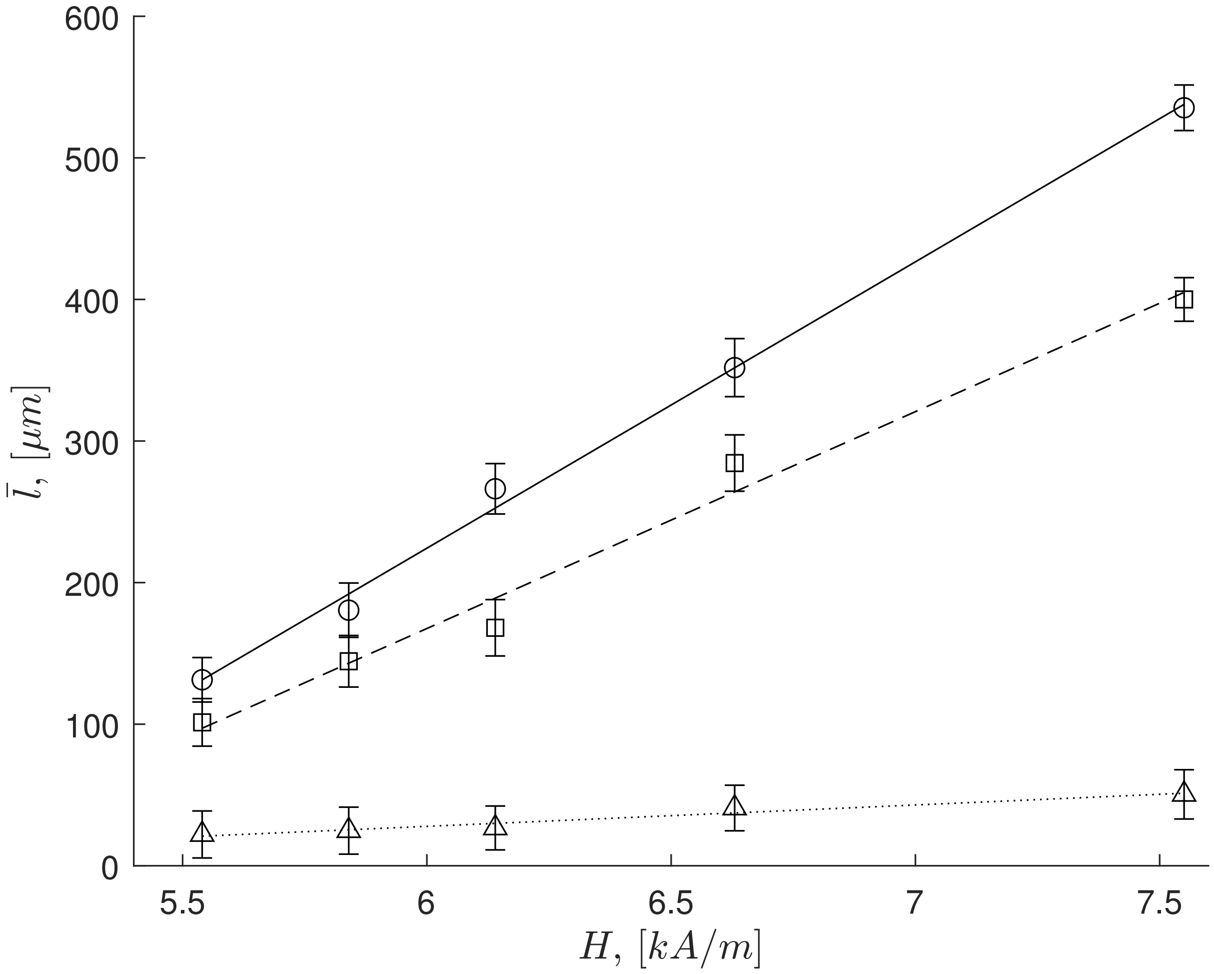

Figure 27 – Mean length of the chain-like structures for the MRS of iron. (△) - $\phi = 0.2\%$, (□) - $\phi = 0.6\%$ and (○) - $\phi = 1\%$.For the MRS with $\phi = 0.2\%$: $a_1 = 15.10$ and $a_2 = -62.79$. For the MRS with $\phi = 0.6\%$: $a_1 = 153.18$ and $a_2 = -751.52$. For the MRS with $\phi = 1\%$: $a_1 = 202.25$ and $a_2 = -989.22$.

To enable a comparison between the anisotropy coefficients of the two magnetorheological suspensions (MRS), the chain structure width a was assumed constant, that is, not varying with H, corresponding to the particle diameter specified by the manufacturer. For magnetite, $a = 8$ nm, and for iron, $a = 7$ μm. As illustrated in Figures (28) and (29), the anisotropy of both MRS is highly dependent on the intensity of the external magnetic field H. This dependency arises because an increase in H enhances dipolar interactions, promoting the formation of larger chain-like structures. Consequently, the anisotropy of the system increases as a secondary effect of the stronger dipolar interactions.

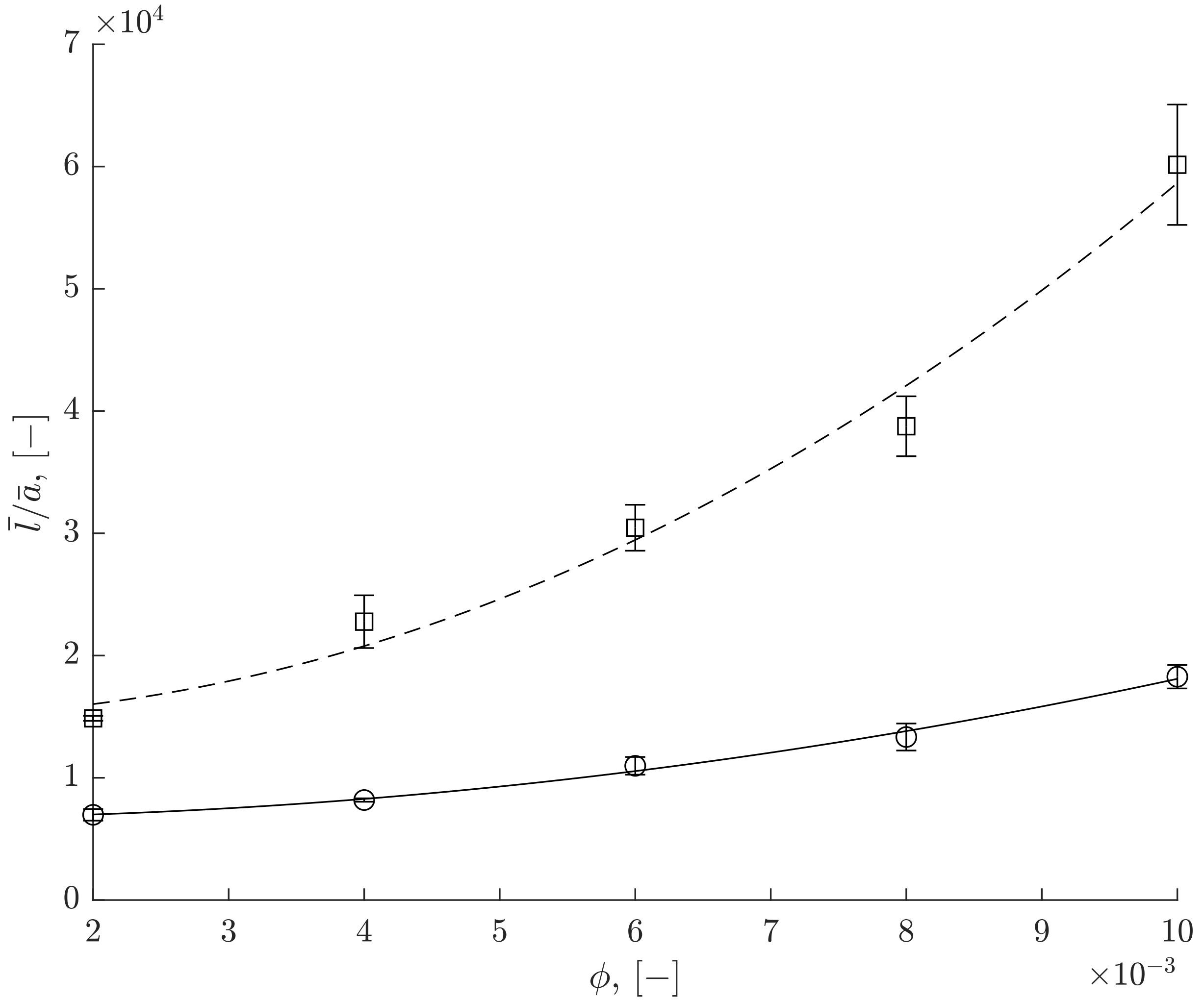

Figure 28 – SMR of magnetite powder - mean anisotropy parameter of the chains $\bar{l}/\bar{a}$ as a function of the volume fraction of magnetic particles ϕ for two distinct conditions of external magnetic field: (- - -) $H = 7.55$ kA/m and (—)$H = 5.54$ kA/m. The curves are fittings of the experimental data to a virial of second order: (- - -): $\bar{l}/\bar{a} = b_0(1 + b_1\phi + b_2\phi^2)$, with the following parameters: $b_0 = 1.05\times10^4$, $b_1 = 4.15\times10^{-1}$ and $b_2 = 1.18\times10^{-1}$. (—): $\bar{l}/\bar{a} = b_3(1+b_4\phi+b_5\phi^2)$, with the following parameters: $b_3 = 2.94 \times 10^4$, $b_4 = 5.71 \times 10^{-1}$ and $b_5 = 1.67 \times 10^{-1}$.

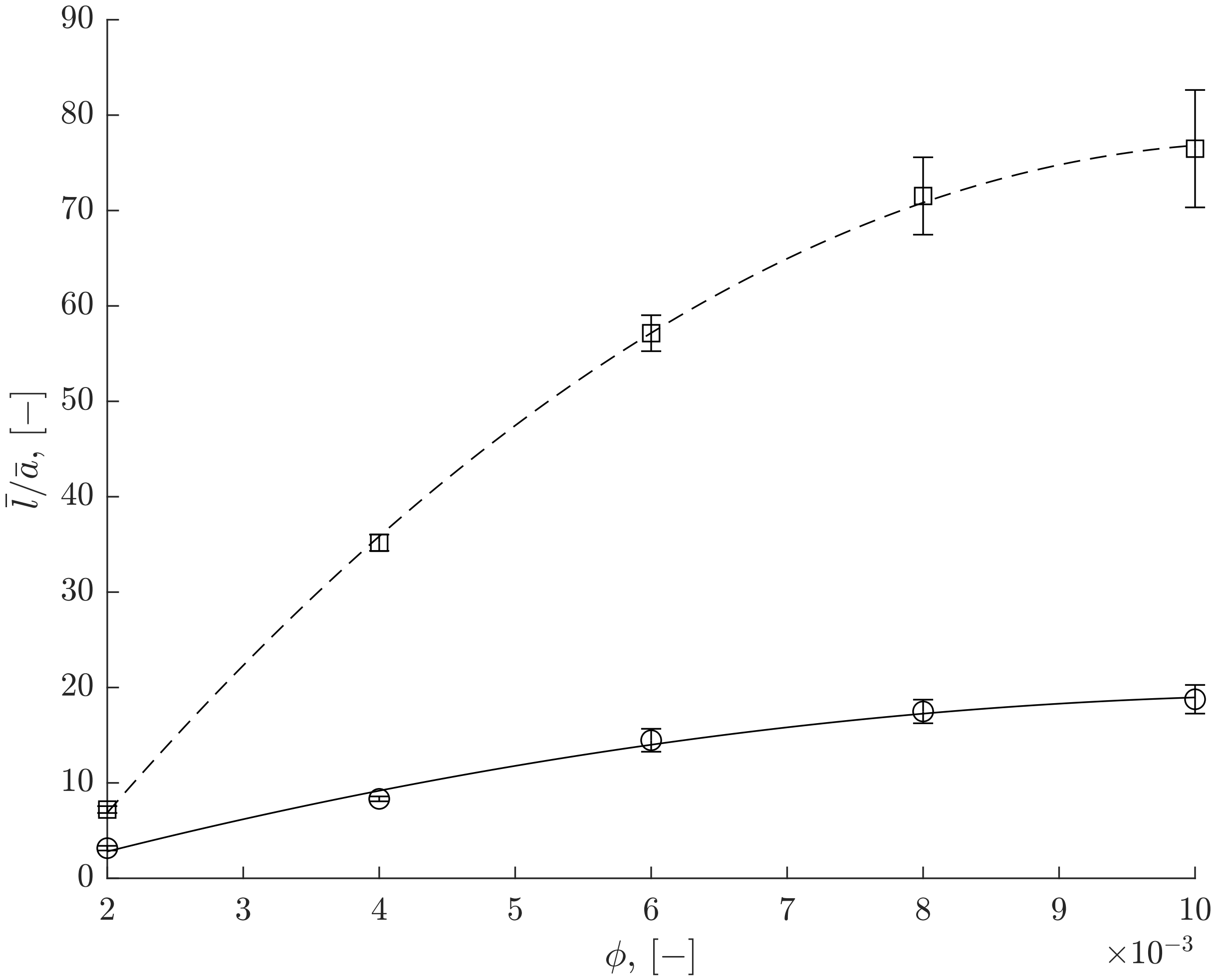

Figure 29 – SMR of iron particles - mean anisotropy parameter of the chains $\bar{l}/\bar{a}$ as a function of the volume fraction of magnetic particles ϕ for two distinct conditions of external magnetic field: (- - -) $H = 7.55$ kA/m and (—)$H = 5.54$ kA/m. The curves are fittings of the experimental data to a virial of second order: (- - -): $\bar{l}/\bar{a} = b_0(1 + b_1\phi + b_2\phi^2)$, with the following parameters: $b_0 = 1.39 \times 10^1$, $b_1 = 4.61 \times 10^{-1}$ and $b_2 = -1.39 \times 10^{-1}$. (—): $\bar{l} = b_3(1 + b_4\phi + b_5\phi^2)$, with the following parameters: $b_3 = 5.71 \times 10^1$, $b_4 = 4.83 \times 10^{-1}$ and $b_5 = -1.67 \times 10^{-1}$.

4.3 Permanent shear analysis

In this section, it will be shown and discussed the experimental results concerning the rheological behavior of the apparent viscosity η as a function of the magnetic particles' volume fraction, of the magnetic field intensity H and of the shear flow intensity $\dot{\gamma}$. As a result, three effects will be analyzed:

1. The dependence of the magnetorheological suspensions' viscosity on the magnetic particles' volume fraction;
2. The magnetoviscous effect, which is the elevation of the viscosity of a magnetorheological suspension when it is placed under the influence of an external magnetic field; and

3. Pseudoplastic effect, which is the shear rate dependence of the magnetorheological suspension's viscosity, which appears both in the presence and in the absence of an external magnetic field.

In order to focus on the physical meaning of the material functions and the variables on which they depend, they are going to be denoted by nondimensional parameters. Regarding this context, the intensity of the effective applied magnetic field is expressed by the magnetic parameter α, defined as:

$$\alpha = \frac{\mu_0 m H}{k_{\mathrm{B}} T}, \tag{4.3}$$

where, μ_0 is the vacuum magnetic permeability, $\mu_0 = 4\pi \times 10^5$ H/m, m is the intensity of the magnetic dipole momentum of a magnetic particle, H is the modulus of the effective magnetic field, k_{B} is the Boltzmann constant, $k_{\mathrm{B}} = 1.38 \times 10^{-23}$ Nm/K, and T is the absolute temperature, which was held constant in all experiments at 298 K . Besides that, the intensity of the magnetic dipole of a single-domain particle can be expressed in terms of its magnetization of saturation by

$$m = v_p M_d, \tag{4.4}$$

in which, $v_{\mathrm{p}} = 4\pi a^3/3$ is the volume of a magnetic particle of radius a and M_{d} is the magnetization of the material that composes the particles. For the powder of mgnetite $a = 4\mathrm{nm}$ and $M_d = 446\mathrm{kA/m}$ (ROSENSWEIG, 2013). For the iron powder, the physical parameters are: $a = 5\mathrm{nm}$ and $M_d = 1715\mathrm{kA/m}$ (DUNLOP; ÖZDEMIR; SCHUBERT, 2015). Replacing equation (4.4) into (4.3) one obtains:

$$\alpha = \frac{\mu_0 v_p M_d H}{k_{\mathrm{B}} T}. \tag{4.5}$$

It is important to remark that this parameter is a ratio between the magnetic and the Brownian forces.

Other important parameter is the ratio between the magnetic dipolar force and the Brownian force, named parameter of dipolar interaction,

$$\lambda = \frac{\mu_0 \pi v_p M_d^2}{24 k_B T} \tag{4.6}$$

It is important to note that this parameter is intrinsically related to the formation of particles chains. Big values of λ indicate that the magnetic force is much intenser than the Brownian one, making it possible for aggregates to form. Regarding this context, in this work, the parameter of dipolar interaction is constant for both magnetorheological suspensions, being equals to 2.1 fot the suspension composed by the magnetite powder and 7.7 for the suspension of iron powder.

The intensity of the flow is measured by its shear-rate ($\dot{\gamma}$), which unit of measurement is $1/s$. However, this property will be made nondimensional by dividing it by the minimum shear-rate applied $\dot{\gamma}_0$.

The apparent viscosity of a magnetorheological suspension is composed, when in the presence of an external magnetic field, by Einstein's viscosity η_ϕ, which is a correction to the viscosity of the base fluid originated from the presence of the rigid particles in the suspension, by a correction of the viscosity of the base fluid due to hydrodynamic iterations η_h between the particles, by the rotational viscosity η_r, induced by the external magnetic field and also, by a correction to the viscosity of the suspension owing to dipolar interactions between the magnetic particles, η_d. This apparent viscosity function is made nondimensional by defining its characteristic scale η_c as the viscosity of the base fluid η_0, which is the viscosity of the mineral oil at $25°C$ (see subsection (3.3.1)). As a result, the nondimensional viscosity is given by:

$$\eta^* = \frac{\eta}{\eta_c} = \frac{\eta}{\eta_0}. \tag{4.7}$$

4.3.1 Particle volume fraction analysis

In this subsection, it will be analyzed the influence of the particle volume fraction ϕ on the rheological behavior of both magnetorheological suspensions: the one composed by agglomerates of magnetite powder and the other composed by agglomerates of iron powder. It is important to remark that the base fluid for both suspensions is mineral oil.

4.3.1.1 Experimental procedure

As stated on subsection (3.3.1), two ferromagnetic materials were used to produce the magnetorheological suspensions, being: the magnetite powder and the iron powder. For each kind of magnetic particles, suspensions with the following particle volume fraction ϕ were prepared: 0.1%, 0.2%, 0.3%, 0.4%, 0.5%, 0.6%, 0.7%, 0.8% and 1%.

Samples of the suspensions are tested in the rheometer using the magnetorheological assembly, described on subsection (3.1.1.2). As a wide range of magnetic particle volumetric fractions were analyzed, an study of the the optimal testing gap between the disks of the rheometer was carried out. In this type of test each sample of suspension is sheared using different gaps between the disks of the rheometer and the viscosity is obtained as a function of time. The gap that provides a measure of viscosity with the lowest uncertainty is defined as the optimal gap. The results are shown on table (7).

Table 7 – Optimal gap ϵ as a function of the volume fraction ϕ of magnetic particles. The results apply to both suspensions composed of magnetite powder and iron powder.

ϕ [%]	ϵ [mm]
0.1	0.3
0.2	0.3
0.3	0.3
0.4	0.4
0.5	0.4
0.6	0.4
0.7	0.5
0.8	0.5
1.0	0.5

The dependence of the suspensions viscosity on the magnetic particles' volume fraction was determined as follows:

1. A sample of a magnetorheological suspension with a defined magnetic particles' volume fraction is chosen;
2. The volume necessary to fill the optimum gap is calculated. Using a volume variable pipette, the right volume of fluid is placed in the test zone (gap);
3. A shear-rate of $5s^{-1}$ is applied and the viscosity is measured as a function of time;
4. This process is repeated 10 times for each value of magnetic particles' volume fraction.

A post-processing data analysis is performed for each time series of viscosity. The mean value of the viscosity, for the k-th realization, is defined as:

$$\bar{\eta}_k(\phi) = \frac{1}{t_f - t_i}\int_{t_i}^{t_f} \eta_k(t,\phi)dt, \tag{4.8}$$

where $\eta(t)_k$ is the k-th time series of viscosity, t_i is the initial time and t_f is the final time. As ten realizations were carried out for each value of magnetic particle's volume fraction, the value of the viscosity associated with ϕ is then:

$$\eta(\phi) = \frac{\sum_k^{10} \bar{\eta}_k(\phi)}{10}. \tag{4.9}$$

The uncertainty of the viscosity associated with a given magnetic particles' volume fraction is given by:

$$E(\eta) = \max(E_i(\eta), E_r(\eta)), \tag{4.10}$$

where, $E_i(\eta)$ is the instrumental error and $E_r(\eta)$ is the random error. $E_i(\eta)$ is calculated as described in the appendix (A.1). In this case, $E_r(\eta)$ is calculated as:

$$E_r(\eta) = \sqrt{\frac{\sum_k^{10}(\bar{\eta}_k - \eta)^2}{10}}. \tag{4.11}$$

The viscosity and its associated error are made non-dimensional using the viscosity of the base fluid η_0, which is mineral oil at $25°C$. The non-dimensional variables are then: $\eta^* = \eta/\eta_0$ and $E(\eta)/\eta_0 = E^*(\eta)$. A point in the graph of η^* as a function of ϕ is given by $\eta^* \pm E^*(\eta)$.

4.3.1.2 Discussion

Figures (30) e (31) present a series of pictures displaying the microstructure of some magnetorheological suspensions in the absence and in the presence of an external magnetic field $\boldsymbol{B}$. Figure (30) shows the micrographies of the magnetorheological suspension composed by magnetite powder in four different volume fractions: 0.1%, 0.4%, 0.8% and 1%. Figure (31) presents the same results, but for the suspension composed by iron powder.

It can be observed from figures (30) and (31) that in the absence of an external magnetic field, the micrographies portrait microstructures formed by almost sphere-shaped agglomerates of magnetic particles well dispersed in the base fluid. Nonetheless, the application of the external magnetic field induced the formation of highly anisotropic microstructures. The agglomerates of particles that start relatively homogeneously distributed in the absence of magnetic field turn to fiber-shaped structures aligned with the direction of the applied magnetic field.

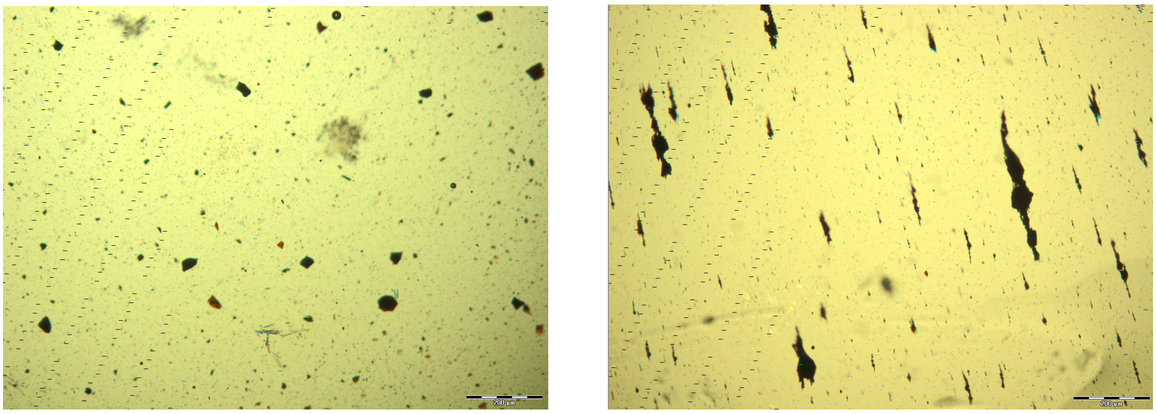

(a) $\phi = 0.1\%$ in the absence of external magnetic field.

(b) $\phi = 0.1\%$ in the presence of $H = 4.7 \times 10^4$ kA/m.

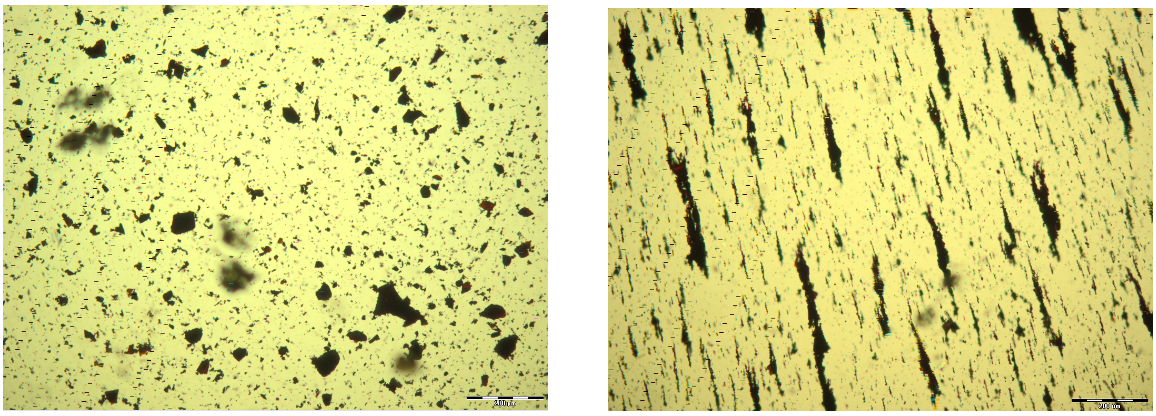

(c) $\phi = 0.4\%$ in the absence of external magnetic field.

(d) $\phi = 0.4\%$ in the presence of $H = 4.7 \times 10^4$ kA/m

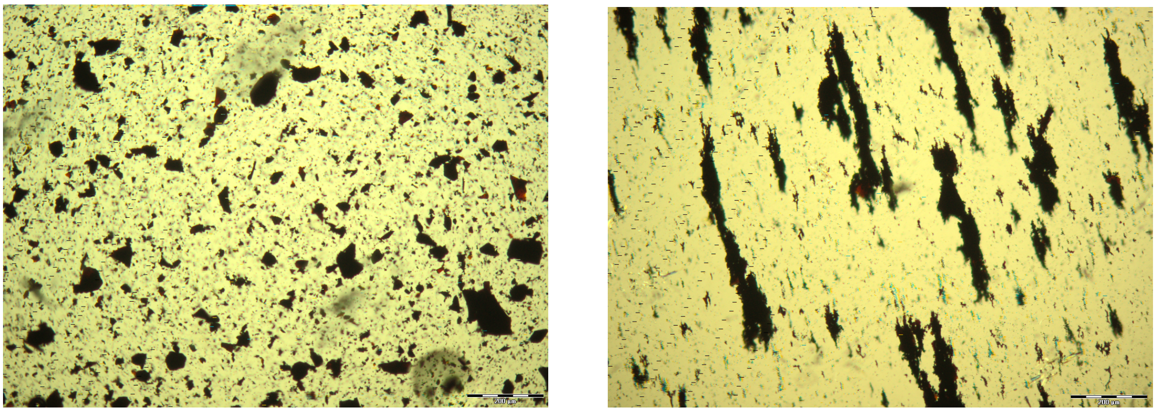

(e) $\phi = 0.8\%$ in the absence of external magnetic field.

(f) $\phi = 0.8\%$ in the presence of $H = 4.7 \times 10^4$ kA/m.

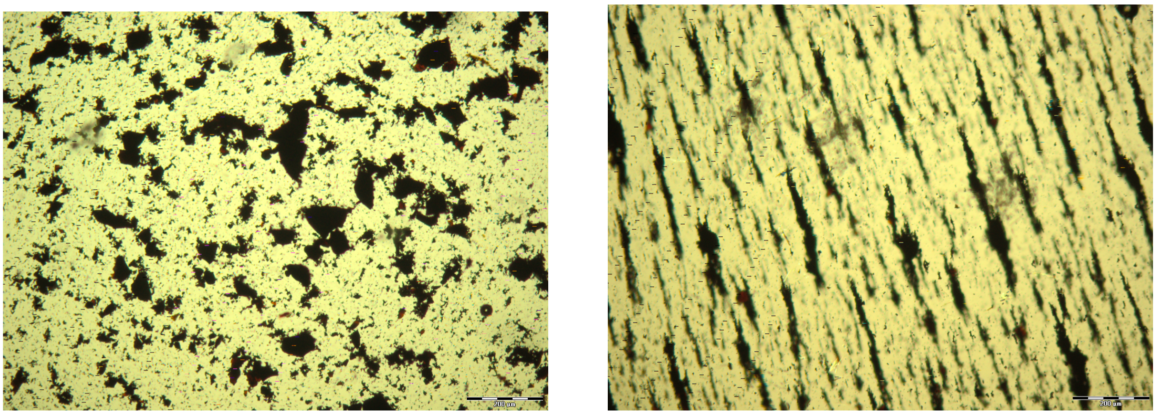

(g) $\phi = 1\%$ in the absence of external magnetic field.

(h) $\phi = 1\%$ in the presence of $H = 4.7 \times 10^4$ kA/m.

Figure 30 – Microstructures of samples of the magnetorheological suspensions composed of magnetite powder agglomerates.

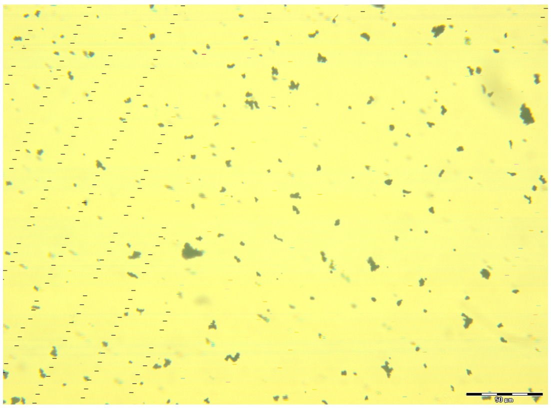

(a) $\phi = 0.1\%$ in the absence of external magnetic field.

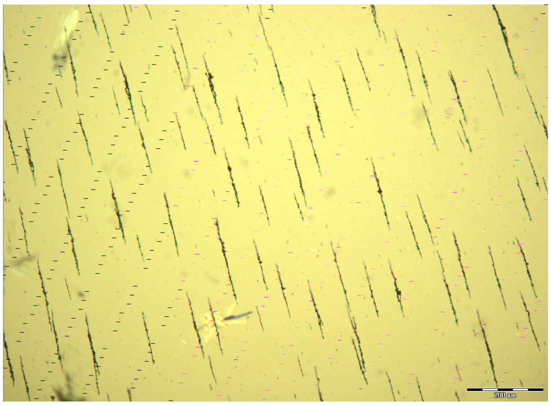

(b) $\phi = 0.1\%$ in the presence of $H = 4.7 \times 10^4$ kA/m.

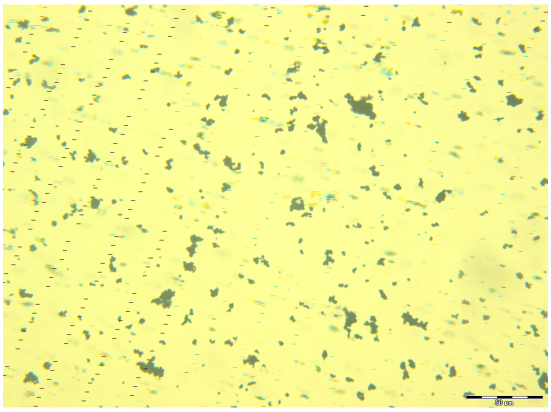

(c) $\phi = 0.4\%$ in the absence of external magnetic field.

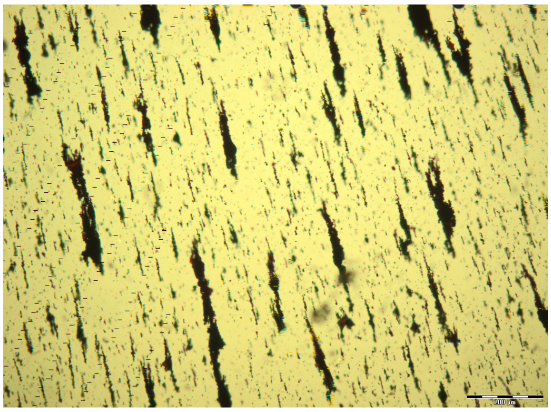

(d) $\phi = 0.4\%$ in the presence of $H = 4.7 \times 10^4$ kA/m.

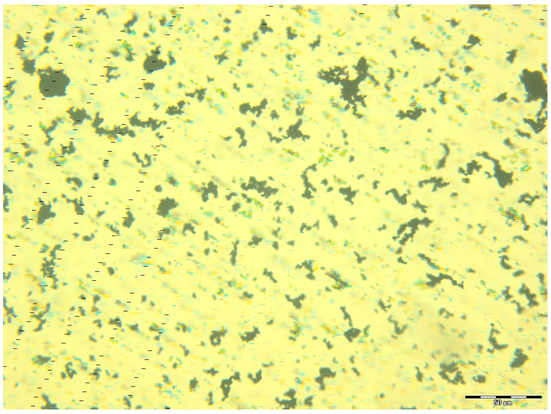

(e) $\phi = 0.8\%$ in the absence of external magnetic field.

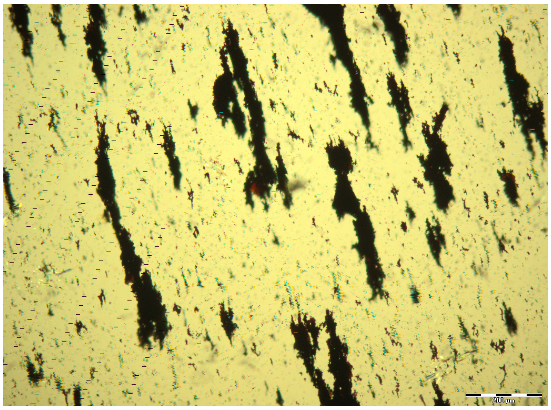

(f) $\phi = 0.8\%$ in the presence of $H = 4.7 \times 10^4$ kA/m.

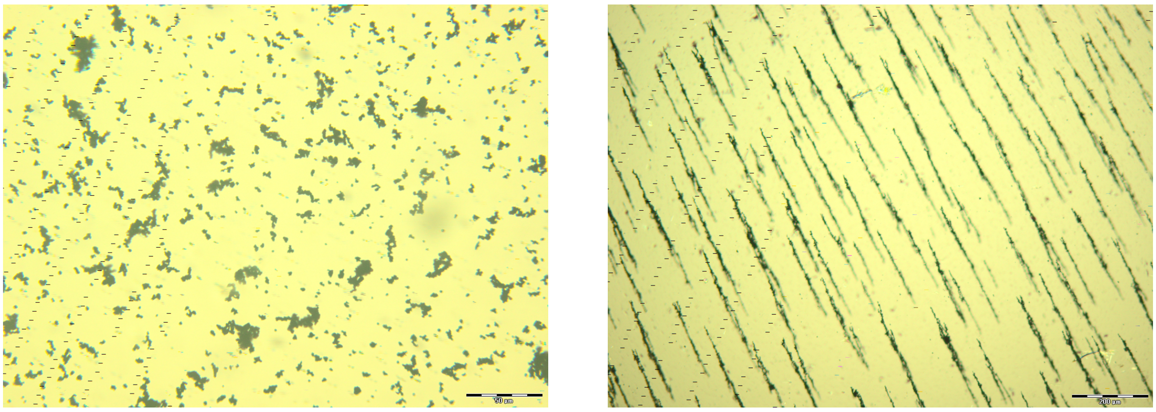

(g) $\phi = 1\%$ in the absence of external magnetic field.

(h) $\phi = 1\%$ in the presence of $H = 4.7 \times 10^4$ kA/m.

Figure 31 – Microstructures of samples of the magnetorheological suspensions composed of iron powder agglomerates.

All the magnetorheological suspensions produced can be considered diluted due to the fact that the maximum particle volume fraction is 1% for both types of suspension. Figures (32) and (33) depict, respectively for the suspension of magnetite powder and for the one made of iron powder, the relative viscosity as a function of the magnetic particle volume fraction.

For very diluted regimes, $\phi \leq 0.4\%$, it is shown in figures (32) and (33) that the relation between the relative viscosity and the particle volume fraction follows closely the linear Einsteins' relation $\mathcal{O}(\phi)$. This result comes as a direct consequence of the microstructure overall shape, which is, as can be seen in figures (30a), (30c), (31a) and (31c), composed of almost small bounding spherical micro-aggregates. The distribution of these agglomerates are approximately homogeneous, what makes the order $\mathcal{O}(\phi)$ of Einstein's law (EINSTEIN, 1911) applicable.

As the particle volume fraction rises above $\phi \approx 0.4\%$, the nondimensional viscosity is observed to increase in an non-linear fashion, requiring corrections of higher order such as $\mathcal{O}(\phi^2)$ or even $\mathcal{O}(\phi^3)$. According to Cunha, Rosa and Dias (2016), Considering the limit of very small volume fraction ($\phi \to 0$), one can relate the relative viscosity to particle volume fraction by an expansion in Taylor's series of the following relation:

$$\eta^*(\phi, \alpha, Pe) = k_1(\alpha, Pe) e^{k_2(\alpha, Pe)\phi}, \tag{4.12}$$

which n-th term is equal to $(n!)^{-1} k_2^n \phi^n$. Thus:

$$\eta^* = 1 + k_1\phi \left(1 + k_2\phi + \frac{k_2^2\phi^2}{2}\right) + \mathcal{O}(\phi^4). \tag{4.13}$$

This equation is used to fit the experimental data concerning both magnetorheological suspensions.

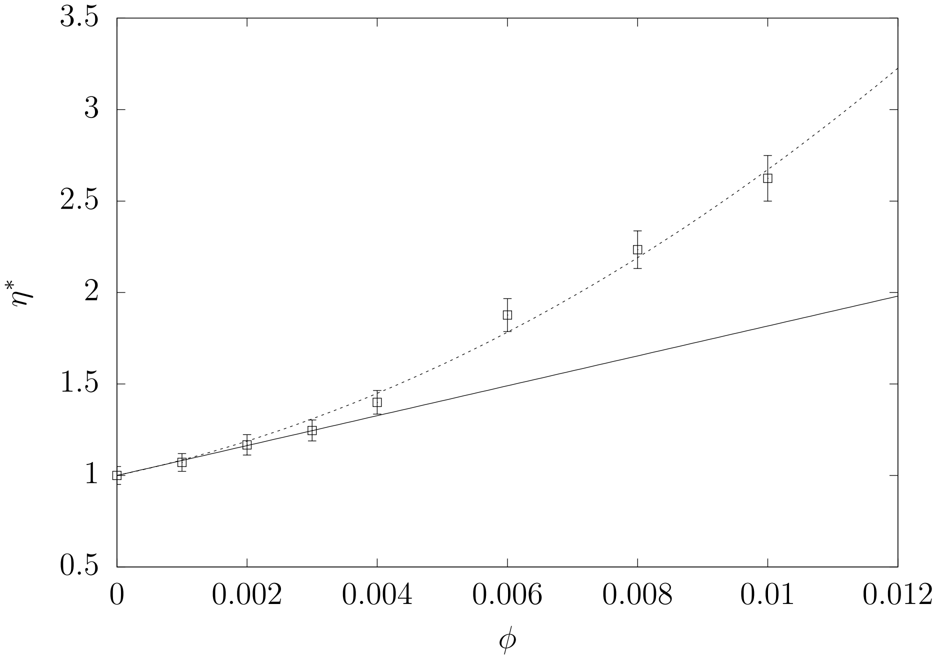

Figure 32 – Relative viscosity η^* as a function of the magnetite particles' volumetric fraction ϕ. The continuous curve (—) is a fit of the experimental data, for $\phi \leq 0.004$, to an equation of the following form: $\eta = 1 + k_1\phi$. The dashed curve (- - -) is a fit of the experimental data to an equation of the given form: $\eta = 1 + k_1\phi(1 + k_2\phi + k_2^2\phi^2/2)$. Here, $k_1 = 8.70 \times 10^1 \pm 1.96 \times 10^0$ and $k_2 = 6.86 \times 10^1 \pm 2.89 \times 10^0$.

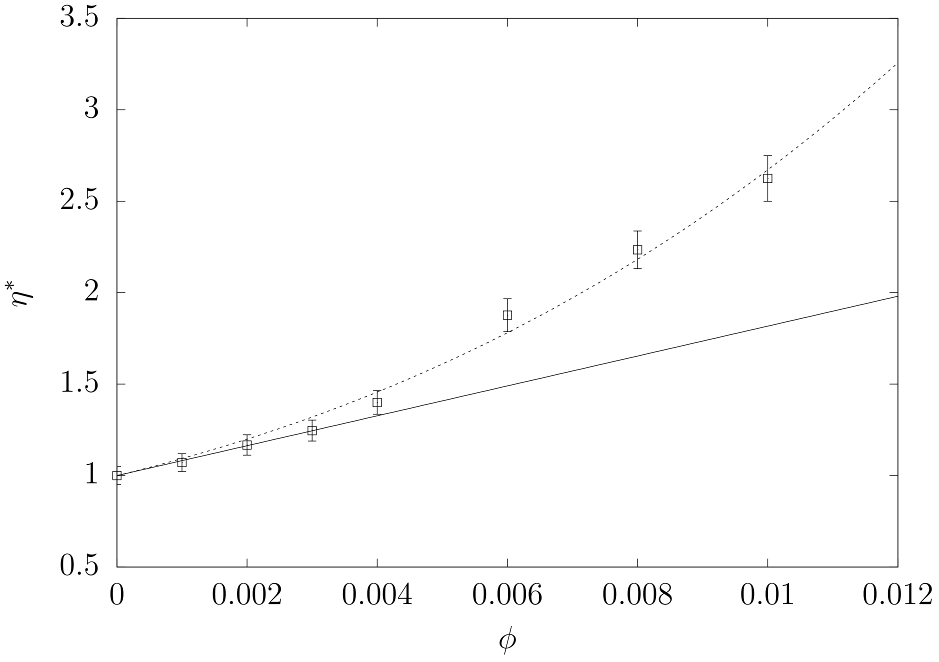

Figure 33 – Relative viscosity η^* as a function of the iron particles' volumetric fraction ϕ. The continuous curve (—) is a fit of the experimental data , for $\phi \leq 0.004$, to an equation of the following form: $\eta = 1 + k_1\phi$. The dashed curve (- - -) is a fit of the experimental data to an equation of the given form: $\eta = 1 + k_1\phi(1 + k_2\phi + k_2^2\phi^2/2)$. Here, $k_1 = 8.63 \times 10^1 \pm 5.18 \times 10^0$ and $k_2 = 1.02 \times 10^2 \pm 1.56 \times 10^1$.

4.3.2 Magnetoviscous effect

In this subsection, it is presented the magnetoviscous effect of the magnetorheological suspensions, that is, the increase of their viscosity in response to an elevation on the intensity of the applied magnetic field.

4.3.2.1 Experimental procedure

The magnetoviscous effect of a sample of magnetorheological suspension is evaluated by fixing the shear flow intensity and applying a continuous increase of magnetic field intensity H[2], which is varied, in the experiments here detailed, from 0 to 1.96×10^5 A/m, considering three fixed intensities of the shear flow $\dot{\gamma}$: 10, 100 and 1000s^{-1}.

The determination of the optimized gap between the disks of the rheometer, which is used in the experimental trials must be chosen carefully, due to the fact that both magnetorheological suspensions present a severe change on their viscosity as the intensity of the magnetic field strengthens. For each of the three flow intensities, the process of choosing the optimal gap for each magnetorheological suspension was carried out following these steps:

1. In the absence of external magnetic field, the viscosity of both magnetorheological suspensions, at 25°C, is at least approximately the viscosity of the base fluid, which is the mineral oil. For this range of viscosity the minimum gap usually used is 0.3mm. This gap value was considered the bottom limit for choosing the optimal gap;

2. For a condition of medium magnetic field intensity, five gaps were tried for both magnetorheological suspensions, 0.3, 0.4, 0.5, 0.6 and 0.7. The ones that resulted in a lower variation of the viscosity were chosen;

3. The same process was repeated for the highest intensity of magnetic field applied. Gaps that implicated on lower variability of the viscosity being measured were chosen as alternatives for the optimized gap;

4. Regarding the results obtained in the last two steps, one chooses an intermediate gap for each fluid that, when applied to the limit conditions of low and high magnetic field intensities, generates variability in the viscosity results lower than 5%.

For each of the flow intensities, the gaps chosen for the magnetorheological suspensions are displayed on table (8)

---

[2] The intensity of the magnetic field is a part of the intensity of the induced magnet field B, generated by the application of a current to the coils located under the lower fixed disk of the rheometer.

Table 8 – Optimal gaps used in the experimental evaluations of the magnetoviscous effect of both magnetorheological suspensions (magnetite powder and iron powder) for different flow intensities.

$\dot{\gamma}$ (s^{-1})	Volume fraction (ϕ)	Optimal gap (mm)
10	0.1%	0.4
	0.2%	0.4
	0.3%	0.5
	0.4%	0.5
	0.5%	0.5
	0.6%	0.6
	0.7%	0.6
	0.8%	0.6
	1.0%	0.7
100	0.1%	0.3
	0.2%	0.3
	0.3%	0.3
	0.4%	0.4
	0.5%	0.4
	0.6%	0.5
	0.7%	0.5
	0.8%	0.6
	1.0%	0.6
1000	0.1%	0.3
	0.2%	0.3
	0.3%	0.3
	0.4%	0.3
	0.5%	0.4
	0.6%	0.4
	0.7%	0.4
	0.8%	0.5
	1.0%	0.5

Having chosen the optimal gap, the experimental evaluation of the magetoviscous effect, for each fixed condition of flow intensity (constant shear rate), presented by both magnetorheological suspensions was done by applying the following experimental protocol:

1. The volume of magnetorheological suspension needed to fulfill the optimum gap is calculated and, after, this quantity is pipetted in the testing area;

2. The upper disk is lowered until the prescribed gap is achieved between the two disks. The gap is visually inspected in order to identify possible leakages of the sample, which, if found, must be cleaned due to the fact that they can severely increase the experimental error;

3. The magnetic yoke is placed around the measuring device. A demagnetization procedure is applied to the sample, in order to free the magnetorheological suspensions

of any previous magnetic effects;

4. The temperature of the experiment, 25°C, is set on the thermal bath attached to the rheometer. After this, enough time is waited for the temperature of the sample, here defined as the temperature of the lower plate, which is measured by the rheometer, to reach the target temperature;

5. Using the software *Rheoplus*, the flow condition is set, which is resumed to define a constant value of shear-rate for the experimental trial;

6. Using the software *Rheoplus*, the magnetic field conditions are programmed indirectly by controlling the electric current that the power supply (PS-MRD) provides to the coils located under the bottom disk of the rheometer (see figure 5.8). The current is programmed to vary from 0 to 4A, following a linear increase ramp. Between these limits, data points are collected, each one with a variable time of measurement, due to the fact that the option "*no time setting*" is active during the data acquisition. This feature ensures that enough time is being waited at each data acquisition in order to guarantee that the steady state has been achieved when the data collection is done.

7. The viscosity and the shear stress are acquired as a function of the magnetic field intensity for a given constant condition of shear rate.

This process was carried out 5 times, for each magnetic particles' volume fraction of both magnetorheological suspension, at every condition of flow intensity prescribed. The experimental errors were calculated using the methodology presented on appendix (A.1).

4.3.2.2 Magnetoviscous effect - discussion I: diluted suspensions

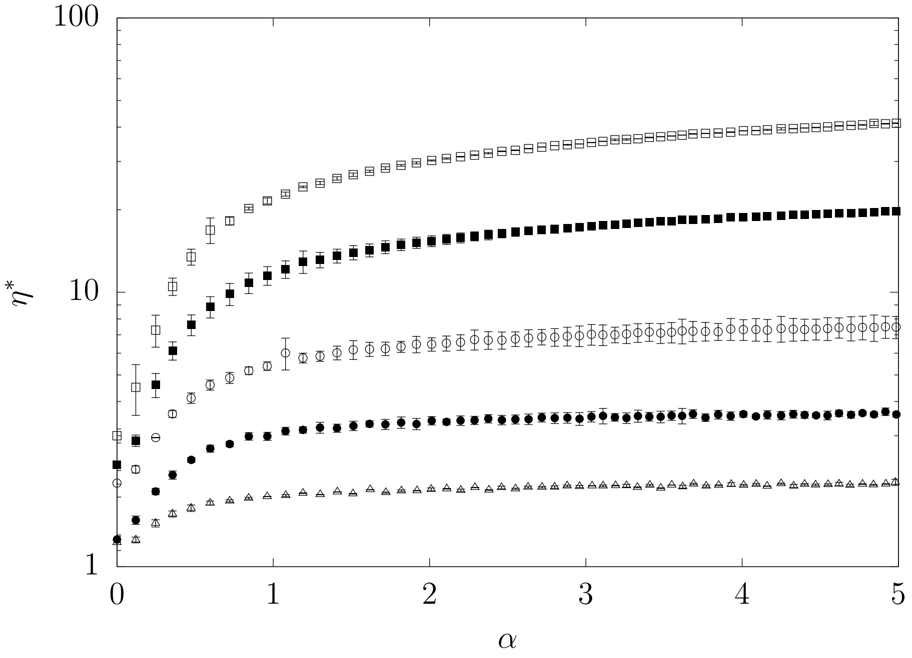

Figure 34 – Magnetorheological suspension of magnetite: effective viscosity η^* as a function of the magnetic parameter α considering a constant shear-rate $\dot{\gamma}$ equals to 10 s^{-1}. (△) - 0, 2%, (●) - 0, 4%, (○) - 0, 6%, (■) - 0, 8% e (□) - 1%.

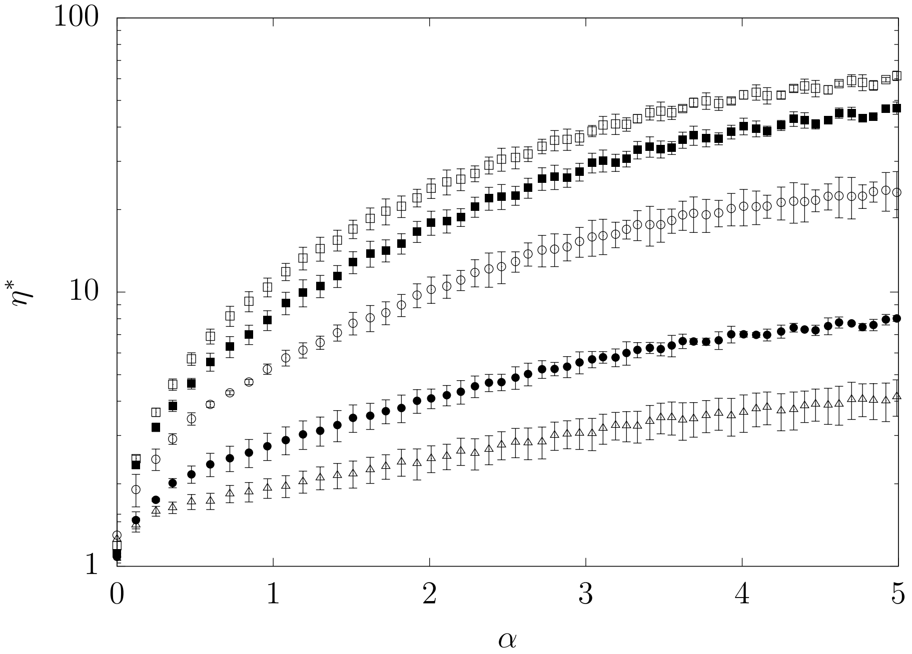

Figure 35 – Magnetorheological suspension of iron: effective viscosity η^*as a function of the magnetic parameter α considering a constant shear-rate $\dot{\gamma}$ equals to 10 s^{-1}. (△) - 0, 2%, (●) - 0, 4%, (○) - 0, 6%, (■) - 0, 8% e (□) - 1%.

Figures (34) and (35) show plots of the non-dimensional effective viscosity of the magnetic suspension as a function of the non-dimensional magnetic field α for a constant shear-rate of $10s^{-1}$. The results are presented for five particle volume fractions ϕ. It is immediate from this result that, in both suspensions, enhancing the magnetic field strength yields an increase of the suspension viscosity. This is called the magnetoviscous effect. It happens due to a competition between the magnetic torque and the mechanical torque that act upon a magneitc particle dispersed in a fluid when an external magnetic field and a flow is applied. The magnetic particle is subjected to the magnetic torque that tends to align the particles magnetic dipole vector with the direction of the external magnetic field and held the particles in this configuration. However, the mechanical torque, acting upon the particle via viscous forces, tries to make the particle rotate according to the flow's vorticity evaluated on the particles center of mass. This hindrance of movement caused by the action of the magnetic torque increases the local dissipation in the particle, due to the fact that it is no-longer allowed to rotate freely with the flow. The bulk effect of this mechanism is the increase of the effective viscosity.

It is important to remark that in magnetorheological suspensions the magnetoviscous effect is usually much stronger in comparison to ferrofluids when subjected to the same conditions of flow and external magnetic field. This is due to the fact that, by the action of the dipolar interactions, the microstructure of the magnetorheological suspensions are populated by chains and agglomerate of magnetic particles when in the presence of an external magnetic field. That is, the mean size of magnetic-induced structures is bigger for the magnetorheological suspensions when compared to ferrofluids, which is directly linked to the fact that the increase increase in viscosity is more intense for magnetorheological suspensions.

From figures (34) and (35) we can also see that the higher the particle volume fraction ϕ, the strongest is the magnetoviscous effect obtained as the magnetic field intensity α is enhanced. This is related to the fact that in magnetorheological suspensions that have higher ϕ, more magnetic particles are avaliable in a given volume of suspension when compared to suspensions with lower ϕ. This can be also understood by the fact that it is easier for the dipolar interactions to form more complex structures like chains and aggregates of magnetic particles in more concentrated magnetorheological suspensions.

As it can be seen from the plots on figures (34) and (35), for high values of the magnetic field strength α and for each value of the particle volume fraction, the viscosity curves tend, each one, to a plateau. This constant value is called viscosity of saturation η_∞. According to Cunha, Rosa and Dias (2016), the saturated values of the viscosity η_∞ for each volume fraction correspond to an equilibrium configuration of particle orientation and size distribution of structures defined, in average, as the balance between mechanical torque of shear and the magnetic torque on the aggregate-like structures at large values of α, when the effect of Brownian motion can be neglected.

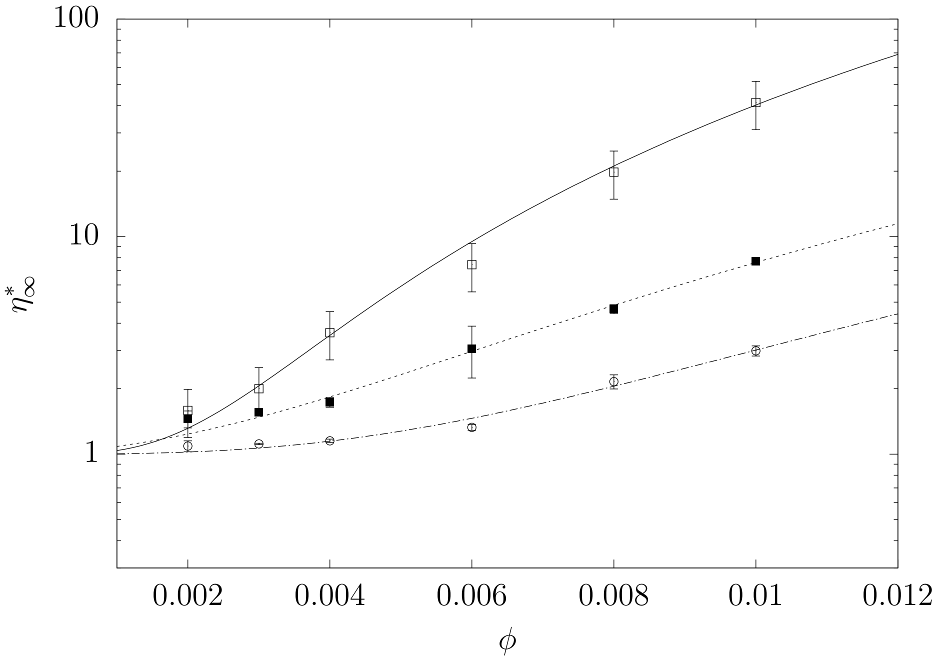

Figure 36 – Magnetorheological suspension of magnetite: relative viscosity of saturation $\eta^*_\infty = \eta^*(\phi, \alpha \to \infty)$ as a function of the magnetic particles' volume fraction. For: $\dot{\gamma} = 10$ s^{-1} (□), $\dot{\gamma} = 100$ s^{-1} (■) and $\dot{\gamma} = 1000$ s^{-1} (○). The curves are fits of the experimental data to the following equation: $\eta^*_\infty = 1 + k_1\phi\,(1 + k_2\phi + k_2^2\phi^2/2)$. The fitting parameters are: (—) $k_1 = 5.52 \times 10^{-2} \pm 3.61 \times 10^{-3}$ and $k_2 = 3.76 \times 10^3 \pm 1.23 \times 10^0$; (- - -) $k_1 = 6.06 \times 10^1 \pm 1.92 \times 10^{-1}$ and $k_2 = 3.56 \times 10^2 \pm 7.82 \times 10{-}1$; (-·-·) $k_1 = 8.52 \times 10^{-1} \pm 3.57 \times 10{-}3$ and $k_2 = 2.071 \times 10^3 \pm 4.59 \times 10^0$.

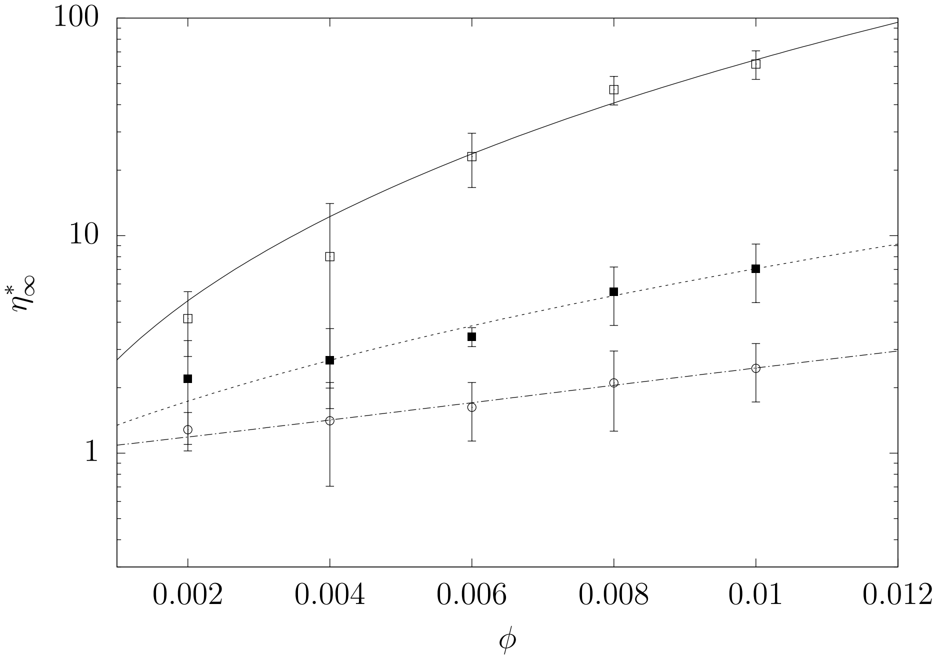

Figure 37 – Magnetorheological suspension of iron: relative viscosity of saturation $\eta^*_\infty = \eta^*(\phi, \alpha \to \infty)$ as a function of the magnetic particles' volume fraction. For: $\dot\gamma = 10$ s^{-1} (□), $\dot\gamma = 100$ s^{-1} (■) and $\dot\gamma = 1000$ s^{-1} (○). The curves are fits of the experimental data to the following equation: $\eta^*_\infty = 1 + k_1\phi\,(1 + k_2\phi + k_2^2\phi^2/2)$. The fitting parameters are: (—) $k_1 = 1.40 \times 10^3 \pm 7.65 \times 10^0$ and $k_2 = 1.83 \times 10^2 \pm 9.22 \times 10^0$; (- - -) $k_1 = 3.22 \times 10^2 \pm 8.17 \times 10^0$ and $k_2 = 6.61 \times 10^0 \pm 3.21 \times 10^{-1}$; (-···-) $k_1 = 8.33 \times 10^1 \pm 1.72 \times 10^{-1}$ and $k_2 = 5.85 \times 10^1 \pm 2.57 \times 10^{-1}$.

Figures (36) and (37) present the behavior of the viscosity of saturation η_∞ as a function of the magnetic particle volume fraction ϕ considering three conditions of shear-rate: $10s^{-1}$, $100s^{-1}$ and $1000s^{-1}$. The fluid under analysis in figure (36) is a magnetorheological suspension of magnetite and in (37) is a magnetorheological suspension of iron. From both figures, it can be seen that the viscosity of saturation increases as the magnetic particle volume fraction ϕ grows, which is associated to the fact that in the resulting dynamic equilibrium between the magnetic and the shear torques the magnetic structures (chains and agglomerate of particles) are bigger, resulting in an increased viscous dissipation. Considering a fixed magnetic particle volume fraction, the viscosity of saturation is observed to decrease as the shear-rate enhances. This fact can be understood by looking upon the effect of the shear over the magnetic field induced microstructure, which is the promotion of break-up. This mechanism decreases the average size of the magnetic structures, leading to a microstructure that generates less viscous dissipation the higher the intensity of the shear is. Another effect related to the shear is the redistribution of particles via hydrodynamic interactions, which tends to homogenize the structures in the fluid, decreasing the overall number of agglomerates in the fluid.

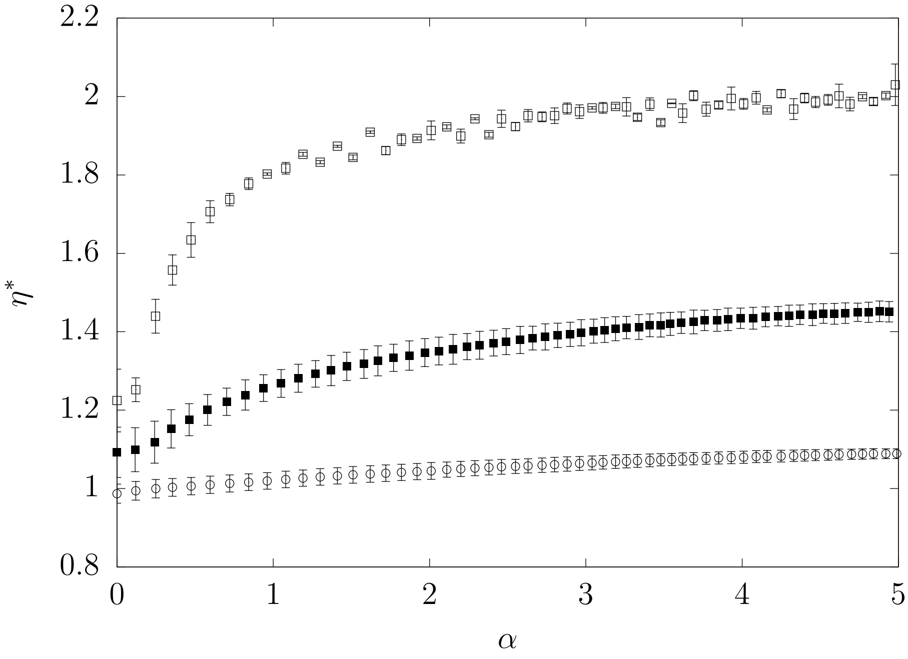

Figure 38 – Magnetorheological suspension of magnetite: relative viscosity η^* as a function of the nondimensional magnetic parameter α for a magnetorheologic suspension with ϕ equals to 0.2%. Each data set corresponds to a level of constant applied shear-rate $\dot{\gamma}$: (□) - 10s^{-1}, (■) - 100s^{-1} e (○) - 1000s^{-1}.

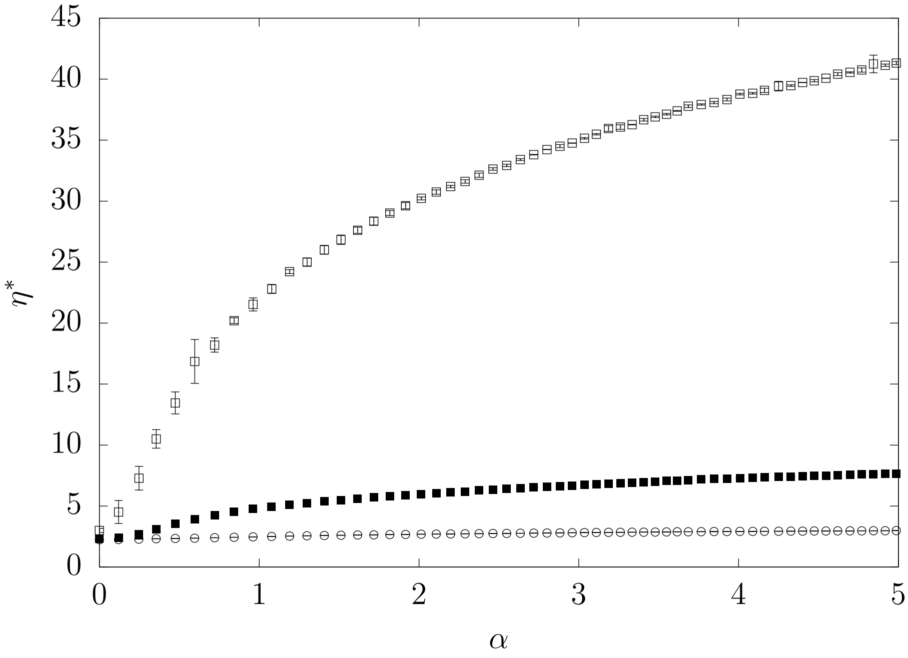

Figure 39 – Magnetorheological suspension of magnetite: relative viscosity η^* as a function of the nondimensional magnetic parameter α for a magnetorheologic suspension with ϕ equals to 1%. Each data set corresponds to a level of constant applied shear-rate $\dot{\gamma}$: (□) - 10s^{-1}, (■) - 100s^{-1} e (○) - 1000s^{-1}.

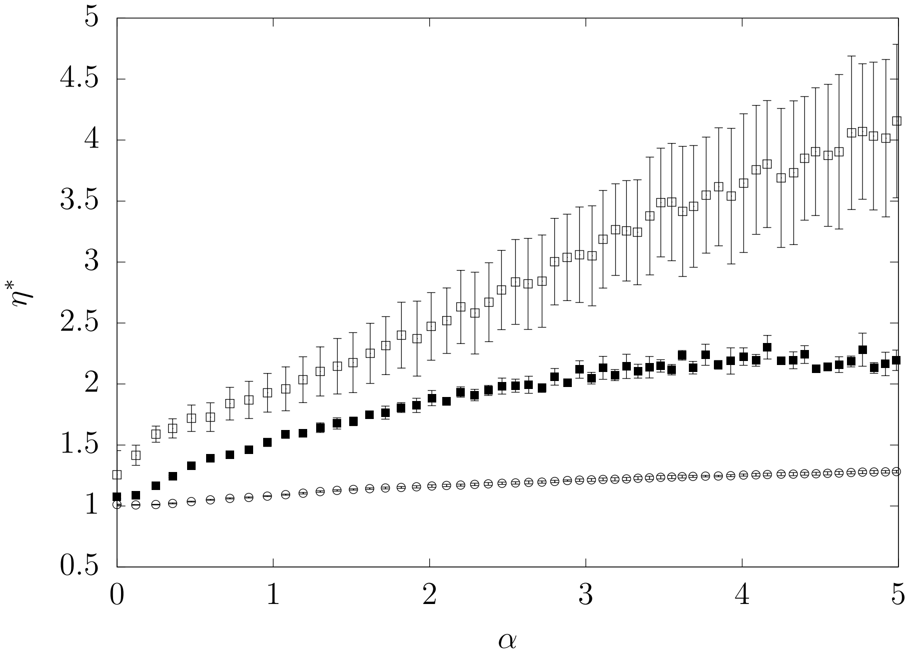

Figure 40 – Magnetorheological suspension of iron: relative viscosity η^* as a function of the nondimensional magnetic parameter α for a magnetorheologic suspension with ϕ equals to 0.2%. Each data set corresponds to a level of constant applied shear-rate $\dot{\gamma}$: (□) - $10\mathrm{s}^{-1}$, (■) - $100\mathrm{s}^{-1}$ e (○) - $1000\mathrm{s}^{-1}$.

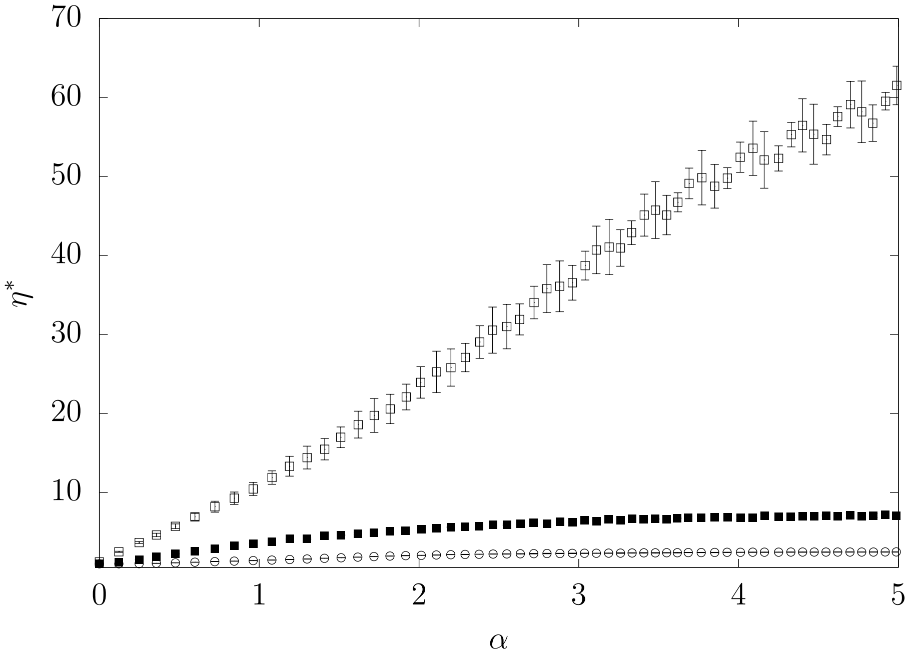

Figure 41 – Magnetorheological suspension of iron: relative viscosity η^* as a function of the nondimensional magnetic parameter α for a magnetorheologic suspension with ϕ equals to 1%. Each data set corresponds to a level of constant applied shear-rate $\dot{\gamma}$: (□) - $10\mathrm{s}^{-1}$, (■) - $100\mathrm{s}^{-1}$ e (○) - $1000\mathrm{s}^{-1}$.

Figures (38), (39), (40) and (41) depict the behavior of the relative viscosity as a function of the magnetic field intensity considering three intensities of the shear: $10s^{-1}$, $100s^{-1}$ and $1000s^{-1}$. Figures (38) and (39) present the referred result for the magnetorheological of magnetite while figures (40) and (41) present these results for the magnetorheological suspension of iron. Figure (38) corresponds to a suspension with ϕ of 0.2% as well as (40). Figure (39) corresponds to a suspension with ϕ of 1% as well as (41).

Comparing figures (38) and (39), it is obvious the impact of increasing the particle volume fraction ϕ, especially for the lowest intensity of the flow. In this case the, for α equals to 5, the suspension with ϕ equals to 1% presented a relative viscosity 20 times higher than the suspension with ϕ equals to 0.2%. This difference decreases to 5 times as $\dot{\gamma}$ approaches $100s^{-1}$ and to 1 time as $\dot{\gamma}$ increases to $1000s^{-1}$. It is important to remark that the increase of the relative viscosity as the magnetic particle volume fraction ϕ heightens is related to the fact that for higher values of ϕ, more magnetic particles are available to form structures. This tends, for higher values of ϕ and lower of $\dot{\gamma}$, to generate microstructures with higher characteristic size, which leads to an increased viscous dissipation and, as a result, to a higher bulk viscosity. The increase of $\dot{\gamma}$ decreases the difference of the results shown in both figures due to the fact that in medium-high conditions of $\dot{\gamma}$, the flow breaks-up the microstructure of the fluid and, thus, the magnetic field is unable to induce the formation of chains and aggregates of particles. The same insights can be drawn by comparing figures (40) and (41).

Comparing figures (39) and (41), it can be seen that the magnetic effects on the rheology of the magnetorheological suspension of iron are much stronger then the ones presented by the magnetorheological suspension of magnetite. This can be understood as a direct effect of the fact that the magnetization of saturation of the iron is about one order of magnitude bigger that the magnetization of saturation of magnetite. As a result the intensity of the magnetic dipole vector on each particle of the iron is higher than in the particles of magnetite. As a result the magnetic attraction between the particles in the suspension of iron is more relevant and thus, the process of formation of chains and agglomerates of magnetic particles is facilitated. This leads to a more robust magnetoviscous effect in the magnetorheological suspension of iron. The same can be said for the comparison of figures (38) and (40), however all the rheological behaviors of each magnetorheological suspension are weaker when compared to figures (39) and (41). This is due to the fact that the magnetic particle volume fraction on the suspensions of figures (38) and (40) is much smaller than in the suspensions of figures (39) and (41).

4.3.2.3 Magnetoviscous effect - discussion II: concentrated suspensions

Figures (42) and (43) present the magneto-viscous effect of magnetorheological suspensions (MRS) of iron and magnetite, respectively, at a constant shear rate of $10\,\mathrm{s}^{-1}$. Comparing these figures, we observe that the viscosity increases much more intensely for the iron MRS as a function of α. This behavior can be attributed to the higher concentration of iron particles, which allows their magnetic properties, such as magnetization, to significantly influence the rheological response of the fluid as a result of heightening the dipolar interactions.

It is important to note that for diluted suspensions, the rheological responses of both suspensions were quite similar. This is because, at low concentrations, the micrometric size of iron particles results in an insufficient number of particles in suspension to exhibit significant magnetic interactions.

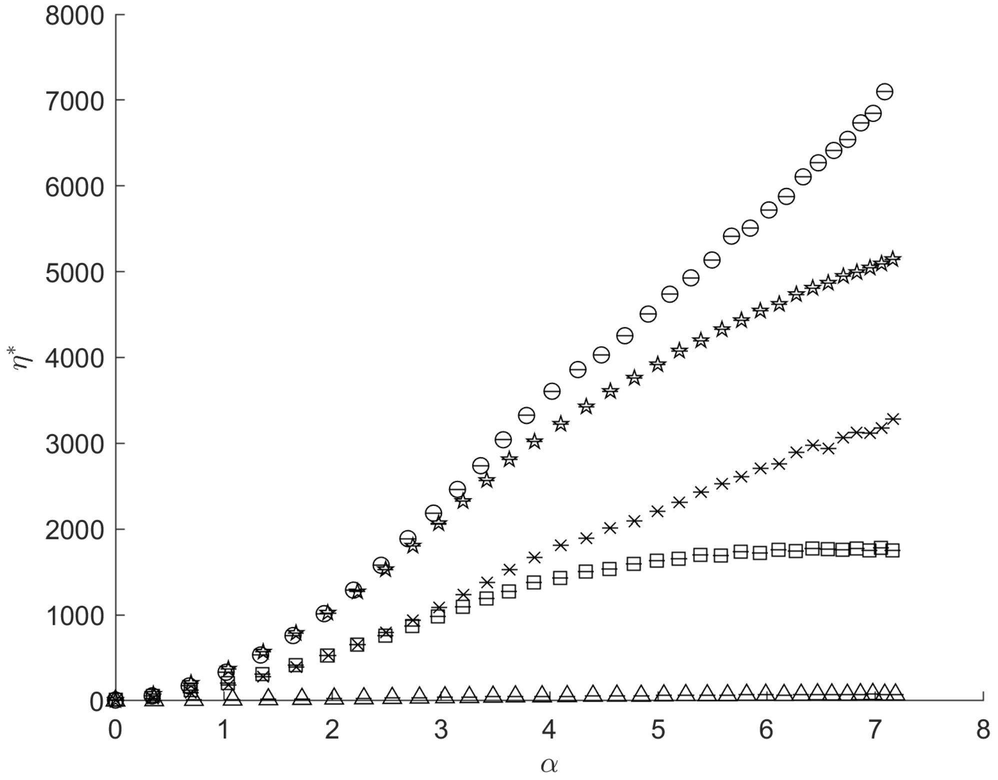

Figure 42 – Magnetorheological suspension of iron: relative viscosity η^* as a function of the magnetic parameter α for a shear rate of $10\,\mathrm{s}^{-1}$. ○ - $\phi = 5\%$, ★ - $\phi = 4\%$, × - $\phi = 3\%$, □ - $\phi = 2\%$, and △ - $\phi = 1\%$.

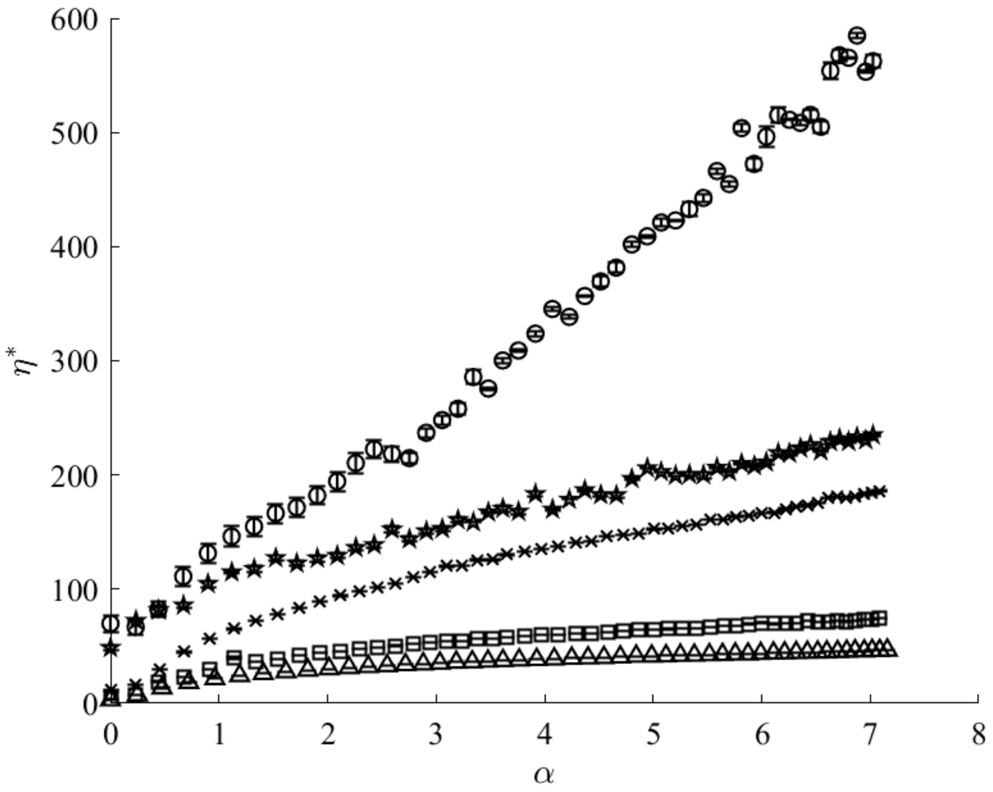

Figure 43 – Magnetorheological suspension of magnetite: relative viscosity η^* as a function of the magnetic parameter α for a shear rate of $10\,\mathrm{s}^{-1}$. ○ - $\phi = 5\%$, ★ - $\phi = 4\%$, × - $\phi = 3\%$, □ - $\phi = 2\%$, and △ - $\phi = 1\%$.

4.3.3 Pseudo-plasticity

In this subsection, it is discussed the experimentally observed pseudoplastic behavior of magnetorheological suspensions. This effect appears when those fluids flow in the presence of an external magnetic field, being characterized by an intense decrease on their apparent viscosity η when subjected to the action of a strengthening shear flow.

4.3.3.1 Experimental procedure

The pseudoplastic effect of a magnetorheological suspension (MRS) sample is evaluated by fixing the magnetic field intensity and applying a continuous increase of shear rate. Both magnetorheological suspensions were tested in three conditions of magnetic field intensity: $H = 0$ (absence of magnetic field), $H = 9.69 \times 10^3$ A/m ($i = 0.125$A) and $H = 1.97 \times 10^4$ A/m ($i = 0.25$A). The shear rate was varied from 0.1 to 1000s^{-1}. As both magnetorheological suspension present shear rate dependence when they are in the presence of a magnetic field, it is important to choose an appropriate length of gap to obtain consistent results from the experiments. The process of choosing the optimal gap is similar to the one described on subsection (4.3.2.1) for dealing with the same issue on the analysis of the magnetoviscous effect. This process, for each magnetorheological suspension followed these steps:

1. In the absence of external magnetic field, both magnetorheological suspensions present viscosity similar to mineral oil, thus a gap of 0.3mm is an appropriate choice for this condition;
2. For the first non-zero magnetic field condition applied, that is, $H = 9.69 \times 10^3$ A/m ($i = 0.125$A), the viscosity was evaluated for the minimum and the maximum values of $\dot{\gamma}$, which are, respectively, 0.1 and 1000s^{-1}. This tests are carried out for five values of the gap: 0.3, 0.4, 0.5, 0.6 and 0.7 . A value of gap that permits the evaluation of the viscosity in both conditions is searched;
3. The last step is repeated, but considering the highest value of magnetic field intensity, $H = 1.97 \times 10^4$ A/m ($i = 0.25$A);
4. The gaps chose are displayed in table (9).

Table 9 – Optimal gaps for both magnetorheological suspensions used in the pseudoplasticity experiments.

Volume fraction (ϕ)	Optimal gap (mm)
0.1%	0.3
0.2%	0.3
0.3%	0.4
0.4%	0.4
0.5%	0.4
0.6%	0.5
0.7%	0.5
0.8%	0.6
1.0%	0.6

Having chosen the optimal gap, the experimental evaluation of the pseudoplastic effect, for each fixed condition of magnetic field intensity, presented by both magnetorheological suspensions, was done by applying the following experimental protocol:

1. The volume of magnetorheological suspension necessary to fulfill its optimum gap is calculated and, then, this quantity is pipetted in the testing area;
2. The upper disk is lowered until the prescribed gap is achieved between the two disks. The gap is visually inspected in order to identify possible leakages of MRS, which, if found, must be trimmed and cleared;
3. The magnetic yoke is placed around the measuring rod and a process of demagnetization is applied in order to free the magnetic fluid of any previous influences of external magnetic fields;

4. The temperature of the experiment, 25°C, is set on the thermal bath attached to the rheometer. After this, enough time is waited for the temperature of the sample, here defined as the temperature of the lower plate, which is measured by the rheometer, to reach the target temperature;

5. Using the software *Rheoplus*, the magnetic field intensity condition is set. It is resumed to define a constant value of current in order to provide a constant magnetic field intensity when passing through the coils underneath the bottom plate of the measuring device (see figure 5.8);

6. Using the software *Rheoplus*, the shear rate is programmed to vary from 0.1 to 1000 s^{-1} according to a logarithmic ramp, with increase rate of 10 points per decade. Each data point has a variable time of collection due to the fact that the option "*no time setting*" is active during the data acquisition process. This feature ensures that enough time is being waited at each data acquisition, what aims to guarantee that the steady state has been achieved while data collection is being done.

7. The viscosity is acquired as a function of shear rate for a given constant magnetic field intensity.

This process was carried out 10 times, for each MRS, at every condition of magnetic field intensity prescribed.

The experimental errors were calculated using the methodology presented on appendix (A.1).

4.3.3.2 Pseudoplasticity discussion I: diluted suspensions

When an external magnetic field is applied to a magnetorheological suspension, another phenomenon emerges: pseudo-plasticity, closely tied to the magnetoviscous effect analyzed in the previous subsection. Figures (44) and (45) illustrate that, under a constant external magnetic field, the apparent viscosity η^* of the analyzed magnetorheological suspensions decreases significantly as the non-dimensional shear rate, $\dot{\gamma}^*$, increases, revealing a shear-thinning behavior in both fluids.

Shear-thinning is typically attributed to microstructural changes driven by the intensity of the flow, specifically the shear rate. This behavior is observed in both magnetorheological suspensions, but it is crucial to note that the microstructural formation and complexity of these fluids depend strongly on the applied magnetic field strength, α. When the magnetic field is present, ferromagnetic particles align with it, and dipolar interactions promote the formation of anisotropic chains and clusters at the micrometer scale. According to equation (4.6), an increase in the particle structure's length scale significantly intensifies the dipolar interactions. As chains of aligned particles form, the length scale of the resulting structure rapidly increases, which in turn amplifies the dipolar interactions, leading to the development of larger, stiffer, and more stable structures.

To enable a comparison of the shear-thinning behavior observed in both magnetorheological suspensions, the relaxation time τ_m, obtained from tests on the magnetite-based MRS and τ_c, obtained for the MRS of iron, both under the weakest magnetic field intensity, are used to nondimensionalize the shear rate for both suspensions. The relationship between these non-dimensional shear rates is given by:

$$\dot{\gamma}_c^* = \dot{\gamma}_s^* \left(\frac{\tau_c}{\tau_s}\right) = 0.15\dot{\gamma}_s^*, \tag{4.14}$$

where $\dot{\gamma}_c^*$ is the non-dimensional shear rate for the MRS of iron and $\dot{\gamma}_s^*$ for the MRS of magnetite.

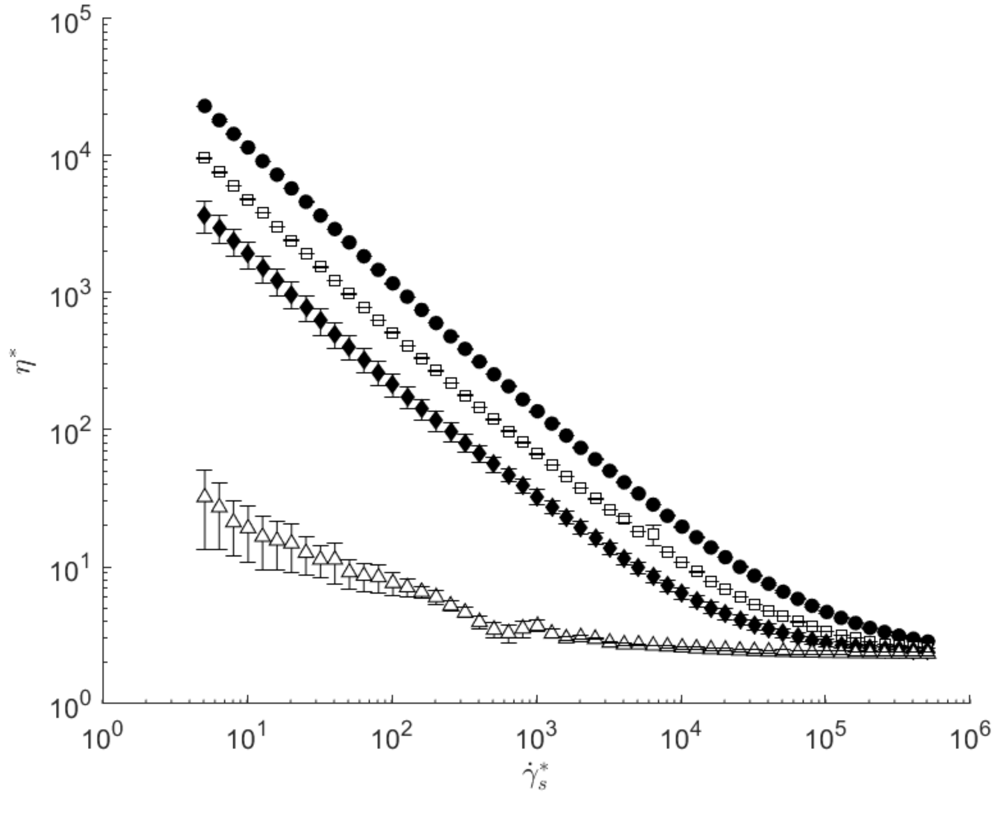

Figure 44 – Magnetorheological suspension of magnetite: relative viscosity η^* as a function of the non-dimensional shear-rate for a suspension with $\phi = 1\%$. Each data set corresponds to a condition of external magnetic field intensity α: (●) - 2.63, (○) - 0.72, (◇) - 0.36 and (△) - 0.

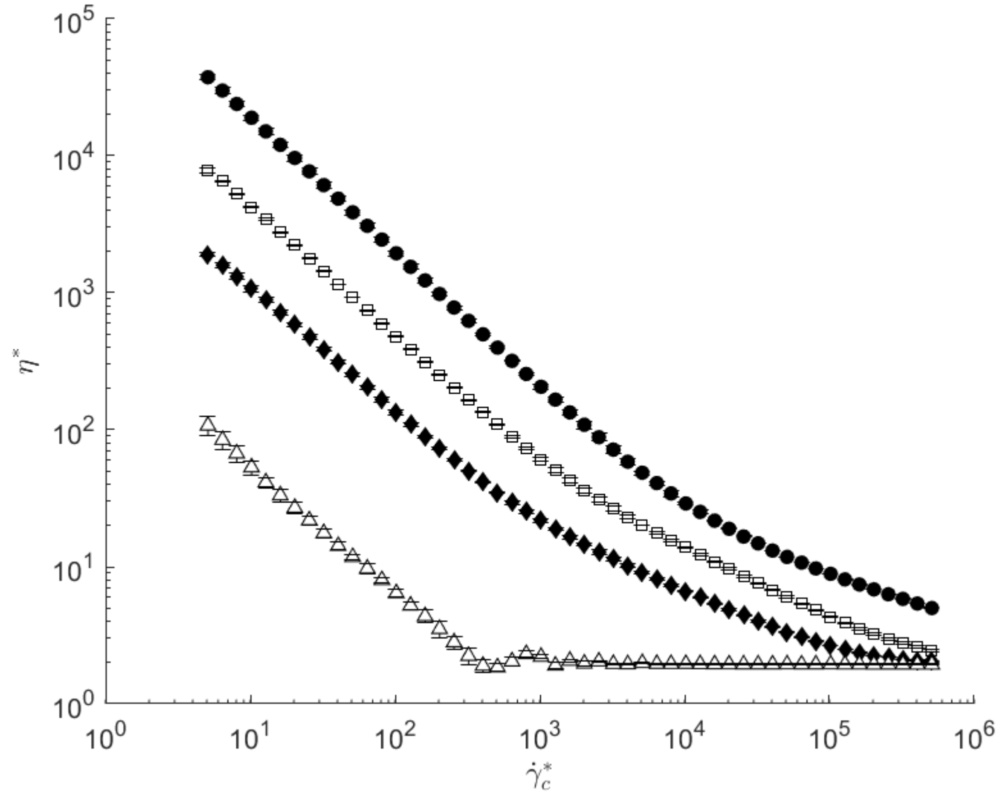

Figure 45 – Magnetorheological suspension of iron: relative viscosity η^* as a function of the non-dimensional shear-rate for a suspension with $\phi = 1\%$. Each data set corresponds to a condition of external magnetic field intensity α: (●) - 2.63, (○) - 0.72, (◊) - 0.36 and (△) - 0.

In the context of constant external magnetic fields, the apparent viscosity of magnetorheological suspensions shows a significant reduction as non-dimensional shear rate increases as illustrated in figures (44) and (45). This behavior can be attributed to two interrelated mechanisms. First, as shear flow intensifies, it aligns the magnetically induced microstructure along the flow streamlines. This alignment reduces the drag associated with the microstructure, leading to a notable decrease in the suspension's viscosity. The smoother flow facilitated by this alignment minimizes resistance and enhances fluidity.

In stronger flow regimes, the magnetic microstructure begins to break down due to increasing shear stresses associated with elevated $\dot{\gamma}^*$,. This breakdown results in smaller particle agglomerates, which decrease local drag and mitigate the hindrance effects that particles impose on flow. The reduction in energy dissipation mechanisms manifests as a marked decrease in apparent viscosity.

Importantly, at high values of $\dot{\gamma}^*$—indicating very strong flows—the apparent viscosity approaches that of the fluid in the absence of a magnetic field, denoted as η_0. Under these conditions, the magnetic field-induced microstructure is nearly entirely disrupted, resulting in behavior similar to that of the fluid without magnetic influence.

As shown in Figure (46), the behavior of viscosity as a function of time was studied for three nondimensional shear rates ($\dot{\gamma}^*$): 2.5, 6.3, and 25.5, to better understand the transition zone observed between $\dot{\gamma}^* = 10^2$ and $\dot{\gamma}^* = 10^3$ in Figure (45). These three values were selected to span the transition range, providing detailed insights into the dynamics of viscosity during this critical phase.

For $\dot{\gamma}^* = 2.5$, pronounced fluctuations in viscosity are observed, indicating transient behaviors potentially linked to structural rearrangements in the fluid. At $\dot{\gamma}^* = 6.3$, the fluctuation continue, showing that the instability between alignment and breakup of structures. Only for $\dot{\gamma}^* = 25.5$, it can be seen that the viscosity stabilizes relatively quickly, suggesting a steady-state flow regime.

These temporal profiles reveal that the transition region is characterized by a complex interplay between the fluid's microstructure and external forces, leading to significant variations in viscosity. This highlights the importance of time-resolved measurements for capturing the intricate dynamics within non-Newtonian fluids. Further investigation into the underlying mechanisms is necessary to fully understand the contributions of particle interactions and flow instabilities in this regime.

Thixotropy is a reversible long time-dependent decrease in the apparent viscosity due to microstructural change when the material is subjected to constant or increasing shear stress, followed by a recovery of the original viscosity once the stress is removed. We could say that this phenomenon corresponds to a time-dependent shear thinning property of certain fluids. In this context, the phenomenon illustrated in Figure (46) can be interpreted as a case of local thixotropy. Specifically, the viscosity changes over time even though the shear rate is held constant. For $\dot{\gamma}_c^* = 2.5$ and $\dot{\gamma}_c^* = 6.3$, which are maintained constant, it is clear the existence of a long time dependent viscosity as a consequence of microstructure changes such as structure breakups and orientation.

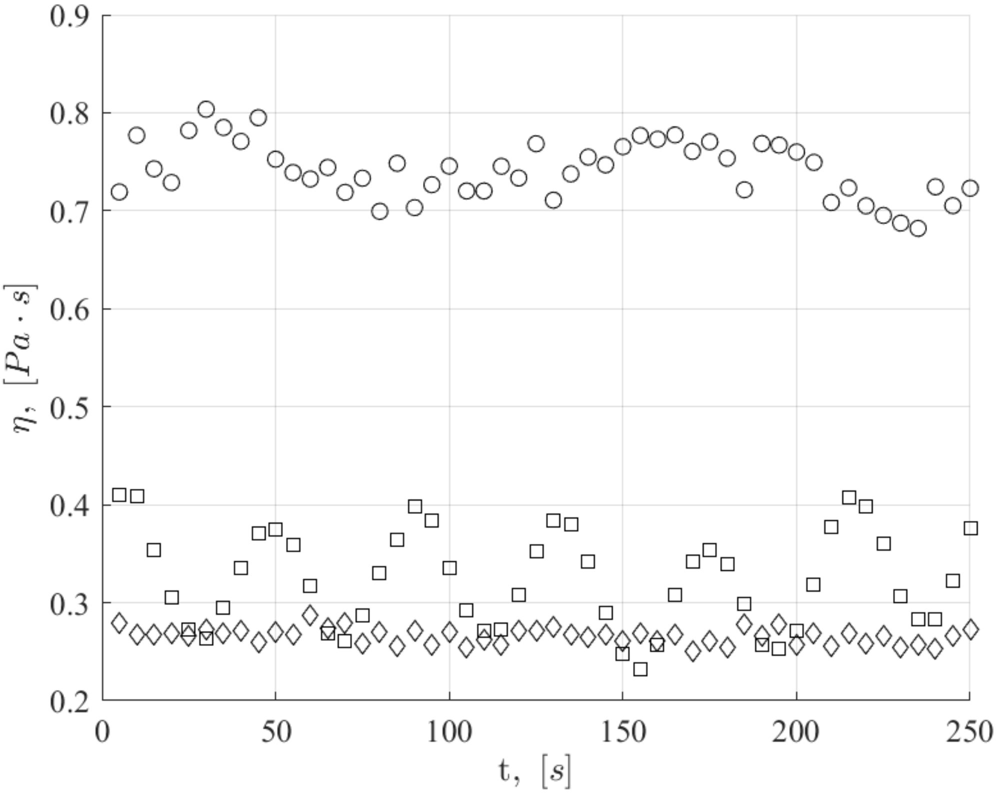

Figure 46 – Viscosity as a function of time for the MRS of iron. (◇) - De=25.5, (□)-De=6.3 and (○)-De=2.5.

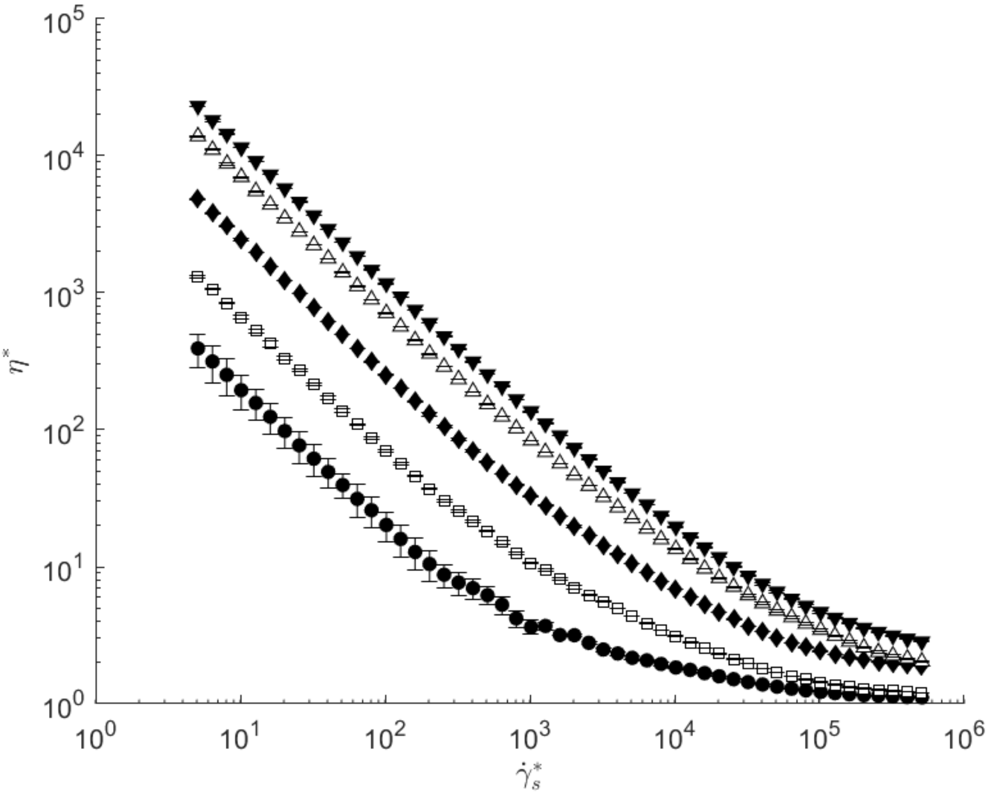

Figure 47 – Magnetorheological suspension of magnetite: relative viscosity η^* as a function of the nondimensional shear-rate for different magnetic particles' volume fraction subjected to an homogeneous magnetic field. The nondimensional magnetic parameter α is held constant and equals to 2.63. Each set of data corresponds to a magnetorheological suspension with different particles' volume fraction: (▼) - 1%, (△) - 0.8%, (◆) - 0.6%, (□) - 0.4% e (●) - 0.2%.

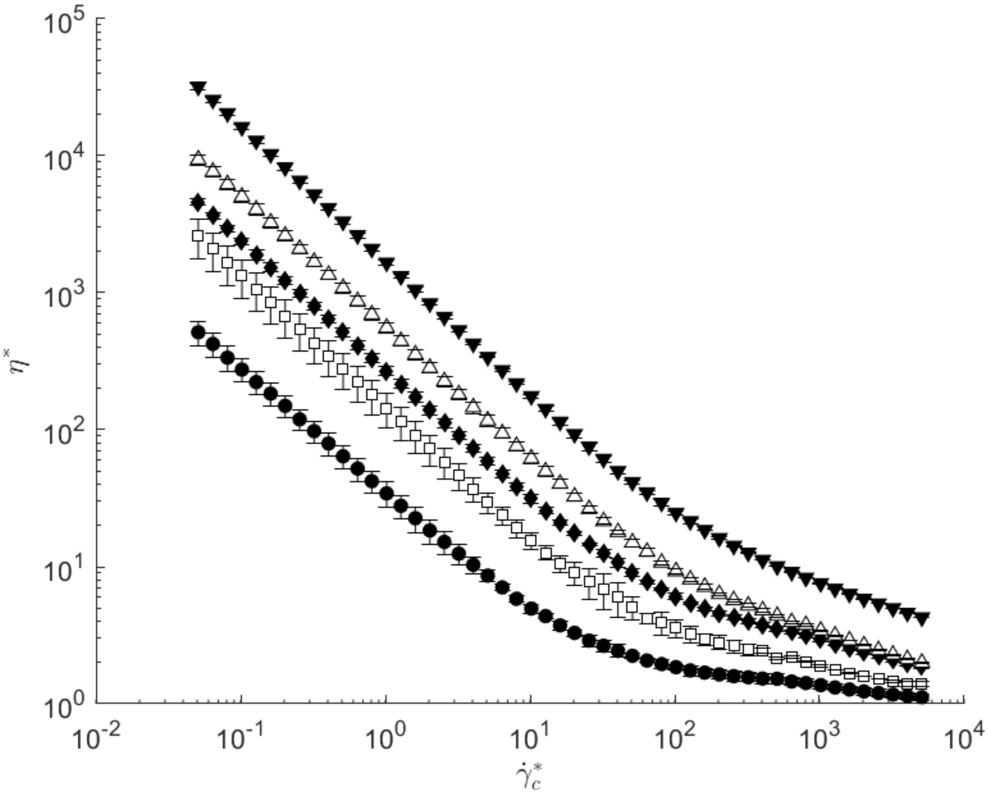

Figure 48 – Magnetorheological suspension of iron: relative viscosity η^* as a function of the nondimensional shear-rate for different magnetic particles' volume fraction subjected to an homogeneous magnetic field. The nondimensional magnetic parameter α is held constant and equals to 2.63. Each set of data corresponds to a magnetorheological suspension with different particles' volume fraction: (▼) - 1%, (△) - 0.8%, (◆) - 0.6%, (□) - 0.4% e (●) - 0.2%.

Figures (47) and (48) illustrate the dependence of dimensionless viscosity on the non-dimensional shear rate ($\dot{\gamma}^*$) for various volume fractions of magnetic particles (ϕ), with the magnetic parameter held constant at $\alpha = 2.63$. The shear-thinning effect is evident in both suspensions across all evaluated ϕ values. Notably, samples with higher ϕ consistently exhibit greater viscosity throughout the entire $\dot{\gamma}^*$ range compared to those with lower ϕ.

This behavior can be understood by considering the physical implications of increased ϕ, which directly relates to the availability of particles for forming magnetic-induced structures. Suspensions with higher ϕ contain more particles per unit volume than their more diluted counterparts. Consequently, the likelihood of generating complex microstructures—such as chains and agglomerates of particles—due to the application of an external magnetic field is significantly higher in concentrated suspensions. As previously discussed, these more complex microstructures lead to increased local viscous dissipation within the fluid. The collective effect of this mechanism is a marked increase in the overall viscosity of the suspension.

4.3.3.3 Pseudoplasticity discussion II: concentrated suspensions

In the previous section, we presented results regarding the pseudoplastic effect of the magnetorheological suspensions (MRS) of iron and magnetite. It was observed that the dependence of η^* on De was remarkably similar for both systems, despite the significant difference in their dipolar parameter λ. This suggests that the MRS of iron should exhibit a much more pronounced pseudoplastic effect compared to that of magnetite, given the significantly higher magnetization of iron relative to magnetite.

The issue lies in the particle size used to form the MRS. To produce MRS of iron and magnetite with the same particle volume fraction, significantly fewer iron particles are required due to their micrometric size. In contrast, the magnetite particles are nanometric, necessitating a much larger quantity of material to achieve the desired composition. It is important to note that the MRS of magnetite attains a micrometric minimum length only in the presence of an external magnetic field.

When evaluating more concentrated suspensions, the impact of magnetization on the rheology becomes evident, as there are sufficient iron particles in the suspension. Figure (49) presents the nondimensional relative viscosity of the magnetite MRS as a function of De for different external magnetic field intensities. The viscosities shown are lower than those in Figure (50), which depicts the same relationship for the iron MRS.

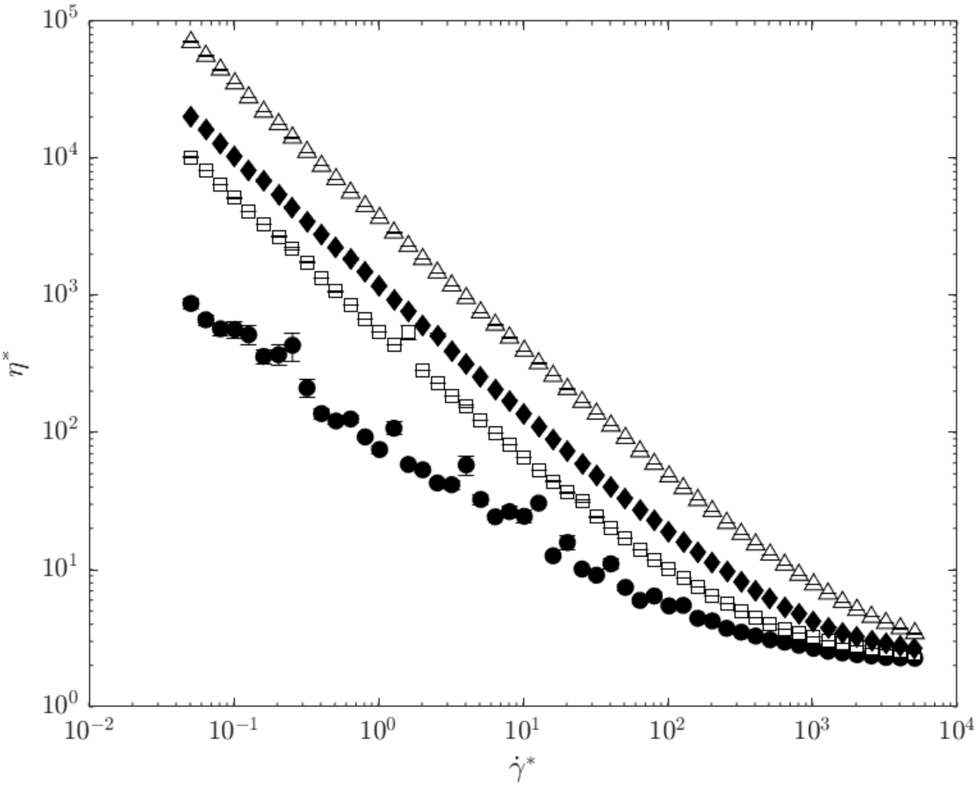

Figure 49 – Magnetorheological suspension of magnetite: relative viscosity η^* as a function of the nondimensional shear rate for a suspension with $\phi = 4\%$. Each data set corresponds to a condition of external magnetic field intensity α: (△) - 2.63, (◆) - 0.72, (□) - 0.36 and (●) - 0.

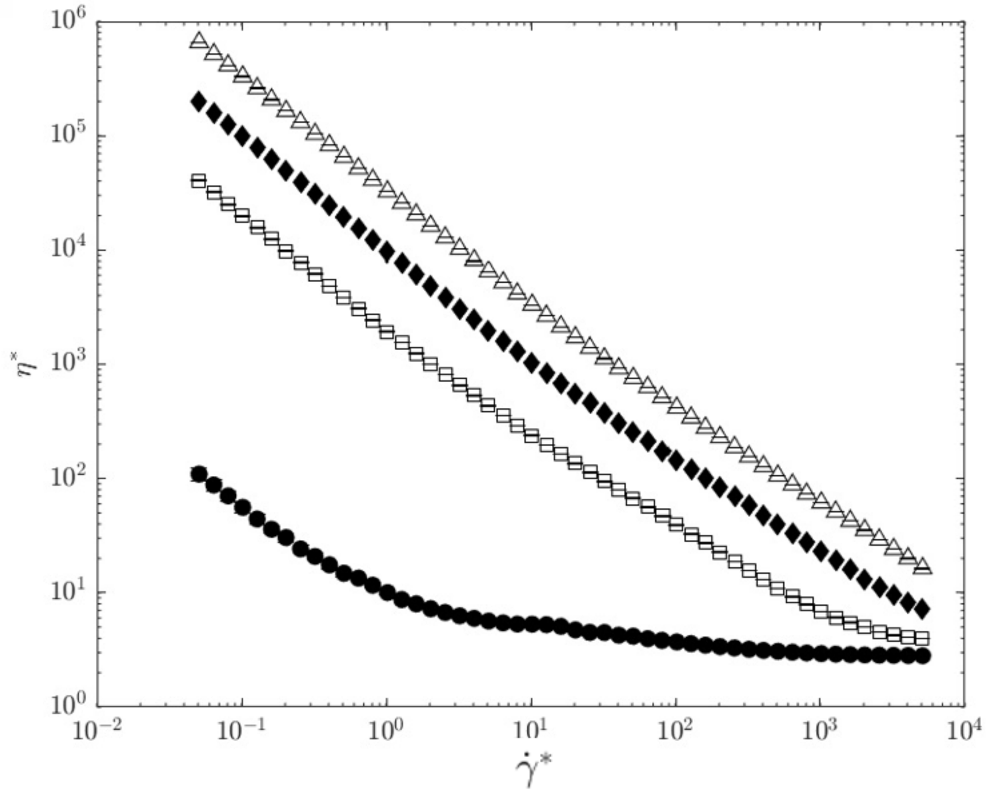

Figure 50 – Magnetorheological suspension of iron: relative viscosity η^* as a function of thenondimensional shear rate for a suspension with $\phi = 4\%$. Each data set corresponds to a condition of external magnetic field intensity α: α: (△) - 2.63, (◆) - 0.72, (□) - 0.36 and (●) - 0.

Figure (51) displays the nondimensional zero-shear viscosity, η_0^*, as a function of ϕ. As observed, the viscosity is significantly higher for the iron MRS, indicating that in concentrated suspensions, the higher magnetization of the iron particles substantially influences the rheology. This effect becomes more pronounced as ϕ increases, due to the larger number of particles present in the suspension.

Both suspensions exhibited a virial fitting of $\mathcal{O}(2)$, indicating that the system is no longer statistically homogeneous. In these cases, particle interactions extend beyond individual behavior, as the localization of one particle depends on the positions of others. It is important to note that not only dipolar interactions occur but also hydrodynamic interactions, which further influence the suspension's rheological properties.

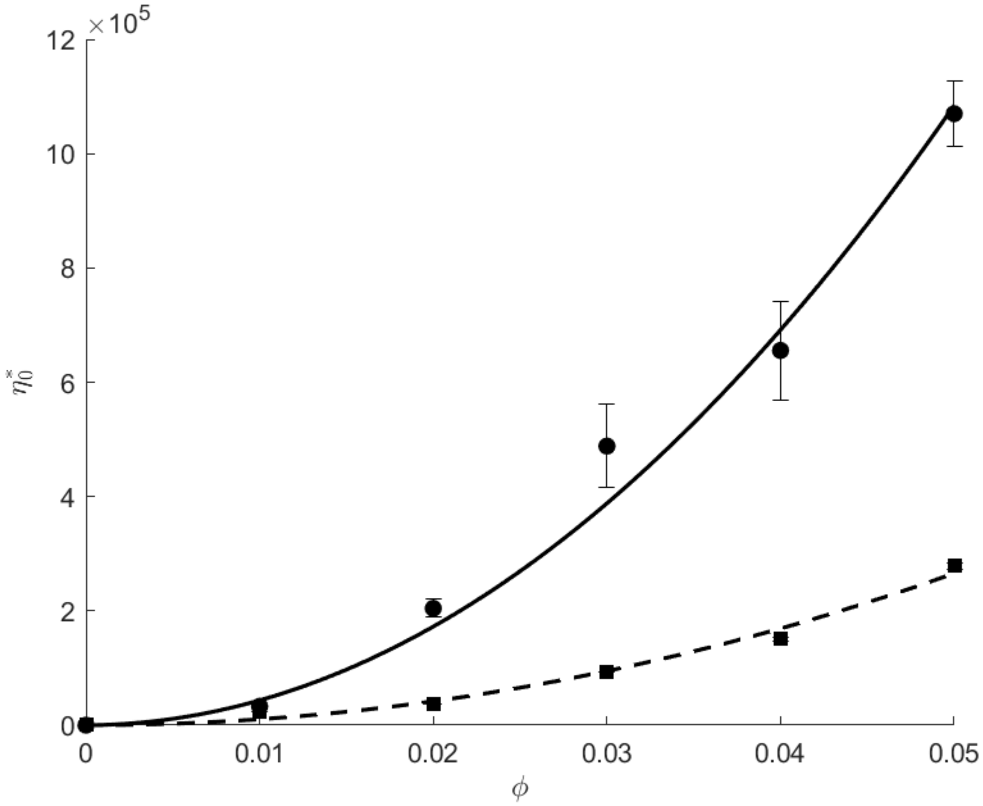

Figure 51 – Nondimensional zero shear viscosity η_0^* as a function of the magnetic particle volume fraction ϕ for: (●) - magnetorheological suspension of iron and (■) - magnetorheological suspension of magnetite. The curves are fittings of the experimental data to a virial equation like $\eta_0^* = 1 + k_1\phi(1 + k_2\phi + k_2\phi^2/2)$. For the MRS of iron, $k_1 = 1.28 \times 10^5$ and $k_2 = 3.28 \times 10^3$. For the MRS of magnetite, $k_1 = 1.67 \times 10^3$ and $k_2 = 6.21 \times 10^4$.

4.4 Transient shear analysis

Experimental trials have been executed in the regime of transient shear flow in order to evaluate how the shear stress relaxes when the fluid is subjected to different conditions of external magnetic field intensities α. Those experiments have made possible the determination of the spectrum of relaxation times of each magnetorheological suspension and also the measurement of their residual stresses as functions of the applied magnetic field and of the shear flow intensities.

4.4.1 Step-strain: Magnetic field influence

Step-strain experiments are used in this section to evaluate the dependence of the stress relaxation function $\Phi(s)$[3] of both magnetorheological suspensions on the intensity of

---

[3] It is important to remember that s is the time shift, defined as $s = t - t'$, in which t is the actual time and t' is a reference time, usually the instant in which the instantaneous strain is applied to the fluid on a step-strain experiment. Further details are given on subsection (2.2.3).

the applied magnetic field. Based on the time behavior of the referred material function, it was possible to determine the spectrum of times of relaxation for each fluid at each condition of magnetic field intensity. Besides that, the residual stress relaxation parameter Φ_∞ was also obtained as function of the magnetic field intensity for both magnetorheological suspensions.

4.4.1.1 Experimental procedure

The step-strain experiment is used to obtain the stress relaxation function $\Phi(s)$ of a given complex fluid. Based on this material function, it is possible to determine the spectrum of relaxation times characteristic of the fluid.

This experimental protocol is composed by the following steps:

1. For each magnetorheological suspension (fixed magnetic particles volume fraction ϕ), the optimized gap between the disks of the rheometer is chosen based on the viscosity exhibited by them on each of the four magnetic field intensities applied. The gaps used on this experiment are displayed on table (10);

2. The volume of magnetorheological suspension needed to fulfill the gap is calculated and, after, this quantity is pipetted and placed in the test area;

3. The upper disk is lowered until the precise gap between the disks is reached. Eventual leakages of fluid from the gap are trimmed and cleaned;

4. The magnetic yoke is placed around the measuring rod and a process of demagnetization is applied in order to free the magnetic fluid of any previous influences of external magnetic fields;

5. Through the software *Rheoplus* a fixed current is set to be provided by the PS-MRD DC power supply to the coils in the magneto-rheology assembly, which generate a homogeneous magnetic field in the gap, where a sample of magnetorheological suspension is located;

6. The temperature of the experiment, 25°C, is set on the thermal bath attached to the rheometer. After this, enough time is waited for the temperature of the sample, here defined as the temperature of the lower plate, which is measured by the rheometer, to reach the target temperature;

7. A step-strain with a fixed angular strain γ_0 is applied to the sample. It is important to note that the angular strain, which is applied instantaneously to the fluid, should be as small as possible to ensure that the flow regime is linear viscoelastic. However, it should be noted that the smaller this parameter is, the smaller the applied torque will be. Therefore, one can easily enter a torque condition lower than the minimum torque required for meaningful measurements to be made. Regarding this context,

for both magnetorheological suspension in all the specified magnetic particles volume fraction ϕ: 0.2%, 0.4%, 0.6%, 0.8%, 1%, γ_0 was set as 0.1;

8. The data concerning the stress relaxation function is acquired as a function of time every 0.01s.

Table 10 – Gaps chosen for each magnetorheological suspension (MRS) considering four different magnetic field intensities, denoted by the originating electric current.

Current (A)	ϕ (%)	MRS - Magnetite (h [mm])	MRS - Iron (h [mm])
1	0.2	0.3	0.3
	0.4	0.3	0.3
	0.6	0.4	0.5
	0.8	0.5	0.6
	1.0	0.6	0.6
2	0.2	0.4	0.4
	0.4	0.4	0.4
	0.6	0.5	0.5
	0.8	0.6	0.7
	1.0	0.7	0.7
3	0.2	0.4	0.4
	0.4	0.5	0.5
	0.6	0.6	0.6
	0.8	0.7	0.7
	1.0	0.8	0.8
4	0.2	0.4	0.4
	0.4	0.5	0.5
	0.6	0.6	0.6
	0.8	0.7	0.7
	1.0	0.8	0.8

The experimental errors were calculated using the methodology presented on appendix (A.1).

4.4.1.2 Discussion

In this subsection, it will be analyzed and discussed the results obtained by applying a step-strain reometric flow to samples of the magnetorheological suspension of magnetite and iron, in the presence of a constant homogeneous magnetic field. The realization of this kind of experiments, led to the obtainment of the stress relaxation functions $\Phi(s)$ for different intensities of the external magnetic field H.

The results are presented here on their dimensionless form. The magnetic field intensity is traduced, as usually, by the magnetic parameter α. Regarding this context, the stress relaxation function, for a fixed intensity of external magnetic field, $\Phi(s)|_\alpha$ was made dimensionless using the following time and viscosity characteristic scales:

$$t^c \sim \tau_m, \tag{4.15}$$

$$\eta^c \sim \eta_0, \tag{4.16}$$

where τ_m is the principal time of relaxation of the fluid evaluated in the presence of the lowest magnetic field intensity applied, η_0 is the viscosity of the base fluid of the magnetorheological suspesnsions, mineral oil, at 25°C. Using those scales, the typical scale of the stress relaxation function, which has unit of stress is given by:

$$[\Phi|_\alpha]^c \sim \frac{\eta_0}{\tau_m}. \tag{4.17}$$

Besides that, the time shift, $s = t - t'$, has the following typical scale:

$$s^c \sim t^c \sim \tau_m. \tag{4.18}$$

Therefore, the nondimensional form of the stress relaxation function, considering a fixed condition of α, is given by:

$$\Phi^*(s^*)|_\alpha = \frac{\Phi(s/s^c)|_\alpha}{[\Phi|_\alpha]^c} = \frac{\Phi(s/\tau_m)\tau_m}{\eta_0} = \frac{\Phi(s^*)\tau_m}{\eta_0}, \tag{4.19}$$

where $\tilde{s}$ is the nondimensional time shift.

Figures (52) to (55) present the nondimensional stress relaxation function Φ^* as a function of time shift for the magnertorheological suspension of magnetite with magnetic particles volume fraction ϕ equals to 0.2%. Figures (56) to (59) show the same analysis but for a suspension with ϕ equals to 1%. The referred material function is evaluated considering four intensities of the homogeneous magnetic field applied H: 7.18×10^4A/m ($\alpha = 2.63$), 1.24×10^5A/m ($\alpha = 4.55$), 1.66×10^5A/m ($\alpha = 6.11$) and 1.96×10^5A/m ($\alpha = 7.19$).

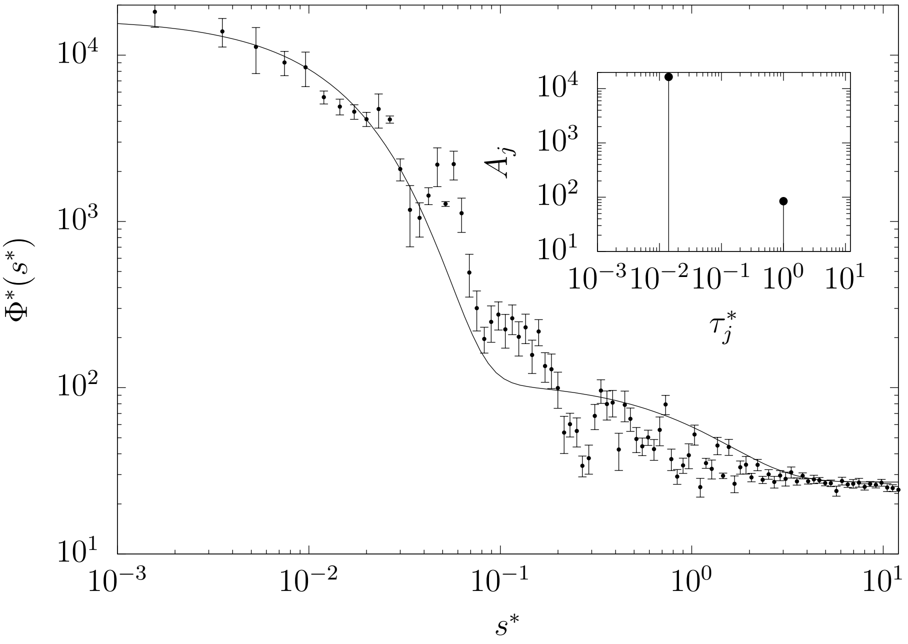

Figure 52 – Magnetorheological suspension of magnetite ($\phi = 0.2\%$): non-dimensional stress relaxation function Φ^* for $\alpha = 2.63$ (relative to a current of 1A). The curve is a fit of the experimental data to the following expression: $\Phi^*(s^*) = \Phi_R^* + \sum_{i=1}^{2} A_j \exp(s^*/\tau_j^*)$. The fit parameters are: $A_1 = 1.97 \times 10^2 \pm 6.20 \times 10^0$, $A_2 = 5.07 \times 10^1 \pm 1.14 \times 10^{-1}$, $\tau_1^* = \tau_m^* = 1$, $\tau_2^* = 9.52 \times 10^{-2} \pm 1.21 \times 10^{-3}$ and $\Phi_R^* = 5.96 \times 10^0 \pm 1.96 \times 10^{-1}$.

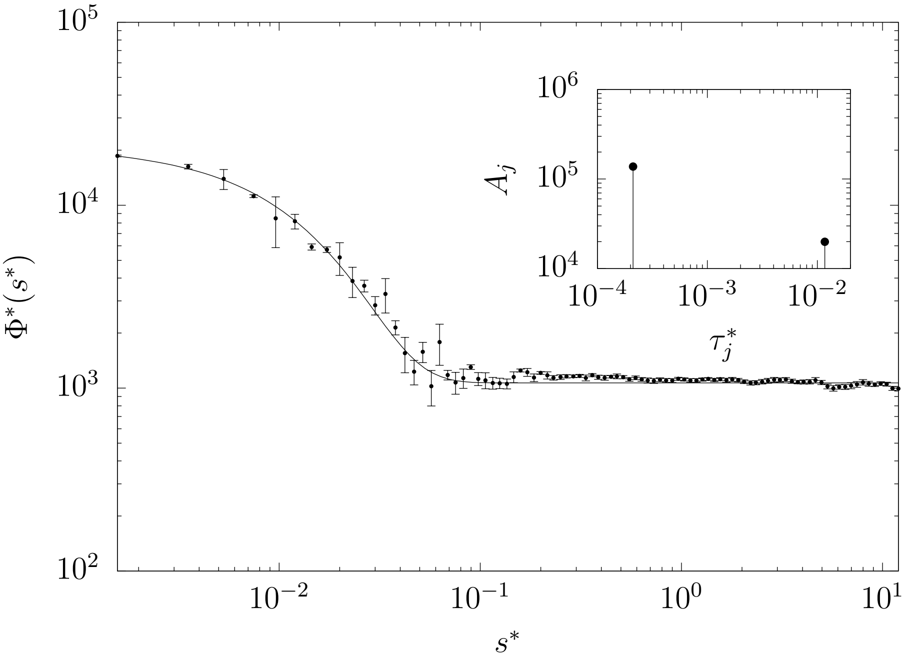

Figure 53 – Magnetorheological suspension of magnetite ($\phi = 0.2\%$): non-dimensional stress relaxation function Φ^* for $\alpha = 4.55$ (relative to a current of 2A). The curve is a fit of the experimental data to the following expression: $\Phi^*(s^*) = \Phi_R^* + \sum_{i=1}^{2} A_j \exp(s^*/\tau^*)$. The fit parameters are: $A_1 = 1.35 \times 10^3 \pm 5.20 \times 10^1$, $A_2 = 6.59 \times 10^0 \pm 1.11 \times 10^{-2}$, $\tau_1^* = 1.07 \times 10^0 \pm 2.48 \times 10^{-1}$, $\tau_2^* = 2.01 \times 10^{-2} \pm 1.95 \times 10^{-3}$ and $\Phi_R^* = 7.61 \times 10^0 \pm 3.32 \times 10^{-2}$.

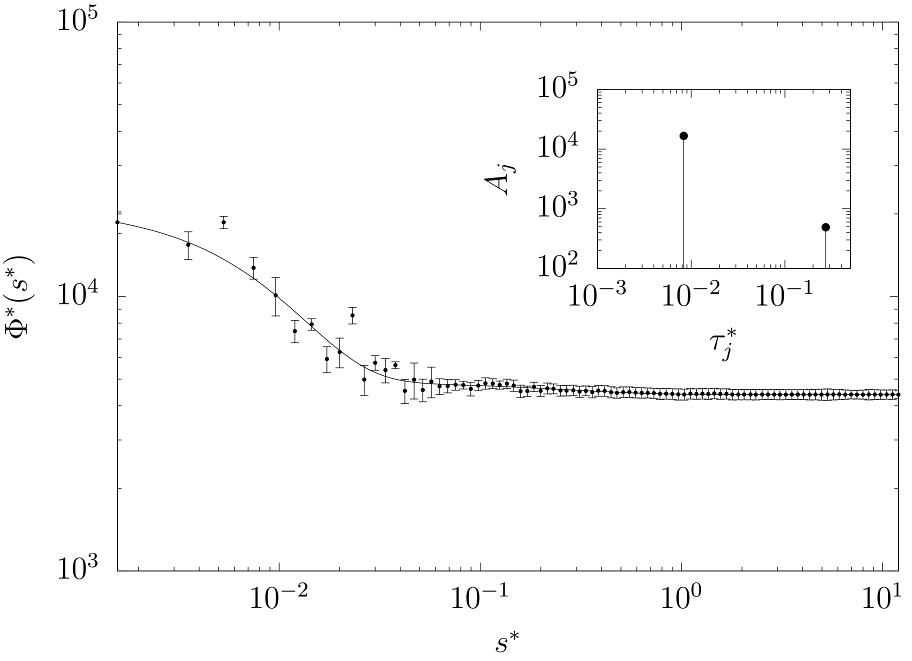

Figure 54 – Magnetorheological suspension of magnetite ($\phi = 0.2\%$): non-dimensional stress relaxation function Φ^* for $\alpha = 6.11$ (relative to a current of 3A). The curve is a fit of the experimental data to the following expression: $\Phi^*(s^*) = \Phi^*_R + \sum_{i=1}^{2} A_j \exp(s^*/\tau^*)$. The fit parameters are: $A_1 = 1.71 \times 10^3 \pm 8.56 \times 10^1$, $A_2 = 6.54 \times 10^1 \pm 6.43 \times 10^{-1}$, $\tau^*_1 = 5.08 \times 10^{-1} \pm 1.12 \times 10^{-2}$, $\tau^*_2 = 4.12 \times 10^{-2} \pm 5.87 \times 10^{-3}$ and $\Phi^*_R = 9.69 \times 10^2 \pm 2.93 \times 10^0$.

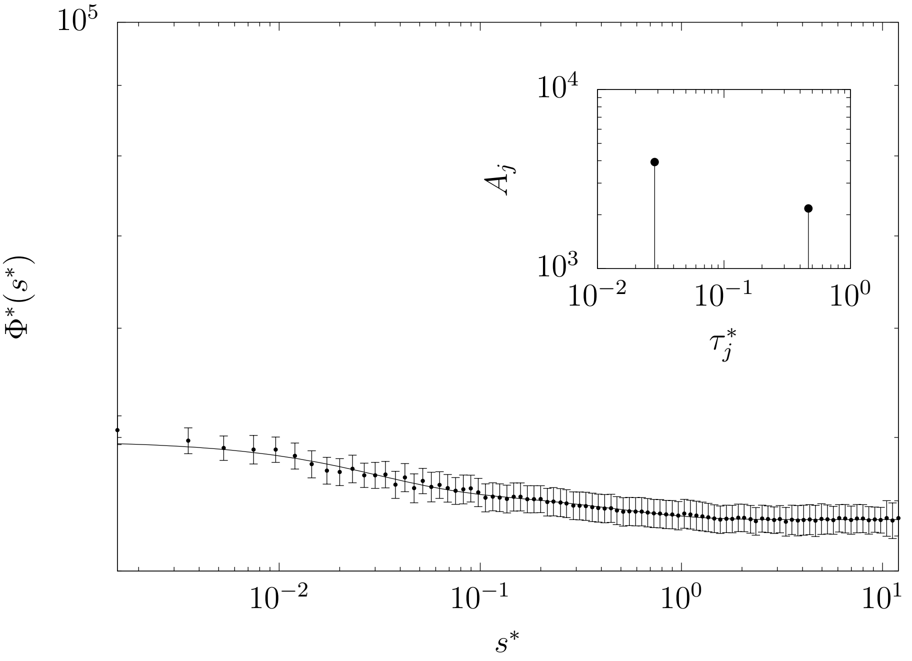

Figure 55 – Magnetorheological suspension of magnetite ($\phi = 0.2\%$): non-dimensional stress relaxation function Φ^* for $\alpha = 7.19$ (relative to a current of 4A). The curve is a fit of the experimental data to the following expression: $\Phi^*(s^*) = \Phi^*_R + \sum_{i=1}^{2} A_j \exp(s^*/\tau^*)$. The fit parameters are: $A_1 = 9.75 \times 10^4 \pm 7.28 \times 10^2$, $A_2 = 1.52 \times 10^2 \pm 4.78 \times 10^0$, $\tau^*_1 = 2.52 \times 10^0 \pm 1.17 \times 10^{-1}$, $\tau^*_2 = 2.68 \times 10^{1 \pm 3.45 \times 10^{-2}}$ and $\Phi^*_R = 9.19 \times 10^3 \pm 4.21 \times 10^0$.

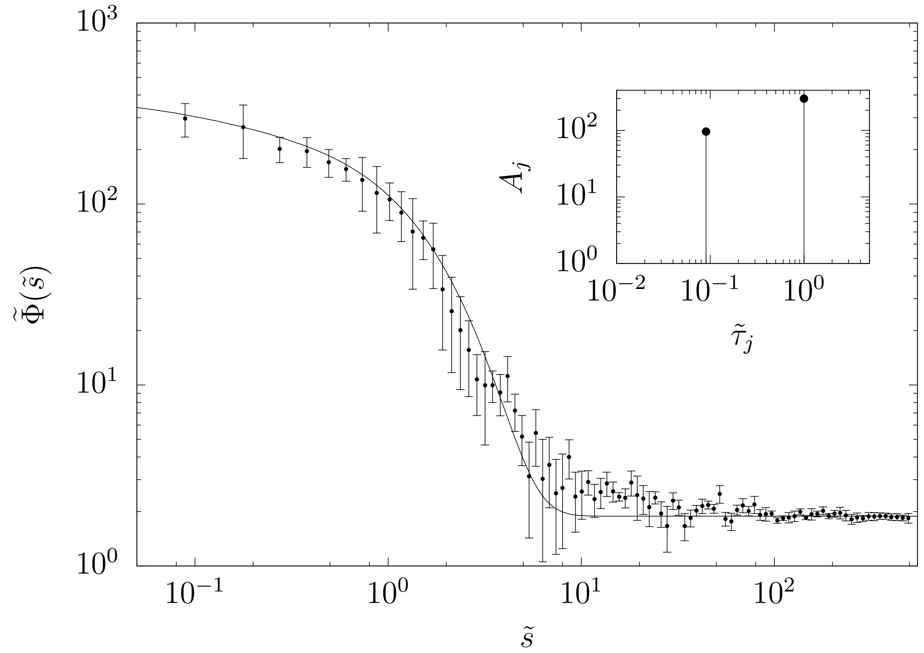

Figure 56 – Magnetorheological suspension of iron ($\phi = 0.2\%$): non-dimensional stress relaxation function Φ^* for $\alpha = 2.63$ (relative to a current of 1A). The curve is a fit of the experimental data to the following expression: $\Phi^*(s^*) = \Phi^*_\infty + \sum_{i=1}^{2} A_j \exp(s^*/\tau^*)$. The fit parameters are: $A_1 = 3.51 \times 10^2 \pm 3.96 \times 10^0$, $A_2 = 1.59 \times 10^2 \pm 2.20 \times 10^0$, $\tau_1^* = \tau_m^* = 1$, $\tau_2^* = 1.87 \times 10^{-1} \pm 8.65 \times 10^{-2}$ and $\Phi_R^* = 1.47 \times 10^0 \pm 7.11 \times 10^{-1}$.

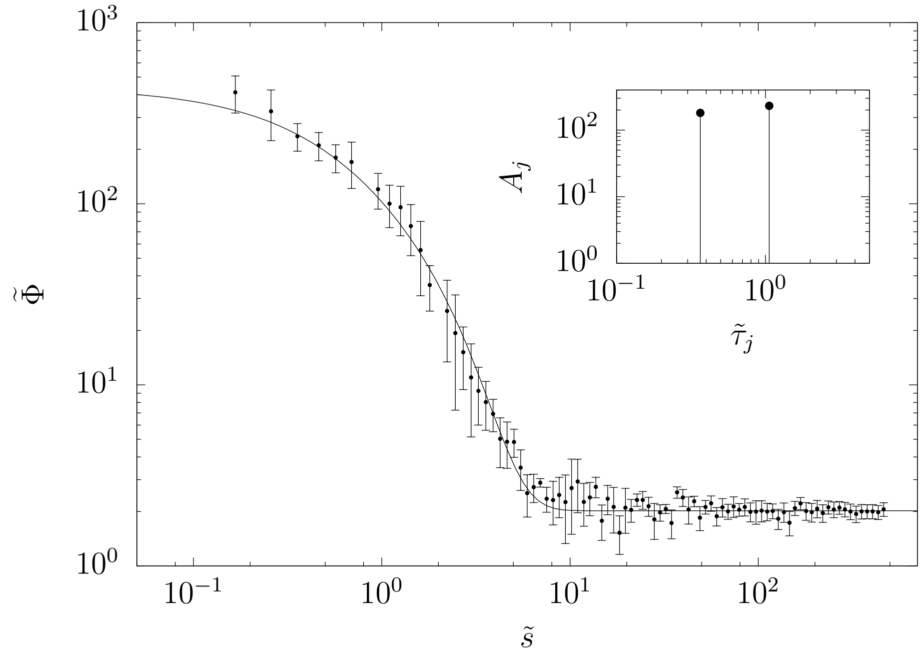

Figure 57 – Magnetorheological suspension of iron ($\phi = 0.2\%$): non-dimensional stress relaxation function Φ^* for $\alpha = 4.55$ (relative to a current of 2A). The curve is a fit of the experimental data to the following expression: $\Phi^*(s^*) = \Phi^*_\infty + \sum_{i=1}^{2} A_j \exp(s^*/\tau^*)$. The fit parameters are: $A_1 = 3.04 \times 10^2 \pm 1.86 \times 10^0$, $A_2 = 1.14 \times 10^2 \pm 5.21 \times 10^0$, $\tau_1^* = 1.23 \times 10^0 \pm 1.93 \times 10^{-1}$, $\tau_2^* = 3.31 \times 10^{-1} \pm 2.67 \times 10^{-2}$ and $\Phi_R^* = 1.76 \times 10^0 \pm 1.75 \times 10^{-1}$.

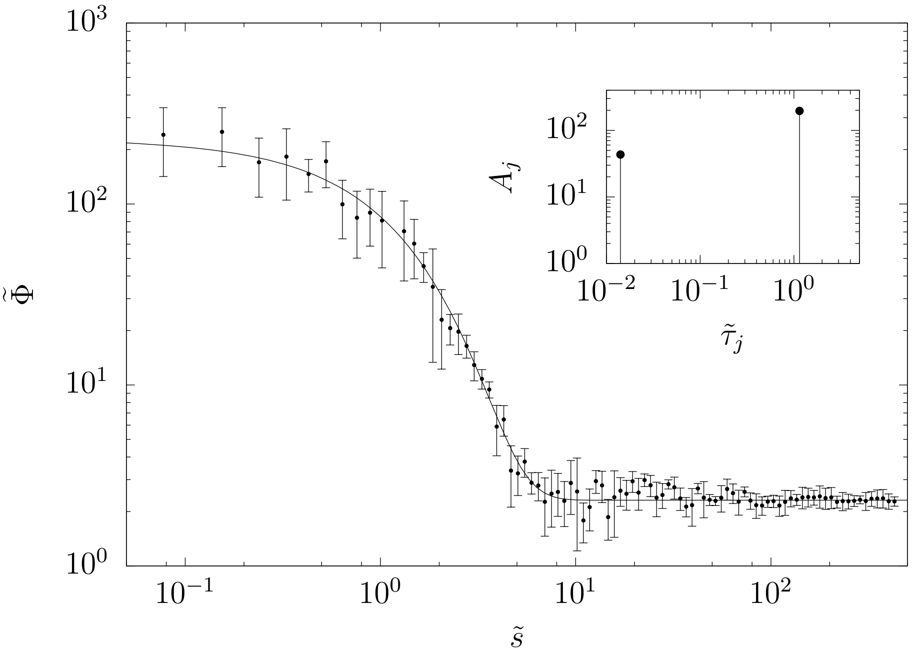

Figure 58 – Magnetorheological suspension of iron ($\phi = 0.2\%$): non-dimensional stress relaxation function Φ^* for $\alpha = 6.11$ (relative to a current of 3A). The curve is a fit of the experimental data to the following expression: $\Phi^*(s^*) = \Phi^*_\infty + \sum_{i=1}^{2} A_j \exp(s^*/\tau^*)$. The fit parameters are: $A_1 = 2.46 \times 10^2 \pm 2.77 \times 10^0$, $A_2 = 1.14 \times 10^2 \pm 5.21 \times 10^0$, $\tau_1^* = 6.32 \times 10^{-1} \pm 3.07 \times 10^{-2}$, $\tau_2^* = 6.99 \times 10^{-2} \pm 3.76 \times 10^{-3}$ and $\Phi_R^* = 2.22 \times 10^0 \pm 1.43 \times 10^{-1}$.

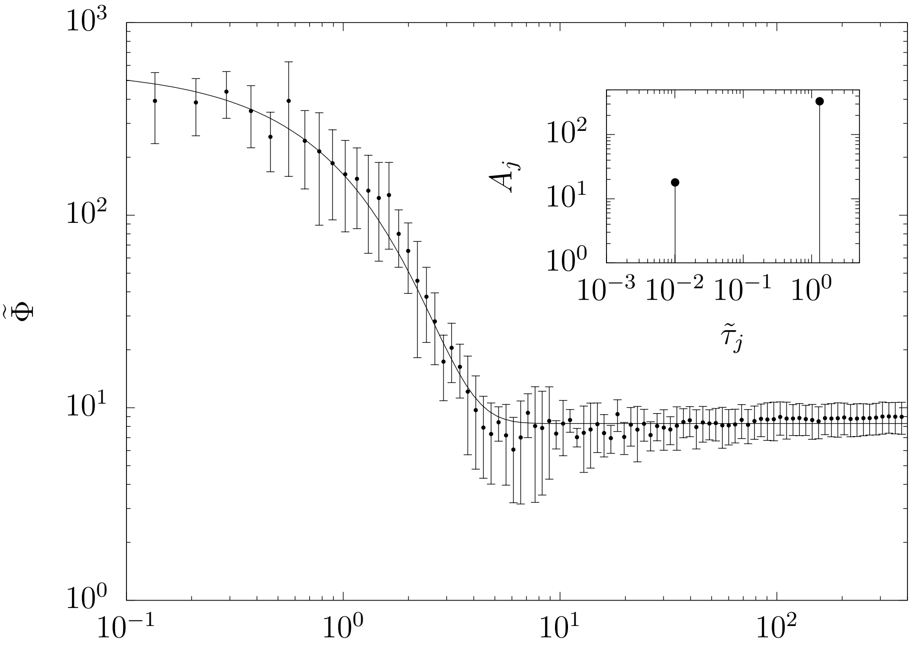

Figure 59 – Magnetorheological suspension of iron ($\phi = 0.2\%$): non-dimensional stress relaxation function Φ^* for $\alpha = 7.19$ (relative to a current of 4A). The curve is a fit of the experimental data to the following expression: $\Phi^*(s^*) = \Phi^*_\infty + \sum_{i=1}^{2} A_j \exp(s^*/\tau^*)$. The fit parameters are: $A_1 = 3.33 \times 10^2 \pm 1.80 \times 10^0$, $A_2 = 2.22 \times 10^2 \pm 7.93 \times 10^0$, $\tau_1^* = 5.38 \times 10^{-1} \pm 2.57 \times 10^0$, $\tau_2^* = 6.99 \times 10^{-2} \pm 1.96 \times 10^{-3}$ and $\Phi_R^* = 1.28 \times 10^0 \pm 4.44 \times 10^{-1}$.

It can be observed from the two set of figures, (52) to (55) and (56) to (59), that in every case the magnetorheological suspensions undergo a long-time stress relaxation process after the aplication of the step-strain, which is an almost instantaneous shear flow. This process was carried out under the permanent action of a series of external magnetic field intensities. The fact that the stress relaxation function does not relax to zero instantaneously, when in the presence of an external magnetic field, indicates that the rheology of the magnetorheological suspensions change towards a viscoelastic behavior. Bird et al. (1987) affirms that the time retardation on the stress relaxation of complex fluids are intimately related to elastic effects arising from its microstructure. The formation of a magnetic filed-induced microstructure injects elasticity in the system of the fluid. This mechanism delays the process of stress relaxation due to the fact that the microstructure, by means of elastic deformation, absorb a part of the energy of the shearing flow, liberating it after the flow is ceased. The fact that the fluid is non-instantaneous is very well characterized by the fact that it presents a spectrum of relaxation times, which can be seen, in a dimensionless fashion, in the inserts of the figures (52) to (59). It is important to remark that the mean time of relaxation is the one characterized by having the biggest amplitude of stress (A_j). This context strongly suggests the utilization of a viscoelastic constitutive model for describing the relaxation of the shear stress on these fluids. As a result, it has been used Maxwell's generalized viscoelastic model, due to the fact that it predicts the stress relaxation function behavior as a summation of exponentials, which are pondered by the a series of characteristics viscosities and times, that simulate the effects of relaxation due to viscous dissipation and elastic energy storage.

The constitutive equation for Maxwell's generalized viscoelastic model is presented on (2.27). In order to obtain its dimensionless form, expression (2.27) will be substituted on equation (4.19), which leads to

$$\Phi^*(s^*)|_\alpha = \frac{\Phi(s^*)\tau_m}{\eta_0} = \sum_{j=1}^{N} \frac{\eta_j/\eta_0}{\tau_j/\tau_m} \exp\left(-\frac{s^*}{\tau_j/\tau_m}\right) = \sum_{j=1}^{N} \frac{\eta_j^*}{\tau_j^*} \exp\left(-s^*/\tau_j^*\right). \tag{4.20}$$

Defining,

$$A_j = \frac{\eta_j^*}{\tau_j^*}, \tag{4.21}$$

equation (4.20) can be rewritten as

$$\Phi^*(s^*)|_\alpha = \sum_{j=1}^{N} A_j \exp\left(s^*/\tau_j^*\right), \tag{4.22}$$

where, $\Phi^*(s^*)|_\alpha$ is the nondimensional stress relaxation function, considering a fixed α, for a generalized Maxwell's fluid, A_j is the j-th amplitude of nondimensional shear stress,s^* is the nondimensional time shift and τ_j^* is the nondimensional time associated to the j-th Maxwell's element. However, analyzing carefully the results present on figures (52) to (59), it can be seen that the stress relaxation function does not reaches zero for long times. Instead of this, the referred material function relaxes for a constant non-zero value, which was named, in this work, as the residual stress relaxation parameter $\Phi_R^*|_\alpha$. From this observation, an adaptation of the constitutive equation (4.22) was proposed in order to take into account $\Phi_R^*|_\alpha$, which resulted in:

$$\Phi^*(s^*)|_\alpha = \Phi_R^*|_\alpha + \sum_{j=1}^{N} A_j \exp\left(s^*/\tau_j^*\right). \tag{4.23}$$

Using equation (4.23) to fit the experimental data obtained for each magnetorheological suspension , at four different conditions of magnetic field intensity α, it was possible to determine the dimensionless times of relaxation $\tilde{\tau}_j$ and nondimensional shear stress amplitudes A_j. It is important to note that the main time of relaxation $\tilde{\tau}_m$ for each value of α was obtained previously by numerical integration of equation (2.66). As a result, the fitting process have been carried out already considering defined the referred parameter.

Figures (60) and (61) present, for several magnetic particles volume fraction ϕ, the behavior of the dimensionless time of relaxation as a function of the magnetic parameter α. Figure (60) deals with the results for the MRS of magnetite and Figure (61) for the MRS of iron. From figure (60), it can be seen that for the lower magnetic particles volume fraction ϕ, the increase of the magnetic parameter increases more intensely the dimensionless time of relaxation, when compared with the same effect on suspensions with higher ϕ. Bird, Armstrong and Hassager (1987) emphasize that, in a relaxation process, each characteristic time is intimately related to a physical relaxation mechanism. This is related to the fact that in diluted magnetic suspensions, the magnetic field has to be more intense in order to produce a magnetic-induced microstructure of saturation, that is a configuration of particles, chains and agglomerates that does not change with further increases of the magnetic field intensity. As ϕ grows, the intensity of the magnetic field in order to achieve saturation (dynamical equilibrium) decreases, so almost no change is observed in the values of τ as α heightens. The conclusions for the MRS of iron are almost the same, however, it can be seen from figure (61) that the MRS with lower ϕ presents an approximately constant time of relaxation in relation to the applied magnetic field intensity. This anomalous behavior suggests that the MRS of iron may not form complex structures, such as agglomerates, presenting only a more simple microstructure that rapidly saturates, which leads to a lower injection of elasticity in the system of the suspension, resulting in lower values of τ that do not change much as α increases.

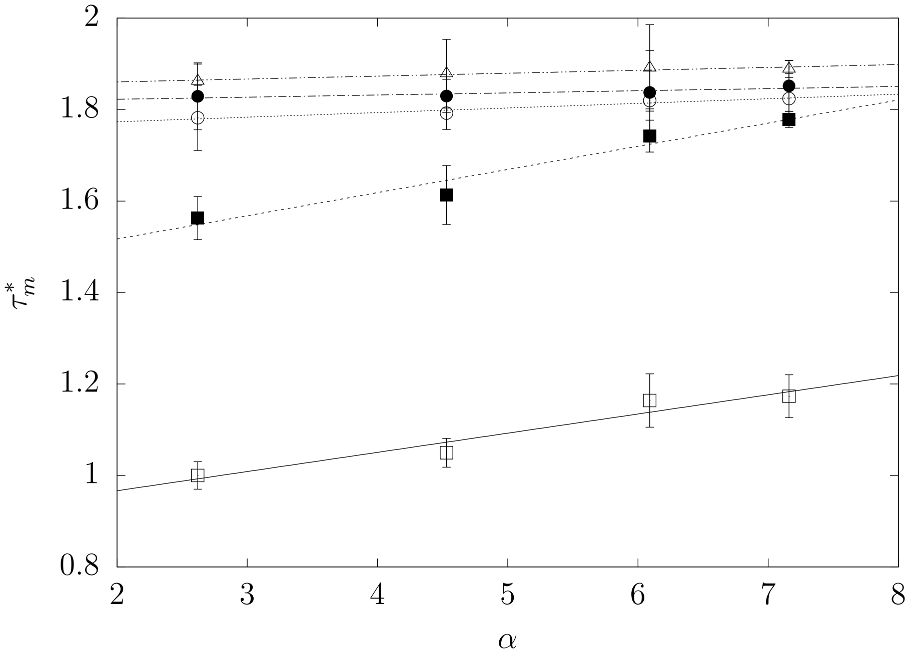

Figure 60 – Magnetorheological suspension of magnetite: dimensionless mean time of relaxation τ^* as a function of the magnetic parameter α. The data points correspond to different values of magnetic particle volume fraction: (□) - 0.2%, (■) - 0.4%, (○) - 0.6%, (●) - 0.8% and (△) - 1%. The curves are fits of the experimental data to the following equation: $\tau_m^* = c_0 + c_1\alpha$. The parameters are: (—): $c_0 = 8.82 \times 10^{-1} \pm 4.08 \times 10^{-2}$ and $c_1 = 4.20 \times 10^{-2} \pm 7.59 \times 10^{-3}$; (- - -): $c_0 = 1.42 \times 10^{0} \pm 4.37 \times 10^{-2}$ and $c_1 = 5.10 \times 10^{-2} \pm 8.13 \times 10^{-3}$; (······): $c_0 = 1.75 \times 10^{0} \pm 9.68 \times 10^{-3}$ and $c_1 = 1.00 \times 10^{-2} \pm 1.80 \times 10^{-3}$; (-·-·): $c_0 = 1.81 \times 10^{1} \pm 9.85 \times 10^{-3}$ and $c_1 = 4.68 \times 10^{-3} \pm 1.83 \times 10^{-3}$ and (-···-): $c_0 = 1.85 \times 10^{1} \pm 7.98 \times 10^{-3}$ and $c_1 = 6.32 \times 10^{-2} \pm 1.48 \times 10^{-3}$.

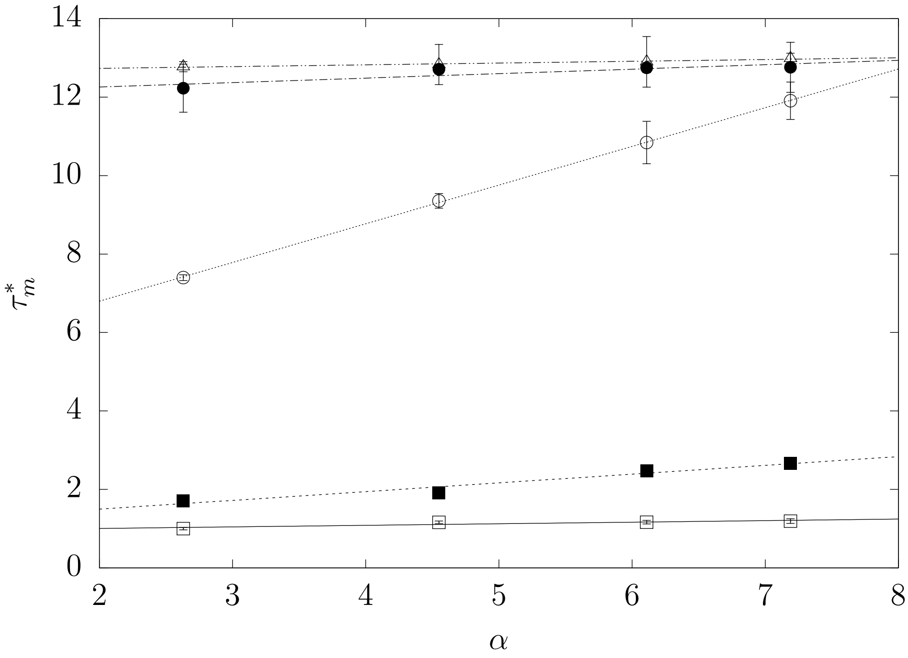

Figure 61 – Magnetorheological suspension of iron: dimensionless time of relaxation τ^* as a function of the magnetic parameter α. The data points correspond to different values of magnetic particle volume fraction: (□) - 0.2%, (■) - 0.4%, (○) - 0.6%, (●) - 0.8% and (△) - 1%. The curves are fits of the experimental data to the following equation: $\tau_m^* = c_0 + c_1\alpha$. The parameters are: (—): $c_0 = 9.25 \times 10^{-1} \pm 7.10, \times 10^{-2}$ and $c_1 = 3.99 \times 10^{-2} \pm 1.32 \times 10^{-2}$; (- - -): $c_0 = 1.05 \times 10^{0} \pm 2.01 \times 10^{-1}$ and $c_1 = 2.23 \times 10^{-1} \pm 3.73 \times 10^{-2}$; (······): $c_0 = 4.83 \times 10^{0} \pm 5.31 \times 10^{-2}$ and $c_1 = 9.86 \times 10^{-1} \pm 9.84 \times 10^{-3}$; (-·-·): $c_0 = 1.20 \times 10^{1} \pm 2.36 \times 10^{-1}$ and $c_1 = 1.14 \times 10^{-1} \pm 4.37 \times 10^{-2}$ and (-··-): $c_0 = 1.26 \times 10^{1} \pm 3.84 \times 10^{-1}$ and $c_1 = 4.50 \times 10^{-2} \pm 7.11 \times 10^{-3}$.

As it can be seen from figures (62) and (63), the dimensionless residual stress increases both as a function of the magnetic intensity parameter α and of the magnetic particles volume fraction ϕ. It is important to remark that the stress relaxation function of saturation $\Phi_r^*|_\alpha$ is related to the residual stress $\sigma_R|_\alpha$ by the following relation:

$$\sigma_R|_\alpha = \gamma_0 \Phi_r^*|_\alpha, \tag{4.24}$$

where, γ_0 is the angular strain. Therefore, regarding the results displayed on figures (52) and (59), it can be said that a residual stress $\tilde{\sigma}_R$ is observed for both fluids at each constant intensity of magnetic field applied. According to Borin et al. (2014), this increase is related to the enhancement of the size and intensification of the stability of the magnetic field-induced aggregates as the intensity of the magnetic field rises. This effect is stronger on the MRS of iron than on the MRS of magnetite, owing to its bigger magnetization of saturation. Figures (62) and (63) show the dependence of the residual stress $\tilde{\sigma}_R^*$ as a function of the nondimensional magnetic field α. It was proposed a power-law relation to model such dependence, resulting on the following expression:

$$\tilde{\sigma}_R = c_0 \alpha^{c_1}, \tag{4.25}$$

where c_0 and c_1 are constants obtained from a non-linear regression of the experimental data to the model. The values obtained for these constants are shown on on the captions of figures (62) and (63). It is important to note that for each MRS, the volume fraction of magnetic particles play a very important role on the overall behavior of the suspensions. As it can be seen, an increase in ϕ elevates dramatically the viscosity of the suspension. As stated previously, an improvement in ϕ signifies a situation characterized by more availability of magnetic particles to form chains and agglomerates. As this microstructures cause more viscous dissipation locally, in a bulk analysis, they cause an elevation of the suspension viscosity.

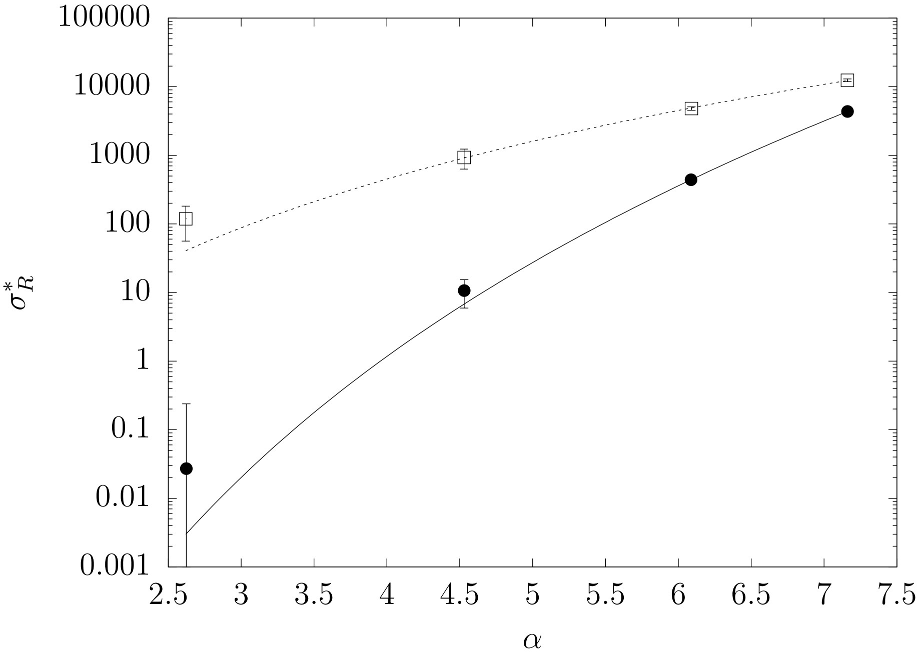

Figure 62 – Magnetorheological suspension of magnetite: dimensionless residual stress σ_R^* as a function of the magnetic parameter α. The data points correspond to different values of magnetic particle volume fraction: (●) - 0.2%, (□) - 1%. The curves are fits of the experimental data to the following equation: $\sigma_R^* = c_0\alpha^{c_1}$. The parameters are: (—): $c_0 = 3.69 \times 10^0 \pm 9.94 \times 10^{-2}$ and $c_1 = 1.41 \times 10^1 \pm 1.37 \times 10^{-2}$; (- - -): $c_0 = 1.70 \times 10^{-1} \pm 1.17 \times 10^{-2}$ and $c_1 = 5.68 \times 10^0 \pm 3.61 \times 10^{-1}$.

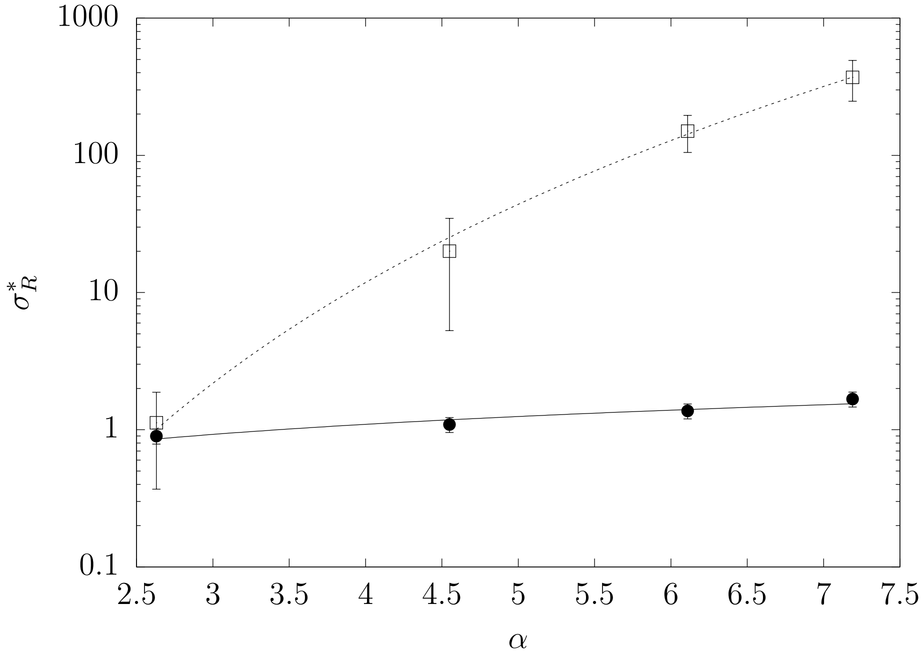

Figure 63 – Magnetorheological suspension of iron: dimensionless residual stress σ_R^* as a function of the magnetic parameter α. The data points correspond to different values of magnetic particle volume fraction: (●) - 0.2%, (□) - 1%. The curves are fits of the experimental data to the following equation: $\sigma_R^* = c_0\alpha^{c_1}$. The parameters are: (—): $c_0 = 4.85 \times 10^{-1} \pm 9.39 \times 10^{-2}$ and $c_1 = 5.87 \times 10^{-1} \pm 1.21 \times 10^{-1}$; (- - -): $c_0 = 6.72 \times 10^{-3} \pm 2.55 \times 10^{-3}$ and $c_1 = 5.53 \times 10^{0} \pm 2.44 \times 10^{-2}$.

5 RHEOLOGY OF AQUEOUS SUSPENSIONS OF MULTI-WALLED CARBON NANOTUBES

5.1 Multi-walled carbon nanotubes length characterization

The double-walled carbon nanotubes (DWCN) used in this work were characterized using an Olympus LEXT OLS4000 3D confocal laser microscope.[1] To begin, an aqueous suspension of DWCN, with a total volume of 50 mL, was prepared. The particle volume fraction of DWCN in this suspension was 1%. Five sets of glass slides, each containing a small portion of the suspension, were prepared for analysis under the microscope. The optical magnifications used to visualize the sample details were 5x, 10x, 20x, and 50x.

Using the microscope software, a total of 30 measurements were made across the five glass slides to determine the mean length of the nanotubes, $\ell = 36.88 \pm 15.43$ μm (arithmetic average). This result contrasts significantly with the manufacturer's claim that the mean length, based on arithmetic average evaluation, is around 6 μm, with a maximum length of approximately 30 μm (CASTRO et al., 2019). For the nanotube diameter a, the manufacturer's data was used: $a = 19$ nm. Notably, the measured aspect ratio $\left(\frac{\ell}{a}\right)_m$ is 1941.11, while the aspect ratio provided by the manufacturer $\left(\frac{\ell}{a}\right)_p$ is 316.79.

It is important to highlight that Batchelor (1970a) demonstrated that the effective viscosity of a suspension of rigid rods with high aspect ratios depends directly on ℓ^3. Batchelor's model, however, does not account for hydrodynamic interactions between the rods. A subsequent correction, which considers pairwise hydrodynamic interactions, was proposed by Shaqfeh and Fredrickson (1990), yet still predicts the same dependence on ℓ^3. Therefore, it is critical to use the measured value of ℓ, given its substantial impact on

---

[1] Equipment provided through a partnership with the Laboratory of Materials and Microscopy, part of the Group of Fatigue, Fracture, and Materials of the Department of Mechanical Engineering at the University of Brasília.

the calibration of rheological models and the interpretation of the results.

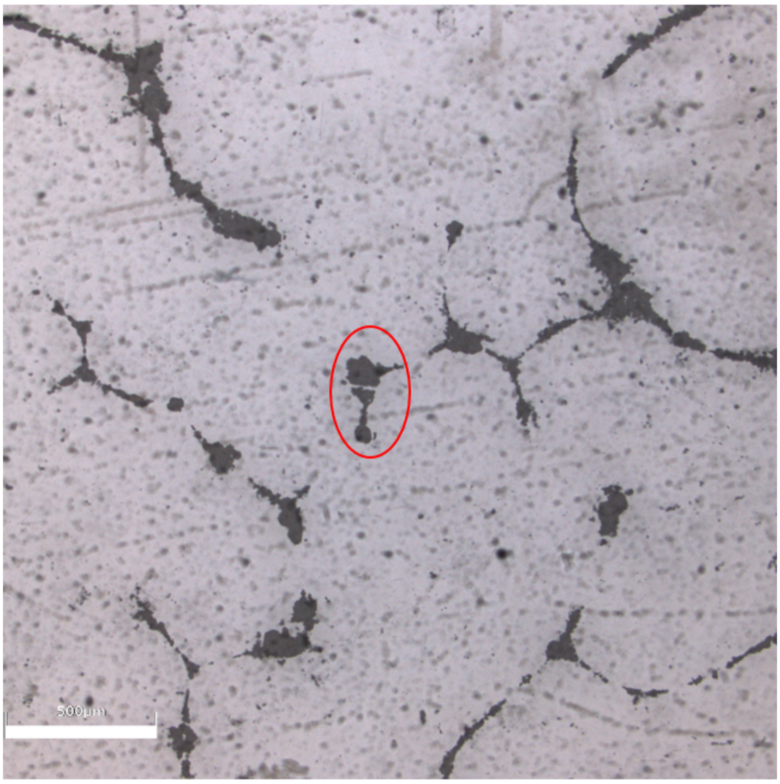

(a) Micrography of an aqueous suspension of DWCN (augmentation of 5x). The red ellipsis indicates a typical agglomerate of carbon nanotubes. Observe that the background scale is 500μm.

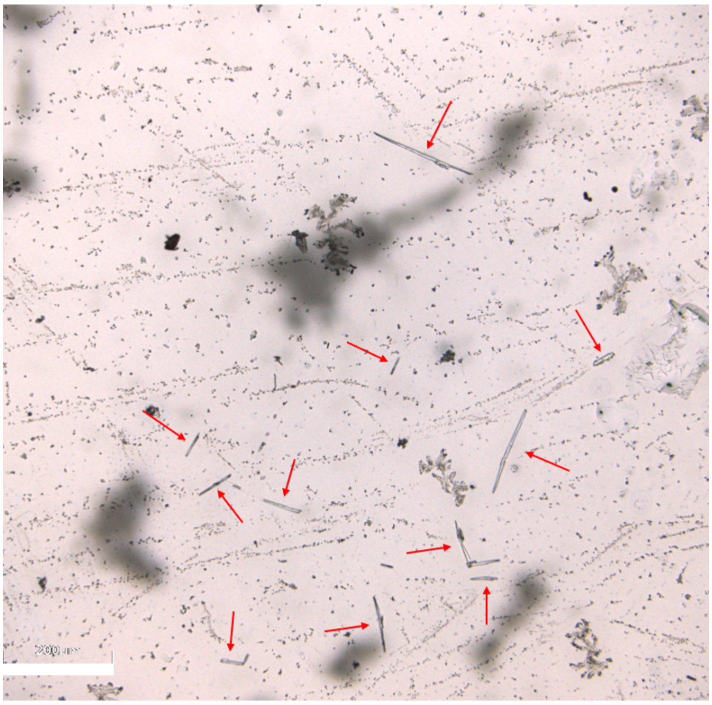

(b) Micrography of an aqueous suspension of DWCN (augmentation of 10x). The red arrows indicate the location of individual carbon nanotubes. Observe that the background scale is 200μm.

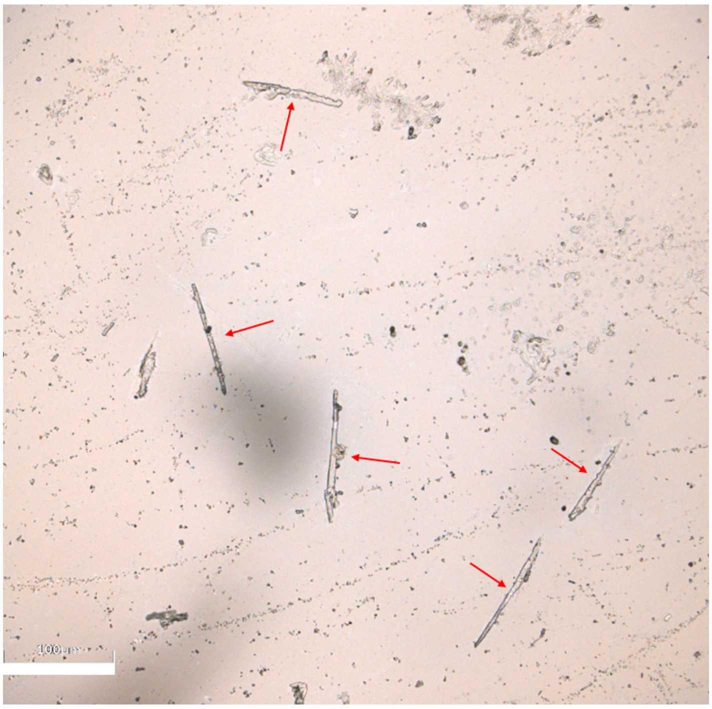

(c) Micrography of an aqueous suspension of DWCN (augmentation of 20x). The red arrows indicate the location of individual carbon nanotubes. Observe that the background scale is 100μm.

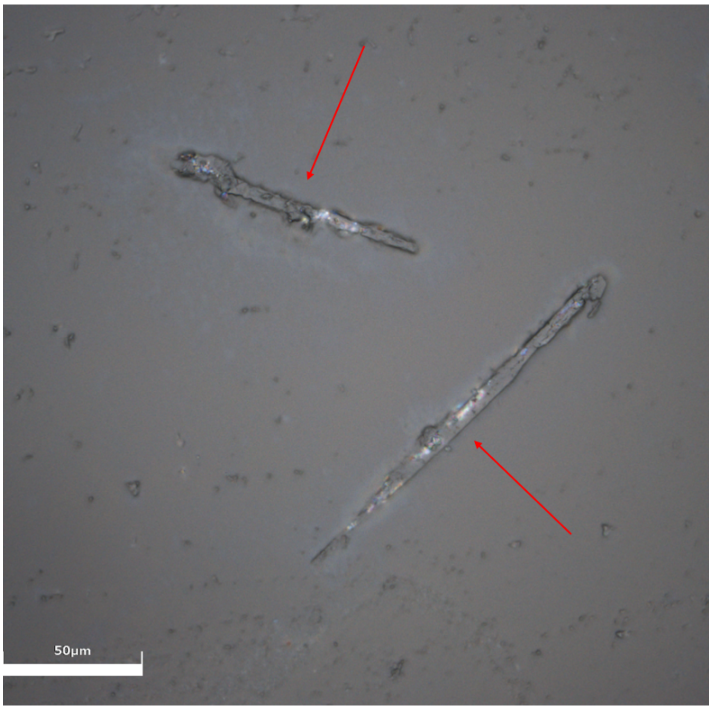

(d) Micrography of an aqueous suspension of DWCN (augmentation of 50x). The red arrows indicate the location of individual carbon nanotubes. Observe that the background scale is 50μm.

Figure 64 – Micrographies of an aqueous suspension of DWCN observed using different optical augmentations.

5.2 Rheology

5.2.1 Permanent shear analysis

In this analysis, our objective is to capture the pseudoplastic behavior of suspensions containing multi-walled carbon nanotubes (MWCN). To achieve this, we employed the standard assembly of the rheometer, utilizing the PP-50 measuring system. Initially, a test was conducted to determine the optimal gap for the experiments. The gap that resulted in the lowest variance was 0.4 mm, and it was subsequently chosen for all experiments.

The test procedure began by depositing the required amount of suspension to completely fill the gap. The sample was maintained at a constant temperature of 20°C. Following this, the Rheoplus software was programmed to apply an increasing shear rate, ranging from 0.1 s^{-1} to 100 s^{-1}. Each test was repeated five times to ensure reliability. The collected data were processed as described in Appendix (**??**).

5.2.1.1 Pseudoplastic effect

In this section, we examine the behavior of aqueous suspensions of multi-walled carbon nanotubes (MWCNs) under a steady simple shearing flow. Figure (65) clearly demonstrates that all analyzed suspensions exhibit shear-thinning behavior. The presence of a single slope in the power-law region for each suspension suggests that one primary physical phenomenon governs the reduction in viscosity as the Deborah number (De) increases.

This phenomenon arises from the random dispersion of nanotubes when no flow is applied. In this state, the tubes are oriented randomly, leading to a large collision area between the nanotubes and the flow, which results in significant localized energy dissipation and, consequently, high viscosity. However, as the flow intensifies, the nanotubes rotate and begin to align with the flow's streamlines, reducing their collisional area and thereby decreasing the viscosity.

Unlike magnetic responsive suspensions (MRS), where particle chains may be disrupted under shear, carbon nanotubes are well-known for their exceptional mechanical strength, especially when subjected to loads along their preferred orientation (CASTRO et al., 2019). Therefore, it is reasonable to predict that the applied shear flow is insufficient to break the nanotubes, meaning this phenomenon does not contribute to the viscosity reduction as De increases.

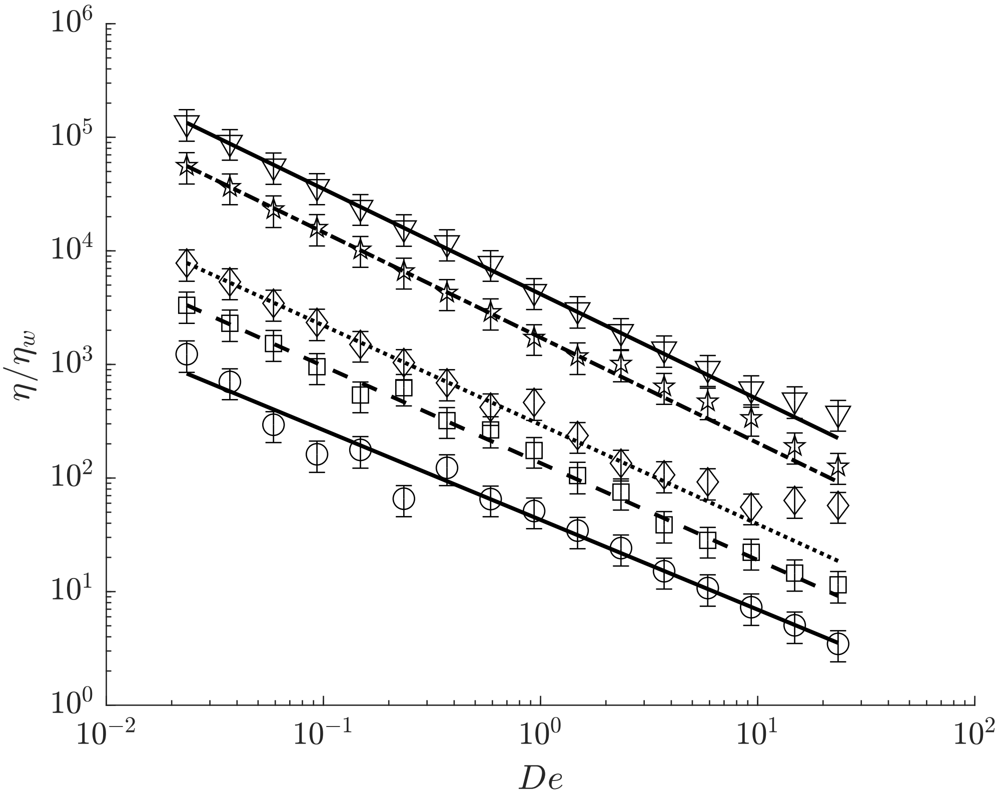

Figure 65 – Relative viscosity η/η_w as a function of De for suspensions of multi-walled carbon nanotubes. (○) - 0.4%, (□) - 0.5%, (◊) - 0.6%, (⋆) - 0.7% and (▽) - 0.8%. The curves are fits of the experimental data to the following expression: $\eta/\eta_w = KDe^{n-1}$. The fitting parameters are shown in table.

ϕ	K	n
0.004	1.234	0.678
0.005	2.345	0.789
0.006	3.456	0.89
0.007	4.567	0.901
0.008	5.678	1.012

Table 11 – Power-law coefficients

Analyzing Figure (65), we observe that for a fixed Deborah number (De), the relative viscosity η/η_w increases as the particle volume fraction ϕ rises. This behavior is attributed to the greater availability of particles in the suspension as ϕ increases. As a result, the fluid encounters more particles, leading to stronger interactions between the flow and the dispersed particles. Consequently, higher particle volume fractions lead to higher viscosities. The increased energy dissipation due to viscosity stems from the process of rotating and aligning the nanotubes, which explains why the curves for suspensions with higher ϕ values lie above those for lower ϕ.

Two examples of this process are illustrated in Figures (66) and (67). At very low shear rates, close to equilibrium, figure (66) shows that the viscosity is exceptionally high for all suspensions, and this property is amplified as ϕ increases. It is important to observe that even for small values of ϕ, the dependence of the relative viscosity on the particle volume fraction is given by: $\eta_0/\eta_w = 1 + b_1\phi + \frac{b_1^2\phi^2}{2}$, which implies that in the condition of weak-flows at least par-wise interactions occur between the nanotubes. Above $\phi = 0.003$, the relative viscosity increase in an exponential fashion. This occurs because, in such conditions, nanotube aggregates are present in the suspension (see Figure (64a)), creating a substantial collisional area, which significantly impacts the bulk viscosity.

As the shear rate increases, however, the microstructure of the aggregates is broken down, and the influence of individual nanotubes becomes more prominent. This reduction in collisional area results in a general decrease in viscosity as shown in figure (67). We can clearly see in this plot that the relative viscosity depend on ϕ linearly for $\phi \leq 0.002$. This implicates that, in this specific region, there are no hydrodynamic interactions between the nanotubes and the increment on the bulk viscosity is only a consequence of the average stresslet generated by the tubes (rods) individually. Above $\phi = 0.002$ the relative viscosity starts to depend very non-linearly on ϕ, indicating that the interactions between the tubes in suspension get much more complex.

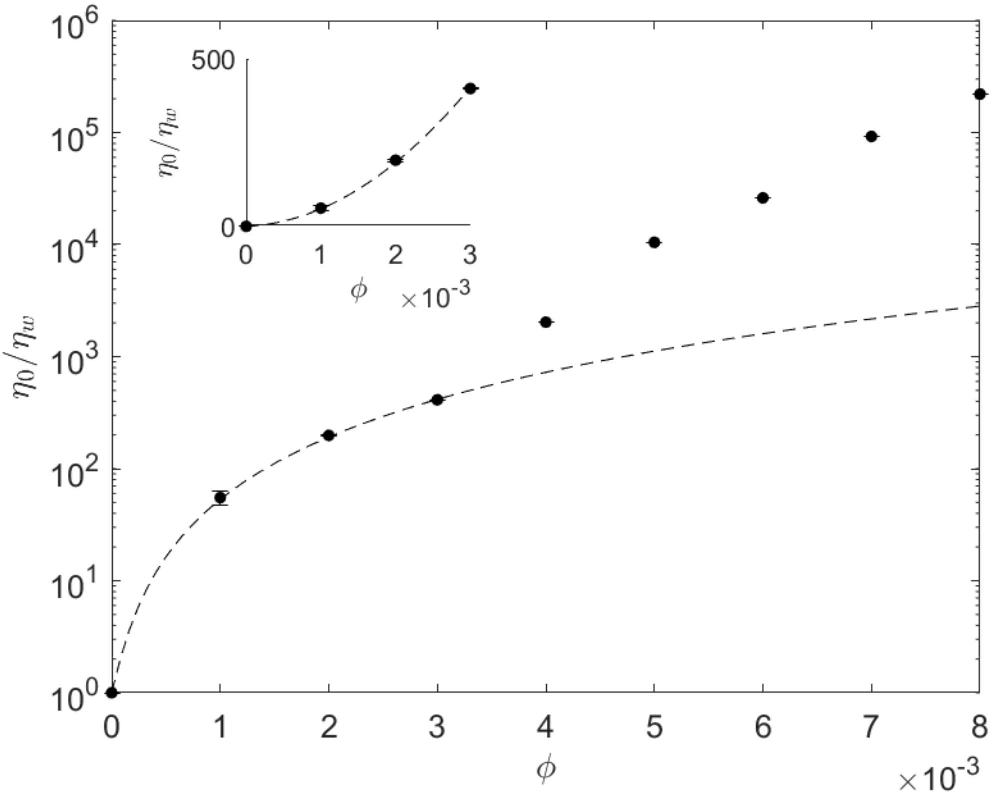

Figure 66 – Apparent viscosity evaluated in the vicinity of equilibrium η_0/η_w as a function of the volumetric fraction ϕ of multi-walled carbon nanotubes (MWCN). The curve is a fit of the first four experimental points to the following equation: $\eta_0/\eta_w = 1 + b_1\phi + \frac{b_1^2\phi^2}{2}$. The fitting parameter is: $b_1 = 9.26 \times 10^3$.

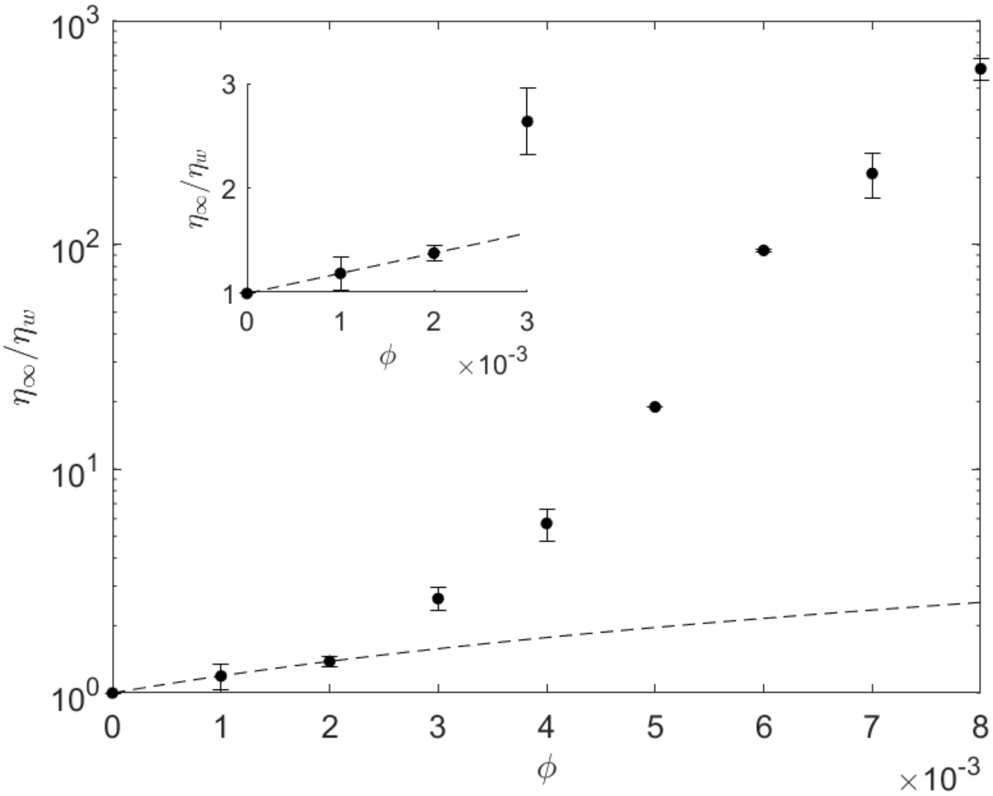

Figure 67 – Apparent viscosity evaluated evaluated at the strongest flow applied η_∞/η_w as a function of the volumetric fraction ϕ of multi-walled carbon nanotubes (MWCN). The curve is a fit of the first four experimental points to the following equation: $\eta_\infty/\eta_w = 1 + b_1\phi$. The fitting parameter is: $b_1 = 1.92 \times 10^2$.

As nanotubes are naturally anisotropic, it can be calculated the modification that the presence of the tubes add to the stress tensor of the suspension σ^f, that is: $\boldsymbol{\Sigma} = -p\boldsymbol{I} + 2\mu\boldsymbol{D} + \boldsymbol{\sigma}^f$. Batchelor (1970a), using slender body theory, calculates for fibers of lenght "2ℓ" and diameter "a" the following tensor for a highly diluted and statistically homogeneous dispersed suspension:

$$\boldsymbol{\sigma}^f = \frac{4\pi\eta n l^3}{3\ln(2\ell/a)} \left(\hat{\boldsymbol{p}} \cdot \boldsymbol{D} \cdot \hat{\boldsymbol{p}}\right) \hat{\boldsymbol{p}}\hat{\boldsymbol{p}}, \tag{5.1}$$

where n is the density number, $\boldsymbol{p}$ is the director vector in the direction of the fibers and $\boldsymbol{D}$ is the strain rate tensor. Observe that $n = \phi/v_p$, where v_p is the volume of the particle, given by $v_p = \pi a^2\ell$. Thus:

$$\boldsymbol{\sigma}^f = \frac{4\pi\eta\phi l^3}{3v_p\ln(2\ell/a)} \left(\hat{\boldsymbol{p}} \cdot \boldsymbol{D} \cdot \hat{\boldsymbol{p}}\right) \hat{\boldsymbol{p}}\hat{\boldsymbol{p}} = \tag{5.2}$$

$$\boldsymbol{\sigma}^f = \frac{2}{3}\left(\frac{\ell}{a}\right)^2 \frac{\eta\phi}{\ln(2\ell/a)} \left(\hat{\boldsymbol{p}} \cdot \boldsymbol{D} \cdot \hat{\boldsymbol{p}}\right) \hat{\boldsymbol{p}}\hat{\boldsymbol{p}} = \tag{5.3}$$

$$\boldsymbol{\sigma}^f = \eta_e \left(\hat{\boldsymbol{p}} \cdot \boldsymbol{D} \cdot \hat{\boldsymbol{p}}\right) \hat{\boldsymbol{p}}\hat{\boldsymbol{p}}. \tag{5.4}$$

Observe that equation (5.1) tells us that the extensional viscosity η_e depends on nl^3. In this sense, one can argument that considering an homogeneous equivalent fluid, the tubes generate an extra stress (stresslet) comparable to a suspension formed by boundary spheres with radius ℓ.

It is important to remark that the calculation we are using, based on (BATCHELOR, 1970a), refers to the magnitude of the extensional viscosity η_e, which is, in fact, an anisotropic fourth-order quantity. The anisotropic formulation implies that viscosity depends not only on intensity but also on the flow direction and particle orientation, requiring the use of fourth-order tensors to properly describe the material's behavior.

As we have information on ℓ/a from the manufactures and from our measurements, we ploted in Figure (68) the nondimensional extensional viscosity as a function of $\phi(\ell/a)^2$, which is the same as $n\ell^3$. One can easily see that the extensional viscosity based on the values collected by our measurements is much higher then based in the manufacturer's information on ℓ/a. This implies that the real suspensions are able to generate a much more intense stress along the streamlines of the flow. This can be very beneficial in situations like drag reduction, since less material (nanotubes) are needed.

It can be seen from Table (12) that for $\phi \leq 0.005$, the nondimensional extensional viscosity is higher than the nondimensional shear viscosity, but this trend reverses for $\phi > 0.005$. This implies that the particle volume fraction of DWCN has a more pronounced effect on shear viscosity than on extensional viscosity.

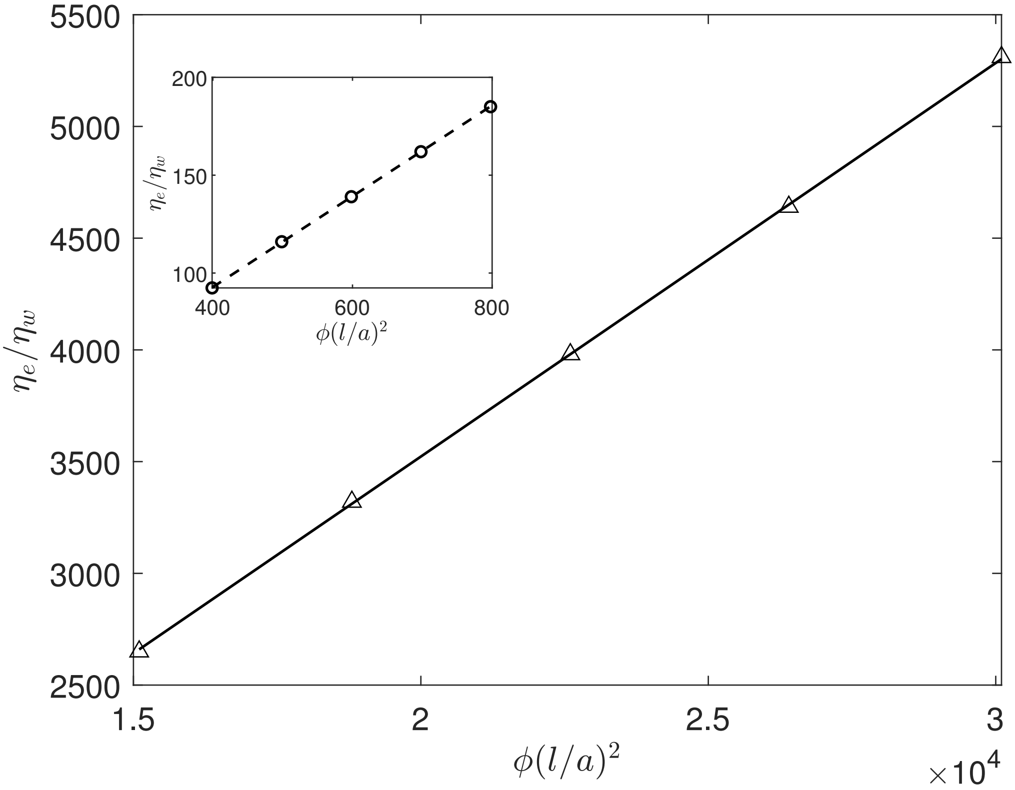

Figure 68 – Non-dimensional extensional viscosity η_e/η_w as a function of $\phi(l/a)^2$ for the multi-walled carbon nanotubes (MWCN) suspensions. ($\triangle$) - Measured $\ell/a = 1.94 \times 10^3$, ($\circ$) - manufacturer $\ell/a = 3.16 \times 10^2$ (CASTRO et al., 2019). The curves are lines given by $\eta_e/\eta_w = \dfrac{2}{3\ln(2\ell/a)}\phi\left(\dfrac{\ell}{a}\right)^2 = c\phi\left(\dfrac{\ell}{a}\right)^2$. Following the manufactor information, $c = 1.16 \times 10^{-1}$ and based on our measurementes, $c = 8.81 \times 10^{-2}$.

ϕ	$\phi \cdot (\ell/a)^2 = n\ell^3$	η_0/η_w	η_e/η_w
0.004	1.51×10^4	1.23×10^3	2.65×10^3
0.005	1.88×10^4	3.22×10^3	3.32×10^3
0.006	2.26×10^4	1.61×10^4	3.98×10^3
0.007	2.64×10^4	5.60×10^4	4.64×10^3
0.008	3.01×10^4	1.34×10^5	5.31×10^3

Table 12 – Nondimensional shear viscosity and nondimensional extensional viscosity as funcrions of ϕ.

5.2.2 Transient shear analysis

5.2.3 Step-strain

5.2.3.1 Experimental procedure

To obtain the stress relaxation function $\Phi(s)$ of a given complex fluid, a step-strain experiment is performed. Determining this material function is crucial, as it allows the relaxation spectrum of the suspension to be evaluated. According to (BIRD; ARMSTRONG; HASSAGER, 1987), this spectrum is associated with the physical mechanisms governing stress relaxation.

The experimental protocol involves the following steps:

1. The volume of the MWCN suspension required to fill the 0.4 mm gap is calculated. This volume is then pipetted and deposited in the testing area;
2. The upper disk is lowered until the precise gap between the disks is achieved. Any fluid leakage from the gap is carefully trimmed and cleaned;
3. The experiment temperature is set to 25°C using the Peltier system integrated into the lower plate of the rheometer. Adequate time is allowed for the sample temperature—defined as the temperature of the lower plate, measured by the rheometer—to stabilize at the target value;
4. A step-strain with a fixed angular strain, γ_0, is applied to the sample. The angular strain, applied instantaneously to the fluid, must be as small as possible to ensure the linear viscoelastic regime. However, reducing γ_0 excessively can lead to applied torques below the rheometer's minimum measurable threshold, compromising data reliability. To balance these factors, γ_0 was set to 0.1 for all MWCN suspensions with volume fractions (ϕ) of 0.4%, 0.5%, 0.6%, 0.7%, 0.8%, and 1%;
5. Data for the stress relaxation function is recorded as a function of time, with measurements taken every 0.01 s.

The experimental errors were calculated following the methodology outlined in Appendix (**??**).

5.2.3.2 Discussion

In this section, we discuss the results concerning the relaxation of shear stress following the sudden application of a small strain, which falls within the linear regime. All suspensions exhibited elastic behavior, as clearly shown in Figures (69), (70), (71), and (72), which present the nondimensional stress relaxation function Φ^* as a function of the time shift s^*. These figures demonstrate that the shear stress does not relax instantaneously. Moreover, the stress relaxes to a plateau where the shear stress remains non-zero, further highlighting the elastic nature of the suspensions.

The elastic properties arise from the microstructure, which in this case consists of agglomerates of multi-walled carbon nanotubes. The fact that the stress does not fully vanish over long times suggests the presence of a residual structure that requires a minimum stress to initiate flow. In light of these observations, the modified Maxwell viscoelastic model can be applied to fit the experimental data. As discussed in Section

(4.4.1), the relationship between the nondimensional time shift and the nondimensional stress relaxation function is given by:

$$\Phi^*(s^*) = \sum_j^N \frac{\eta^*}{\tau^*} \exp\left(-s^*/\tau^*\right) + \Phi_R^* = \sum_j^N A_j \exp\left(-s^*/\tau^*\right) + \Phi_R^*, \tag{5.5}$$

where A_j is j-th amplitude of stress and τ_j^* the j-th nondimensional time of relaxation of the suspension.

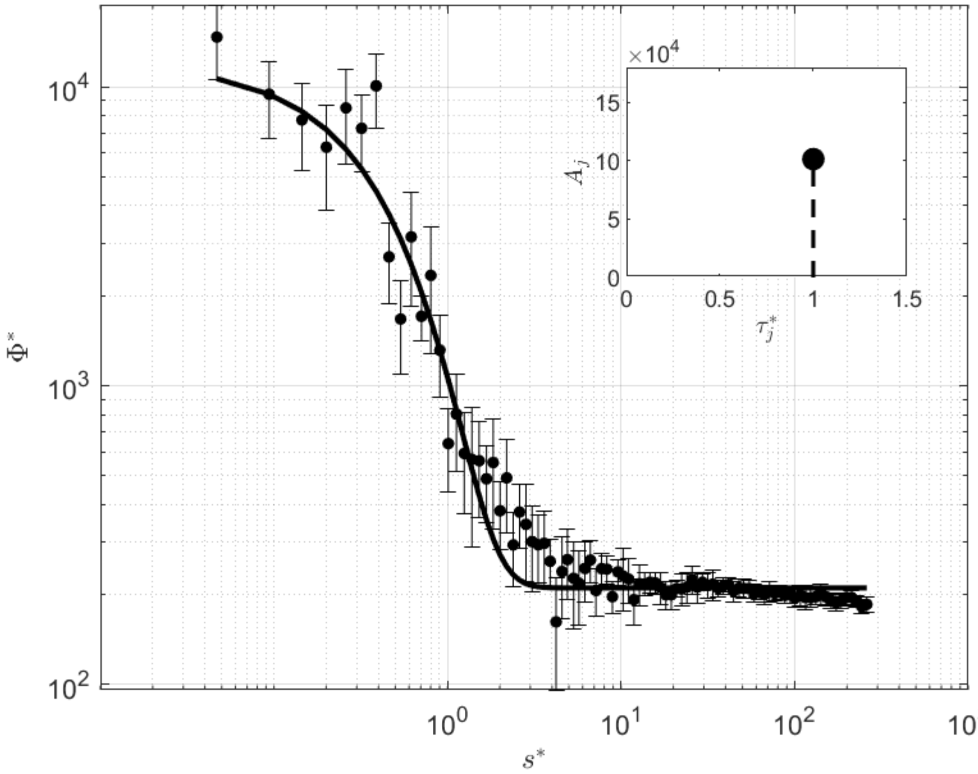

Figure 69 – Stress relaxation function for the suspension of MWCN with $\phi = 0.002$. In the insert is shown the amplitude of stress A_j as a function of the time of relaxation τ_j^*. The curve is a fit of the experimental data to the modified Maxwell's viscoelastic model given by equation (5.5). The adjustment parameters are shown at table (13).

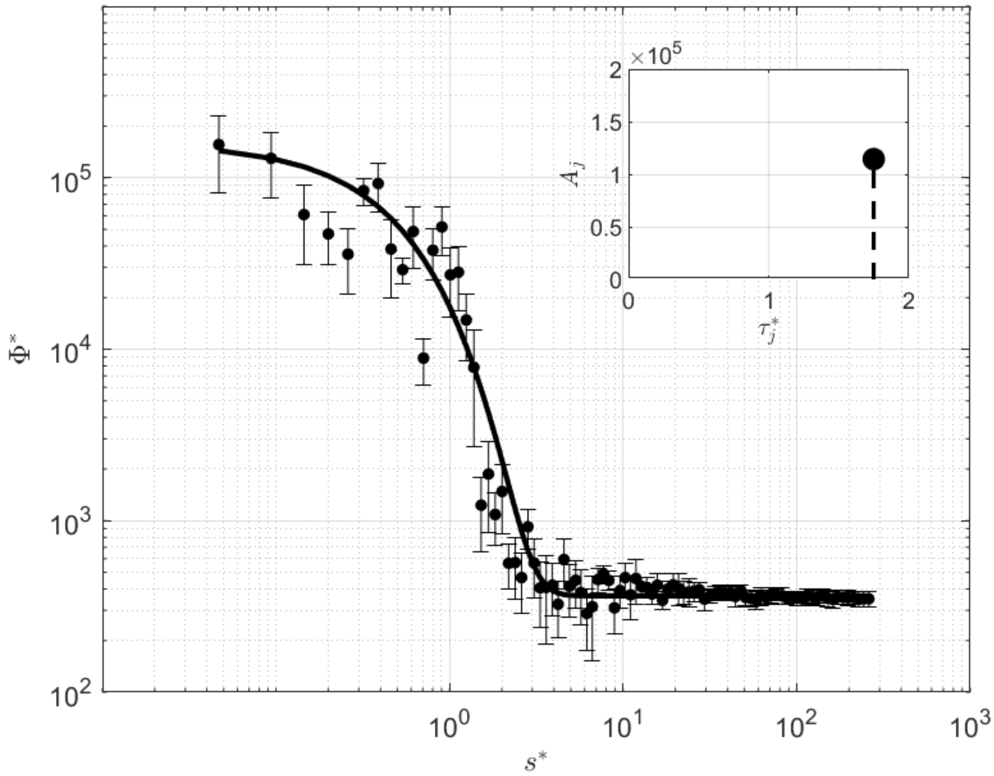

Figure 70 – Stress relaxation function for the suspension of MWCN with $\phi = 0.004$. In the insert is shown the amplitude of stress A_j as a function of the time of relaxation τ_j^*. The curve is a fit of the experimental data to the modified Maxwell's viscoelastic model given by equation (5.5). The adjustment parameters are shown at table (13).

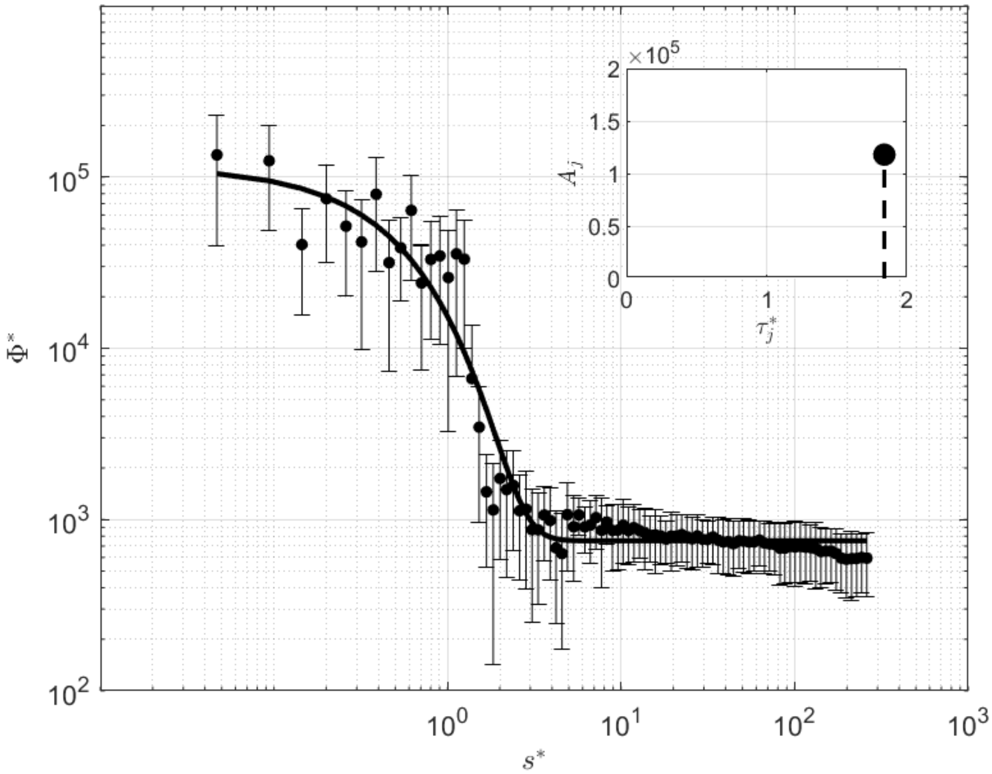

Figure 71 – Stress relaxation function for the suspension of MWCN with $\phi = 0.006$. In the insert is shown the amplitude of stress A_j as a function of the time of relaxation τ_j^*. The curve is a fit of the experimental data to the modified Maxwell's viscoelastic model given by equation (5.5). The adjustment parameters are shown at table (13).

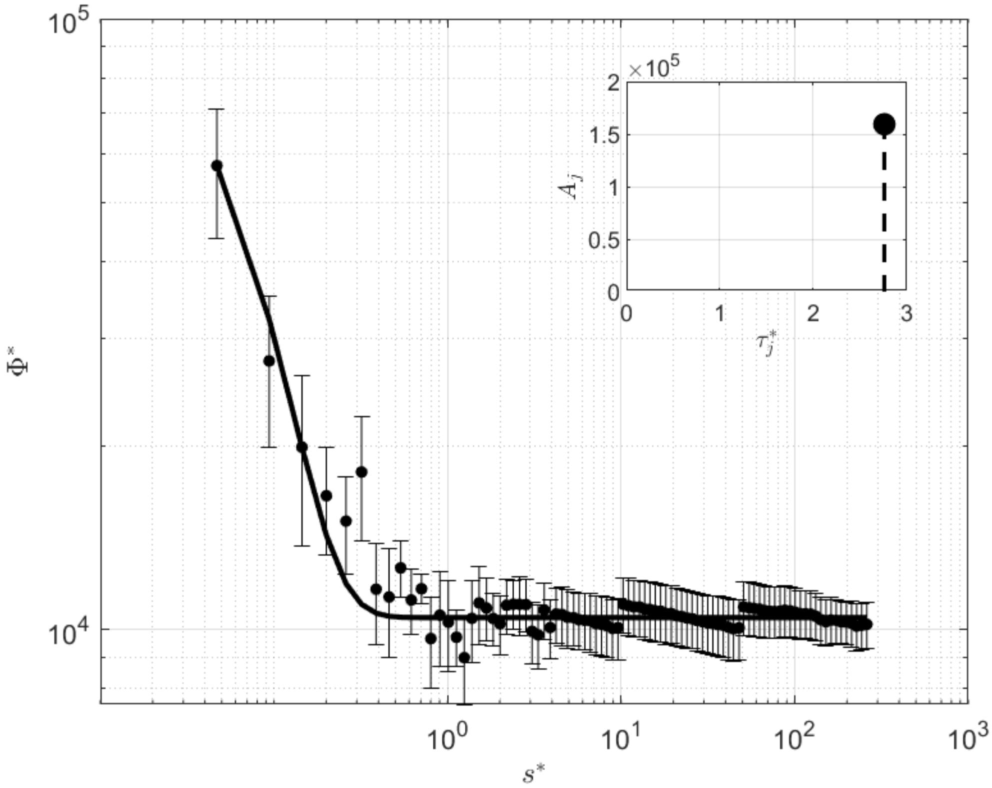

Figure 72 – Stress relaxation function for the suspension of MWCN with $\phi = 0.008$. In the insert is shown the amplitude of stress A_j as a function of the time of relaxation τ_j^*. The curve is a fit of the experimental data to the modified Maxwell's viscoelastic model given by equation (5.5). The adjustment parameters are shown at table (13).

Table (13) presents the fitting parameters concerning the experimental data of each MWCN suspension. It can be observed that only one term of the modified Maxwell model was necessary to fit the nondimensional stress relaxation functions. Additionally, it is evident that the relaxation times τ_1^* increased as the particle volume fraction ϕ rose. From Figure (73), we can see that the dependence of τ_1^* on ϕ is linear within the investigated range of ϕ. The increase in τ_1^* with higher ϕ indicates that adding more nanotubes injects more memory into the dynamic system of the suspension, causing a retardation in stress relaxation that is directly linked to elastic effects.

Table 13 – Parameters of the fits of experimental data to the modified Maxwell's viscoelastic model. The minimum principal relaxation time is $\tau_1 = 2.34 \times 10^{-1}$ s. Each parameter is defined as follows: ϕ - particle volume fraction; $A_1 = \eta_j^*/\tau_j^*$ - amplitude; $\tau_1^* = \tau_j^*/\tau_1^*$ - nondimensional relaxation time; Φ_R^* - nondimensional residual stress relaxation parameter.

ϕ	A_1	τ_1^*	Φ_R^*
0.002	1.01×10^5	1.00	211
0.004	1.14×10^5	1.75	365
0.006	1.18×10^5	1.85	752
0.008	1.60×10^5	2.76	10500

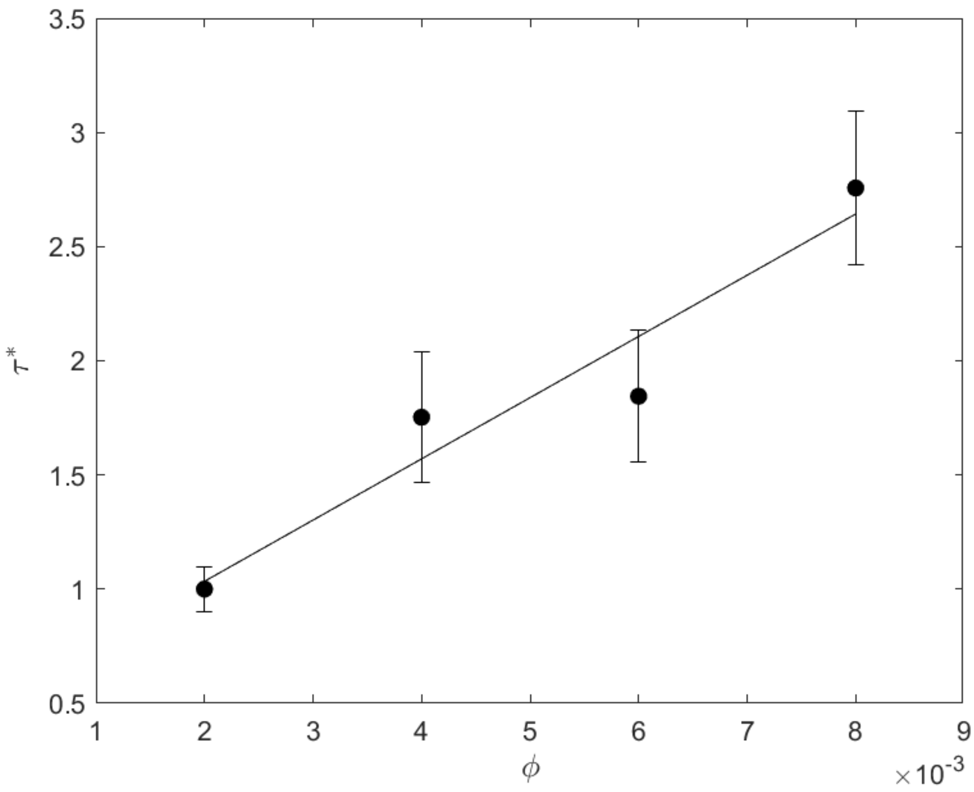

Figure 73 – Nondimensional times of relaxation τ^* as functions of the particle volume frtaction ϕ with errorbars. The fit is an adjustment of the experimental data to a linear equation: $\tau^* = a\phi + b$. The fitting parameters are: $a = 268.09 \pm 23.61$ and $b = 0.45 \pm 0.22$.

Table (13) presents the nondimensional residual stress relaxation parameter Φ_R^*. Based on the definition of the stress relaxation function, it is possible to determine the nondimensional residual stress σ_R^* using the following relation:

$$\sigma_R^* = \gamma_0 \Phi_R^*. \tag{5.6}$$

The values of σ_R^* calculated for each particle volume fraction ϕ are shown in Table (14). It can be observed that σ_R^* depends directly on ϕ, as illustrated in Figure (74). Notably, the first four data points in the plot shown in Figure (74) are well-fitted by a second-order polynomial in relation to ϕ. However, as ϕ increases, σ_R^* exhibits a sudden spike. This trend can be understood by the increasingly complex microstructure of the nanotubes agglomerates as ϕ rises. Such complexity leads to greater coherence in the suspension, requiring a higher minimum stress tension to initiate flow. It is important to note that σ_R^* provides an indication of the yield stress of complex fluids. However, these values are not necessarily equivalent in all cases, as the rheological parameters of a complex fluid depend on the type of flow applied. Therefore, since yield stress is measured in permanent shear tests, it can differ from σ_R^*, which is evaluated in a step-strain experiment.

Table 14 – Nondimensional residual stress σ_R^* for the MWCN suspensions.

ϕ	σ_R^*
0	0
0.002	6.32×10^1
0.004	1.09×10^2
0.006	2.26×10^2
0.008	3.14×10^3

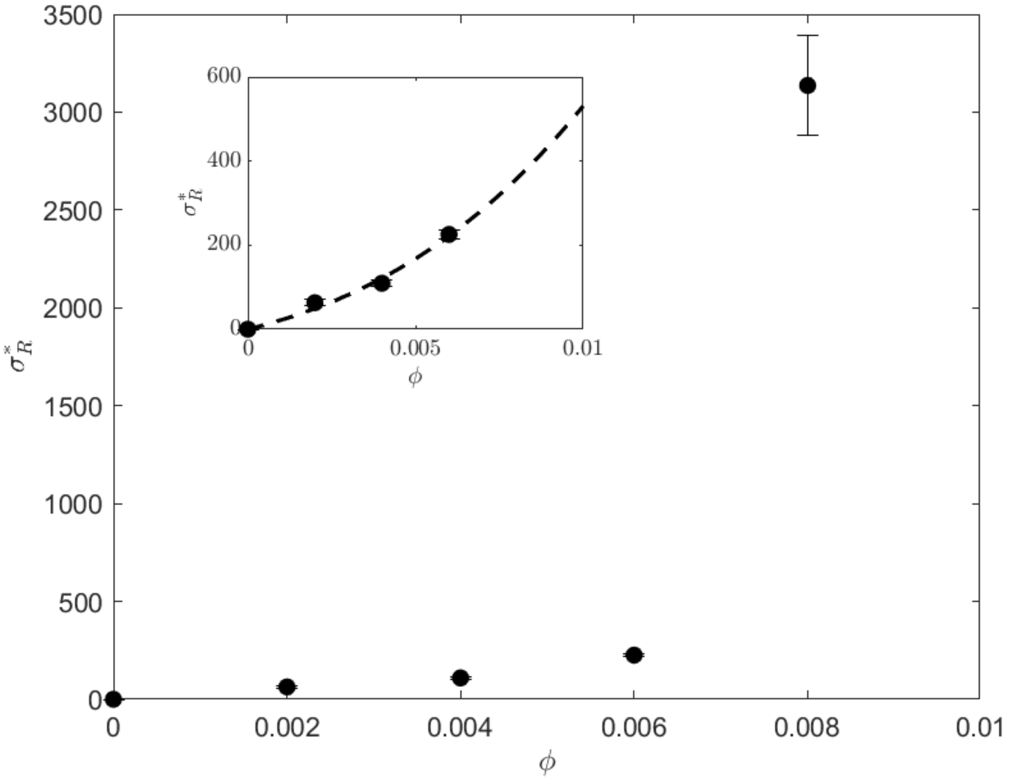

Figure 74 – Nondimensional residual stress σ_R^* as a function of the particle volume fraction ϕ of MWCN. In the insert, it is presented a zoom of the first four points, with a third order virial curve adujsted to them: $\sigma_R^* = c\phi(1 + b\phi + b\phi^2/2)$. The fitting parameters are: $c = 1.98 \times 10^4$ and $b = 1.02 \times 10^2$.

5.2.4 Oscillatory shear

5.2.4.1 Procedure

First, the temperature at which the experiment will be conducted must be set. In this study, the tests were performed at 20°C. Additionally, the optimal gap between the rheometer plates must be determined. Once the gap is set, the sample is pipetted into the rheometer, and sufficient time is allowed for it to reach thermal equilibrium at the experimental temperature.

Following this preliminary stage, the angular strain, γ, must be determined to ensure the test remains in the linear viscoelastic regime. This is done by fixing the highest frequency intended for the test and performing a strain sweep, varying the strain from 0.01% to 1%. The goal is to identify the region where the elastic modulus, G', remains invariant with respect to angular strain. In this region, a specific angular strain value is chosen for the frequency sweep experiments.

In the next stage, the previously determined angular strain is fixed, and the frequency is varied logarithmically, from a small frequency to the maximum frequency that ensures the system remains linear. The Rheoplus software collects data on viscometric properties, $\eta'(\omega)$, $\eta''(\omega)$, $G'(\omega)$, and $G''(\omega)$, for each frequency. Five experimental runs are performed for each sample during this stage.

5.2.4.2 Discussion

Experiments in small amplitude oscillatory shear (SAOS) are indeed crucial for understanding the viscoelastic behavior of complex fluids. The key aspect of SAOS is that the strain amplitude γ_0 is kept small enough to ensure that the material response remains within the linear viscoelastic regime. In this regime, the stress oscillates with the same frequency as the applied strain but can exhibit a phase lag due to the viscoelastic nature of the fluid.

The in-phase component of the stress corresponds to the storage modulus G', which represents the elastic or energy-storing behavior. The out-of-phase component corresponds to the loss modulus G'', reflecting the viscous or energy-dissipating behavior. These viscoelastic functions—G' and G''—are essential for characterizing the material's response.

To ensure that the SAOS experiment is conducted within the linear regime, it is necessary to establish a range of strain amplitudes γ_0 for which the storage modulus G' (and typically the loss modulus G'' as well) remains independent of γ_0. This independence implies that the material response is purely linear and unaffected by nonlinearities that may arise at higher strain amplitudes.

In your case, as shown in Figure (75), the nondimensional elastic modulus G'^{*} is observed to be constant within the strain amplitude range $10^{-4} \leq \gamma_0 \leq 3 \times 10^{-3}$, confirming that this range corresponds to the linear viscoelastic regime. This allows for reliable analysis of the viscoelastic properties within this strain range. A strain amplitude $\gamma_0 = 0.003$ is suitable for the frequency sweep experiments, particularly given that it falls within the linear viscoelastic range determined from the analysis of the MWCN suspension at $\phi = 0.008$. This ensures that the results reflect the intrinsic viscoelastic properties of the material without introducing nonlinear effects.

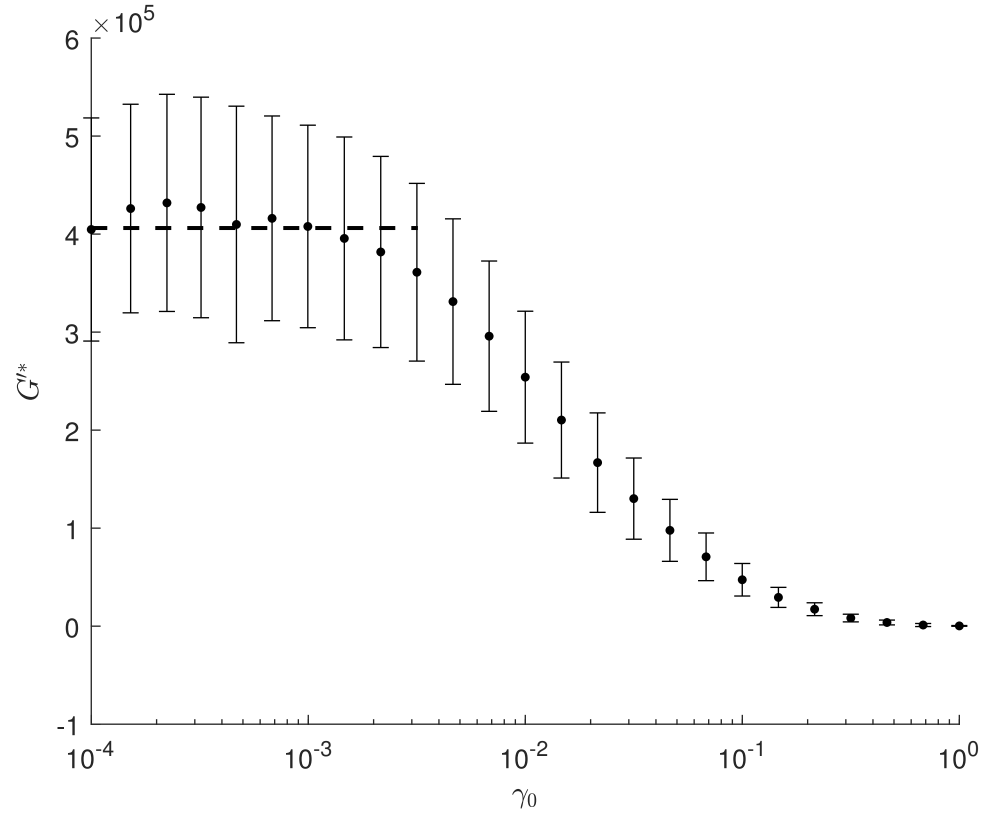

Figure 75 – Nondimensional elastic modulus G'^* as a function of the angular strain γ_0 for the MWCN suspension with $\phi = 0.008$. The linear dashed curve shows the region where G'^* is independent of γ_0. The fitting curve is $G'^* = b$, with $b = 4.06 \times 10^5$.

Figures (76), (77), (78), and (79) depict the dependence of the nondimensional elastic modulus and the nondimensional loss modulus on the Deborah number (De). It is evident across the entire range of De that the nondimensional elastic modulus consistently exceeds the loss modulus. This observation indicates that the microstructures formed by agglomerates of double-walled carbon nanotubes impart a significant memory effect to the suspension system, thereby enhancing its elastic behavior.

The dominance of the elastic modulus over the loss modulus suggests a predominantly elastic response, which may enhance the material's performance in applications that require structural integrity and resilience. The memory effect associated with these microstructures allows the material to store and recover energy, a vital characteristic for various applications, including advanced composites and biomedical devices.

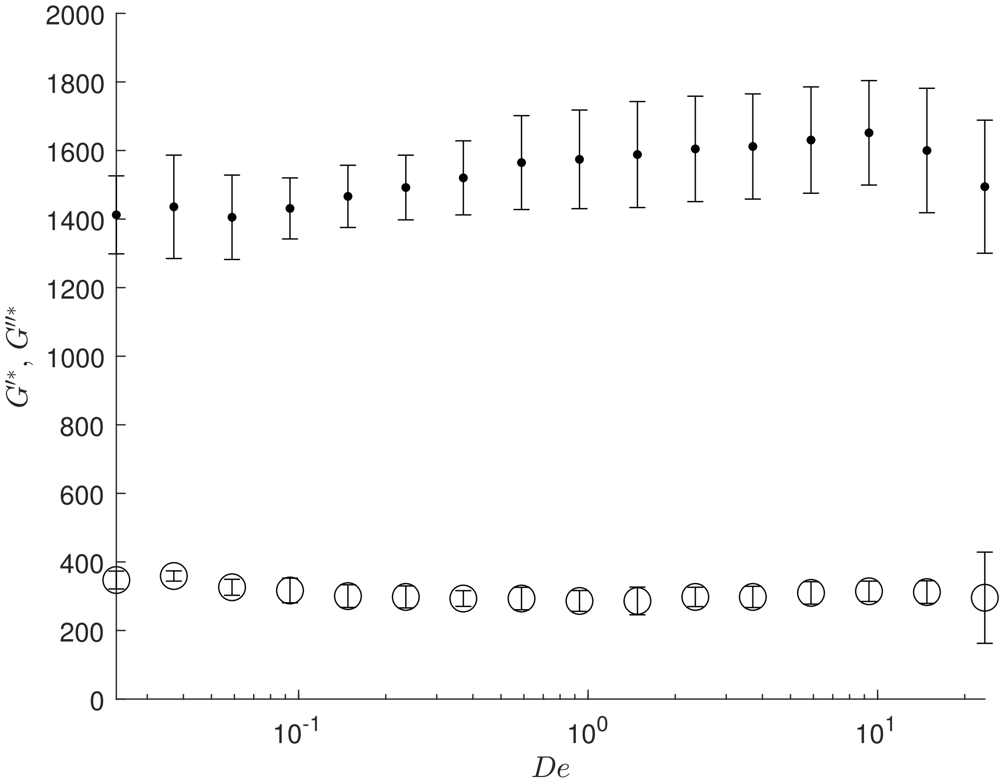

Figure 76 – (●) - Nondimensional elastic modulus and - (○) - nondimensional loss modulus as functions of Deborah number (De) for the MWCN suspension with $\phi = 0.004$, with errorbars.

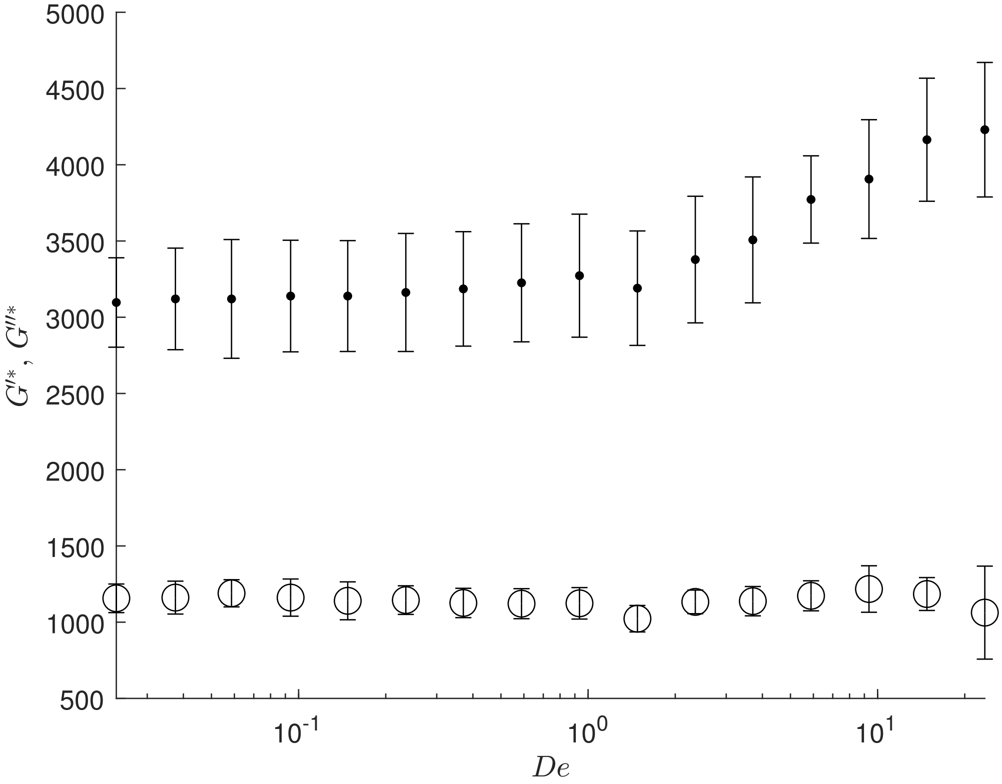

Figure 77 – (●) - Nondimensional elastic modulus and - (○) - nondimensional loss modulus as functions of Deborah number (De) for the MWCN suspension with $\phi = 0.004$, with errorbars.

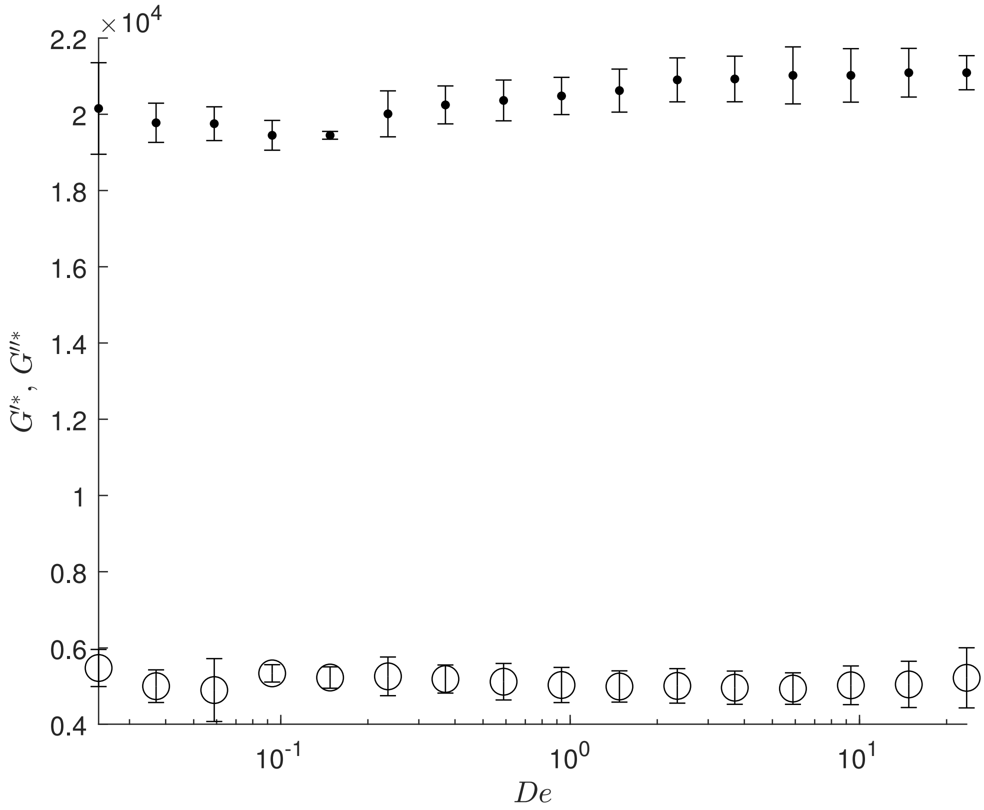

Figure 78 – (●) - Nondimensional elastic modulus and - (○) - nondimensional loss modulus as functions of Deborah number (De) for the MWCN suspension with $\phi = 0.006$, with errorbars.

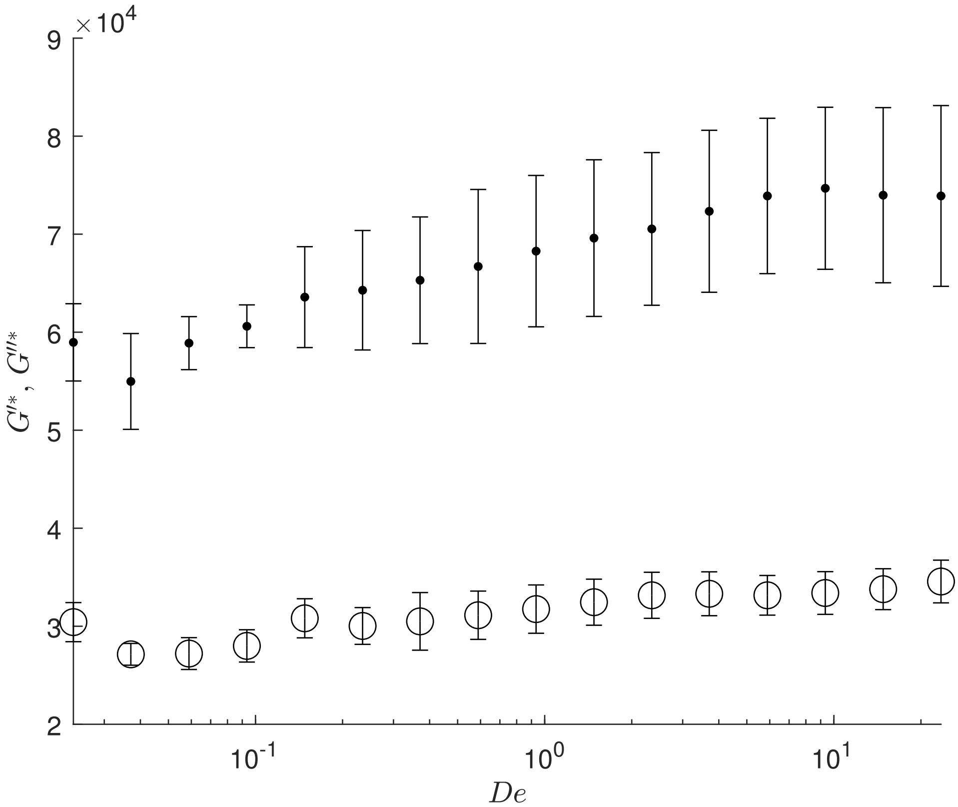

Figure 79 – (●) - Nondimensional elastic modulus and - (○) - nondimensional loss modulus as functions of Deborah number (De) for the MWCN suspension with $\phi = 0.008$, with errorbars.

The nondimensional shear elastic modulus G_0^*, representing the limit of the storage modulus $G'^*(De)$ as the Deborah number De approaches zero, underscores the distinctive behavior of the system due to the microstructure of double-walled carbon nanotubes (DWCN). In contrast to typical complex fluids, where the elastic modulus approaches zero as $De \to 0$, G_0^* retains a non-zero value. This indicates the elastic contribution from DWCN agglomerates that have already established a stable equilibrium.

In relation to Figures (76), (77), (78), and (79), we determined G_0^* by extrapolating as $De \to 0$, allowing us to derive the relationship between G_0^* and the volume fraction ϕ. As depicted in Figure (80), the relationship between G_0^* and ϕ is notably nonlinear. This nonlinearity further supports the assertion that the suspensions exhibit a well-coherent microstructure of MWCN at equilibrium.

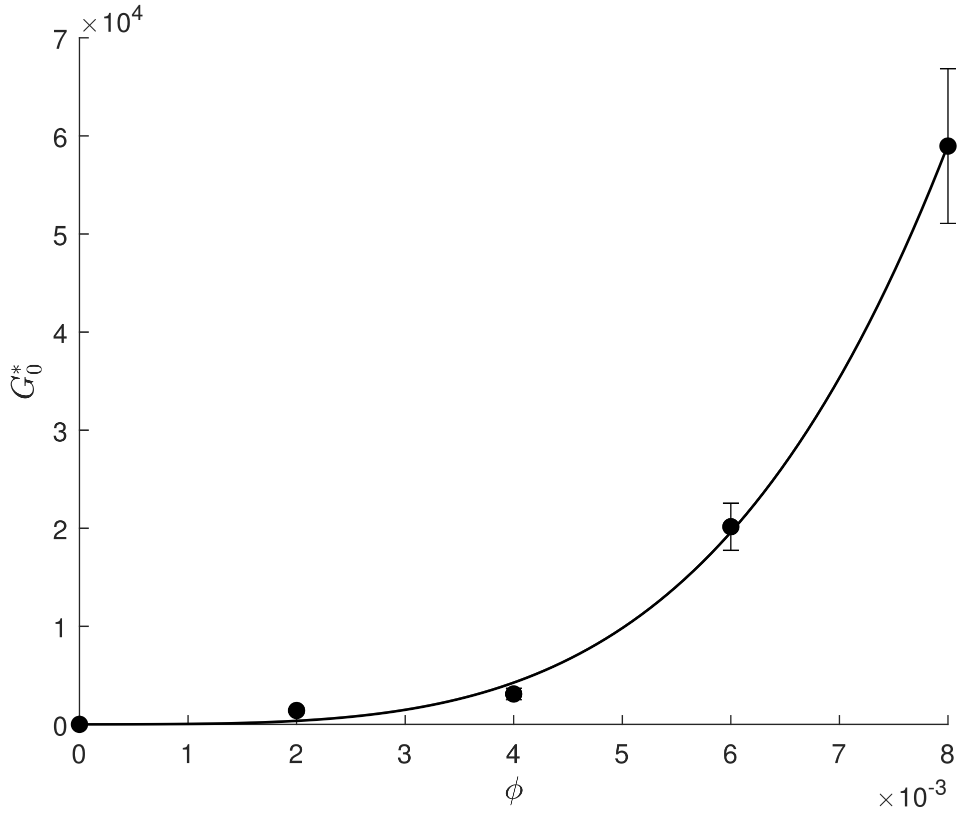

Figure 80 – The nondimensional shear elastic modulus, denoted as G_0^*, is presented as a function of the particle volume fraction of multi-walled carbon nanotubes (MWCN), complete with error bars. The experimental data points are well fitted to a fourth-order virial expansion. The fitting function for the virial expansion is given by $G_0^* = c\phi\left(1 + b\phi + \frac{b^2\phi^2}{2} + \frac{b^3\phi^3}{6}\right)$, with parameters $c = 3.51 \times 10^3$ and $b = 2.78 \times 10^3$.

The nondimensional viscosity η_0^*, which represents the equilibrium viscosity, is defined as the limit of the viscous modulus $\eta'^*(De)$ as the Deborah number De approaches zero:

$$\eta_0^* = \lim_{De \to 0} \eta'^*(De),$$

where $\eta'^*(De)$ is the viscous modulus. We can easily obtain η'^* from G''^* using the definition $\eta'^* = G''^*/De$. As shown in Figure (81), $\eta'^*(De)$ exhibits a strong dependence on the particle volume fraction ϕ. This relationship arises because higher ϕ values lead to the formation of more cohesive and complex microstructures, which increase local dissipation during flow. Larger microstructures not only contribute to increased resistance but also present larger collision areas, intensifying energy dissipation under shear flow. This process is so pronounced as ϕ increases that the relationship between η'^* and ϕ was found to be exponential. In the insert of Figure (81), we can see that even for the most diluted suspensions, the relationship between η_0^* and ϕ is already non-linear, fitting well with a fourth-order virial on ϕ. This indicates that these suspensions cannot be treated as highly diluted because at least hydrodynamic interactions between four particles begin to take place. From another perspective, we can say that the probability distribution of particles in the suspension becomes conditional, contrasting with Batchelor's model for the suspension of rods (BATCHELOR, 1970a), where the probability is unconditional, that is the position of a given particle does not depend on the position of the others.

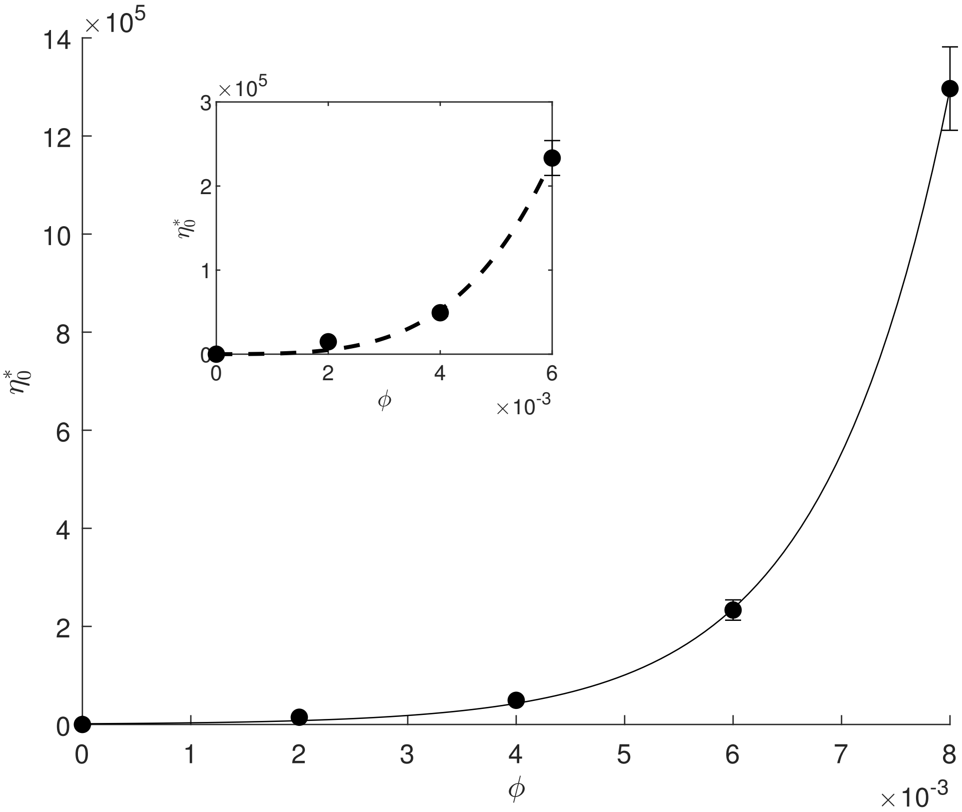

Figure 81 – The nondimensional viscosity near equilibrium, denoted as η_0^*, is presented as a function of the particle volume fraction of multi-walled carbon nanotubes (MWCN), complete with error bars. The main graph demonstrates that this relationship is well-represented by an exponential function of the form $\eta_0^* = a\exp(b\phi)$, where $a = 1.43 \times 10^3$ and $b = 8.51 \times 10^{-2}$. An inset highlights the four initial data points, illustrating that a fourth-order virial expansion fits the experimental data exceptionally well within this region. The fitting function for the virial expansion is given by $\eta_0^* = 1 + c\phi\left(1 + b\phi + \frac{b^2\phi^2}{2} + \frac{b^3\phi^3}{6}\right)$, with parameters $c = 1.04 \times 10^5$ and $b = 1.99 \times 10^3$.

6 RHEOLOGY OF OLEGELS

6.1 Rheological analysis under steady simple shear flow

6.1.1 Micrographies

In this section, we examine the microstructures of oleogels through images captured using an Olympus BX51 optical microscope equipped with a UC30 digital camera. The micrographs provide valuable insights into the microstructural arrangement of these complex fluids, particularly regarding particle orientation and its effects on flow anisotropy. Figure (82) illustrates that the S100C0 oleogel forms a reticulated structure due to the arrangement of potato starch macromolecules. Figure (83) presents a digital image of the S50C50 sample, where cotton cellulose fibers are dispersed within this starch network. Figure (84) shows a sample of S0C100, which consists solely of cellulose fibers.

It is crucial to note that the particle distributions depicted in Figures (82), (83), and (84) correspond to the equilibrium conditions of the oleogels (i.e., the initial state of the microstructure) in the absence of shearing flows. As clearly seen in the micrographs, the initial particle configurations within the oleogels do not follow the common statistically homogeneous distribution typical of a fluid at equilibrium. In fact, the presence of both starch reticulates and cellulose fibers results in strongly anisotropic suspensions. Consequently, the viscosity in the vicinity of equilibrium, referred to as η_0 (i.e., as $\dot{\gamma} \to 0$), cannot be accurately evaluated in steady shear experiments, as demonstrated in the plot of viscosity as a function of shear rate shown in Figure (92). In other words, the apparent viscosity does not appear to stabilize as $\dot{\gamma}$ approaches zero.

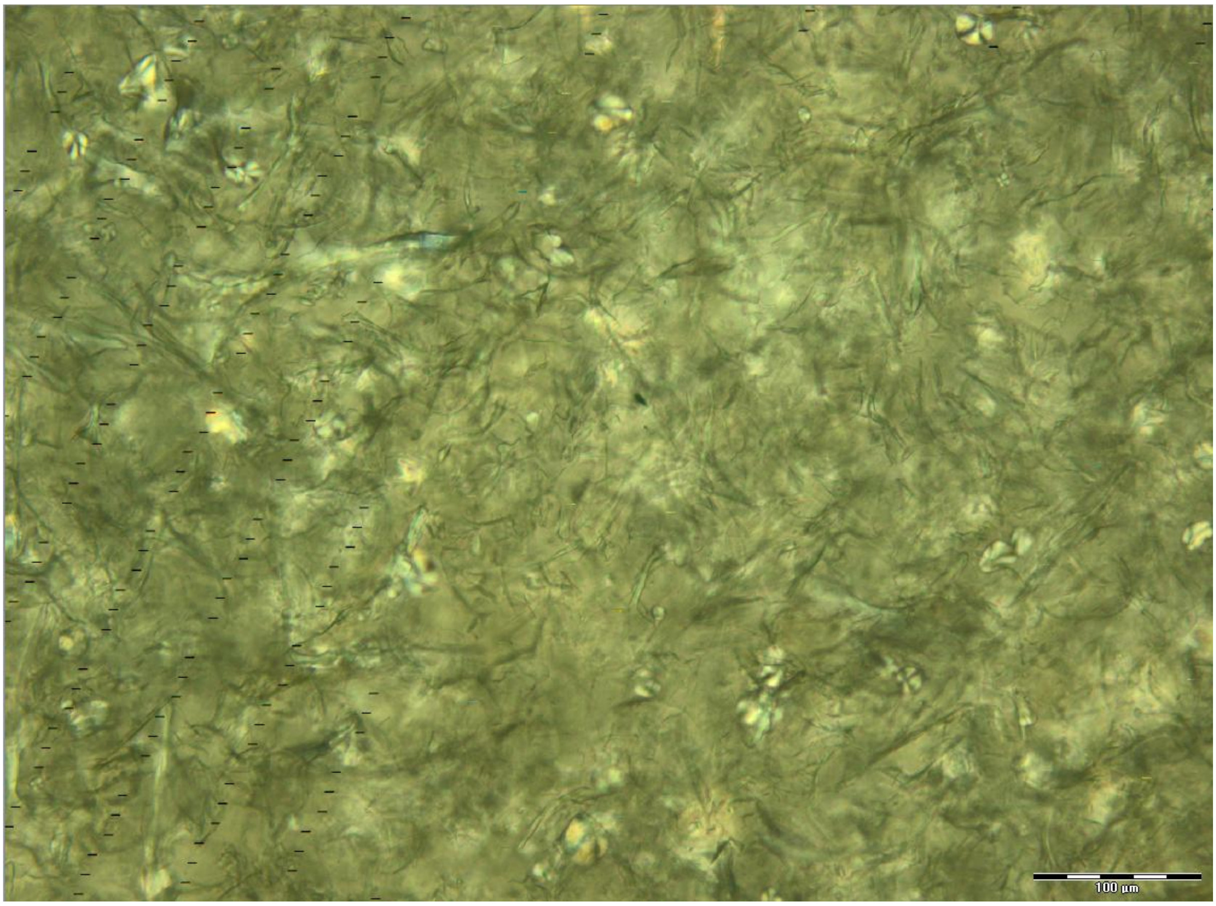

Figure 82 – Micrography of a sample of the oleogel S100C with 50X magnification.

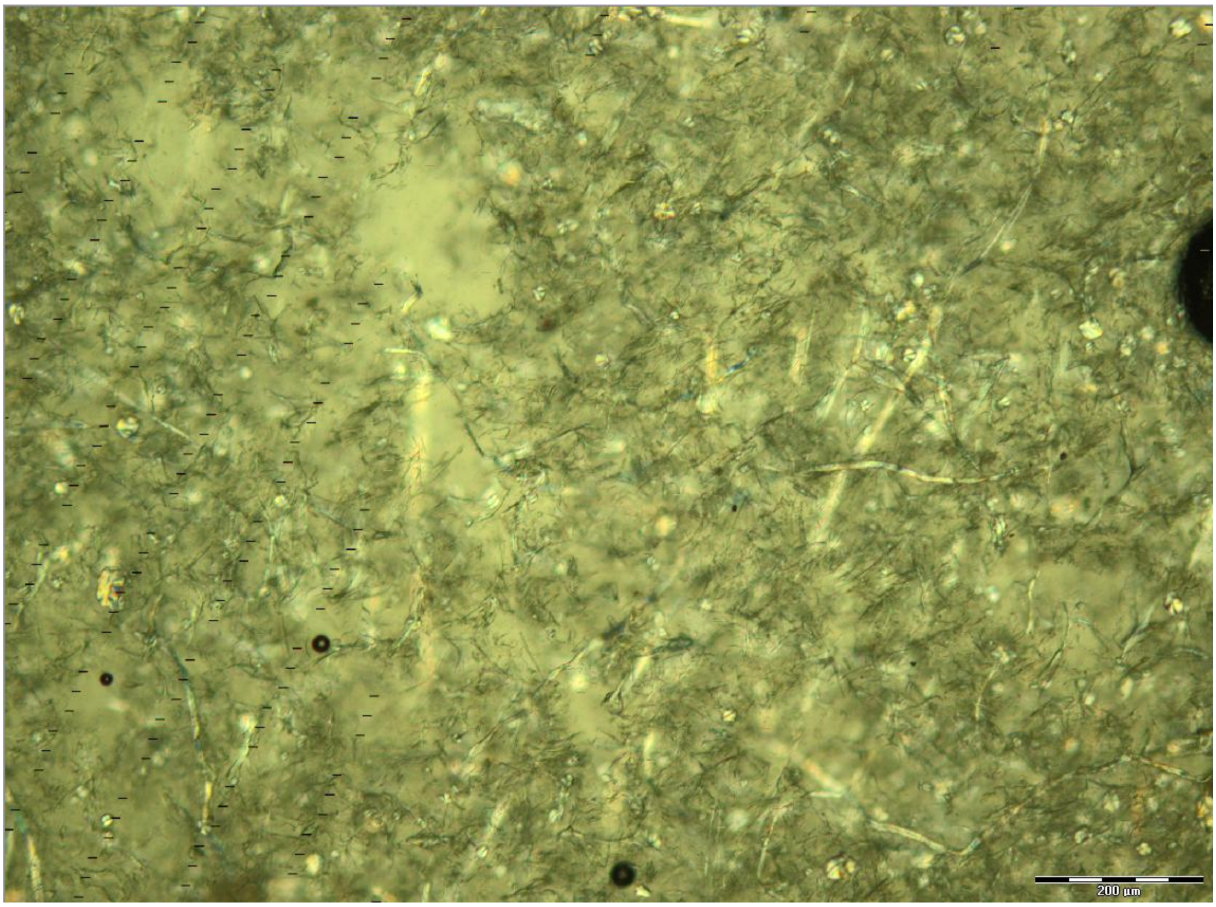

Figure 83 – Micrography of a sample of the oleogel S50C50 for the same magnification of 50X magnification.

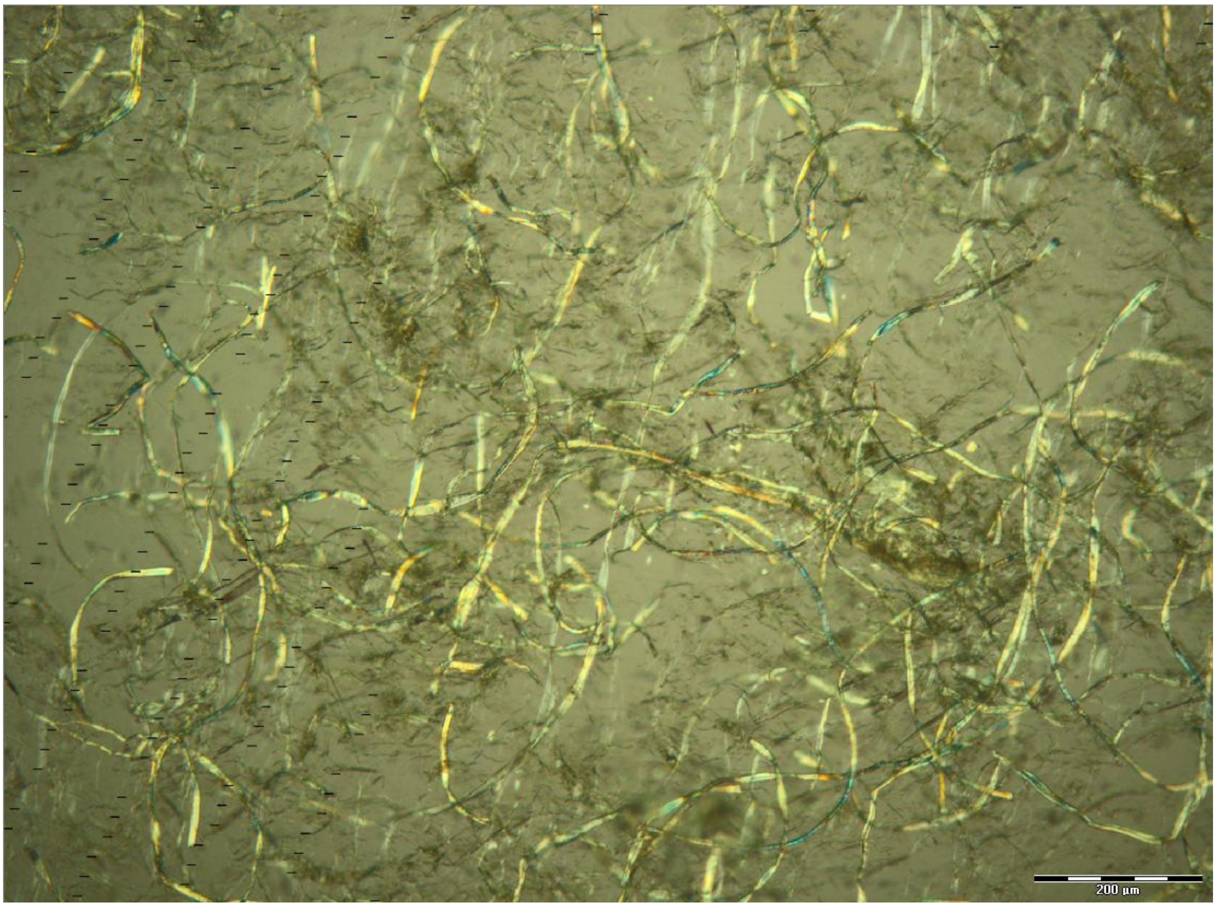

Figure 84 – Micrography of a sample of the oleogel S50C50 for the same magnification of 50X magnification.

6.1.2 Base fluids

The base fluids of the oleogels are soybean oil and a mixture of potato starch and cellulose fibers, present in different volume fractions. Initially, we investigate the behavior of each base fluid under variations in temperature and shear rate. It is well known that soybean oil behaves as a Newtonian fluid, meaning its viscosity remains constant regardless of the applied shear rate. Therefore, the primary rheological interest for this fluid lies in how its viscosity changes with temperature.

As shown in Figure (85), the viscosity of soybean oil decreases with increasing temperature. Moreover, by analyzing Figure (86), we observe that this decrease follows an exponential trend with temperature. This is evidenced by the fact that the experimental data can be well-fitted to an Arrhenius-type equation, confirming the temperature dependence of the viscosity.

The mixture of potato starch and cellulose fibers, on the other hand, exhibits non-Newtonian behavior across all volume fractions of the components in suspension. As shown in Figure (87), the mixture (S80C20—80% potato starch, 20% cellulose fiber) demonstrates shear-thinning behavior, which is consistent across five different temperatures. However, if we fix the shear rate, it becomes apparent that the viscosity of this complex fluid also decreases with increasing temperature.

Figure (88) illustrates that in both weak flow regions ($\dot{\gamma} \ll 1$) and strong flow regions ($\dot{\gamma} \gg 1$), the viscosity still exhibits an exponential dependence on temperature. This behavior holds true regardless of the flow regime, indicating that temperature plays a significant role in controlling the viscosity of the mixture.

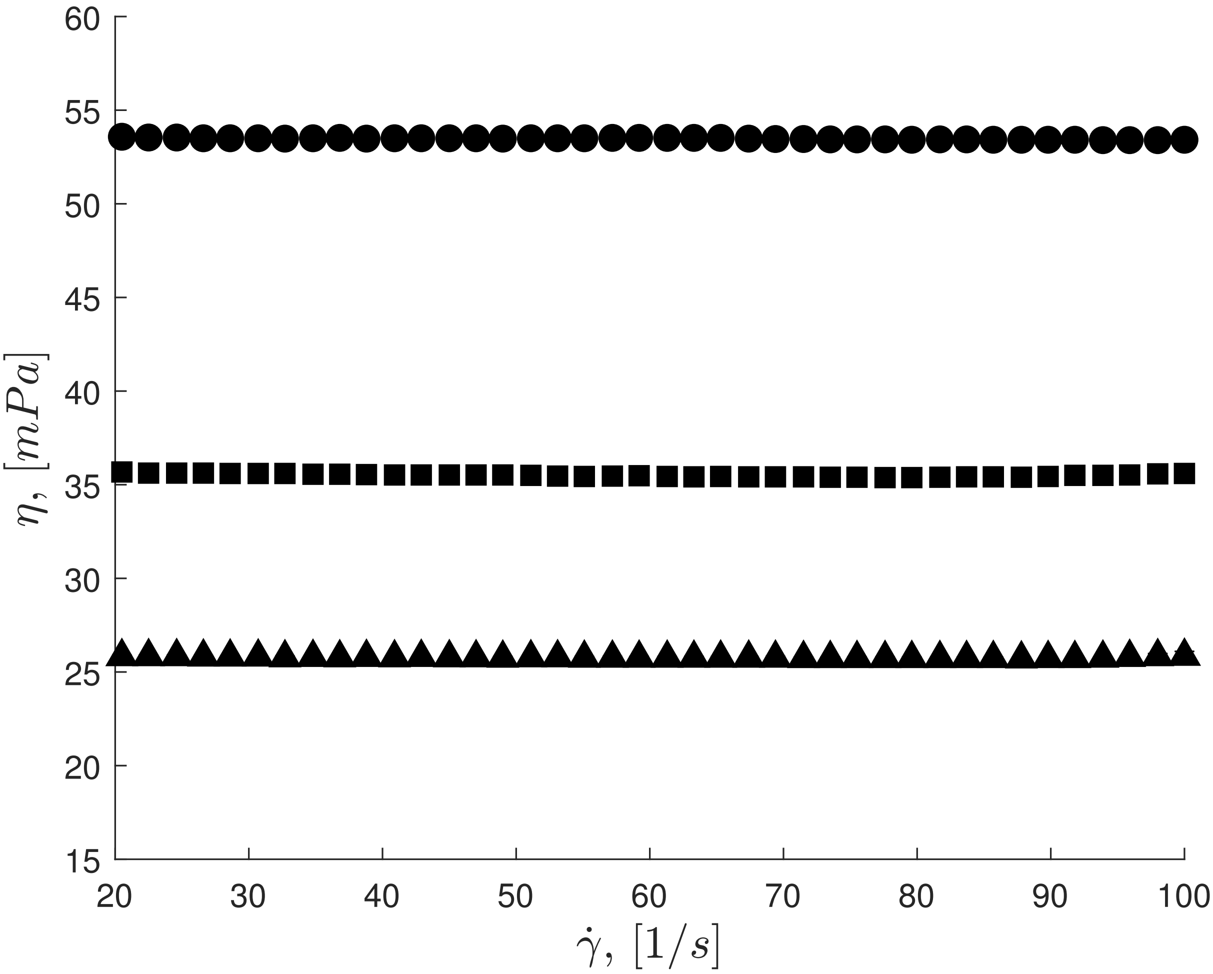

Figure 85 – Viscosity as a function of shear rate for soybean oil at different temperatures. ● - T= 20°C, ■ - T= 30°C, and ▲ - T= 40°C. Experimental error bars are shown. The behavior is notably Newtonian across all tested temperatures.

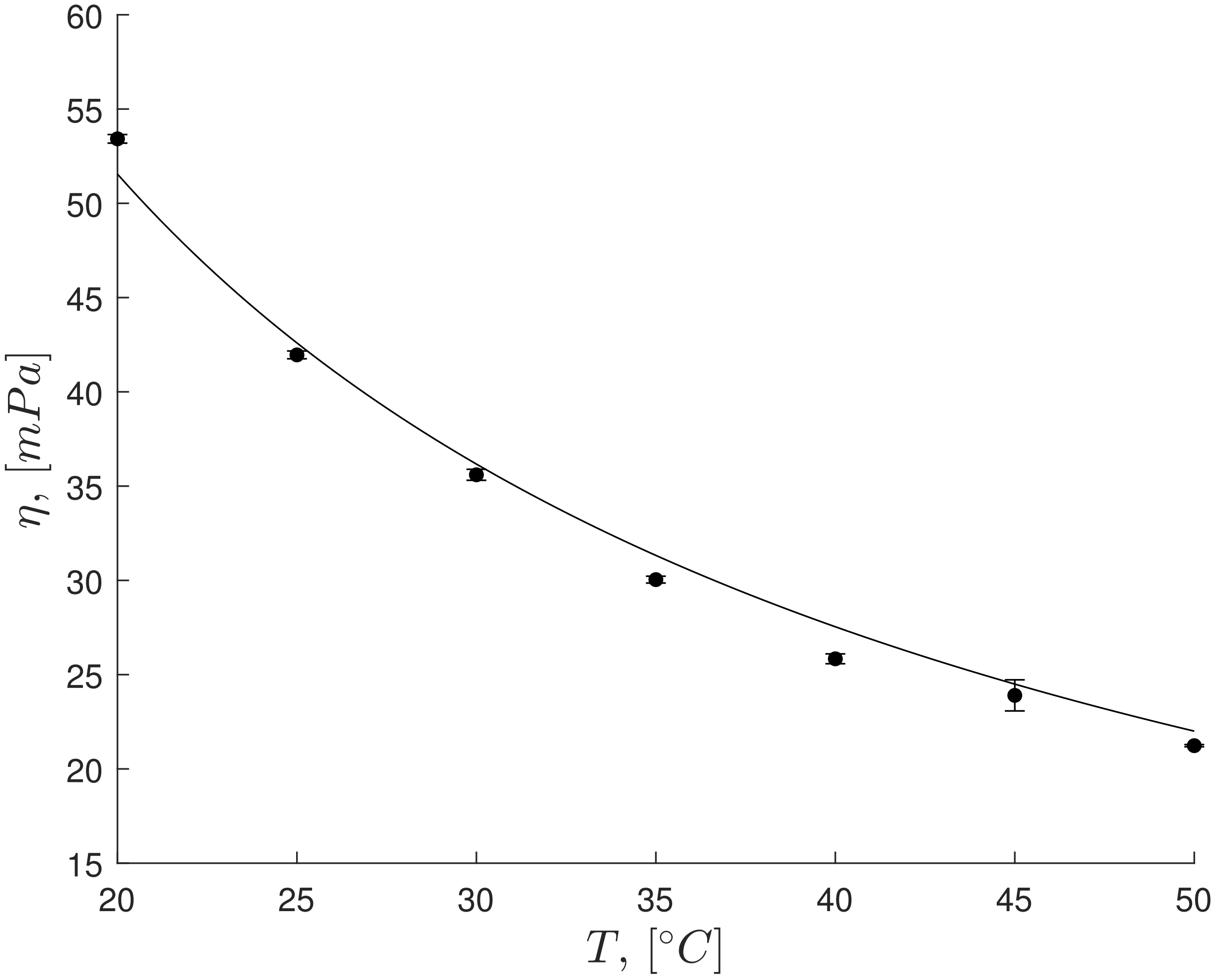

Figure 86 – Viscosity as a function of temperature for soybean oil. Experimental error bars are displayed for each point. The fitted curve follows the Arrhenius model: $\eta(T) = p_1 \exp(-p_2 T^{p_3})$, with constants $p_1 = 1.81 \times 10^3$, $p_2 = 1.77 \times 10^0$, and $p_3 = 2.34 \times 10^{-1}$.

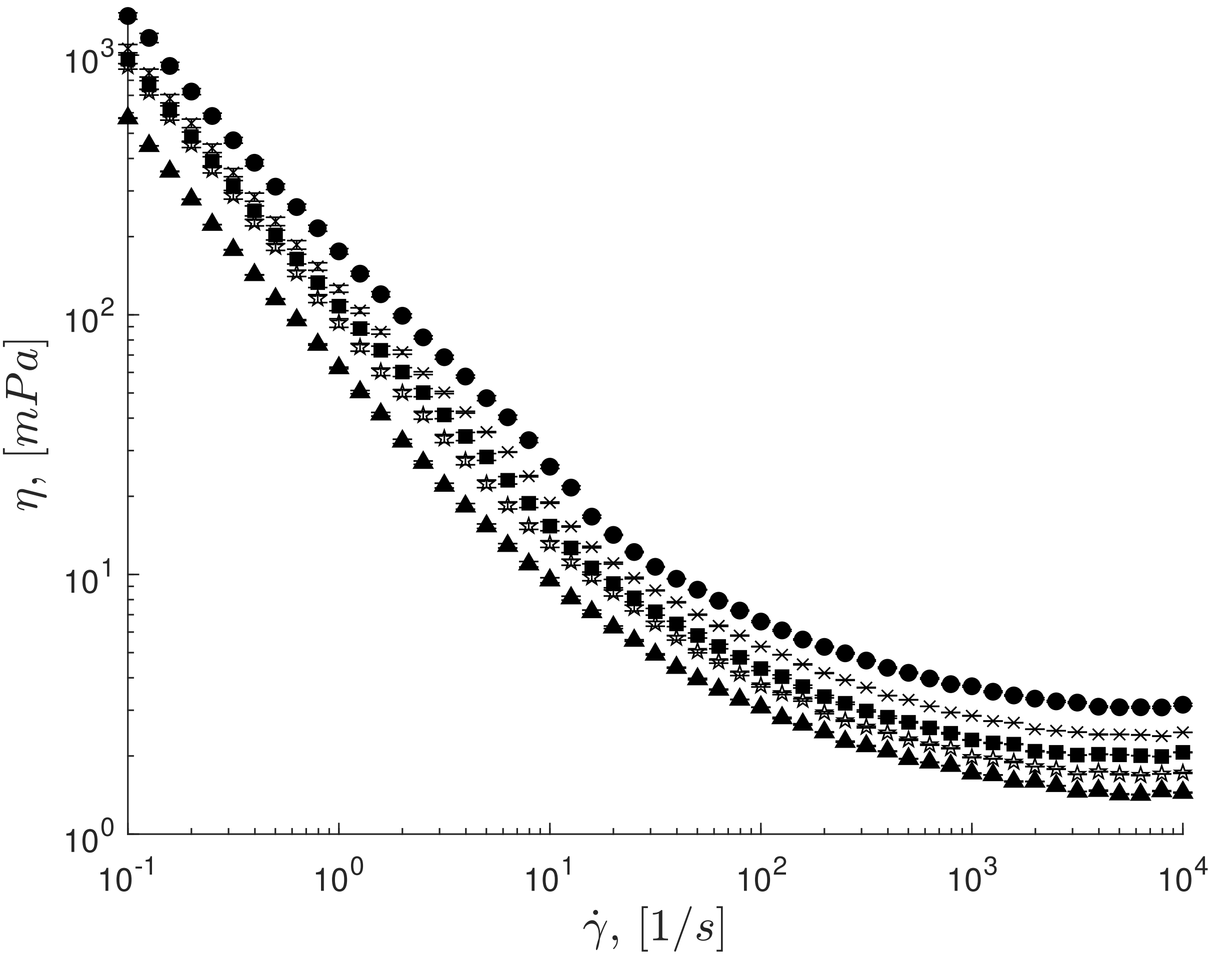

Figure 87 – Viscosity as a function of shear rate for the base mixture S80C20. ● - T= 20°C, × - T= 30°C, ■ - T= 40°C, ★ - T= 50°C, and ▲ - T= 60°C. Experimental error bars are shown.

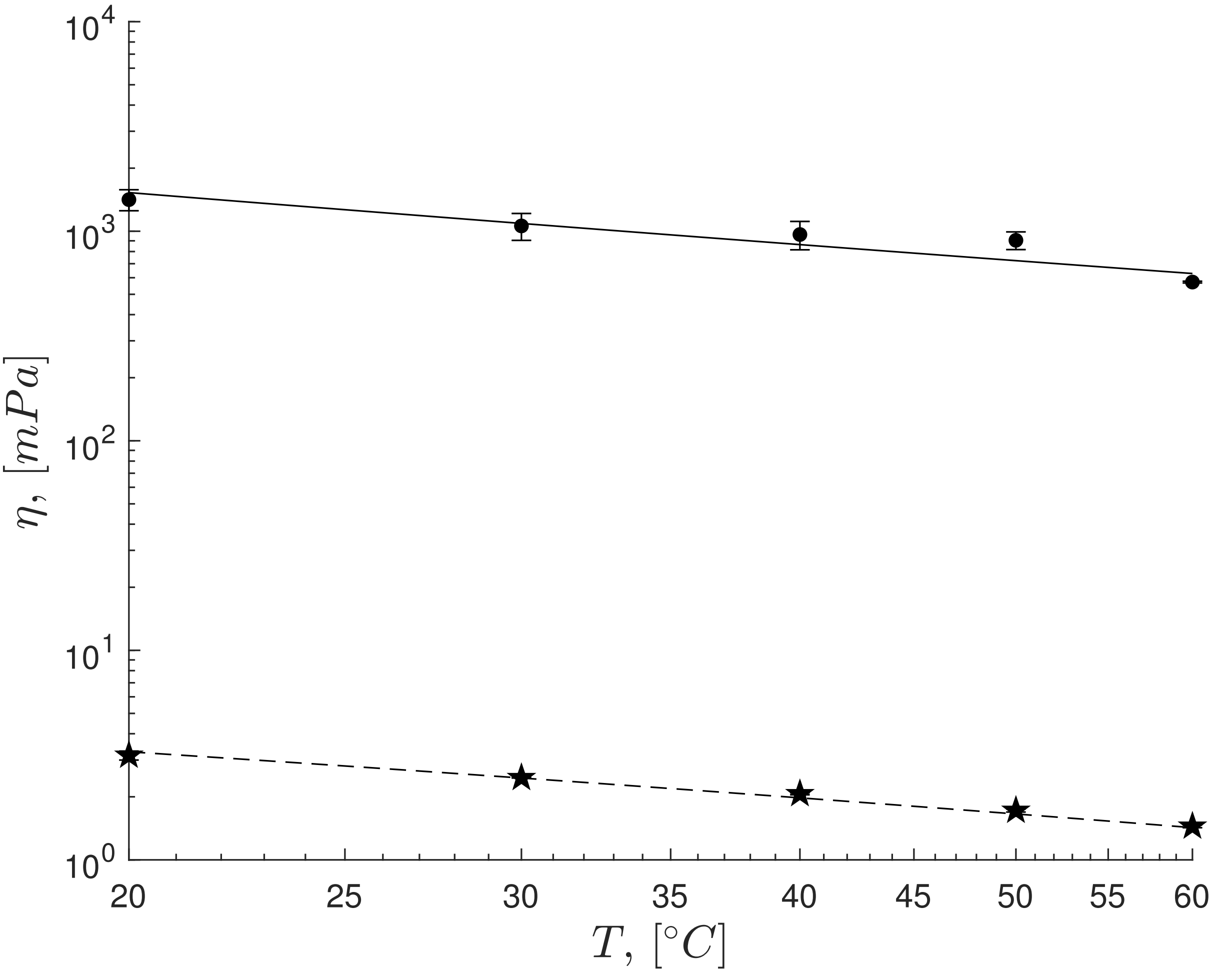

Figure 88 – Viscosity as a function of temperature for the base mixture S80C20 under two shear rate conditions: ● - $\dot{\gamma} \ll 1$ and ★ - $\dot{\gamma} \gg 1$. Experimental error bars are shown. The fitted curves follow the Arrhenius model, with the first (-) given by $\eta(T) = p_1 \exp(-p_2 T^{p_3})$, where $p_1 = 1.76 \times 10^{-1}$, $p_2 = -1.21 \times 10^{1}$, and $p_3 = -9.39 \times 10^{-2}$. The second (- -) is given by $\eta(T) = p_4 \exp(-p_5 T^{p_6})$, where $p_4 = 1.41 \times 10^{2}$, $p_5 = 2.17 \times 10^{0}$, and $p_6 = 1.83 \times 10^{-1}$.

6.2 Rheological analysis under permanent shear

In this section, we will examine the behavior of the oleogels (soybean oil + potato starch + cellulose fibers) under permanent shear. These fluids are quite complex, and as such, it is expected that their viscosity will depend on the shear rate. Figures (89) and (90) demonstrate that both S100C0 and S80C20 exhibit shear-thinning behavior. As the shear rate increases, the flow induces the rotation the breakup of the starch reticulates, the alignment and stretch of the microstructure along the streamlines of the flow, which reduces the collisional area and local energy dissipation, ultimately decreasing the viscosity of the fluid.

However, upon comparing the two figures, we observe that the rheogram for the oleogel S80C20 displays two distinct slopes, whereas the rheogram for oleogel S100C0 shows a consistent slope without any changes. This suggests that the shear-thinning process in fluid S80C20 is more complex, involving at least two underlying mechanisms.

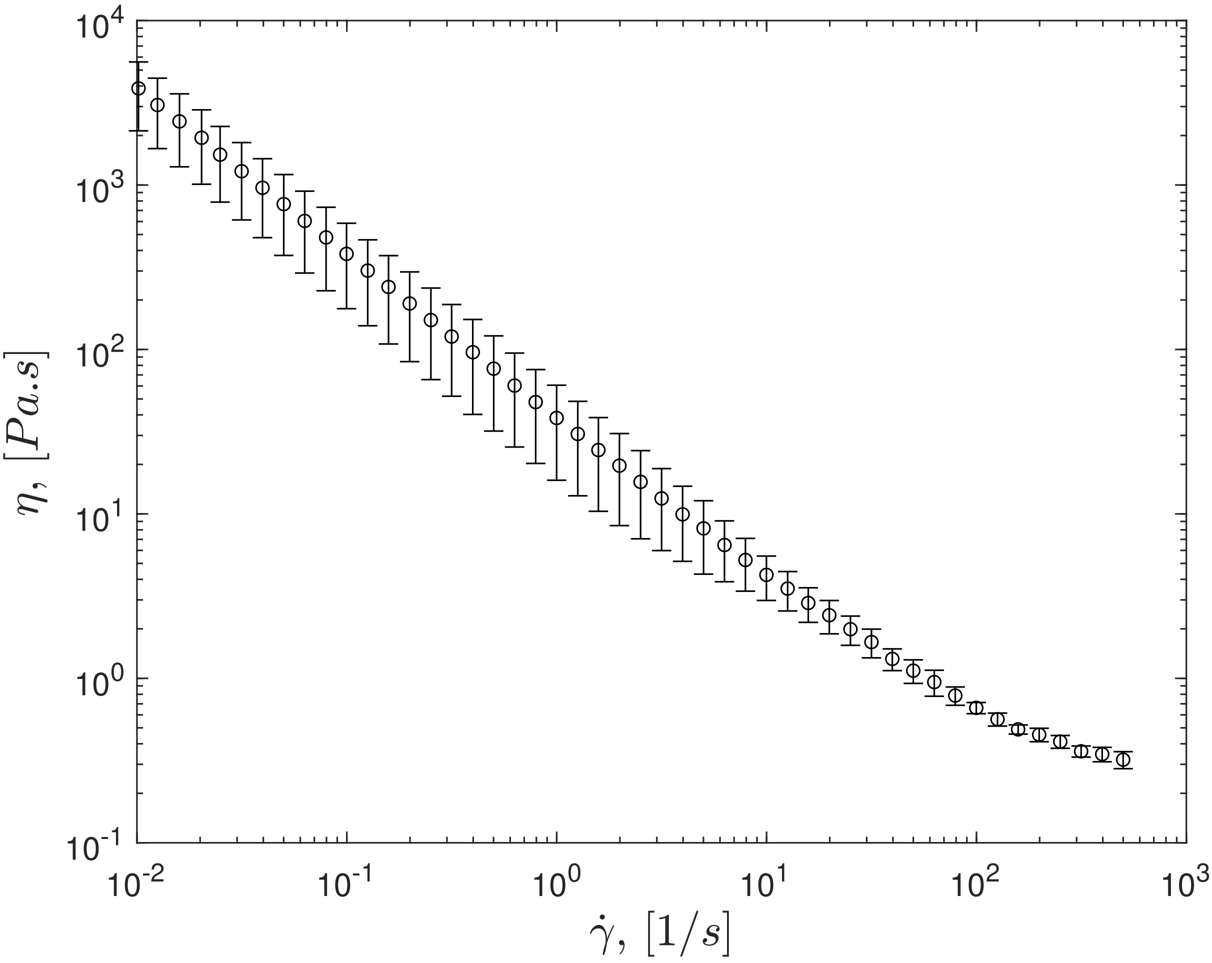

Figure 89 – Apparent viscosity as a function of shear rate for the oleogel with composition S100C0 in soybean oil. The experiment was conducted at a constant temperature of 20°C. Experimental error bars are shown.

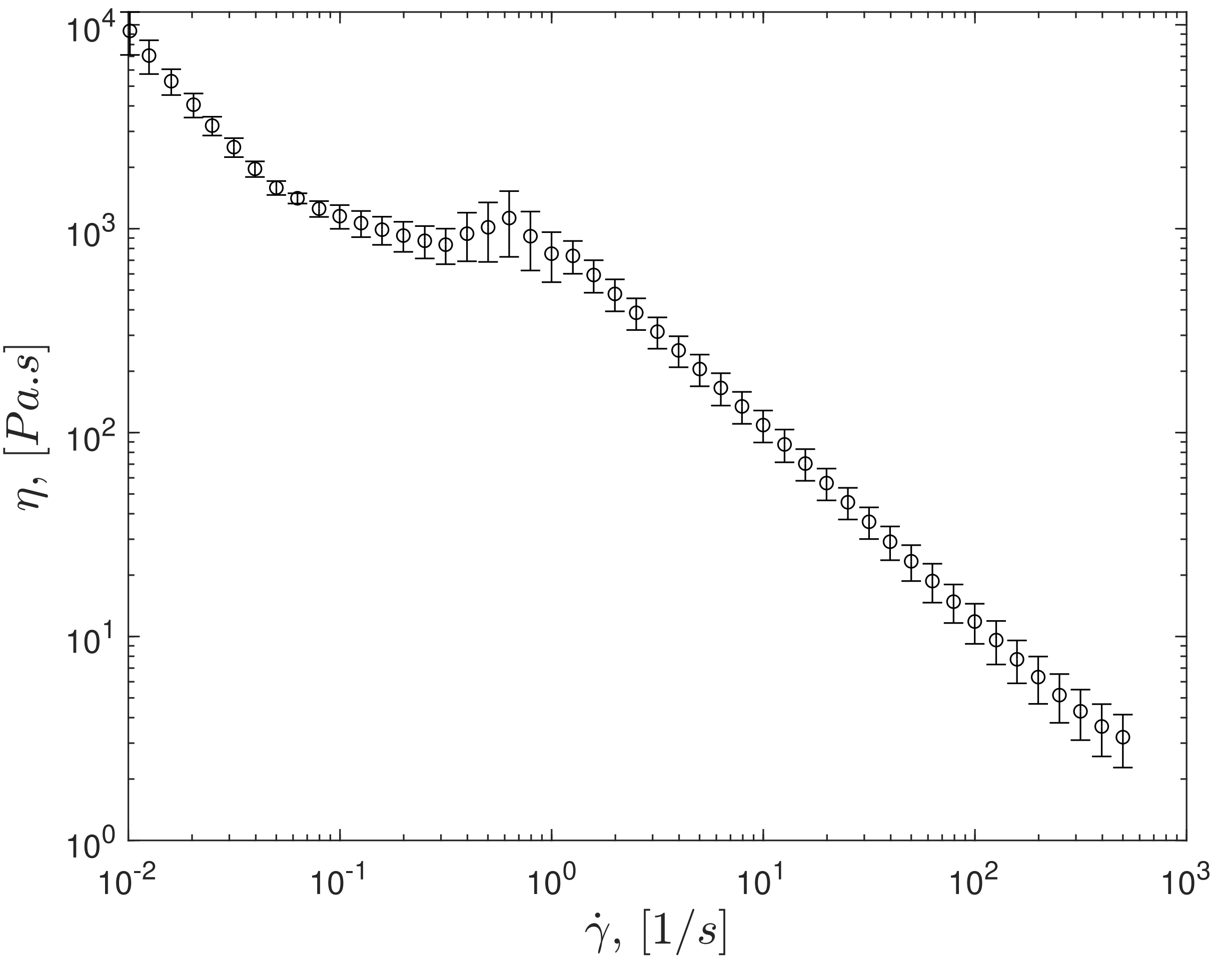

Figure 90 – Apparent viscosity as a function of shear rate for the oleogel with composition S80C20 in soybean oil. The experiment was conducted at a constant temperature of 20°C. Experimental error bars are shown.

The shear rate that marks the transition between different slopes in the rheological behavior is termed the critical shear rate $\dot{\gamma}_c$. To further investigate the rheology of fluid S80C20 in the vicinity of $\dot{\gamma}_c$, we experimentally measured the viscosity as a function of time at three distinct shear rates: $\dot{\gamma}_1 < \dot{\gamma}_c < \dot{\gamma}_2$. As illustrated in Figures (90) and (91), the relationship $\eta(\dot{\gamma}_c) > \eta(\dot{\gamma}_1) > \eta(\dot{\gamma}_2)$ indicates an anomalous behavior, where viscosity experiences a sudden increase even as the shear rate rises.

Additionally, the fluid requires a longer duration to achieve a steady-state regime specifically at $\dot{\gamma}_c$, with the time estimated to be $t_{RP} = 200\,\mathrm{s}$. Notably, throughout our experiments, the rheometer's "no time setting" option was consistently activated. This feature ensures that the system allows sufficient time for the steady-state condition to be reached, thereby respecting the material's characteristic response times.

In the region marked by $\dot{\gamma} < \dot{\gamma}_c$, the rheology is primarily influenced by the flow of the corn starch, essentially by the breakup of the starch reticulates. However, when the shear rate becomes sufficiently strong ($\dot{\gamma} \geq \dot{\gamma}_c$), the rheological behavior transitions to being dominated by the rotation and alignment of the cellulose fibers in suspension. This shift highlights the complex interactions between the different components of the oleogel and their respective contributions to the overall rheological response.

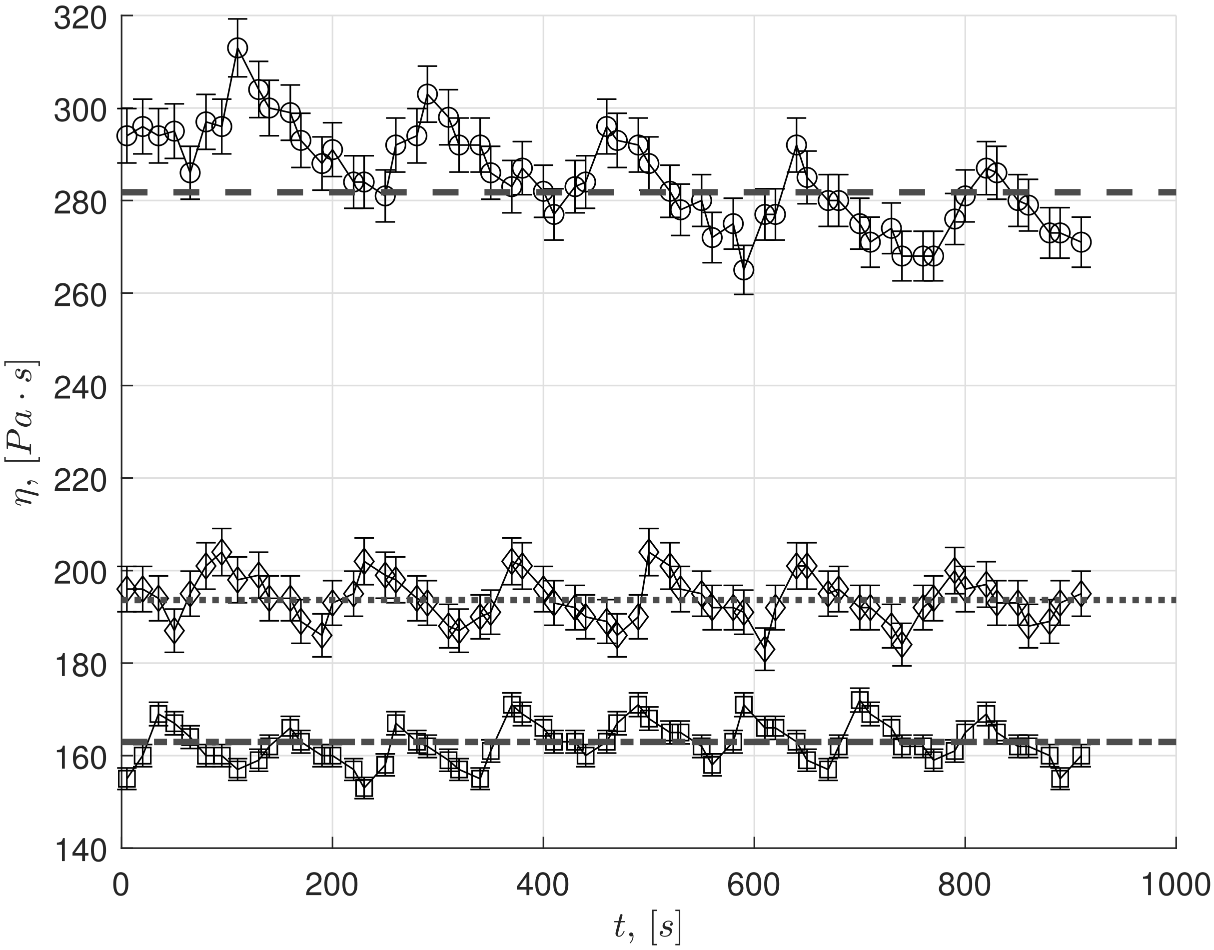

Figure 91 – Oleogel S80C20 - Apparent viscosity as a function of time for three different shear rates: the critical rate, one just below the critical rate, and one above. For this fluid, the critical shear rate was determined to be $\dot{\gamma}_c = 1.26 \times 10^0\, s^{-1}$. The shear rates in the vicinity, based on experimental data, are: $\dot{\gamma}_1 = 9.98 \times 10^{-1}\, s^{-1}$ and $\dot{\gamma}_2 = 1.58 \times 10^0\, s^{-1}$. Note that ○ $- \eta(\dot{\gamma}_c) >$ ◊ $- \eta(\dot{\gamma}_1) >$ □ $- \eta(\dot{\gamma}_2)$, characterizing anomalous behavior. The lines correspond to the average viscosity value assigned to each applied shear rate. The experiment was conducted at a constant temperature of 20°C. Experimental error bars are shown.

Figure (92) illustrates the behavior of all oleogels subjected to a shear flow with intensities exceeding $\dot{\gamma}_c$. As shown, all fluids exhibit pseudoplastic behavior, which is characterized by a decrease in viscosity as the shear rate increases. In this regime, the rheology is predominantly influenced by the rotation and alignment of the cotton cellulose fibers. This experimental data is well fitted by Sisko's rheological model (BARNES; HUTTON; WALTERS, 1989), with parameters shown at table (15).

The figure illustrates the behavior of the saturated viscosity, η_∞, at high shear rates (i.e., in the strong flow regime) for oleogels as a function of the mass fraction of cotton cellulose, w_c. As shown, the addition of cellulose fibers significantly increases the viscosity of the fluid, from values below 1 Pa · s to approximately 6 Pa · s—about six times higher. Notably, this increase in viscosity occurs even under strong flow conditions, where the mechanisms of intensive fiber alignment and microstructure disruption are likely dominant.

The reason behind this lies in the increased complexity of the microstructure with higher cellulose content, which makes it more difficult for the flow to deform it, leading to greater local energy dissipation. The particle stress, or stresslet (BATCHELOR, 1970b), is directly proportional to the structure's volume, L^3, where L is the average size of the structure at a given shear rate.

An important observation is the nonlinear dependence of viscosity on the mass fraction of cellulose, indicating the presence of complex internal mechanisms within the fluid. These involve structures of varying sizes interacting hydrodynamically—through far-field viscous interactions—and through near-field mechanisms such as structure collisions. The virial expansion $O(w_c^3)$ reflects how strong this nonlinear behavior is, driven by the different particle interaction mechanisms shaping the internal structure of the oleogel. Interestingly, the relationship between η_∞ and w_c is found to be linear.

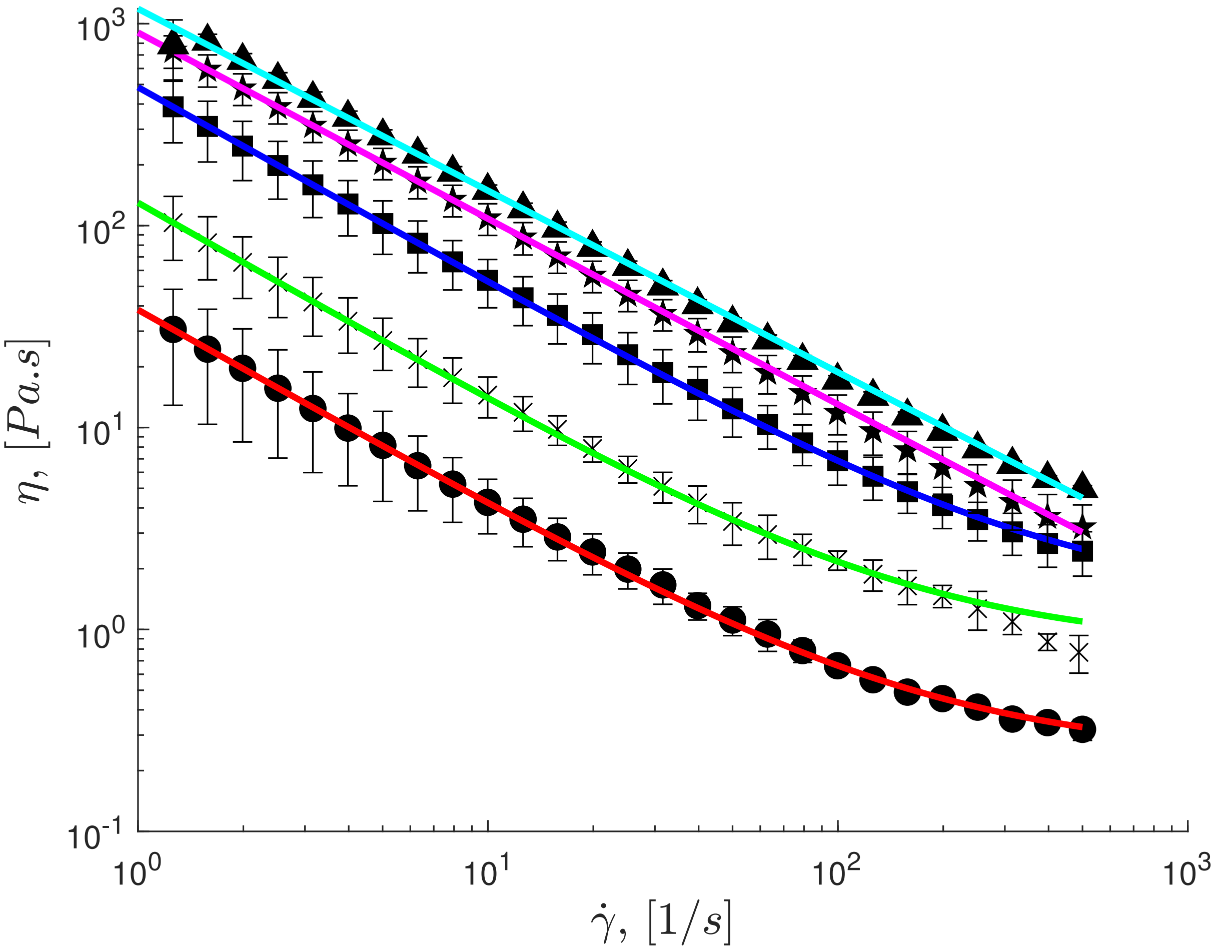

Figure 92 – Apparent viscosity as a function of shear rate for all tested oleogels, with only the typical behavior range ($\dot{\gamma} > 1\,s^{-1}$) depicted. Experiments were conducted at a constant temperature of 20°C. Experimental error bars are shown. The curves represent fits of the experimental data to the generalized Sisko fluid rheological model. ● - S100C0 + soybean oil, × - S80C20 + soybean oil, ■ - S50C50 + soybean oil, ⋆ - S20C80 + soybean oil, and ▲ - S0C100 + soybean oil.

Table 15 – Fitting parameters for the Sisko model.

Oleogel	η_∞ $[Pa.s]$	K $[Pa.s^n]$	n
S0C100 + Soybean oil	6.32	1185.7	0.09
S20C80 + Soybean oil	4.97	129.05	0.01
S50C50 + Soybean oil	2.44	483.17	0.02
S80C20 + Soybean oil	0.77	903.79	0.08
S100C0 + Soybean oil	0.32	38.04	0.02

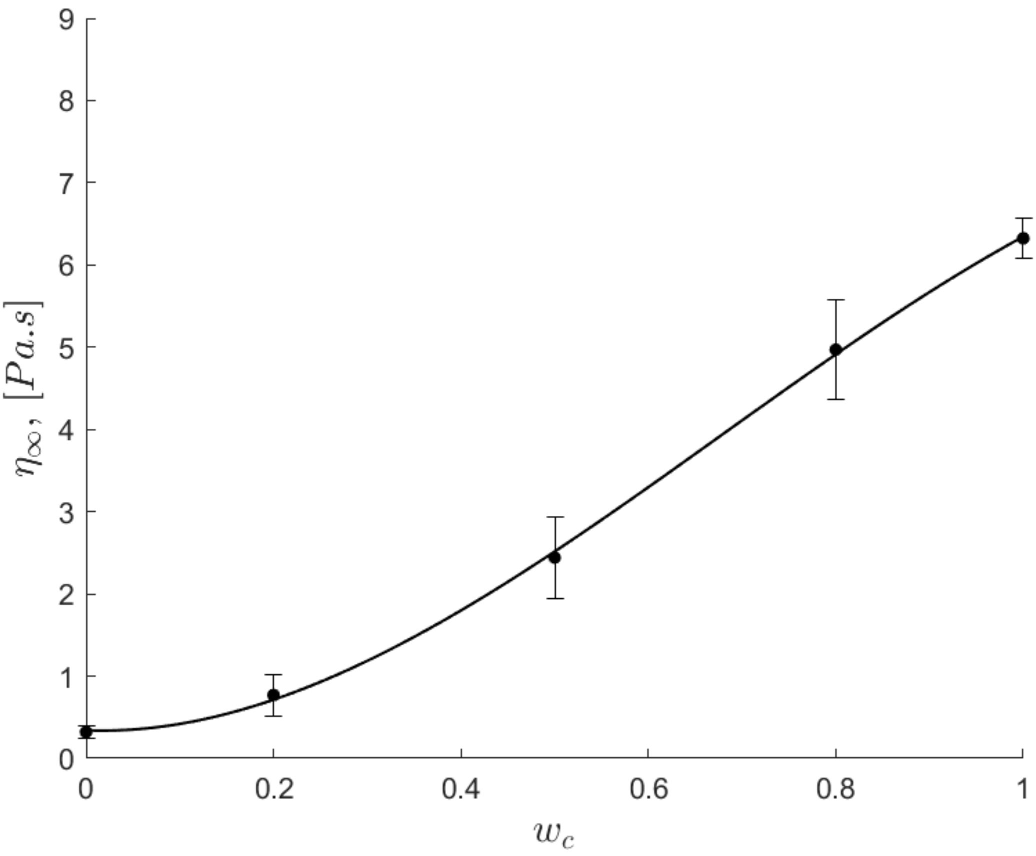

Figure 93 – The figure shows the effective viscosity as a function of the mass fraction of cellulose fibers, w_c, with error bars. The solid line represents the fit to the experimental data using a third-order virial expansion: $\eta_\infty = b_0(1 + b_1 w_c + b_2 w_c^2 + b_3 w_c^3)$, where $b_0 = 0.34$, $b_1 = -1.22$, $b_2 = 37.09$, and $b_3 = -18.26$.

Figure (94) shows that the viscosity below the critical shear rate is pseudoplastic. However, it also reveals that the oleogels with the highest cellulose fiber content, S0C100 and S20C80, exhibit lower viscosity than S50C50 over most of this range. In this region, the rheology is primarily governed by the flow of the corn starch reticulates. Once the shear rate exceeds $\dot{\gamma}_c$, the flow becomes dominated by the effects of the cotton cellulose fibers.

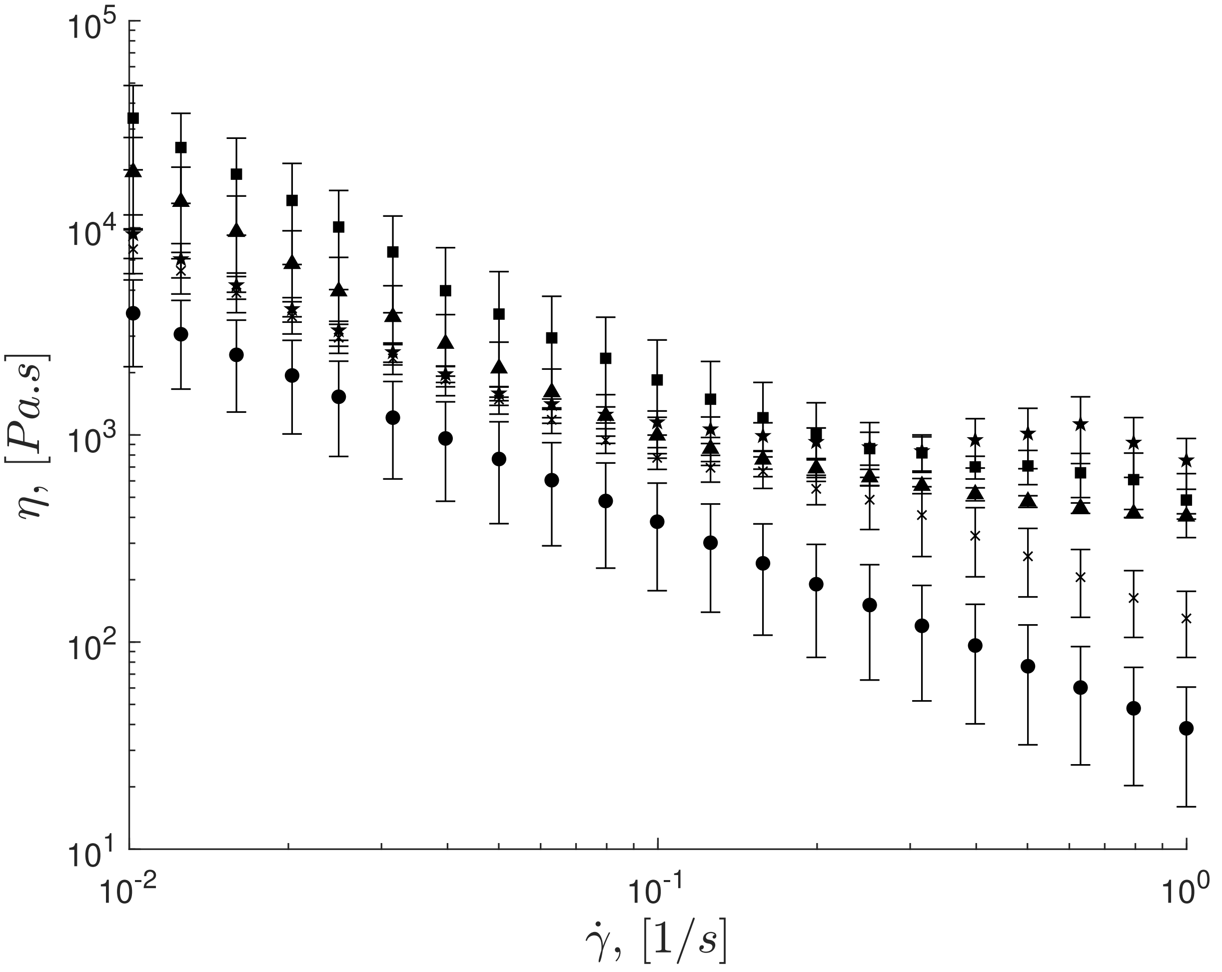

Figure 94 – Apparent viscosity as a function of shear rate for all tested oleogels, with only the anomalous behavior range ($\dot{\gamma} \leq 1\,s^{-1}$) depicted. Experiments were conducted at a constant temperature of 20°C. Experimental error bars are shown. ● - S100C0 + soybean oil, × - S80C20 + soybean oil, ■ - S50C50 + soybean oil, ⋆ - S20C80 + soybean oil, and ▲ - S0C100 + soybean oil.

6.3 Rheological analysis under small amplitude oscillatory shear (SAOS)

Dynamic small amplitude oscillatory shear (SAOS) tests are crucial in characterizing the viscoelastic behavior of complex fluids. By applying a small oscillatory strain, we can observe both the elastic (storage modulus G') and viscous (loss modulus G'') components of the stress response. These moduli are frequency-dependent and help in distinguishing the solid-like (elastic) from the liquid-like (viscous) behavior of the fluid. The data from SAOS tests reveal how a material will react under various conditions, including short-term (instantaneous) and long-term (steady-state) deformations, which is essential for applications in materials science, food technology, pharmaceuticals, and more.

6.3.1 Oleogels

6.3.1.1 Determination of the reference strain - linear regime

Establishing the linear viscoelastic region is a critical step before conducting small amplitude oscillatory shear (SAOS) tests. In this linear regime, the elastic modulus G' is independent of the strain amplitude γ, allowing the intrinsic viscoelastic properties to be measured without introducing nonlinear effects.

In Figure (95), the dependence of G' on γ for the three oleogels (S0C100, S50C50, and S100C0) indeed reveals that within the range $0.001 < \gamma < 0.01$, G' remains nearly constant, confirming that this is the linear range. The choice of $\gamma = 0.001$ for frequency sweep experiments is appropriate, as it ensures measurements within this range, where the response is purely linear and free of strain-induced nonlinearities.

By setting $\gamma = 0.001$, our frequency sweep experiments will yield more accurate and reliable data on the viscoelastic characteristics of these oleogels across different frequencies, ensuring that the elastic and viscous moduli are representative of the material's intrinsic properties.

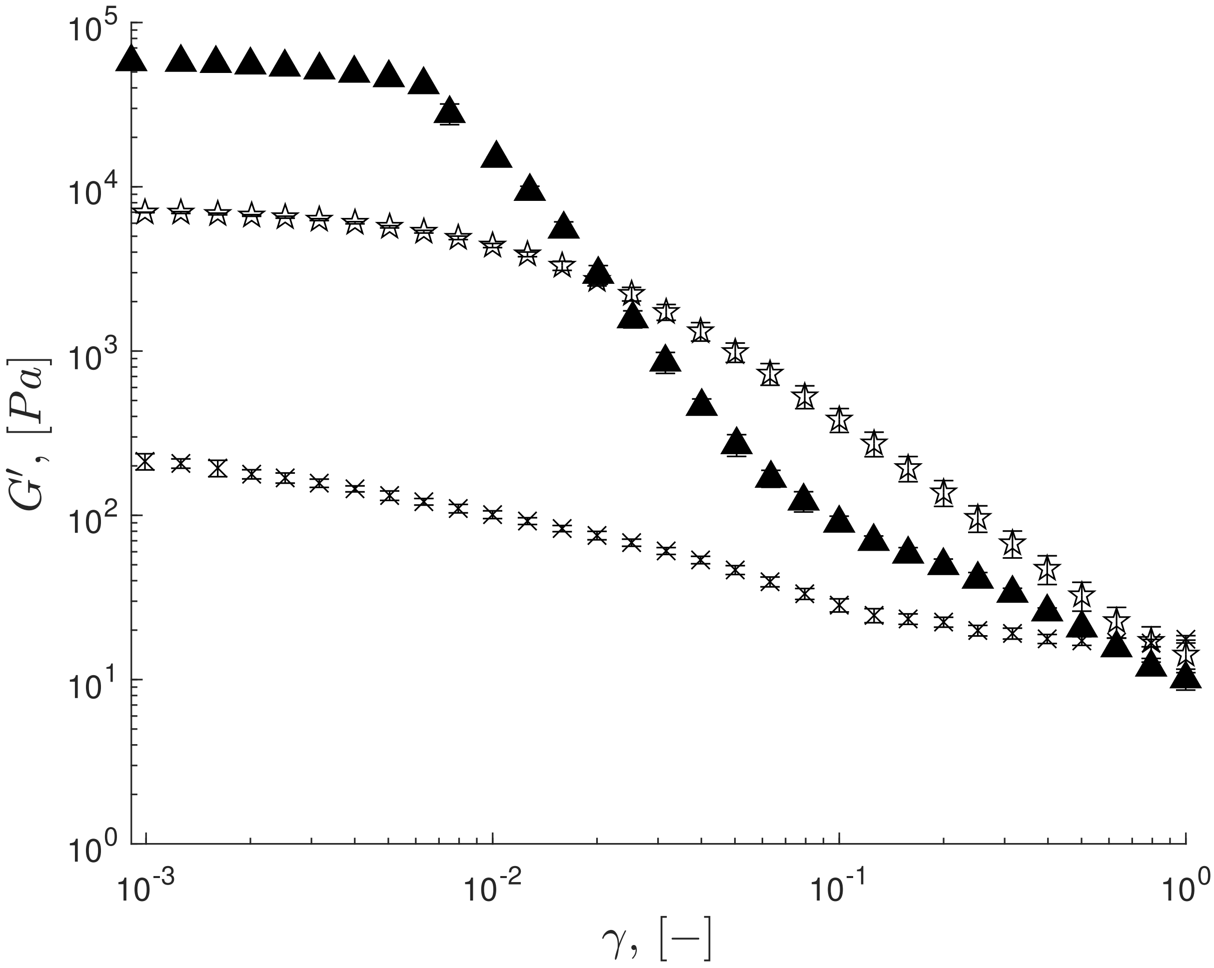

Figure 95 – Elastic modulus G' as a function of shear strain γ for a fixed excitation frequency ω of 100 rad/s, with experimental error bars. The temperature is fixed at $20°C$. This graph shows the behavior of all tested oleogels. ▲ - S0C100, $\star$ - S50C50, and $\times$ - S100C0. Based on these results, the reference strain $\gamma_0 = 0.001$ was selected for frequency sweep experiments.

6.3.1.2 Linear viscoelastic response in frequency

In Figure (96), the elastic modulus G' of the oleogels is plotted as a function of the forcing frequency, illustrating the viscoelastic properties of these materials in the low-frequency, near-equilibrium regime. Due to the anisotropic and coherent microstructure of the oleogels, G' remains constant across the frequency range of 0 to 100 rad/s, which is typical for viscoelastic materials that exhibit solid-like behavior at lower frequencies. This behavior allows us to determine the shear elastic modulus, $G_0 = \lim_{\omega \to 0} G'(\omega)$, an important parameter that quantifies the solid-like response of a viscoelastic fluid.

As shown in Figure (96), increasing the mass fraction of cotton cellulose fibers w_c results in a higher G' and consequently a larger G_0. This is because higher fiber content induces significant changes in the shape and distribution of internal structures within the oleogel, leading to stronger interactions and correlations between fiber-like agglomerates. These enhanced structural interactions increase the resistance of the oleogel to shear deformation from its equilibrium state. The yield stress σ_0 required to initiate flow can be approximated by the relationship $\sigma_0 = \gamma_0 G_0$, directly connecting G_0 with the material's resistance to flow.

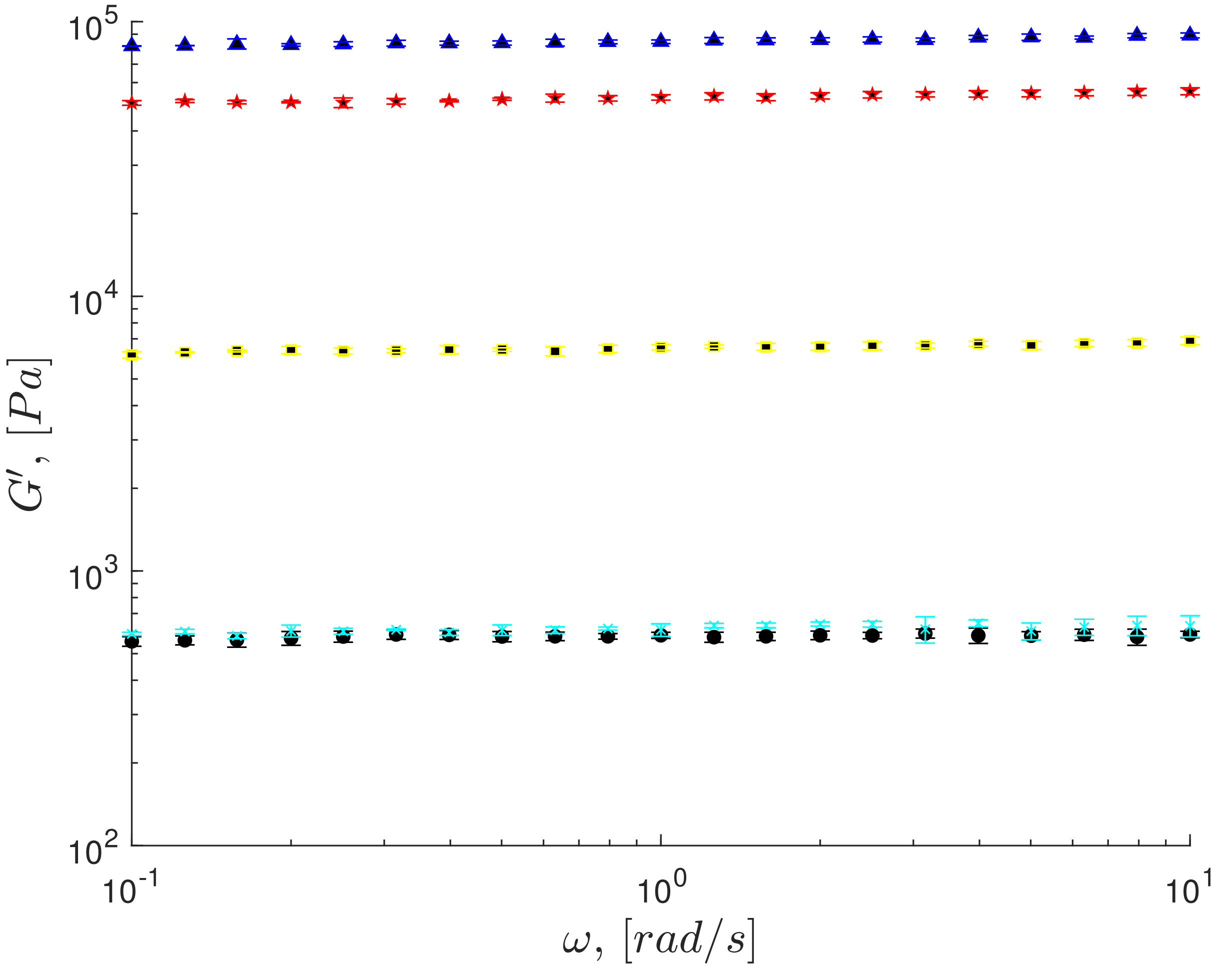

Figure 96 – Elastic modulus G' as a function of excitation frequency ω for all analyzed oleogels, with experimental error bars. The reference strain γ_0 is fixed at 0.001. ▲ - S0C100, ★ - S20C80, ■ - S50C50, × - S80C20, and ● - S100C0. The temperature is fixed at 20°C.

Figure (97) further emphasizes the dependence of G_0 on w_c, showing a notably strong, typically exponential relationship. This trend indicates that as w_c increases, the network density within the oleogel grows, significantly enhancing its elastic response. Understanding this relationship provides crucial insights into how cellulose fiber content affects the mechanical properties of oleogels, which is essential for applications where specific structural stability and resistance to deformation are required.

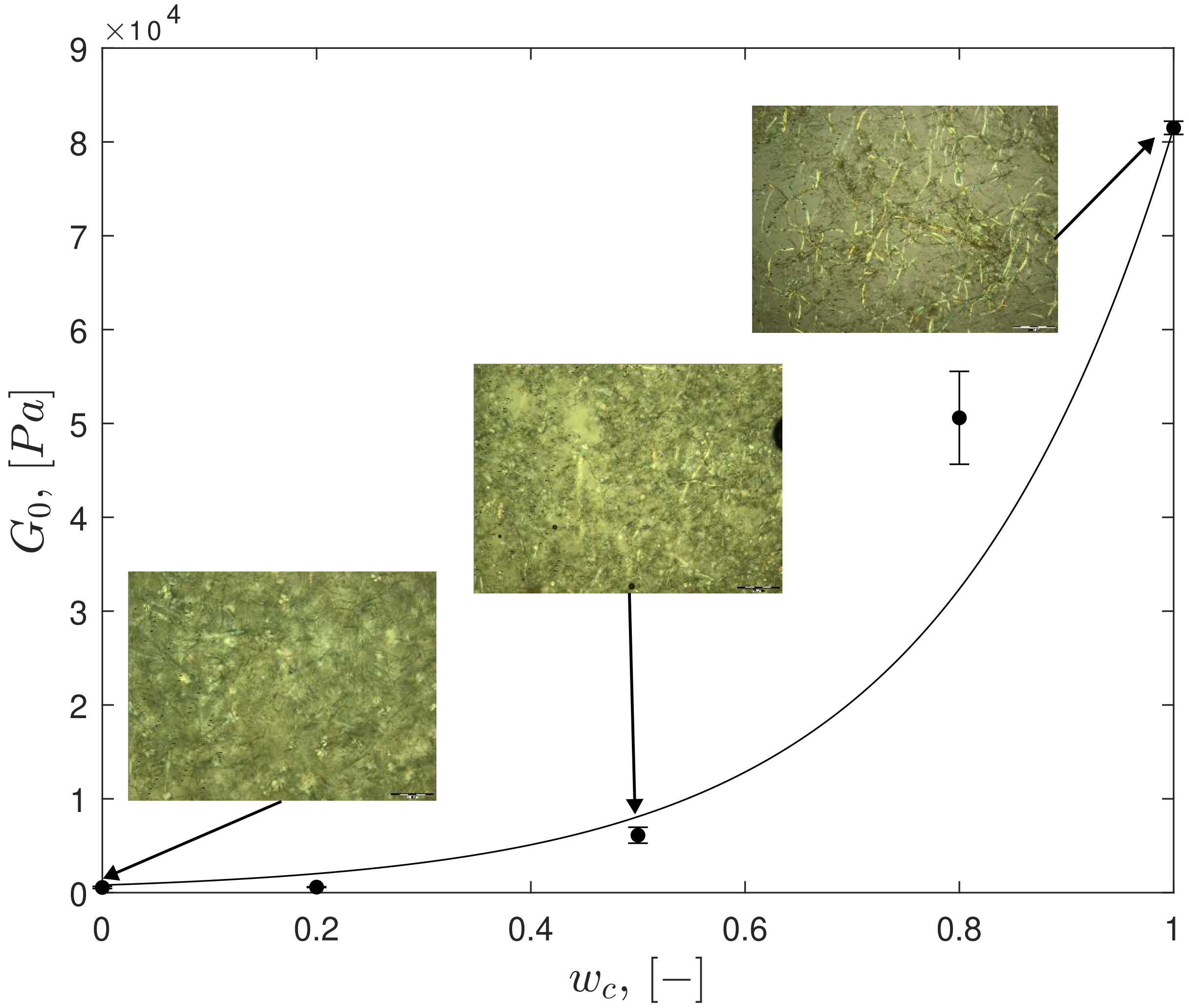

Figure 97 – Shear elastic modulus G_0 for the oleogels as a function of cellulose mass fraction w_c, with experimental error bars. The experiment was conducted at a controlled temperature of $20°C$. The curve is a fit of the experimental data to an expression of the type: $G_0(w_c) = p_1 \exp(p_2 w_c)$. The fitting parameters are: $p_1 = 8.05 \times 10^2$ and $p_2 = 4.62 \times 10^0$.

The datasets from the SAOS experiments also allow us to analyze the dissipative (viscous) behavior of the oleogels. To this end, we plot the loss modulus G'' as a function of the forcing frequency, as shown in Figure 16. It is evident from Figure 16 that increasing the mass fraction of cotton cellulose fibers w_c leads to a notable enhancement of the fluid's dissipative response. As discussed earlier, a higher w_c promotes the formation of more complex fiber agglomerates of larger size, which increases the particle stresslet, scaling with the average structure size L^3. Additionally, these larger fiber structures interact over a greater collisional area, contributing to a higher dissipation rate in the bulk flow. Figure 16 clearly shows that G'' values rise substantially with w_c across the entire frequency range studied, while remaining nearly constant with respect to the forcing frequency.

Furthermore, comparing the values of $G'(\omega)$ and $G''(\omega)$ from Figures (96) and (98), respectively, reveals that G' is at least an order of magnitude greater than G'' across the full frequency range examined. This demonstrates that at low frequencies, the oleogels exhibit behavior that is much more elastic and solid-like than viscous and liquid-like.

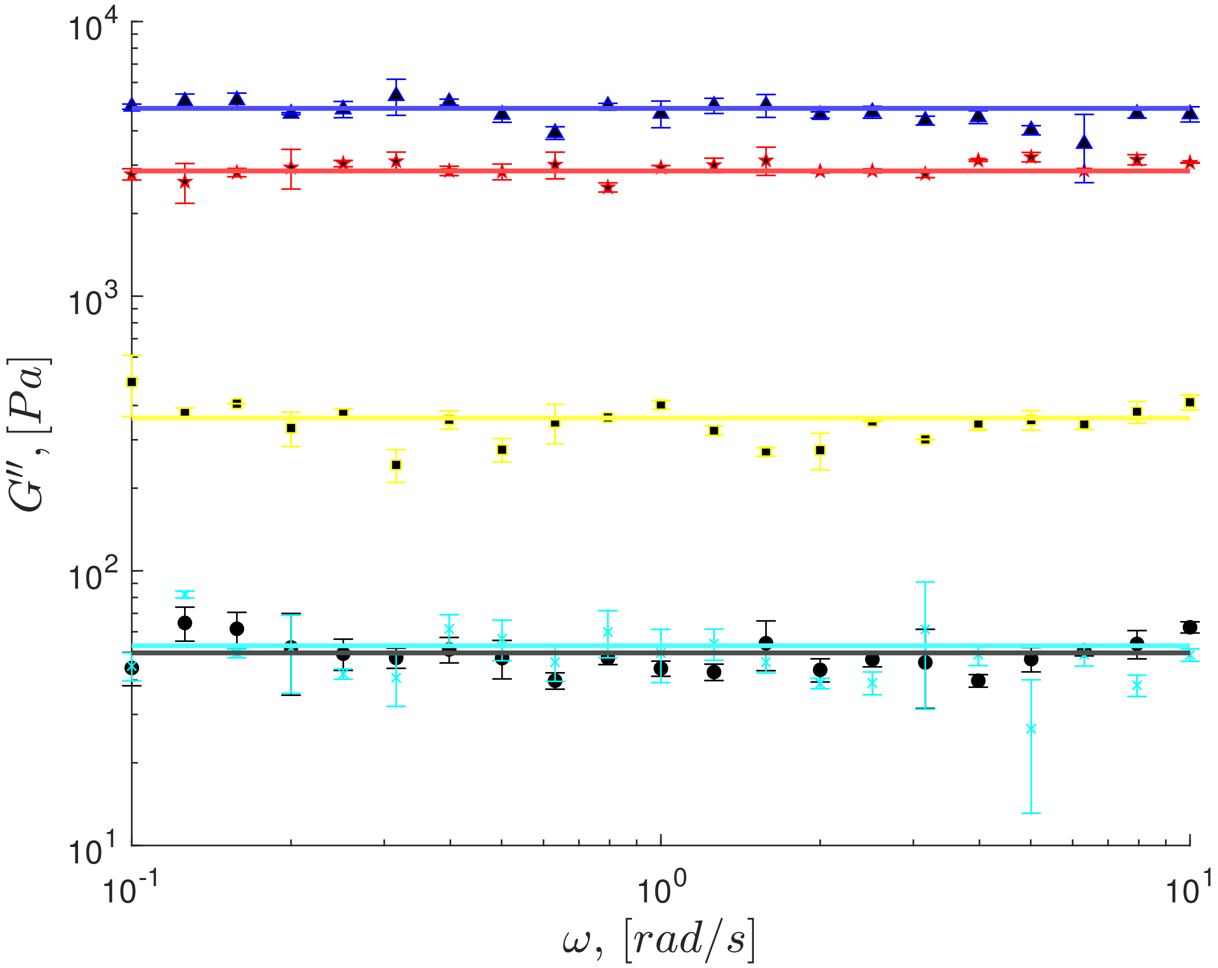

Figure 98 – Loss modulus (viscous) G'' as a function of excitation frequency ω for all analyzed oleogels, with experimental error bars. The reference strain γ_0 is fixed at 0.001. ▲ - S0C100, ★ - S20C80, 🟨 - S50C50, × - S80C20, and • - S100C0. The temperature is fixed at $20°C$. The lines represent the average values of G'' evaluated under small amplitude oscillatory shear.

The effective zero-shear viscosity (η_0) can be extracted from the $G''(\omega)$ data, defined as $\eta_0 = \lim_{\omega\to 0} \eta'(\omega)$, where $\eta'(\omega)$ is the viscous modulus given by $\eta'(\omega) = \frac{G''(\omega)}{\omega}$. This quantity, η_0, reflects the viscous characteristics of oleogels when in equilibrium. Therefore, in applications where the fluid remains at rest for long periods, this viscoelastic modulus is crucial for evaluating dissipative properties such as the fluid viscosity as a function of the mass fraction of additives like cotton cellulose fibers.

In contrast to the algebraic dependence $O(\omega_c^3)$ of η_∞ under strong flow (as shown in Figure (93)), Figure (99) suggests an exponential dependence of η_0 on ω_c, resembling the behavior of G_0 with ω_c depicted in Figure (97).

We conjecture that this remarkable difference observed in viscosity behavior at low shear rates (weak flow conditions) and at high shear rates (strong flow) is intrinsically linked to the microstructural changes in oleogels from equilibrium to strong flow conditions. We expect that the interactions among fiber aggregates, which have non-uniform and anisotropic shapes, are much more complex under low shear conditions than in high shear rates. Specifically, strong flows typically cause breakage and alignment of structures, resulting in a distribution of smaller-sized structures oriented in the flow direction. In contrast, when the flow is weak, the structures remain large, leading to a significant collisional area during the interactions of fiber agglomerations dispersed in the surrounding medium. This results in much larger values of effective viscosity since the additional particle stresslet contribution increases with L^3, where L is a typical large structure size that tends to grow with the increase in the mass fraction of cotton fibers in the oleogels. The differing behaviors of effective viscosity in weak and strong flows, characterized by a transition from exponential to algebraic dependence of viscosity on the fiber additive fraction, represent an important finding in this rheological characterization of oleogels.

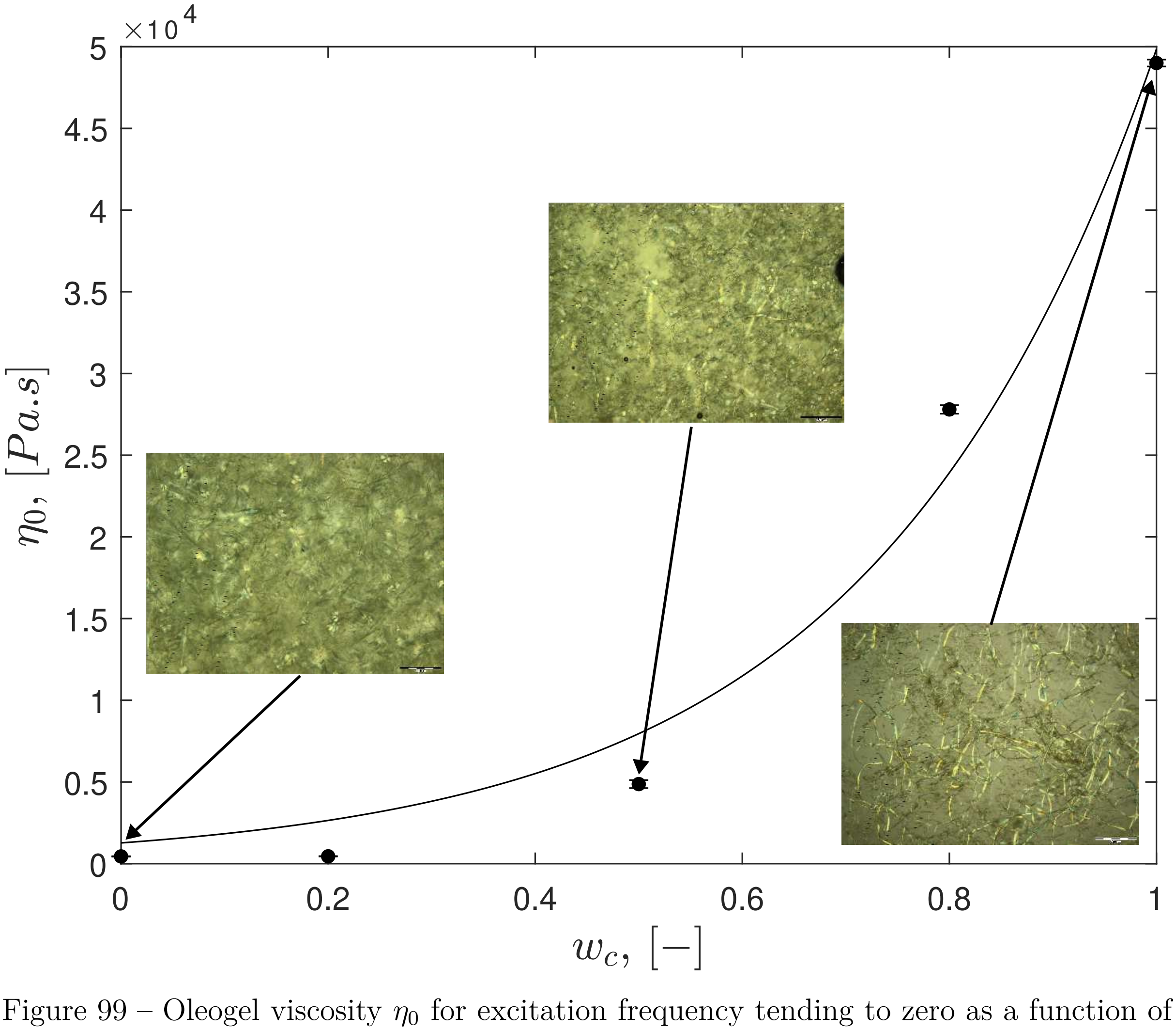

Figure 99 – Oleogel viscosity η_0 for excitation frequency tending to zero as a function of cellulose mass fraction w_c. Experimental error bars are shown for the data points. The experiment was conducted at a controlled temperature of $20°C$. The curve is a fit of the experimental data to an expression of the type: $\eta_0(w_c) = p_1 + p_2 \exp(p_3 w_c)$. The fitting parameters are: $p_1 = 4.09 \times 10^5$, $p_2 = 3.67 \times 10^0$, and $p_3 = 1.27 \times 10^3$.

The primary relaxation times τ for each oleogel can be calculated using the formula $\tau = \frac{\eta_0}{G_0}$. Figure (100) illustrates that the average relaxation time of the oleogels exhibits an exponential dependence on the mass fraction of cotton cellulose. This finding indicates that cellulose fibers introduce a memory effect into the dynamic system of the oleogel, suggesting the presence of elastic properties that increase significantly with the addition of more cellulose.

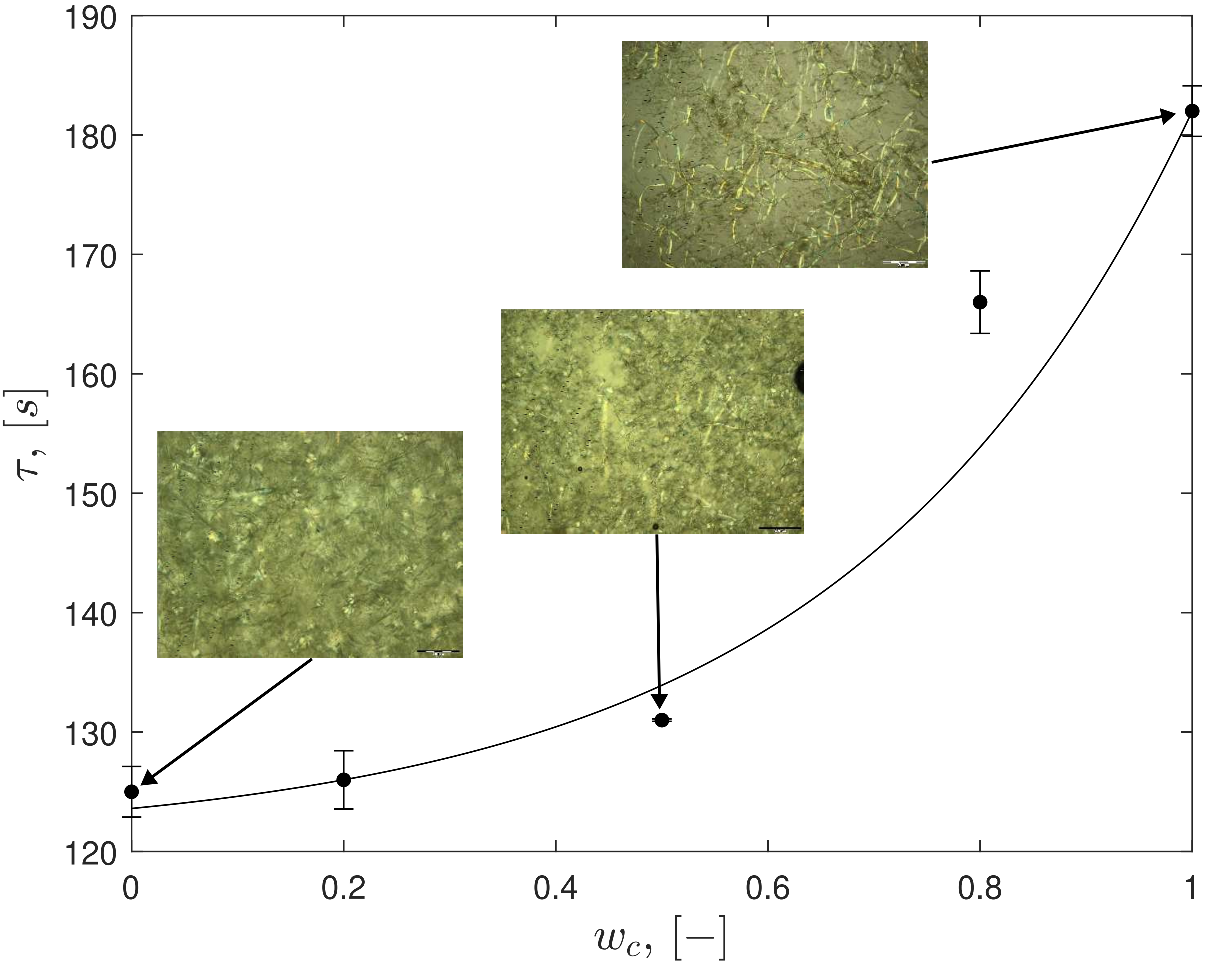

Figure 100 – Main relaxation time τ of the oleogels as a function of cellulose mass fraction w_c, with experimental error bars. The experiment was conducted at a controlled temperature of $20°C$. The curve is a fit of the experimental data to an expression of the type: $\tau(w_c) = p_1 + p_2 \exp(p_3 w_c)$. The fitting parameters are: $p_1 = 1.20 \times 10^2$, $p_2 = 2.82 \times 10^0$, and $p_3 = 3.08 \times 10^0$.

7 Final Considerations and Next Steps of the Work

7.1 Final Considerations

The viscosity of the magnetorheological fluids of magnetite and carbonyl-iron increased when they were subjected to an increasing external magnetic field. This behavior is called magnetoviscous effect and it has its origin in the fact that when a magnetic particle is subjected to an external magnetic field, its moment of dipole aligns with the direction of the applied field, what implies that the particle is no longer free to rotate with the vorticity of the flow. This effect was very intense in both magnetovrheological suspensions, due to the fact that the magnetic suspensions form chains and aggregates of particles by the action of dipolar interactions. Moreover, this structures provoke higher hindrances of rotation when aligned to the magnetic field owing to its larger characteristic lengths, what increases the local drag. These mechanisms induce energy dissipation and are the motives behind the strong magnetoviscous effect observed. It is important to remark that the magnetoviscous effect of the MRS of carbonyl-iron was much more pronounced than the one observed for the MRS of magnetite. This result is correlated to the more pronounced magnetization of saturation of the MRS of carbonyl-iron, what facilitates the formation of bigger and stabler complex microstructures on this fluid.

It has also been observed a pseudoplastic behavior for both magnetorheological suspensions when under the action of a magnetic field and also in the absence of it. This shear-tinning behavior was characterized by the observation of a strong decrease of the apparent viscosity of the magnetorheological suspensions, when they were subjected to increasingly strong shear rates. This effect is associated to the fact that in concentrated MRS, like the ones treated in this work, the application of a magnetic field is followed by the formation of chains and aggregates of particles. For weak flow conditions, the viscosity of both fluids was observed to reach high values, what is a natural consequence of the magnetoviscous effect previously discussed. However, when the flow starts to intensify, the viscosity starts to decrease rapidly, showing a power-law fashion. This behavior is explained by two process: the first one is related to the weak flow region, in which the flow starts to induce an alignment of the field induced microstructure with its streamlines, in a process that results on the reduction of local drag and, as a result, of the suspension's viscosity. Nontheless, the main process responsible for the reduction of viscosity is the breakup of the field induced microstructures, leading to chains and agglomerates with ever small length scales, that generate less energy dissipation effects, leading to the strong reduction of the apparent viscosity. All the effects describe for the shear-thinning behavior were observed to be more intense the higher the intensity of the magnetic field, what is related to the fact that stronger magnetic fields produce microstructures formed by stabler and larger particle's chains and agglomerates.

It was also observed that, in the presence of a magnetic field, the magnethorheological suspension of magnetite and the magnetorheological suspension of carbonyl-iron become viscoelastic liquids. This was first verified in the experiments of step-strain, conducted with a small angular strain, for increasing values of magnetic field intensity. In all field conditions, the fluids presented a delay on its process of stress relaxation, which is a direct sign of the presence of elastic behavior. This elastic properties arise from the formation of a microstructure, due to the action of the magnetic field. The process of relaxation is generally characterized by a single time of relaxation, which traduces the action of the main mechanism of stress relaxation acting in the fluid. In this case, the shear stress relaxes to zero after the cessation of flow. Nonetheless, the relaxation process, of the MRS in analysis, was found to be highly complex, characterized by more than one time of relaxation and by the relaxation of the shear stress for a non-zero value, after the cessation of the flow. The residual stress can be understood as the yield stress of the fluid, due to the fact that it represents the minimum stress to which the stress relax, or from other point of view, the minimum stress that must be applied, in order for the fluid starts to flow. This process of relaxation was found to be well modeled by an adaptation of Maxwell's viscoelastic constitutive model. The adaptation made the inclusion of a term regarding the residual stress. Using this model it was possible to determine the times of relaxation, of each fluid, at each condition of magnetic field intensity. The MRS of magnetite was well described by two relaxation times as well as the MRS of carbonyl-iron, for every condition of field.

The study of aqueous suspensions of double-walled carbon nanotubes revealed that their viscosity depends on both the particle volume fraction (ϕ) and the applied shear rate. These fluids exhibit pseudoplastic behavior. Through experiments conducted under step-strain regimes, the relaxation time of each suspension was determined as a function of ϕ, with the relationship found to be linear. Additionally, it was observed that the shear stress did not relax to zero over time. This behavior indicates the presence of a coherent microstructure of nanotube aggregates within the fluid, responsible for a residual stress that varies with ϕ. The suspensions demonstrated viscoelastic properties with a predominantly elastic response, as evidenced by the determination of the shear elastic modulus as a nonlinear function of ϕ. Finally, the zero-shear viscosity was also quantified and found to exhibit a nonlinear dependence on ϕ, reflecting the complex rheological behavior of these suspensions under varying flow conditions.

The study of oleogels composed of potato starch and cotton cellulose revealed that their viscosity is significantly influenced by temperature changes and shear rate. These fluids exhibit pseudoplastic behavior, demonstrated by a reduction in viscosity as shear rate increases. This phenomenon is associated with the disruption and alignment of the oleogel's internal network structures under shear flow.

Small amplitude oscillatory shear experiments facilitated the indirect determination of relaxation times as a function of the mass fraction of cellulose, w_c, through the analysis of the viscoelastic moduli. Furthermore, the zero-shear viscosity and the shear elastic modulus were determined as functions of w_c. Both relationships exhibited non-linear dependencies, reflecting the complex interplay between the composition of the oleogels and their microstructural properties.

7.2 Suggestion for future works

- Study the complex fluids in the regime of large amplitude oscillatory shear, using methodologies like Fourier transform and Lissajous curves;

- In order to study and account for the influence of formation of very anisotropic structures, like chains of non-magnetic particles, fibers and nanotubes of carbon, we shall add to the stress tensor the following therm, according Albernaz and Cunha (2013):

  $$\langle \boldsymbol{\sigma} \rangle_A = \beta \left[\langle \hat{\boldsymbol{s}} \rangle \cdot \langle \boldsymbol{D} \rangle \cdot \langle \hat{\boldsymbol{s}} \rangle \right] \langle \hat{\boldsymbol{s}}\hat{\boldsymbol{s}} \rangle. \tag{7.1}$$

  In this case, the stress tensor becomes:

  $$\langle \boldsymbol{\sigma} \rangle = -\langle p \rangle \boldsymbol{I} + 2\eta_\phi \langle \boldsymbol{D} \rangle + \beta \left[\langle \hat{\boldsymbol{s}} \rangle \cdot \langle \boldsymbol{D} \rangle \cdot \langle \hat{\boldsymbol{s}} \rangle \right] \langle \hat{\boldsymbol{s}}\hat{\boldsymbol{s}} \rangle. \tag{7.2}$$

  In this case, we have a kinematic equation for the evolution of $\hat{\boldsymbol{s}}$ that shall be considered:

  $$\frac{D\langle \boldsymbol{s} \rangle}{Dt} = \boldsymbol{W} \cdot \langle \boldsymbol{s} \rangle + \boldsymbol{D} \cdot \langle \boldsymbol{s} \rangle - \left(\langle \boldsymbol{s} \rangle \cdot \boldsymbol{D} \cdot \langle \boldsymbol{s} \rangle \right) \langle \boldsymbol{s} \rangle, \tag{7.3}$$

  where $\boldsymbol{D}$ is the rate of deformation tensor and $\boldsymbol{W}$ denotes the rate of rotation tensor.

  In the case of magnetorheological suspension, the anisotropic therm (7.1) will be added to the expression of the stress tensor of a suspension of magnetic particles presented by Cunha and Gontijo (2024). As a result, the constitutive model becomes:

  $$\langle \boldsymbol{\sigma} \rangle = -\langle p \rangle^* \boldsymbol{I} + 2\eta_\phi \langle \boldsymbol{D} \rangle + \frac{\mu_0}{2}(\boldsymbol{HM} - \boldsymbol{MH}) + \beta \left[\langle \hat{\boldsymbol{s}} \rangle \cdot \langle \boldsymbol{D} \rangle \cdot \langle \hat{\boldsymbol{s}} \rangle \right] \langle \hat{\boldsymbol{s}}\hat{\boldsymbol{s}} \rangle. \tag{7.4}$$

  Observe that $\beta = \beta(\ell, n)$ and, in the magnetic case, $\ell = \ell(H, \dot{\gamma})$. Besides that, note that $\langle \boldsymbol{\sigma}' \rangle = \boldsymbol{Q} \cdot \langle \boldsymbol{\sigma} \rangle \cdot \boldsymbol{Q}^T$. We want to apply numerically a simple shearing flow to a fluid modeled by equation (7.4) in the presence of an external magnetic field. The equation for the evolution of the magnetization is the one by Shliomis (1971):

$$\frac{\partial \boldsymbol{M}}{\partial t} = \frac{1}{2}\boldsymbol{\xi} \times \boldsymbol{M} - \boldsymbol{v} \cdot \nabla \boldsymbol{M} - \frac{\mu_0}{6\eta_0 \phi}\boldsymbol{M} \times (\boldsymbol{M} \times \boldsymbol{H}) \tag{7.5}$$

First, it is important to study two asymptotic cases: the first one accounts for a situation where the flow is weak and, thus, the rheology is dominated by the external magnetic field, that is $\hat{\boldsymbol{s}} = \frac{\boldsymbol{H}}{|\boldsymbol{H}|}$. The second situation occurs when the flow is very strong and the magnetic field is weak, as a result $\hat{\boldsymbol{s}} = \frac{\boldsymbol{v}}{|\boldsymbol{v}|}$. At any stage between these situations, one shall use: $\hat{\boldsymbol{s}} = \frac{\boldsymbol{M}}{|\boldsymbol{M}|}$.

We aim to obtain rheological information of the suspension such as viscosity, viscoelastic moduli and difference of normal stresses in order to compare with experimental data.

Bibliography

AGO, M.; FERRER, A.; ROJAS, O. J. Starch-based biofoams reinforced with lignocellulose nanofibrils from residual palm empty fruit bunches: Water sorption and mechanical strength. *ACS Sustainable Chemistry & Engineering*, ACS Publications, v. 4, n. 10, p. 5546–5552, 2016. Citado na página 18.

ALAVI, F.; CIFTCI, O. N. Effect of starch type and chitosan supplementation on physicochemical properties, morphology, and oil structuring capacity of composite starch bioaerogels. *Food Hydrocolloids*, Elsevier, v. 141, p. 108637, 2023. Citado na página 18.

ALBERNAZ, D.; CUNHA, F. Unsteady motion of a spherical bubble in a complex fluid: mathematical modelling and simulation. *Applied Mathematical Modelling*, Elsevier, v. 37, n. 20-21, p. 8972–8984, 2013. Citado na página 157.

ARUTYUNYAN, N.; BAKLASHEV, D.; OBRAZTSOVA, E. Suspensions of single-wall carbon nanotubes stabilized by pluronic for biomedical applications. *The European Physical Journal B*, Springer, v. 75, n. 2, p. 163–166, 2010. Citado na página 1.

ASHTIANI, M.; HASHEMABADI, S.; GHAFFARI, A. A review on the magnetorheological fluid preparation and stabilization. *Journal of magnetism and Magnetic Materials*, Elsevier, v. 374, p. 716–730, 2015. Citado 3 vezes nas páginas 4, 5, and 6.

BARNES, H. A.; HUTTON, J. F.; WALTERS, K. *An introduction to rheology.* [S.l.]: Elsevier, 1989. v. 3. Citado 4 vezes nas páginas 24, 25, 43, and 143.

BATCHELOR, G. Slender-body theory for particles of arbitrary cross-section in stokes flow. *Journal of Fluid Mechanics*, Cambridge University Press, v. 44, n. 3, p. 419–440, 1970. Citado 8 vezes nas páginas 37, 39, 40, 55, 111, 117, 118, and 132.

BATCHELOR, G. The stress system in a suspension of force-free particles. *Journal of fluid mechanics*, Cambridge University Press, v. 41, n. 3, p. 545–570, 1970. Citado na página 144.

BAXTER-DRAYTON, Y.; BRADY, J. F. Brownian electrorheological fluids as a model for flocculated dispersions. *Journal of Rheology*, The Society of Rheology, v. 40, n. 6, p. 1027–1056, 1996. Citado na página 13.

BIRD, R. B.; ARMSTRONG, R. C.; HASSAGER, O. Dynamics of polymeric liquids. volume 1: fluid mechanics. *A Wiley-Interscience Publication, John Wiley & Sons, New York*, 1987. Citado 5 vezes nas páginas 22, 25, 49, 106, and 120.

BIRD, R. B. et al. Dynamics of polymer liquids vol. 2 kinetic theory. *A Wiley-Interscience Publication, John Wiley & Sons, New York*, 1987. Citado 2 vezes nas páginas 43 and 105.

BOMBARD, A. J. et al. Magnetic susceptibility and saturation magnetization of some carbonyl iron powders used in magnetorheological fluids. In: TRANS TECH PUBL. *Materials science forum*. [S.l.], 2003. v. 416, p. 753. Citado na página 47.

BONNECAZE, R.; BRADY, J. Yield stresses in electrorheological fluids. *Journal of Rheology*, The Society of Rheology, v. 36, n. 1, p. 73–115, 1992. Citado na página 8.

BORIN, D. Y. et al. Stress relaxation in a ferrofluid with clustered nanoparticles. *Journal of Physics: Condensed Matter*, IOP Publishing, v. 26, n. 40, p. 406002, 2014. Citado na página 108.

BOSSIS, G. et al. Magnetorheology: fluids, structures and rheology. In: *Ferrofluids*. [S.l.]: Springer, 2002. p. 202–230. Citado 6 vezes nas páginas ix, 8, 9, 10, 11, and 13.

BRADY, J. F.; BOSSIS, G. Stokesian dynamics. *Annual review of fluid mechanics*, Annual Reviews 4139 El Camino Way, PO Box 10139, Palo Alto, CA 94303-0139, USA, v. 20, n. 1, p. 111–157, 1988. Citado na página 8.

CASTRO, V. G. et al. Improved functionalization of multiwalled carbon nanotubes in ultra-low acid volume: effect of solid/liquid interface. *Journal of the Brazilian Chemical Society*, SciELO Brasil, v. 30, p. 2477–2487, 2019. Citado 4 vezes nas páginas xvii, 111, 114, and 119.

CHEN, Z. et al. A novel approach of preparing ultrafine magnetic metallic particles and the magnetorheology measurements for suspensions containing these particles. In: *Proceedings of the 6th International Conference on ER Fluids, MR Suspensions*. [S.l.: s.n.], 1998. p. 486–493. Citado na página 11.

CHIN, B. D.; WINTER, H. H. Field-induced gelation, yield stress, and fragility of an electro-rheological suspension. *Rheologica acta*, Springer, v. 41, n. 3, p. 265–275, 2002. Citado na página 15.

CONTRERAS-MATEUS, M. D. et al. Ferrofluids and magnetism in the oil industry: Theories, challenges, and current applications—a comprehensive review. *Physics of Fluids*, AIP Publishing, v. 36, n. 12, 2024. Citado na página 2.

CUNHA, F. D.; HINCH, E. Shear-induced dispersion in a dilute suspension of rough spheres. *Journal of fluid mechanics*, Cambridge University Press, v. 309, p. 211–223, 1996. Citado na página 46.

CUNHA, F. R. *Lecture notes of the course dinamics of Non-Newtonian fluids*. Tese (Doutorado) — University of Brasília, 2016. Citado na página 25.

CUNHA, F. R. *Lecture notes of the course on microhydrodynamics*. Brasília: [s.n.], 2024. Citado 2 vezes nas páginas 37 and 39.

CUNHA, F. R.; GONTIJO, R. G. Revisiting the governing equations of a magnetic suspension of polar particles: From microhydrodynamics analysis to rheological response. *Physics of Fluids*, AIP Publishing, v. 36, n. 8, 2024. Citado na página 157.

CUNHA, F. R.; ROSA, A. P. Effect of particle dipolar interactions on the viscoelastic response of dilute ferrofluids undergoing oscillatory shear. *Physics of Fluids*, AIP Publishing, v. 33, n. 9, 2021. Citado na página 3.

CUNHA, F. R.; ROSA, A. P.; DIAS, N. J. Rheology of a very dilute magnetic suspension with micro-structures of nanoparticles. *Journal of Magnetism and Magnetic Materials*, Elsevier, v. 397, p. 266–274, 2016. Citado 3 vezes nas páginas 5, 72, and 78.

CUNHA, F. R.; SINZATO, Y. Z.; PEREIRA, I. D. O. An experimental investigation on the magnetoviscous effect and shear rate-dependent viscosity of a magnetic suspension under longitudinal and transverse magnetic fields. *Physics of Fluids*, AIP Publishing LLC, v. 34, n. 9, p. 093314, 2022. Citado na página 2.

DAVIDOVICH-PINHAS, M. Oil structuring using polysaccharides. *Current Opinion in Food Science*, Elsevier, v. 27, p. 29–35, 2019. Citado na página 17.

DESHMUKH, S. S.; MCKINLEY, G. H. Rheological behavior of magnetorheological suspensions under shear, creep and large amplitude oscillatory shear (laos) flow. *Proc. XIVth Int. Congr. on Rheology*, 2004. Citado na página 16.

DUNLOP, D.; ÖZDEMIR, Ö.; SCHUBERT, G. Magnetizations in rocks and minerals. *Treatise on geophysics*, v. 5, p. 277–336, 2015. Citado na página 66.

DYKE, S. et al. Modeling and control of magnetorheological dampers for seismic response reduction. *Smart materials and structures*, IOP Publishing, v. 5, n. 5, p. 565, 1996. Citado na página 1.

EINSTEIN, A. A new determination of the molecular dimensions (vol 19, pg 289, 1906). *Annalen der physik*, v. 34, n. 3, p. 591–592, 1911. Citado na página 72.

FAN, Z.; ADVANI, S. G. Rheology of multiwall carbon nanotube suspensions. *Journal of Rheology*, The Society of Rheology, v. 51, n. 4, p. 585–604, 2007. Citado na página 1.

FELT, D. W. et al. Rheology of a magnetorheological fluid. *Journal of Intelligent Material Systems and Structures*, Sage Publications Sage UK: London, England, v. 7, n. 5, p. 589–593, 1996. Citado na página 13.

FOISTER, R. T.; IYENGAR, V. R.; YURGELEVIC, S. M. *Stabilization of magnetorheological fluid suspensions using a mixture of organoclays*. [S.l.]: Google Patents, 2003. US Patent 6,592,772. Citado na página 6.

FURLANI, E. P. *Permanent magnet and electromechanical devices: materials, analysis, and applications*. [S.l.]: Academic press, 2001. Citado na página 52.

GANS, B. D. et al. The influence of particle size on the magnetorheological properties of an inverse ferrofluid. *The Journal of Chemical Physics*, American Institute of Physics, v. 113, n. 5, p. 2032–2042, 2000. Citado 2 vezes nas páginas ix and 13.

GANS, B.-J. et al. Non-linear magnetorheological behaviour of an inverse ferrofluid. *Faraday discussions*, Royal Society of Chemistry, v. 112, p. 209–224, 1999. Citado na página 13.

GENÇ, S.; PHULÉ, P. P. Rheological properties of magnetorheological fluids. *Smart Materials and Structures*, IOP Publishing, v. 11, n. 1, p. 140, 2002. Citado 2 vezes nas páginas 4 and 12.

GILL, S. K. et al. Dietary fibre in gastrointestinal health and disease. *Nature Reviews Gastroenterology & Hepatology*, Nature Publishing Group UK London, v. 18, n. 2, p. 101–116, 2021. Citado na página 18.

GINDER, J.; DAVIS, L.; ELIE, L. Rheology of magnetorheological fluids: models and measurements. *International journal of modern physics b*, World Scientific, v. 10, n. 23n24, p. 3293–3303, 1996. Citado 2 vezes nas páginas 12 and 15.

HATO, M. J. et al. Magnetic carbonyl iron suspension with organoclay additive and its magnetorheological properties. *Colloids and Surfaces A: Physicochemical and Engineering Aspects*, Elsevier, v. 377, n. 1-3, p. 103–109, 2011. Citado na página 6.

HOBBIE, E. K. Shear rheology of carbon nanotube suspensions. *Rheologica acta*, Springer, v. 49, n. 4, p. 323–334, 2010. Citado na página 1.

IYENGAR, V. R.; FOISTER, R. T. *Use of high surface area untreated fumed silica in MR fluid formulation.* [S.l.]: Google Patents, 2002. US Patent 6,451,219. Citado na página 6.

IYENGAR, V. R.; YURGELEVIC, S. M.; FOISTER, R. T. *Magnetorheological fluid with a fluorocarbon thickener.* [S.l.]: Google Patents, 2010. US Patent 7,731,863. Citado na página 6.

JIANG, F. et al. Magnetorheological materials and their application in shock absorbers. In: *Proceedings of the 6th International Conference on ER Fluids, MR Suspensions and Their Applications, Yonezawa.* [S.l.: s.n.], 1997. p. 22–25. Citado na página 11.

JR, B. S. et al. Phenomenological model for magnetorheological dampers. *Journal of engineering mechanics*, American Society of Civil Engineers, v. 123, n. 3, p. 230–238, 1997. Citado na página 1.

KARAMI, M. et al. A new application of carbon nanotubes nanofluid as working fluid of low-temperature direct absorption solar collector. *Solar Energy Materials and Solar Cells*, Elsevier, v. 121, p. 114–118, 2014. Citado na página 1.

KAVYA, M. et al. Edible oleogels based on high molecular weight oleogelators and its prospects in food applications. *Critical reviews in food science and nutrition*, Taylor & Francis, v. 64, n. 13, p. 4432–4455, 2024. Citado na página 17.

KIM, S.; KARRILA, S. J. *Microhydrodynamics: principles and selected applications.* [S.l.]: Courier Corporation, 2013. Citado na página 36.

KLINE, S. J.; MCCLINTOCK, F. A. Describing uncertainties in single-sample experiments. *Mechanical Engineering*, v. 75, p. 3–8, 1953. Citado na página 168.

KLINGENBERG, D. J. Magnetorheology: Applications and challenges. *American Institute of Chemical Engineers. AIChE Journal*, American Institute of Chemical Engineers, v. 47, n. 2, p. 246, 2001. Citado na página 1.

KORDONSKY, V. et al. Physical properties of magnetizable structure-reversible media. *Journal of Magnetism and Magnetic Materials*, Elsevier, v. 85, n. 1-3, p. 114–120, 1990. Citado na página 12.

KUMAR, J. S. et al. A review of challenges and solutions in the preparation and use of magnetorheological fluids. *International Journal of Mechanical and Materials Engineering*, Springer, v. 14, n. 1, p. 13, 2019. Citado 3 vezes nas páginas 4, 5, and 6.

LAVOINE, N.; BERGSTRÖM, L. Nanocellulose-based foams and aerogels: Processing, properties, and applications. *Journal of Materials Chemistry A*, Royal Society of Chemistry, v. 5, n. 31, p. 16105–16117, 2017. Citado na página 18.

LAVOINE, N. et al. Microfibrillated cellulose–its barrier properties and applications in cellulosic materials: A review. *Carbohydrate polymers*, Elsevier, v. 90, n. 2, p. 735–764, 2012. Citado na página 18.

LI, J. et al. Fabrication of aerogel-templated oleogels from alginate-gelatin conjugates for in vitro digestion. *Carbohydrate Polymers*, Elsevier, v. 291, p. 119603, 2022. Citado na página 17.

LIU, B. et al. A novel oleogel based on porous microgel from egg white. *Food Hydrocolloids*, Elsevier, v. 144, p. 109049, 2023. Citado na página 17.

LÓPEZ-LÓPEZ, M. T.; KUZHIR, P.; BOSSIS, G. Magnetorheology of fiber suspensions. i. experimental. *Journal of Rheology*, The Society of Rheology, v. 53, n. 1, p. 115–126, 2009. Citado 2 vezes nas páginas 5 and 6.

LÓPEZ-LÓPEZ, M. T. et al. Preparation of well-dispersed magnetorheological fluids and effect of dispersion on their magnetorheological properties. *Rheologica Acta*, Springer, v. 47, n. 7, p. 787–796, 2008. Citado 2 vezes nas páginas 5 and 6.

MA, A.; CHINESTA, F.; MACKLEY, M. The rheology and modeling of chemically treated carbon nanotubes suspensions. *Journal of Rheology*, AIP Publishing, v. 53, n. 3, p. 547–573, 2009. Citado na página 17.

MA, A. W.; CHINESTA, F.; MACKLEY, M. R. The rheology of carbon nanotube (cnt) suspensions: Experiments and modelling. In: AMERICAN INSTITUTE OF PHYSICS. *AIP Conference Proceedings*. [S.l.], 2008. v. 1027, n. 1, p. 752–754. Citado na página 16.

MALVAR, S.; CUNHA, F. R. A theoretical model for studying the nonlinear viscoelastic response of an active fluid undergoing oscillatory shear. *Physics of Fluids*, AIP Publishing LLC, v. 33, n. 9, p. 091903, 2021. Citado na página 4.

MANZETTI, S.; GABRIEL, J.-C. P. Methods for dispersing carbon nanotubes for nanotechnology applications: liquid nanocrystals, suspensions, polyelectrolytes, colloids and organization control. *International Nano Letters*, Springer, v. 9, n. 1, p. 31–49, 2019. Citado na página 2.

MANZOCCO, L. et al. Exploitation of κ-carrageenan aerogels as template for edible oleogel preparation. *Food Hydrocolloids*, Elsevier, v. 71, p. 68–75, 2017. Citado na página 17.

MARSHALL, L.; ZUKOSKI, C. F.; GOODWIN, J. W. Effects of electric fields on the rheology of non-aqueous concentrated suspensions. *Journal of the Chemical Society, Faraday Transactions 1: Physical Chemistry in Condensed Phases*, Royal Society of Chemistry, v. 85, n. 9, p. 2785–2795, 1989. Citado na página 13.

MCCAIG, M.; CLEGG, A. G. Permanent magnets in theory and practice. *(No Title)*, 1987. Citado na página 52.

MOHEBI, M.; JAMASBI, N.; LIU, J. Simulation of the formation of nonequilibrium structures in magnetorheological fluids subject to an external magnetic field. *Physical Review E*, APS, v. 54, n. 5, p. 5407, 1996. Citado na página 10.

MORRISON, F. A. *Understanding rheology*. [S.l.]: Oxford University Press, USA, 2001. Citado 2 vezes nas páginas 22 and 23.

ODENBACH, S. *Colloidal magnetic fluids: basics, development and application of ferrofluids*. [S.l.]: Springer, 2009. v. 763. Citado 4 vezes nas páginas x, 50, 51, and 52.

ODENBACH, S.; THURM, S. Magnetoviscous effects in ferrofluids. In: *Ferrofluids*. [S.l.]: Springer, 2002. p. 185–201. Citado na página 51.

OLDROYD, J. Non-newtonian flow of liquids and solids. *Rheology: theory and applications*, New York: Academic, v. 1, p. 653–682, 1956. Citado 2 vezes nas páginas 21 and 25.

ONG, K. J. et al. A 90-day dietary study with fibrillated cellulose in sprague-dawley rats. *Toxicology reports*, Elsevier, v. 7, p. 174–182, 2020. Citado na página 18.

PARTHASARATHY, M.; KLINGENBERG, D. J. Large amplitude oscillatory shear of er suspensions. *Journal of non-newtonian fluid mechanics*, Elsevier, v. 81, n. 1-2, p. 83–104, 1999. Citado 3 vezes nas páginas ix, 14, and 15.

PATEL, A. R. Formation and properties of biopolymer-based oleogels. *Crystallization of lipids: Fundamentals and applications in food, cosmetics, and pharmaceuticals*, Wiley Online Library, p. 385–404, 2018. Citado na página 17.

PATEL, A. R. et al. Biopolymer-based structuring of liquid oil into soft solids and oleogels using water-continuous emulsions as templates. *Langmuir*, ACS Publications, v. 31, n. 7, p. 2065–2073, 2015. Citado na página 17.

PATEL, A. R. et al. A foam-templated approach for fabricating organogels using a water-soluble polymer. *Rsc Advances*, Royal Society of Chemistry, v. 3, n. 45, p. 22900–22903, 2013. Citado na página 17.

PEREIRA, I. D. O.; CUNHA, F. R. Rheological response in shear flows of a thermosensitive elastic liquid in the presence of some additives. *Rheologica Acta*, Springer, v. 59, n. 5, p. 307–316, 2020. Citado na página 2.

PEREIRA, I. D. O.; CUNHA, F. R. Rheological response of ferrofluids undergoing unsteady shear flows in the presence of a magnetic field. *Physics of Fluids*, AIP Publishing, v. 35, n. 11, 2023. Citado na página 50.

PHULÉ, P. P.; MIHALCIN, M. P.; GENC, S. The role of the dispersed-phase remnant magnetization on the redispersibility of magnetorheological fluids. *Journal of Materials Research*, Cambridge University Press, v. 14, n. 7, p. 3037–3041, 1999. Citado 2 vezes nas páginas 5 and 11.

PIPKIN, A. C. *Lectures on viscoelasticity theory*. [S.l.]: Springer Science & Business Media, 2012. v. 7. Citado na página 14.

PORTILLO, M. A.; IGLESIAS, G. Magnetic nanoparticles as a redispersing additive in magnetorheological fluid. *Journal of Nanomaterials*, Hindawi, v. 2017, 2017. Citado 3 vezes nas páginas ix, 6, and 7.

PUșCAș, A. et al. Oleogels in food: A review of current and potential applications. *Foods*, MDPI, v. 9, n. 1, 2020. Citado na página 17.

RABINOW, J. The magnetic fluid clutch. *Electrical Engineering*, IEEE, v. 67, n. 12, p. 1167–1167, 1948. Citado na página 1.

RANKIN, P. J.; HORVATH, A. T.; KLINGENBERG, D. J. Magnetorheology in viscoplastic media. *Rheologica Acta*, Springer, v. 38, n. 5, p. 471–477, 1999. Citado 2 vezes nas páginas 11 and 12.

RAZMARA, N.; NAMARVARI, H.; MENEGHINI, J. R. A new correlation for viscosity of model water-carbon nanotube nanofluids: Molecular dynamics simulation. *Journal of Molecular Liquids*, Elsevier, v. 293, p. 111438, 2019. Citado na página 17.

ROSA, A. P.; CUNHA, F. R. The influence of dipolar particle interactions on the magnetization and the rotational viscosity of ferrofluids. *Physics of Fluids*, AIP Publishing LLC, v. 31, n. 5, p. 052006, 2019. Citado na página 3.

ROSENSWEIG, R. E. *Ferrohydrodynamics*. [S.l.]: Courier Corporation, 2013. Citado 2 vezes nas páginas 8 and 66.

SALAS, F. M. A. *Modelagem microestrutural de líquidos elásticos em escoamentos*. Dissertação (Mestrado) — Programa de pós-graduação em ciências mecânicas. Universidade de Brasília, Brasília - DF, 2006. Citado na página 27.

SARKAR, C.; HIRANI, H. Synthesis and characterization of antifriction magnetorheological fluids for brake. *Defence science journal*, Defence Scientific Information & Documentation Centre, v. 63, n. 4, p. 408, 2013. Citado na página 6.

SHAN, G. et al. Dual-reinforcement strategy: Fabrication of cmc-na/spi aerogel-templated oleogels through electrostatic adsorption and chemical crosslinking. *Food Hydrocolloids*, Elsevier, v. 148, p. 109525, 2024. Citado na página 18.

SHAQFEH, E. S.; FREDRICKSON, G. H. The hydrodynamic stress in a suspension of rods. *Physics of Fluids A: Fluid Dynamics*, American Institute of Physics, v. 2, n. 1, p. 7–24, 1990. Citado 2 vezes nas páginas 55 and 111.

SHLIOMIS, M. I. Effective viscosity of magnetic suspensions. *Zh. Eksp. Teor. Fiz*, v. 61, n. 2411, p. s1971d, 1971. Citado na página 157.

SINZATO, Y. Z.; CUNHA, F. R. Modeling and experiments of capillary flow of non-symmetric magnetic fluids under uniform field. *Journal of Magnetism and Magnetic Materials*, Elsevier, v. 508, p. 166867, 2020. Citado na página 2.

SINZATO, Y. Z.; CUNHA, F. R. Capillary flow of magnetic fluids with effect of hydrodynamic dispersion. *Physics of Fluids*, AIP Publishing LLC, v. 33, n. 10, p. 102006, 2021. Citado na página 3.

SISKO, A. The flow of lubricating greases. *Industrial & Engineering Chemistry*, ACS Publications, v. 50, n. 12, p. 1789–1792, 1958. Citado na página 24.

STURGES, H. A. The choice of a class interval. *Journal of the american statistical association*, New York, v. 21, n. 153, p. 65–66, 1926. Citado na página 55.

SUNKARA, S. et al. Iron oxidation and its impact on mr behavior. In: *Journal of Physics: Conference Series*. [S.l.: s.n.], 2009. v. 149, p. 012081. Citado na página 7.

TANNER, R. I. *Engineering rheology*. [S.l.]: OUP Oxford, 2000. v. 52. Citado na página 46.

UPADHYAY, R.; LAHERISHETH, Z.; SHAH, K. Rheological properties of soft magnetic flake shaped iron particle based magnetorheological fluid in dynamic mode. *Smart materials and structures*, IOP Publishing, v. 23, n. 1, p. 015002, 2013. Citado na página 15.

VICENTE, J. D.; KLINGENBERG, D. J.; HIDALGO-ALVAREZ, R. Magnetorheological fluids: a review. *Soft matter*, Royal Society of Chemistry, v. 7, n. 8, p. 3701–3710, 2011. Citado 12 vezes nas páginas ix, 1, 4, 5, 6, 7, 10, 12, 13, 14, 15, and 16.

VICENTE, J. de et al. Shear flow behavior of confined magnetorheological fluids at low magnetic field strengths. *Rheologica acta*, Springer, v. 44, n. 1, p. 94–103, 2004. Citado na página 14.

VOLKOVA, O. et al. Magnetorheology of magnetic holes compared to magnetic particles. *Journal of Rheology*, The Society of Rheology, v. 44, n. 1, p. 91–104, 2000. Citado na página 14.

WAHID, S. et al. Magneto-rheological defects and failures: A review. *Proceeding of, IOP Publishing*, v. 114, n. 1, p. 1–11, 2016. Citado na página 7.

WANG, J.; CHEN, Y.; BLAU, W. J. Carbon nanotubes and nanotube composites for nonlinear optical devices. *Journal of Materials Chemistry*, Royal Society of Chemistry, v. 19, n. 40, p. 7425–7443, 2009. Citado na página 2.

WANG, J.; CHEN, Z.; NAGUIB, H. E. Preparation of a novel double crosslinked chitin aerogel via etherification with high strength. *Carbohydrate polymers*, Elsevier, v. 265, p. 118014, 2021. Citado na página 17.

WANG, J.; MENG, G. Magnetorheological fluid devices: principles, characteristics and applications in mechanical engineering. *Proceedings of the Institution of Mechanical Engineers, Part L: Journal of Materials: Design and Applications*, SAGE Publications Sage UK: London, England, v. 215, n. 3, p. 165–174, 2001. Citado na página 1.

WÜSTENBERG, T. *Cellulose and cellulose derivatives in the food industry: fundamentals and applications*. [S.l.]: John Wiley & Sons, 2014. Citado na página 18.

YEARSLEY, K. M. et al. The rheology of multiwalled carbon nanotube and carbon black suspensions. *Journal of Rheology*, AIP Publishing, v. 56, n. 6, p. 1465–1490, 2012. Citado 2 vezes nas páginas 16 and 17.

ZHANG, J. et al. Effect of seven different additives on the properties of mr fluids. In: *Journal of Physics: Conference Series*. [S.l.: s.n.], 2009. v. 149, p. 012086. Citado na página 6.

ZHAO, W. et al. Development of food-grade oleogel via the aerogel-templated method: Oxidation stability, astaxanthin delivery and emulsifying application. *Food Hydrocolloids*, Elsevier, v. 134, p. 108058, 2023. Citado na página 18.

ZHAO, Y.-W.; TIAN, M.-Z.; HUANG, P. Starch/clay aerogel reinforced by cellulose nanofibrils for thermal insulation. *Cellulose*, Springer, v. 28, p. 3505–3513, 2021. Citado na página 18.

Appendix

A Uncertainty analysis

The analysis of the experimental error associated to a measured variable follows, in this dissertation, the protocol prescribe on Kline and McClintock (1953). In the referred work, the experimental error of the measured variable $\mathcal{V}$, $E(\mathcal{V})$, is defined as:

$$E(\mathcal{V}) = \max\left(E_i(\mathcal{V}), E_r(\mathcal{V})\right), \tag{A.1}$$

where, $E_i(\mathcal{V})$ is the instrumental error, linked to the intrinsic variabilities of the instruments of measurement, and $E(\mathcal{V})_r$ is the random error, which is associated to the fluctuations of the measured value of the variable $\mathcal{V}$ over a finite number of measurement realizations.

Generally, if a variable is measured directly, the value of the instrumental error is the uncertainty of the instrument used to perform the measurement. However, if the variable is measure indirectly, the estimative of the instrumental error can be obtained by knowing the functional dependence between the indirectly measured variables and the directly measured ones. Regarding this context, consider an indirectly measured variable $\mathcal{V}$, which was calculated based on the directly measures of n quantities $q_1, q_2, ..., q_{n-1}, q_n$, with instrumental uncertainties $E_i(q_1), E_i(q_2), ..., E_i(q_{n-1}), E_i(q_n)$. Thus, according to Kline and McClintock (1953), the instrumental error associated with $\mathcal{V}(q_1, q_2, ..., q_{n-1}, q_n)$is given by

$$E_i(\mathcal{V}) = \left|\frac{\partial \mathcal{V}}{\partial q_1}\right| |E_i(q_1)| + \left|\frac{\partial \mathcal{V}}{\partial q_2}\right| |E_i(q_2)| + ... + \left|\frac{\partial \mathcal{V}}{\partial q_{n-1}}\right| |E_i(q_{n-1})| + \left|\frac{\partial \mathcal{V}}{\partial q_n}\right| |E_i(q_n)|. \tag{A.2}$$

Besides that, considering a process of measurement composed of n evaluations of $\mathcal{V}$, the random error associated with this quantity is defined as the standard deviation of the measuments carried out over the realizations, $\mathrm{SD}(\mathcal{V})$, which is calculated by:

$$E_r(\mathcal{V}) = \mathrm{SD}(\mathcal{V}) = \sqrt{\frac{\sum_{k=1}^{n}(\mathcal{V}_k - \overline{\mathcal{V}})^2}{n-1}}, \tag{A.3}$$

where $\mathcal{V}_k$ is the value of the referred variable in the k-th realization and $\overline{\mathcal{V}}$ is the mean value of $\mathcal{V}$, defined as:

$$\overline{\mathcal{V}} = \frac{\sum_{k=1}^{n}\mathcal{V}_k}{n}. \tag{A.4}$$

It is important to remark that, when the relationship between the quantity being indirectly measured and the ones that are actually being directly measured, is unknown, the experimental error will be defined uniquely by the random error.

In this dissertation, an experimental point, representing the measured variable $\mathcal{V}$ is defined as: $\overline{\mathcal{V}} \pm E(\mathcal{V})$. This representation is used to display, in graphs and on tables, the experimental uncertainty of the quantities measured in the experiments.

A.1 Uncertainty associated with the viscosity measured in simple shear

The uncertainty of the viscosity $E(\eta)$, measured with the parallel disks rheometer, was considered as the maximum of its random error $E_r(\eta)$ and instrumental error $E_i(\eta)$. The instrumental error is estimated here from the expression relating the viscosity to the mechanic torque and the shear rate applied, equation (3.11). Based on this, the instrumental error is given by:

$$E_i(\eta) = \left|\frac{\partial \eta}{\partial \mathcal{T}}\right| |E_i(\mathcal{T})| + \left|\frac{\partial \eta}{\partial R}\right| |E_i(R)| + \left|\frac{\partial \eta}{\partial \dot{\gamma}}\right| |E_i(\dot{\gamma})| \,. \tag{A.5}$$

According to the manufacturer of the rheometer, the torque uncertainty is $0.2\,\mu$N, and the one of the radius of the disk used in the experiment is 1×10^{-5}. The uncertainty associated with the shear rate is 1×10^{-3} s^{-1}.